MECHANICAL PROPERTIES AND *IN VITRO* MODELLING OF THE OSTEOCHONDRAL UNIT

by

MEGAN ELIN COOKE

A thesis submitted to the
University of Birmingham
for the degree of
DOCTOR OF PHILOSOPHY

School of Chemical Engineering
MRC Centre for Musculoskeletal Ageing
College of Engineering and Physical Sciences
University of Birmingham
October 2018

Abstract

The osteochondral unit (OCU) comprises bone and cartilage, with a gradient interface between hard and soft tissues. Damage and diseases, such as osteoarthritis (OA), cause irreversible changes to the cartilage matrix. Early, clinically silent, matrix changes in OA were compared to healthy, post-mortem cartilage using mechanical and physicochemical techniques. It was found that degradation of matrix components leaves the superficial region susceptible to mechanical damage. Strategies to repair cartilage damage have focused on replication of the extracellular matrix using hydrogel scaffolds. Alginate is commonly used, and its positive effects on chondrocyte phenotype have been attributed to maintenance of a spherical cell morphology. Here, an alginate fluid gel was formed to enable the non-invasive delivery of chondrocytes. It was found, however, that a spherical morphology was insufficient for maintenance of chondrocyte phenotype and geometric confinement of chondrocytes in alginate played a significant role in phenotypic recovery and stability. Fluid gels were then utilised as support matrices for bioprinting of bi-layered structures to recapitulate the OCU. This support matrix could suspend low-viscosity hydrocolloid solutions prior to crosslinking to co-culture chondrocyte and osteoblast populations in spatially defined regions. Distinct chemical and mechanical environments allowed the maintenance of primary cell phenotypes and function.

This thesis is dedicated to my
grandmother Nansi Booth who
sadly passed away during the
completion of my PhD.

She would've been incredibly
proud of us all, but I will always
be the smallest, and hence,
always her favourite.

ACKNOWLEDGEMENTS

Enormous thanks go to my supervisors Professor Liam Grover and Dr Simon Jones for all of their time, guidance and encouragement during my PhD. Liam, for always pushing me to be better and giving me so many opportunities, I am immensely grateful. Simon, as much as I will continue to insist that I am not a biologist, with your guidance, I am much closer than I ever expected to be. It's been a team effort.

I would also like to thank Professor Ed Davis, Professor Marytn Snow, the research nurses and patients or their next of kin involved in collection of tissue samples, without which, this PhD would've been impossible. Further I would like to thank the EPSRC Physical Sciences for Health CDT for funding this PhD.

I was incredibly fortunate to be a member of two research groups. The Jones group, who taught me most of the biology I know and put up with all of my questions, thank you. Ash and Mary, through terrifying me into submission you made me a better scientist and have been great friends as well as ridiculous examples of how to smash life. I hope you continue to live vicariously through my antics. TRAILab, a group of insanely competitive, fish and chips loving people, you are great. Special thanks go to all of my co-authors with shout-outs to Bernard Lawless (for the coffee), Sophie Cox (for the "you've got this" attitude), Amy Naylor (for the distractions from my actual PhD) and Neil Eisenstein (for a top-7 sunrise).

The friends on campus who've kept me sane. Phil Emmerson for countless discussions regarding Figure 6, we've made it. Sam Burrows, for winning the race, congratulations. Ollie for a guaranteed pint and Zoe for a rant about something or other I thank you all. Lastly, Kate Franklin you've been there since Day 1 at Birmingham and have been a constant support. How I've put up with you for this long I have no idea.

My final thanks go to the unwavering support of my family. To my parents, who gave me the opportunity to be whoever I wanted to be, by whatever route, you didn't expect me to be the one with a PhD... Sisters, you have been more support than you probably realised over the last 3 years and I know that wherever in the world we all may be, youve always got my back. You may still claim that I can't really read, but you will now refer to me solely as Dr Megs.

CONTENTS

LIST OF FIGURES

LIST OF TABLES

Abbreviation	Description
ACI	Autologous chondrocyte implantation
ADAMTS	A disintegrin and metalloproteinase with thrombospondin motifs
ALM	Additive layer manufacturing
ALP	Alkaline phosphatase
BGLAP	Bone gamma-carboxyglutamate protein (Osteocalcin)
Col I	Collagen type I
Col II	Collagen type II
CS	Chondroitin sulphate
DAMP	Damage associated molecular pattern
DMA	Dynamic mechanical analysis
DMEM	Dulbecco's Modified Eagle's medium
DMSO	Dimethyl sulphoxide
DTG	Dynamic thermogravimetry
ECM	Extracellular matrix
ELISA	Enzyme-linked immunosorbent assay
FBS	Fetal bovine serum
FC	Femoral condyle
FCD	Fixed charge density
FDM	Fused deposition modelling
FH	Femoral head
FI	Freshly isolated
GAG	Glycosaminoglycan
GG	Gellan gum
hAC	Human articular chondrocyte
HRP	Horse-radish peroxidase
IL	Interleukin
KS	Keratan sulphate
LVR	Linear viscoelastic region

MEW	Melt electrospinning writing
MMP	Matrix metalloproteinase
(nano)HAp	(Nanocrystalline) Hydroxyapatite
OA	Osteoarthritis
OCT	Optimal cutting temperature compound
OPG	Osteoprotegerin
PBS	Phosphate buffered saline
PCM	Pericellular matrix
PRG4	Proteoglycan-4
qRT-PCR	Quantitative real-time polymerase chain reaction
RA	Rheumatoid arthritis
RANK(L)	Receptor activator of nuclear factor kappa-B (ligand)
RNA	Ribonucleic acid
RUNX2	Runt-related transcription factor
SCB	Subchondral cortical bone
SEM	Scanning electron microscopy
sGAG	Sulphated glycosaminoglycan
Sox9	SRY (sex-determining region Y)-box-9
STB	Subchondral trabecular bone
SusMan	Suspended manufacture
SZP	Superficial zone protein
TE	Tissue engineering
TGA	Thermogravimetric analysis
THR	Total hip replacement
TKR	Total knee replacement
TP	Tibial plateau
μXRF	Micro x-ray fluorescence spectrometry
μCT	Micro computed tomography
WLI	White light interferometry

Peer-reviewed journal publications

Samuel R. Moxon* and **Megan E. Cooke***, Sophie C. Cox, Martyn Snow, Lee Jeys, Simon W. Jones, Alan M. Smith and Liam M. Grover. Suspended Manufacture of Biological Structures. *Advanced Materials* doi: 10.1002/adma.201605594 (2017)

Megan E. Cooke, Mark J. Pearson, Richard J. A. Moakes, Chris J. Weston, Edward T. Davis, Simon W. Jones and Liam M. Grover. Geometric confinement is required for recovery and maintenance of chondrocyte phenotype in alginate. *APL Bioengineering* doi: 10.1063/1.5006752 (2017)

Erik A. B. Hughes, Sophie C. Cox, **Megan E. Cooke**, Owen G. Davies, Richard L. Williams, Thomas J. Hall and Liam M. Grover. Interfacial Mineral Fusion and Tubule Entanglement as a Means to Harden a Bone Augmentation Material. *Advanced Healthcare Materials* doi: 10.1002/adhm.201701166 (2018)

Trina Majumdar, **Megan E. Cooke**, Bernard M. Lawless, Francis Bellier, Erik A. B. Hughes, Liam M. Grover, Simon W. Jones and Sophie C. Cox. Formulation and viscoelasticity of mineralised hydrogels for use in bone-cartilage interfacial reconstruction. *Journal of the Mechanical Behavior of Biomedical Materials* doi: 10.1016/j.jmbbm.2018.01.016 (2018)

Megan E. Cooke, Simon W. Jones, Britt ter Horst, Naiem Moiemen, Martyn Snow, Gurpreet Chouhan, Lisa J. Hill, Maryam Esmaeli, Richard J. A. Moakes, James Holton, Rajpal Nandra, Richard L. Williams, Alan M. Smith and Liam M. Grover. Structuring of Hydrogels across Multiple Length Scales for Biomedical Applications. *Advanced Materials* doi: 10.1002/adma.201705013 (2018)

Megan E. Cooke, Bernard M. Lawless, Simon W. Jones and Liam M. Grover. Matrix degradation in osteoarthritis primes the superficial region of cartilage for mechanical damage. *Acta Biomaterialia* doi: 10.1016/j.actbio.2018.07.037 (2018)

CHAPTER 1

INTRODUCTION

The osteochondral unit (OCU) encompasses bone, cartilage and their interface; it is structurally and chemically adapted to transfer loads associated with the weight of the body and the changing loads in joint locomotion. Physical, biological and chemical changes to the OCU, as a result of trauma, disease or ageing reduce its ability to function properly. One of the most prevalent diseases that affects the OCU and surrounding joint tissues is osteoarthritis (OA). Generally as a disease of older adults, and with increased body mass index (BMI) as a key risk factor, OA is becoming more prevalent with the world's ageing and increasingly obese population [4]. In the Global Burden of Disease study there was a 64% increase in the prevalence of OA between 1990 and 2010, and in 2012 it was estimated that worldwide, 250 million people were affected by knee OA [85, 140, 225].

Unlike rheumatoid arthritis (RA), which is an inflammatory multi-joint condition, OA is a localised, non-systemic disease. The most researched and most easily diagnosable pathology of OA is degeneration of the articular cartilage; however, the whole joint is affected and there are changes seen in the subchondral bone, synovial fluid, synovium and meniscus [60, 113, 214]. While much research has been done into disease modifying therapeutics, as yet, there are no therapeutics that can stop progression or reverse the effects of OA [166]. Current management strategies for OA are limited to pain relief and intra-articular steroid injections.

When OA reaches 'end-stage' the only treatment option available is partial or to-

tal joint replacement surgery. These procedures are highly invasive and the current gold standard joint replacement options, particularly for the hip joint, have limited life-spans. With high surgical precision, the best materials and low activity levels, a hip or knee implant will last for up to 25 years; however, there is much variability and revision surgeries are common [210, 231]. Therefore, alternative strategies for the treatment of OA are being sought, particularly *via* tissue engineering and regenerative medicine routes [71, 239]. Preventative strategies and those which target early changes in OA may be the most successful as severely degenerate cartilage has a drastically altered mechanical and biochemical environment [59]. A key limitation to implementing early strategies is that the first changes in OA are clinically silent as cartilage matrix is degraded without bulk structural changes [5].

There remain unanswered questions surrounding the effects of clinically silent changes to the articular cartilage in OA. It is known that the mechanical properties are reduced, but quantitative correlation of the changes in viscoelastic, mechanical properties with the physicochemical changes has not yet been achieved. As such, the first aim of this thesis is to investigate this correlation:

- Determine the viscoelastic properties of macroscopically undamaged OA cartilage and healthy, age-matched cartilage.
- Undertake physicochemical and histological analysis of freshly isolated compared to mechanically conditioned tissues.
- Investigate quantitative links between the difference in mechanical properties with matrix changes in disease.

The changing matrix properties in early OA alters the behaviour of chondrocytes [61]. Similarly, in traumatic cartilage injuries, there are disruptions to the structure and integrity of the matrix as well as damage to chondrocytes. These lesions in the cartilage surface are often secondary to larger joint trauma, but left untreated can lead to early-onset OA [200]. There are a number of clinical treatment strategies for cartilage

defects, however none of them are without limitations regarding overall joint function. As a result, tissue engineering has been proposed as a promising solution for replacement or regeneration of damaged cartilage. A common strategy for engineered cartilage is to encapsulate chondrocytes in hydrogel matrices [172, 174, 222]. This can prevent and even reverse dedifferentiation that is seen in monolayer culture of chondrocytes. Alginate is a commonly used hydrogel for chondrocyte culture and the positive effects have often been attributed to maintenance of a spherical cell morphology [16, 95]. The delivery of a bulk hydrogel matrix to a defect site, however, is challenging so novel methods of structuring alginate hydrogels presents a way to deliver material and cells non-invasively. Therefore, the second aim of this thesis is to investigate a deliverable alginate-chondrocyte system:

- Produce and characterise traditionally gelled 'quiescent' and sheared or 'fluid' alginate matrices.
- Seed human chondrocytes into these matrices and determine the effects of varied levels of confinement (or entrapment) on cellular behaviour and phenotype.
- Investigate the use of factors that may help drive native chondrocyte phenotype in these matrices.

As previously mentioned there are currently no disease-modifying therapeutics for OA, and there is a high incidence of failure of candidate drugs in late stage clinical trials. One factor may be the lack of appropriate models to test these therapeutics preclinically [166]. *In vitro* testing is usually performed in monolayer cell cultures and the current *in vivo* preclinical methods are poorly representative of the physiological situation in humans. Animal models of OA are either chemically or mechanically induced by destabilisation of the joint, which is unrepresentative of the chronic degenerative disease in humans. The one animal that spontaneously develops OA is the Dunkin-Hartley guinea pig which exhibits a severely obese OA phenotype so again, is unrepresentative of a lot of OA cohorts [2, 103, 197]. To address this, a new *in vitro* model of the OCU will be developed using 3D printing technology:

- Use and refine an embedded bioprinting technique to print low viscosity hydrocolloid solutions prior to crosslinking.
- Develop a bi-layered scaffold to represent bone and cartilage-like regions.
- Seed primary human chondrocytes and osteoblasts into this bi-layered scaffold to determine the capacity to produce region-specific mechanical, chemical and biological environments.

1.1 The Synovial Joint

This thesis focuses on the changes that occur in OA in the knee joint; therefore the focus here is on the anatomy of this joint. The knee joint acts as a hinge allowing for flexion and extension at the tibia, femur and patella, as well as allowing slight medial and lateral rotation. It has both soft and mineralised tissues including the joint capsule, synovium, the infrapatellar fat pad (IPFP), a number of ligaments and tendons, meniscus, hyaline cartilage and bone. The joint is a relatively hypoxic environment as the only vascularised tissues are the bone and synovium; oxygen and nutrients are delivered to many tissues including the articular cartilage *via* the synovial fluid [215].

Meniscus, ligaments and tendons

Meniscus is a tough fibrocartilaginous tissue that forms a semi-circular wedge between the femoral condyles and tibial plateau. The main functions of meniscus tissue are to stabilise the knee joint in flexion, extension and rotation as well as transferring load across the joint. The main stabilising structures in the knee joint are four large ligaments. The anterior cruciate ligament and posterior cruciate ligament are intracapsular and restrict medial/lateral joint rotation. The extracapsular ligaments include the medial and lateral collateral ligaments which prevent valgus and varus bending. The patellar tendon connects the patella to both the quadriceps and the tibial tuberosity without separation. It is a critical bridge between the femur and tibia that enables flexion and extension of the joint.

Synovium and synovial fluid

The synovium is a vascularised tissue that lines the inner surface of the joint capsule, encasing the joint. It has a small role in stabilising the joint but is mainly responsible for the secretion of synovial fluid; a non-Newtonian fluid that fills the joint space, providing lubrication, a supply of nutrients and also a waste removal system [5]. It has a high (3 mg/mL) hyaluronic acid content, which greatly enhances its viscosity, as well as other proteins secreted by the surrounding joint tissues, some of which act to aid lubrication

[34]. A combination of synovial fluid filling gaps in the cartilage surface and fluid being released from the cartilage matrix allow for 'weeping lubrication' of the cartilage surface [5].

1.2 Hyaline cartilage

Hyaline cartilage is so called because of its white-blueish glossy appearance; it comes from the greek *hyalos*, meaning glass. It forms a 1-3 mm covering to the ends of long bones in diarthrodial joints to allow for low friction joint gliding whilst also acting to distribute compressive forces. It is an avascular and aneural tissue with a dense extracellular matrix (ECM) primarily consisting of collagen type II (Col II) and proteoglycans [202]. Architecturally, cartilage can be sub-divided into regions which form a continuous gradient structure. The distribution of the ECM constituents throughout the structure and their interaction with water dictate its highly specialised mechanical properties [137].

1.2.1 Chondrocytes

Chondrocytes are cells from a mesenchymal lineage and are the only cell type found in cartilage, albeit sparsely, making up less than 5% of the tissue volume [160]. During development, mesenchymal stem cells (MSCs) are stimulated by TGF-β to differentiate into chondroprogenitors which start to express and produce Col II. They then differentiate into chondroblasts which additionally produce aggrecan, Collagen type IX and COMP (cartilage oligomeric matrix protein). They then mature into chondrocytes. In healthy adult cartilage, chondrocytes are very slow to proliferate and there is little turnover of cartilage ECM. As an avascular tissue, delivery of nutrients is only possible *via* diffusion from the synovial fluid which is assisted by compression-driven fluid flow [137]. The exact phenotype of chondrocytes varies throughout the different zonal regions of cartilage, but the key markers are Col II, aggrecan and SRY (sex-determining region Y)-box-9 (Sox9) [33].

1.2.2 Cartilage pericellular matrix

There is a specific pericellular matrix (PCM) that immediately surrounds chondrocytes. Here, there is little evidence of proteoglycan macromolecules and whilst many of the constituent components are present, they are not co-localised. There are small Col II fibres of 10-15 nm in diameter, as well as collagen types VI and IX, fibronectin, perlecan, biglycan, decorin and laminin, at higher concentrations than in the main cartilage ECM [96, 167–169, 209, 213]. It has been hypothesised that the PCM has a mechanosensing role and a mechanoprotective role during compression to prevent damage to chondrocytes [167, 232, 233]. The combination of a chondrocyte and its PCM have been termed a chondron, with the wider matrix between neighbouring chondrocytes referred to as the territorial matrix [168]. Beyond this, the matrix is referred to as interterritorial or extracellular.

1.2.3 Cartilage extracellular matrix

Collagen

Fibrillar collagen types have a hierarchical assembly starting with individual polypeptide monomers with the repeating sequence G-X-Y, most commonly glycine (G), proline and hydroxyproline [93]. These 300 nm monomers form right-handed triple-helices in the endoplasmic reticulum before being secreted from the cell. Extracellular enzymes are then responsible for cleaving the propeptides that flank either end of the trimer, enabling fibres to form that then assemble into fibrils (Figure 1.1) [5, 93].

Collagen makes up 15-20% of hyaline cartilage; Col II is the primary collagen type in hyaline cartilage but collagen types I, VI, IX, X and XI are also present [213]. Col II is a fibrillar homotrimer collagen which acts throughout the extracellular matrix to resist tensile forces and prevent over-swelling of the matrix [104, 189]. Collagen type I (Col I) is also a fibrillar collagen, found in small quantities in the superficial zone of cartilage but in high quantities in fibrocartilage, a mechanically inferior form of cartilage often formed following cartilage injuries. It is also highly expressed in chondrocytes following expansion

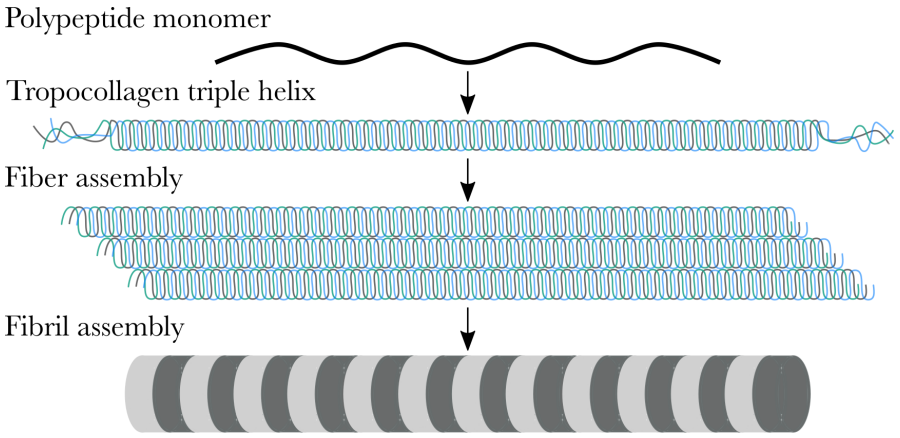

Figure 1.1: Hierarchical collagen fibril assembly. Adapted from Athanasiou et al. [5]

in monolayer so is a key marker of dedifferentiation of chondrocytes in culture [32].

Collagen types IX and XI are involved in templating, crosslinking and diameter control of Col II fibres [44, 213]. Collagen type VI is found in the pericellular matrix and interacts with chondrocyte receptors, while collagen type X is found at the tidemark, in calcified cartilage and is also expressed by hypertrophic chondrocytes [213].

Proteoglycans

Proteoglycans form as a core protein with glycosaminoglycans (GAGs) covalently bound to them. The proteoglycans found in cartilage include biglycan, decorin and aggrecan which is the most abundant. Aggrecan is a core protein which assembles into a bottle brush structure with keratan sulphate (KS) and chondroitin sulphate (CS) groups covalently bound to it (Figure 1.2) [219]. The aggrecan core is non-covalently bound to a hyaluronic acid backbone, so a small glycoprotein (link protein) stabilises the interaction to allow for the aggregation of aggrecan (Figure 1.2) [77, 219]. The carboxyl groups of CS and sulphate groups of KS and CS give the proteoglycan network a highly negative charge. This results in a repulsion between chains referred to as fixed charge density (FCD) [189].

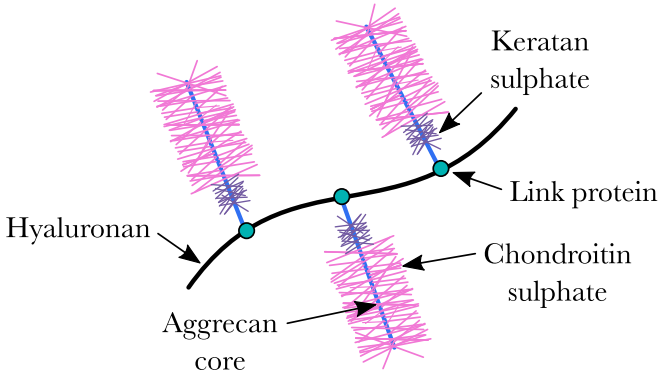

Figure 1.2: Cartilage proteoglycan structure; aggrecan cores with sGAG chains are attached to a hyaluronan back bone by a link protein.

Water

Hyaline cartilage consists of 70-80% water which fills the macropores between the collagen and proteoglycan networks. FCD provided by KS and CS in combination with repulsion between neighbouring negatively charged chains results in a high osmotic pressure [74, 122]. In healthy cartilage this pressure is compensated by the Col II network which restricts over-swelling. Water is critical to cartilage's longevity over repetitive loading in a lifetime; compression results in a fast pressurisation of the confined fluid such that the fluid bears the compressive loading, rather than the solid matrix components [74]. This fluid is also important for the delivery of nutrients and removal of waste from chondrocytes and any matrix breakdown products [87].

1.2.4 Regional organisation of cartilage

The articulating surface

The cartilage surface has a thin layer, the *lamina splendens*, that is around 300-1000 nm thick [117]. It is an acellular region that facilitates the low friction properties of cartilage by the mucinous glycoprotein lubricin which covers the articulating surface. It acts by preventing cell and protein adhesion to the cartilage surface [89].

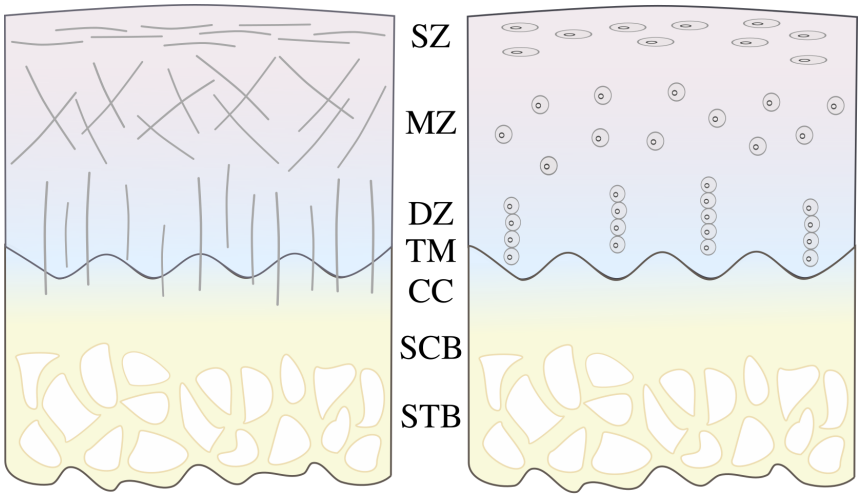

Figure 1.3: Gradient structure of cartilage showing collagen fibril orientation (left) and chondrocyte morphology (right). SZ: superficial zone, MZ: middle zone, DZ: deep zone, TM: tidemark, CC: calcified cartilage, SCB: subchondral cortical bone, STB: subchondral trabecular bone.

The superficial region

Just beneath the lamina splendens is the superficial zone (SZ), which comprises 10-20% of the cartilage thickness [202]. Chondrocytes here are slightly flattened and secrete superficial zone protein (SZP), also known as proteoglycan-4 (PRG4), which helps in lubrication of the articular surface [193, 194]. Col II fibrils here have a small diameter and are aligned parallel to the articulating surface to resist shear forces. There is a relatively low proteoglycan content in this region.

The middle zone

This central region of cartilage makes up 40-60% of the thickness and has spherical chondrocytes that start to form columns towards the deep zone [202]. Cartilage intermediate layer protein (CILP) is highly expressed by these chondrocytes [115]. Col II fibrils here are randomly oriented and of larger diameter than in the superficial zone and proteoglycan content is at its highest.

The deep zone

The deep zone (DZ) of cartilage has large diameter collagen fibrils oriented perpendicular to the articulating surface. These are anchored into the calcified region. Chondrocytes here are organised into columns and are slightly elongated in the direction of the collagen fibrils.

The tidemark and calcified zone

The tidemark (TM) is a distinction visible in histology that marks the region between non-calcified and calcified regions. Beneath the tidemark, cartilage transitions to calcified cartilage (CC) where collagen type X is present and the collagen fibril diameter is at its largest. Beneath CC, is the subchondral cortical bone (SCB).

1.3 Bone

Bone is a highly mineralised tissue of two main types: cortical (or compact) and trabecular (or spongy). Its main solid constituents are Col I and hydroxyapatite (HAp) which are the basis of the commonly described hierarchical structure of bone [229]. The 206 bones of the skeleton serve many functions in the body. The long bones allow for movement by insertion and attachment points for tendons that are attached to muscles and ligaments that prevent joint dislocation. They also have a large marrow cavity which is the major site of production of blood cells and so the long bones are highly vascularised. Short bones such as the carpus and tarsus allow for small amounts of movement and stability. The flat bones such as the sternum and cranial bones provide protection to delicate organs while irregular bones such as the vertebrae have varied functions. Finally the sesamoid bones are those embedded in tendons such as the patella.

1.3.1 Osteoblasts, osteoclasts and osteocytes

The cells involved in the formation and regulation of bone act synergistically resulting in a dynamic tissue with high levels of turnover and remodelling. Disruption to the biochemical balance can result in diseases of under or over-mineralisation of bone [203].

Osteoblasts

These are the matrix-forming cells of bone and make up around 5% of the cells present in bone [52]. They are derived from a mesenchymal lineage, and key differentiating osteoblast markers include Runt-related transcription factor (RUNX2), osterix (OSX) and distal-less homeobox 5 (DLX5). Fully differentiated osteoblasts can be identified by the expression of Col I (COL1A1 and COL1A2), alkaline phosphatase (ALP), bone sialoprotein (BSP) and Bone Gamma-Carboxyglutamate Protein (BGLAP) [45]. As these cells produce high levels of protein, they have large amounts of rough endoplasmic reticulum, free ribosomes, large Golgi apparatus and mitochondria. Mature osteoblasts produce Col I, proteoglycans and other proteins to form the non-mineralised osteoid [205].

Osteoclasts

Osteoclasts are responsible for bone resorption and are derived from a macrophage lineage [205]. They are multinucleated and have a ruffled region of the cell membrane that interacts with the bone matrix during resorption. The production of osteoclasts is dependent on the expression of osteoprotegerin (OPG) from osteoblasts. Receptor activator of nuclear factor kappa-B ligand (RANKL) is a key cytokine for osteoclastogenesis from macrophage precursors in the bone marrow but interaction of precursors with OPG prevents the binding of RANKL to the RANK receptor of the osteoclast. Therefore, the relative levels of OPG and RANKL are important in the differentiation of osteoclasts and hence, the regulation of bone remodelling [52].

Osteocytes

Prior to osteoid mineralisation, around 20% of osteoblasts become entrapped in the matrix and are referred to as pre-osteocytes [205]. During mineralisation, these cells form long processes (canaliculi) that allow communication between these deep embedded cells and those on the bone surface. Osteocytes have an important role in mechanosensing to trigger changes in bone remodelling [203].

Bone remodelling

Osteocytes have canaliculi in the range of tens of microns in length, which allow for both sensing and communication of mechanical forces in bone [10]. The remodelling process is driven by the local mechanical environment as stated by Wolff's law. The magnitude and direction of loading determine the rate of bone formation and the architectural arrangement of trabecular bone, followed by changes to the cortical bone. Together, osteoblasts and osteoclasts make up bone multicellular units, which are responsible for bone remodelling [3]. Bone resorption by osteoclasts is followed by bone formation by osteoblasts. As above, the RANK/OPG balance regulates the rate of bone remodelling and an imbalance can cause over- or under-mineralisation [203].

1.3.2 Bone extracellular matrix

Organic matrix

Collagenous proteins make up 85-90% of the organic matrix of bone; Col I is the main collagen type present alongside collagen types III, V and X. Col I is critical to the structure of bone and is the basis of the hierarchical bone structure. It is a heterotrimer, with two alpha-1 chains and one alpha-2 chain however these ratios can change with disease [165]. Other non-collagenous proteins present in bone include glycoproteins, lipids and glycosaminoglycans which make up the other 10-15% of the organic matrix [52].

Inorganic matrix

Calcium, phosphate and carbonate were first identified as the major bone constituents and then confirmed to be present in the form of HAp using x-ray diffraction in 1930 [183]. HAp ($Ca_{10}(PO_4)_6(OH)_2$) is the main inorganic component of bone, making up 70% of the inorganic matrix. However, HAp is often not completely pure; the most common substitution is of a carbonate anion in place of a phosphate group or (less commonly) a hydroxyl group [229]. There have also been trace amounts of Mg, Na, Si, Sr, Zn and Pb found associated with bone mineral [86].

1.3.3 Hierarchical organisation of bone

Bone is hierarchical in nature; the collagen triple helix assembles as described in Figure 1.1 and in fibril assembly, very thin (3 nm), cuboidal HAp nanocrystals align in the gaps between collagen fibres as in Figure 1.4 [227]. This forms mineralised fibrils which stack into lamellae which then further align depending on whether they form in cortical or trabecular regions of bone [177, 230].

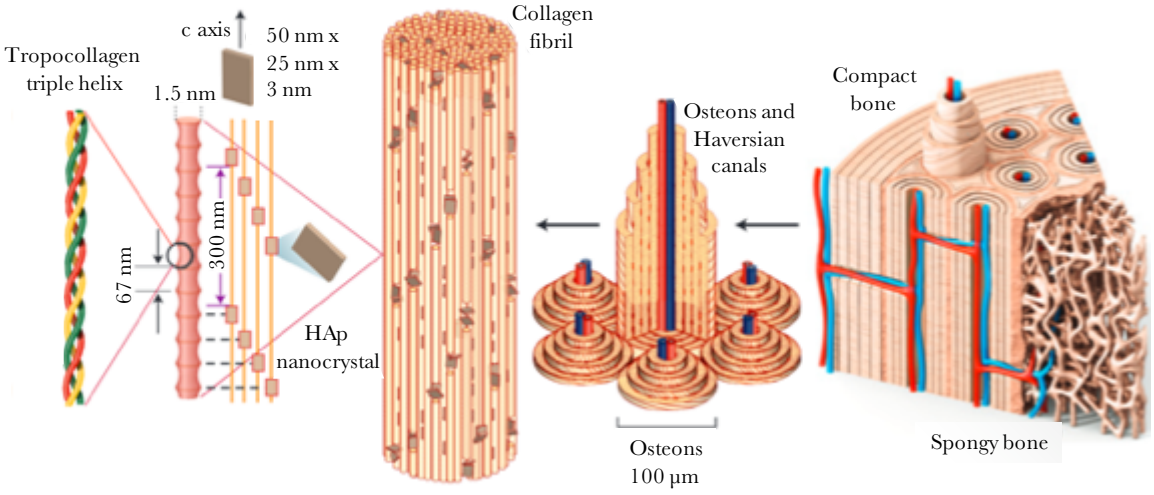

Figure 1.4: Hierarchical bone structure; adapted from Wegst et al. [227].

Inorganic matrix

Calcium, phosphate and carbonate were first identified as the major bone constituents and then confirmed to be present in the form of HAp using x-ray diffraction in 1930 [183]. HAp ($Ca_{10}(PO_4)_6(OH)_2$) is the main inorganic component of bone, making up 70% of the inorganic matrix. However, HAp is often not completely pure; the most common substitution is of a carbonate anion in place of a phosphate group or (less commonly) a hydroxyl group [229]. There have also been trace amounts of Mg, Na, Si, Sr, Zn and Pb found associated with bone mineral [86].

1.3.3 Hierarchical organisation of bone

Bone is hierarchical in nature; the collagen triple helix assembles as described in Figure 1.1 and in fibril assembly, very thin (3 nm), cuboidal HAp nanocrystals align in the gaps between collagen fibres as in Figure 1.4 [227]. This forms mineralised fibrils which stack into lamellae which then further align depending on whether they form in cortical or trabecular regions of bone [177, 230].

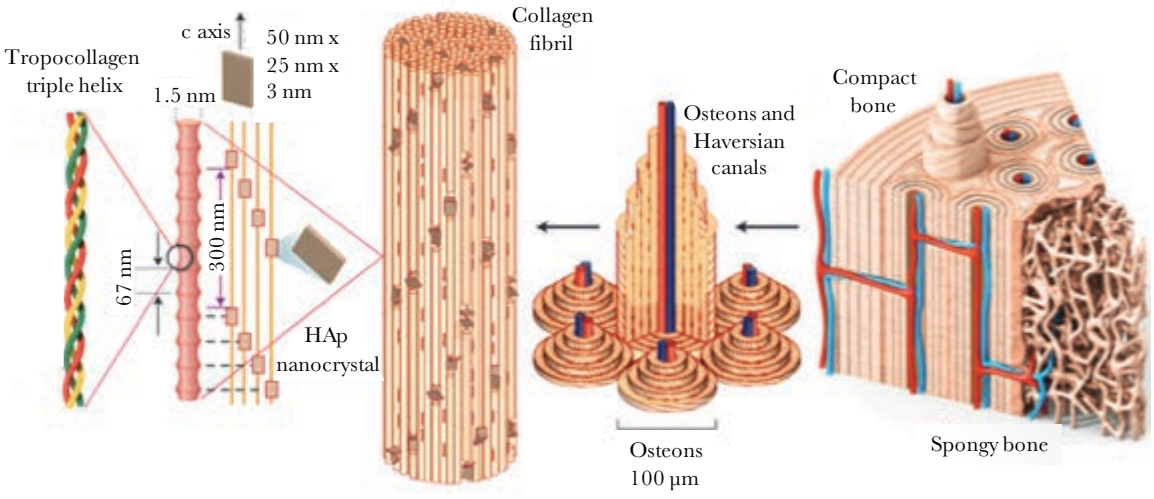

Figure 1.4: Hierarchical bone structure; adapted from Wegst et al. [227].

Cortical bone

In cortical bone, the smallest functional unit is an osteon. These are cylindrical structures formed of sheets of collagen fibrils. The sheets wrap concentrically at 90° to the previous sheet with a central space referred to as a Haversian canal [3]. As can be seen in Figure 1.4, Haversian canals contain blood vessels that supply the length of the bone and are connected to Haversian canals of neighbouring osteons by Volkmann's canals [171]. These are the other vessel-containing channels in long bones and they run perpendicular to the Haversian canals. The tight packing of osteons makes cortical bone very dense with a high fracture toughness (critical stress intensity factor, k_c = 3.5-5 MPa) [146].

Trabecular bone

Trabecular (or spongy) bone is found in the medullary cavity. It is sponge-like in appearance, with variable porosity. Regarding its hierarchical organisation, sheets of collagen fibrils are aligned parallel longitudinally along trabeculae [176]. Trabecular bone is more metabolically active than cortical bone, and its porosity and architecture are highly affected by mechanical loading [229]. The orientation and porosity of trabeculae varies between locations as a result of mechanical influences; this is clearly seen in the proximal femur (Figure 1.5) where the trabecular bone in the femoral head is less porous and becomes more porous distally.

1.4 Osteoarthritis and cartilage lesions

OA is a chronic degenerative disease of the synovial joints; commonly seen in the knee and hip, it is also found in the ankle, shoulder and hands [4]. It is historically associated with wear and tear of articular cartilage, however it is more complex in that many of the joint tissues are disrupted [113]. Repetitive cyclic loading of joints is thought to be the key driver of OA, but age, obesity, joint trauma, genetic factors as well as changes to joint alignment and shape can increase the likelihood of developing OA [58, 67, 156].

Figure 1.5: Trabecular architecture in the proximal femur. Photo: Paul Crompton, Copyright University of Wales College of Medicine.

1.4.1 Cartilage in OA

In healthy cartilage, normal loading maintains matrix homeostasis [67]. In OA, cartilage degradation is a gradual but irreversible sequence of events (Figure 1.6) [5]. The first change to cartilage is its increased ability to hold water as a result of degradation of both the proteoglycan and collagen networks [21, 179]. The proteoglycan matrix is primarily broken down by aggrecanases that are members of the ADAMTS (a disintegrin and metalloproteinase with thrombospondin motifs) family alongside other proteins [53]. Multiple sites in the aggrecan core protein are cleaved which has a large effect on the mechanical properties of the cartilage matrix, however, this first stage is clinically silent [5, 67].

At some stage during aggrecanolysis, the collagen matrix begins to be broken down by both matrix metalloproteinases (MMPs) and physical, mechanical forces. This degradative process begins in the superficial zone and develops through to the deep zone [235]. Breakdown of the Col II matrix reduces the elastic restraint on the proteoglycan and water components, allowing the tissue to swell [216]. Extensive collagenolysis is irreversible

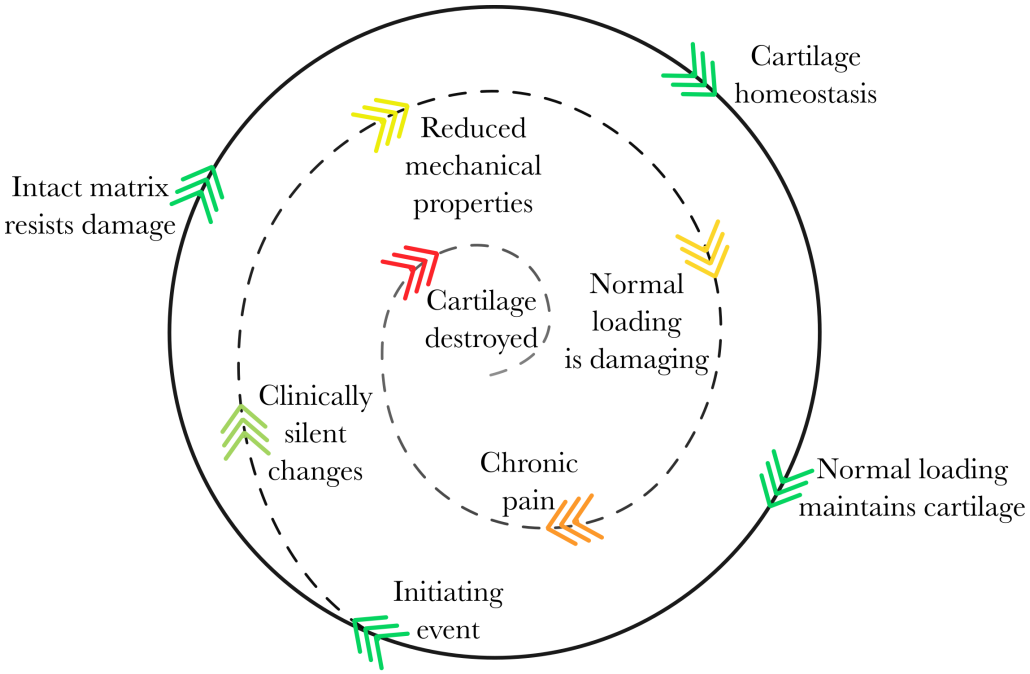

Figure 1.6: Sequence of events in OA-associated cartilage degradation, adapted from Athanasiou et al. [5].

.

in vivo, therefore with normal loading, cracks and fissures start to appear in the cartilage surface [59]. This is associated with increased pain as the aneural cartilage is removed and the neural subchondral bone is exposed [61]. Cartilage calcification (chondrocalcinosis) is often seen in older people with OA, and HAp-based deposits may be responsible for the increased production of inflammatory mediators such as IL-1 and IL-18 [112, 141].

Chondrocytes

Alongside matrix changes, there are also distinct changes to chondrocytes in OA. Changes in the mechanical signals that chondrocytes are exposed to can both change the function of chondrocytes and cause apoptosis, as they are highly mechanosensitive through cell surface mechanosensors [61, 67, 69]. In early stages of disease, chondrocytes become more metabolically active in attempting to repair the matrix and undergo increased proliferation [5]. During this proliferative stage, chondrocytes show an increase in expression of COL10A1, MMP13 and RUNX2; structurally, increased proliferation results in cell clusters within a chondron [169]. As the disease develops chondrocytes produce increased

levels of pro-inflammatory cytokines, MMPs and chemokines which have catabolic functions and degrade cartilage [217]. The final process in OA chondrocytes is cell death; increased cell numbers and insufficient levels of nutrients in the chondron causes cell necrosis [5].

1.4.2 Bone in OA

There are changes to subchondral cortical and trabecular bone as well as formation of bony spurs (osteophytes) in OA, all of which are specific to the stage of OA. Increased loading leads to an increase in bone turnover as stated previously. In OA, there is region-specific thickening of the subchondral cortical and trabecular bone as seen in Figure 1.7 [59, 111]. There is also thinning of the epiphyseal trabecular bone which is likely due to stress shielding by the thickened subchondral plate [20].

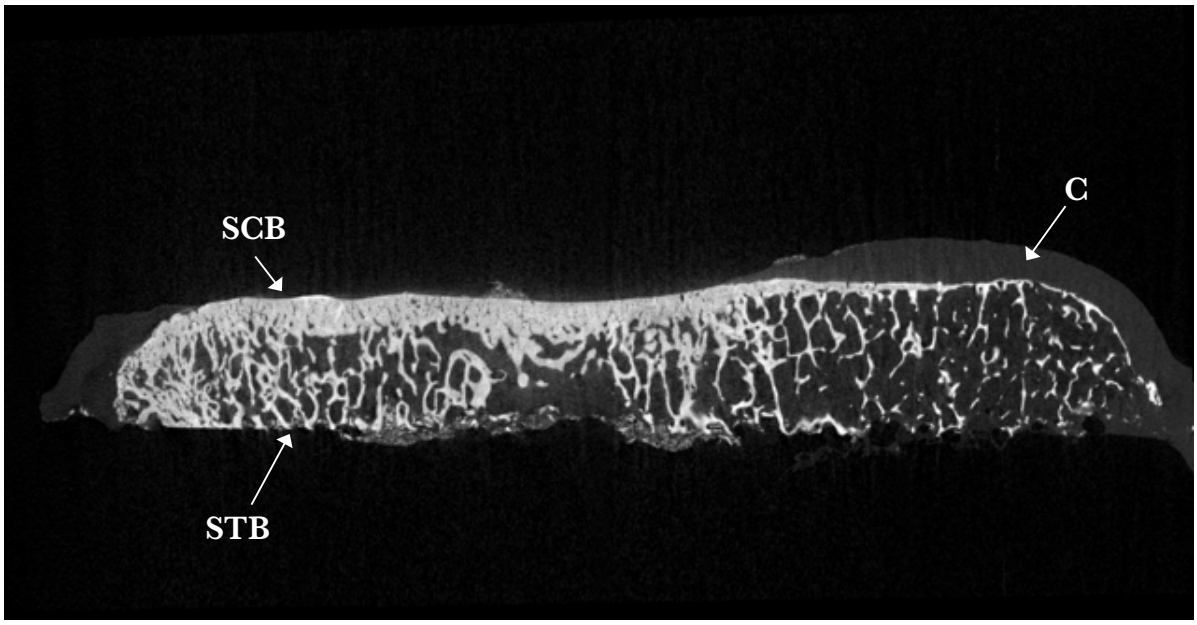

Figure 1.7: Reconstructed μCT image of an OA tibial plateau (sagittal plane) showing thickening of the subchondral cortical bone (SCB) where cartilage (C) is thinning or completed degenerated. The subchondral trabecular bone (STB) architecture is also irregularly thickened.

.

Excessive loading that occurs when cartilage is completely degraded can lead to bone marrow lesions and bone cysts. These defects in the bone have been associated with

increased pain in OA and may be initiated by local damage and subchondral bone necrosis [20]. Another pathological bone condition in OA is the development of osteophytes at the joint margin. Abnormal proliferation of periosteal cells causes the development of these bony protrusions that are radiographic indicators of OA [14, 113].

1.4.3 Inflammation in OA

OA was historically considered as a simple 'wear-and-tear' disease, however it is now well-known that inflammation is an important consideration in OA progression. The commonly accepted series of events that occur during the inflammatory response are summarised in Figure 1.8. Matrix fragments, which are a result of either traumatic damage or degradation by catabolic enzymes, act as DAMPs (damage-associated molecular patterns) [114]; DAMPs prompt an inflammatory response in the synovium, where synovial fibroblasts and macrophages produce catabolic enzymes, chemokines and cytokines [217]. These cells also secrete a number of alarmins, including interleukin-1α (by the macrophage inflammasome), adenosine triphosphate (ATP), heat shock proteins (HSPs), and uric acid (UA). These alarmins induce a positive feedback loop where more catabolic enzymes, chemokines and cytokines are produced in the synovium as well as the bone and cartilage [217].

Overall, this results in a highly inflammatory environment in the joint space such that even the menisci and ligaments are affected, with increased vascularisation and mineral deposition in the menisci and collagen fibre disorganisation in ligaments [113]. In overweight and obese subjects, there is the additional insult of inflammatory adipokines that have been found in the synovial fluid [166, 170].

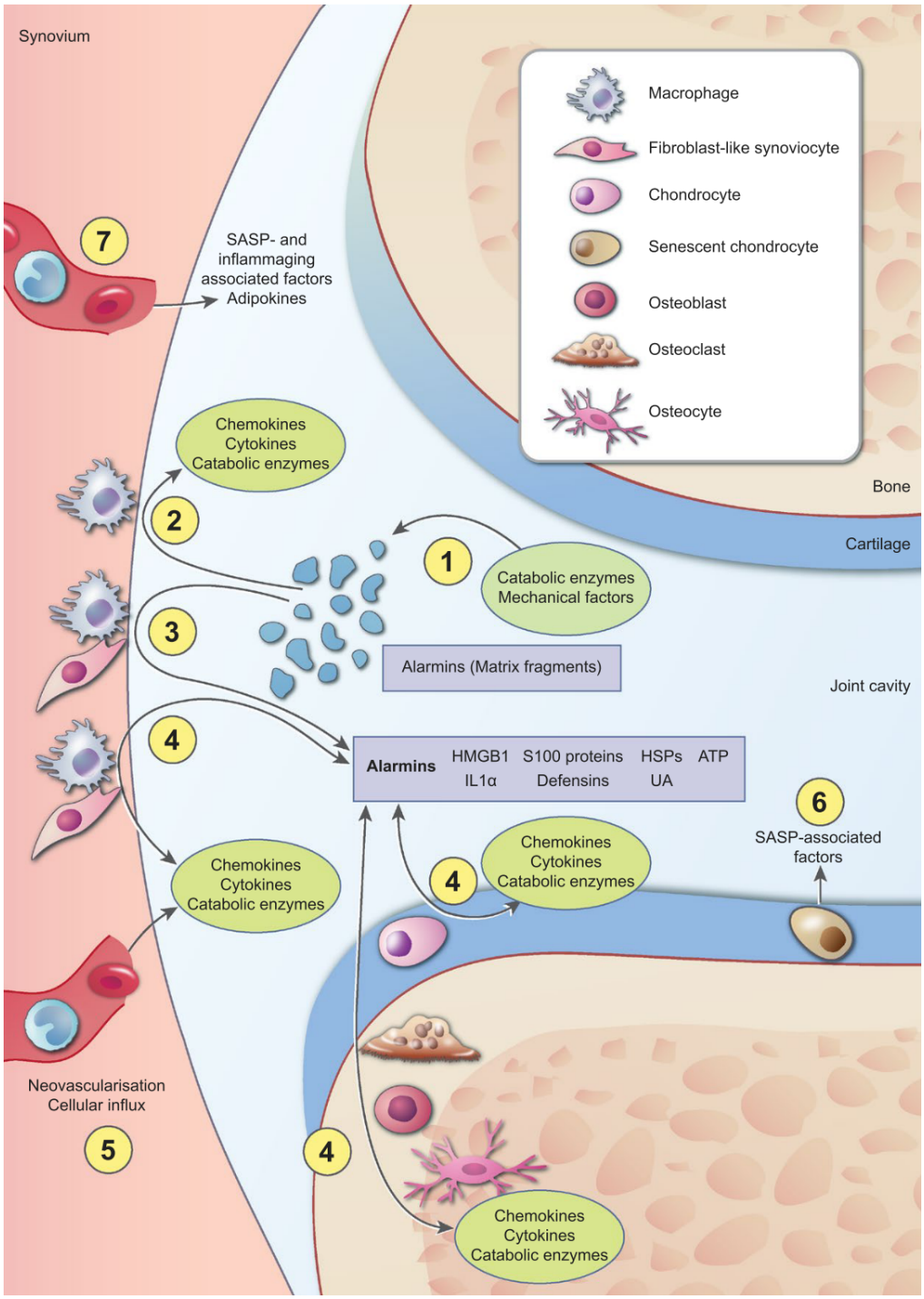

Figure 1.8: Schematic representation of inflammatory processes in OA progression, adapted from van den Bosch [217].

.

1.4.4 Current treatment strategies

Common clinical presenting symptoms of OA are single-joint pain in loading alongside reduced mobility in people over the age of 50. Radiographic narrowing of the joint space is the most common clinical diagnosis. There are currently no disease-modifying therapeutics available for the treatment of OA, however, pain relief and steroid injections are commonly prescribed to alleviate symptoms [214]. When OA reaches 'end-stage', and there is bone-bone contact in the joint, patients are referred for partial or total joint replacement surgery. This involves the removal of the joint surface, drilling a cavity in the neighbouring long bone and inserting a prosthetic implant.

1.4.5 Cartilage lesions and clinical treatments

Traumatic damage to the cartilage surface is fairly common in joint injuries, particularly in the knee joint. In a damaging loading event, the superficial region of cartilage can be abraded resulting in a cartilage lesion. Due to its avascular nature, cartilage lacks an inherent capacity for repair so left untreated, normal mechanical loading can cause these lesions to become larger. As a result, people who experience cartilage lesions are predisposed to the development of OA [200]. Clinically, these lesions are diagnosed by MRI and arthroscopic investigations; lesions with the potential to develop further are then treated, often using one of the following techniques.

Debridement

This is the simplest of the treatments and is carried out arthroscopically. Damaged cartilage is excised from the joint to allow for new tissue to form. This technique has been shown to improve symptoms for five years but is only suitable for relatively small lesions [82].

Microfracture surgery

This procedure was developed in the late 1990s by Steadman et al. [204]. Firstly, the damaged cartilage is debrided down to the subchondral bone before small canals are drilled through the cortical bone. Bone marrow is then able to flow into the debrided region to form a blood clot, or haematoma [200, 204]. Pluripotent stem cells from the bone marrow are then left to differentiate into chondrocytes to form cartilage matrix. Unfortunately the matrix that forms is not hyaline in nature, and is referred to as fibrocartilage. Whilst visually similar to hyaline cartilage, the type and organisation of collagen fibrils is not the same as hyaline cartilage. As a result, the mechanical properties of this tissue are inferior to hyaline cartilage and it is prone to fragment [130].

Autologous chondrocyte implantation

The first stage in autologous chondrocyte implantation (ACI) involves taking a small cartilage biopsy from a non-articulating region of the joint. The tissue is then digested to isolate a population of chondrocytes which are expanded *in vitro*. When sufficient numbers of cells have been produced, they are re-implanted into the cartilage defect and secured with a periosteal flap [37, 218]. An advantage of ACI over microfracture is the use of cartilage-derived cells rather than bone-marrow cells so there is a better chance of high quality hyaline cartilage formation. However, there is still high prevalence of fibrocartilage formation as chondrocytes de-differentiate during their monolayer culture *in vitro* and start expressing Col I [180]. Further limitations include morbidity of the tissue at the site where the initial biopsy is taken from (donor-site morbidity) and there have been cases where the periosteal flap has delaminated from the soft tissue [37].

Mosaicplasty

This technique was first developed in 1993 and has had fairly good clinical uptake since [123]. In mosaicplasty, cylindrical osteochondral cores are removed from a non-articulating region of the joint. The defect site is then debrided and drilled similar to in microfracture

surgery, before the cores are implanted into the defect site and secured [75]. A key advantage of this technique is the transplantation of already mature, autologous hyaline cartilage. Similar to ACI, there is the chance of donor site morbidity and there is limited evidence of lateral integration with the existing cartilage [200].

1.4.6 Summary

The OCU is a complex, multifactorial tissue with distinct regions of precise biochemical composition that give distinct mechanical properties. Self-repair of cartilage matrix is intrinsically limited by its poor ability to regenerate. As a result, matrix alterations due to trauma and degenerative changes in OA are largely irreversible. Increasing the knowledge of the changes that occur in cartilage during OA that are not 'wear and tear' based is critical to developing and improving therapeutic tissue engineering strategies for cartilage regeneration.

1.5 Mechanical properties of materials

In the mechanical characterisation of materials, a force is applied to a test piece and its displacement is measured (or vice versa). The conversion of force and displacement to stress and strain respectively allows for the application of these parameters to different test pieces and testing modalities.

1.5.1 Stress, strain and modulus

Stress (σ), measured in Pascals (Pa) refers to force per unit area as described in Equation 1.1. Strain (ϵ) is unitless but often described as a percentage and refers to the change in length (L) of a test piece relative to a reference length. Strain is calculated as in Equation 1.2.

$$\sigma = \frac{Force}{Area} \tag{1.1}$$

$$\epsilon = \frac{\Delta L}{L} \tag{1.2}$$

The ratio of these two parameters, the stress experienced by a material as a result of an applied strain, is referred to as the modulus and describes the resistance to deformation of a material. There are many modalities of mechanical testing which result in different modes of stress application and as such, different equations are required for calculation of specific moduli. Young's (or elastic) modulus (E) is the most commonly described and is determined by compression and tensile testing of solid materials. It presumes that the material obeys Hooke's law which states that stress is proportional to strain (Equation 1.3). It describes perfectly linear elastic behaviour, as shown to the left of the dashed line in Figure 1.9, where a material can be deformed and will immediately return to its original dimensions when the stress is removed. Young's modulus is calculated from this region as a ratio of stress and strain (Equation 1.3). For most solids, this linear behaviour is only

seen at low strains; above a threshold referred to as the yield stress, the deformation is no longer recoverable. Solid materials then exhibit a phase of plastic deformation prior to fracture or failure. These regions are shown in Figure 1.9.

$$E = \frac{\sigma}{\epsilon} \tag{1.3}$$

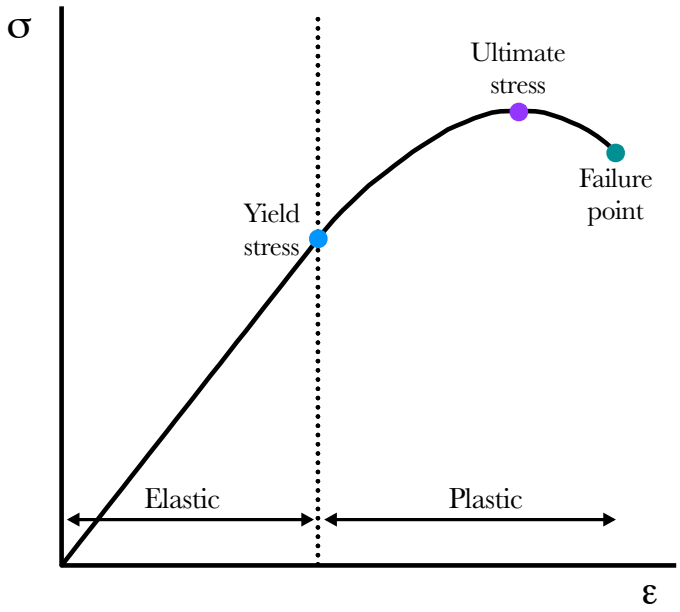

Figure 1.9: Typical solid stress-strain behaviour. The elastic region left of the dashed line shows linear, recoverable behaviour whereas the plastic region to the right shows permanent deformation leading to failure.

1.5.2 Viscosity

Viscosity is a parameter traditionally associated with fluids rather than solids. It describes a material's resistance to flow when subjected to a shear or tensile stress. Importantly, viscosity is not a material constant and may be dependent on other factors such as temperature. Newtonian fluids are those whose viscosity is independent of stress and exhibit linear shear stress/shear strain behaviour, such as water. Most polymer solutions and biological fluids are non-Newtonian in that their viscosities are dependent on stress. Shear-thickening materials, such as a mixture of cornstarch and water, show an increase

in viscosity with an increased shear stress due to coalescence of colloids. Shear-thinning materials such as paint show a decrease in viscosity with increasing shear stress but the recovery of viscosity is very fast. Thixotropic materials such as ketchup also show shear-thinning behaviour but exhibit more time dependent recovery of viscosity upon removal of the shear stress.

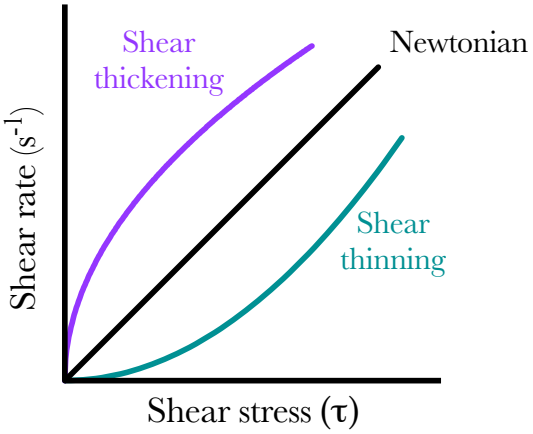

Figure 1.10: Newtonian and non-Newtonian fluid behaviour.

1.5.3 Viscoelasticity

The term viscoelasticity refers to materials that exhibit both solid-like (elastic) and liquid-like (viscous) properties. Purely elastic materials, such as metals, act like a spring in that they strain when a stress is applied and then immediately return to their original state when the stress is removed. Purely viscous materials, such as honey, show time dependent stress-strain behaviour and act like a dashpot. These components are modelled together by the Maxwell and Kelvin-Voigt models (Figure 1.11). In the Maxwell model, the spring and dashpot are arranged in series (Figure 1.11A), such that the stresses in each component are identical but the strains can vary. Contrastingly, in the Kelvin-Voigt model, the two components are arranged in parallel (Figure 1.11B) to model identical strains in each component and the stresses experienced can be different.

The separate elastic and viscous components are characterised by the storage mod-

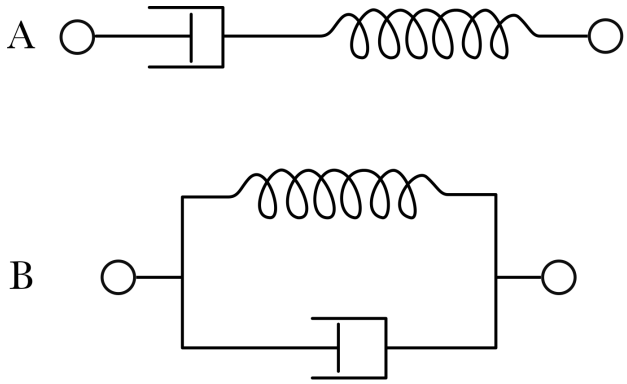

Figure 1.11: Maxwell (A) and Kelvin-Voigt (B) models of viscoelasticity where elastic behaviour is modelled as a spring and viscous behaviour as a dashpot.

ulus (E') and loss modulus (E") respectively. The storage modulus describes the rigidity of the material and its ability to store energy that is then used to recoil elastically when a stress is removed. The loss modulus refers to the materials ability to dissipate energy by polymer chain reorganisation and friction. The energy lost by a viscoelastic material is seen in a hysteresis loop produced by loading and unloading cycles as in Figure 1.12. The energy dissipated is equal to the area inside the loop.

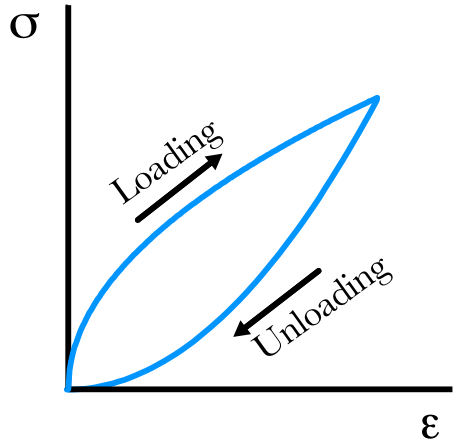

Figure 1.12: Hysteretic stress-strain behaviour in viscoelastic materials.

Alongside the storage (E') and loss (E") moduli, complex modulus can be calculated as Equation 1.4. Complex modulus (E^*) at a certain frequency can be compared to Young's modulus at the same loading frequency, however Young's only considers the

loading and not unloading of a material. This modulus can be calculated from loading and unloading during a cyclic test (see section 2.3.1) or from a creep or stress relaxation test.

$$E^* = \sqrt{E' + E''} \tag{1.4}$$

Creep and stress relaxation

Viscoelastic materials exhibit creep and stress relaxation, which are time-dependent phenomena. When held at a constant stress, viscoelastic materials show increasing strain, which is referred to as creep. Stress relaxation explains how viscoelastic materials show decreasing stress under a constant strain. This form of viscoelastic testing often has very long time constants.

1.5.4 Mechanical analysis of cartilage

Cartilage has two mechanical functions: firstly, it provides a low friction gliding surface for smooth joint articulation; secondly it acts to dissipate and transmit compressive forces to the subchondral bone. The mechanical properties of cartilage vary between its regions due to the collagen organisation and proteoglycan content, which give rise to their specific functions [98]. For example, the surface region is strong in tension to resist shear deformation, while the middle and deep zones are strong in compression to distribute loads. In OA, matrix catabolism causes large reductions in the strength of the tissue [19, 67]. Further, the mechanical properties of articular cartilage vary between anatomical location, species, disease and testing modality [98, 179]. Table 1.1 summarises some of the investigations into the mechanical properties of human articular cartilage.

As Table 1.1 shows, there is variation in mechanical properties of cartilage between joints and disease states. There is however, further variation within each joint. For example, in the study by Peters et al., the shear modulus of cartilage was greater in the femoral condyles than the tibial plateau [164]. Likewise, in the study by Burgin, the mod-

Table 1.1: Values obtained for mechanical testing of human articular cartilage. FH: femoral head; TP: tibial plateau; FC: femoral condyle. All units are MPa except for creep, measured in %.

Condition	**Location**	**Property**	**Value**	**Ref.**
Compression				
Cadaver OA	FH	E	6.1-16.7 1.4-8.3	[179]
Elderly healthy	FH	$E_{Dynamic}$ $E_{Quasi-static}$	51.9-89.9 1.60-2.47	[19]
OA	FC	E	2.42-9.77	[221]
Cadaver 'Unaffected' OA	TP	Compressive strength	14.5±3.3 12.7±6.8	[149]
Cadaver 'Unaffected' OA	TP	Creep (%)	13.8 ±5.6 12.5 ±6.5	[149]
Tension				
Cadaver 10-30 years Cadaver 40-90 years	FC (SZ) FC (DZ) FC (SZ) FC (DZ)	Fracture strength	25-40 17-32 8-30 4-30	[97]
Cadaver OA	FH	UTS	8.2-14.8 3.7-11.8	[179]
Shear				
OA grade 0-1 OA grade 2-4	FC/TP	G	0.57-0.92 0.11-0.27	[164]
OA	FC	G	0.83-3.38	[221]

ulus values were varied across the regions of the femoral heads investigated [19]. Further, age plays an important role in the mechanical properties of cartilage, as was thoroughly investigated by Kempson et al. [97, 98]. These studies have primarily investigated the static properties of cartilage, however, the viscoelastic properties are more relevant to the overall function of cartilage.

Cartilage viscoelastic theories

Cartilage is a viscoelastic material, with time dependent mechanical properties. The cartilage matrix can be considered as a biphasic material consisting of 1) a solid matrix and 2) the interstitial fluid. The mechanical properties of these individual components and their interaction give the unique viscoelastic properties of cartilage. Interactions between the proteoglycan and collagen networks due to physical entanglements, friction, chemical and electrostatic interactions are responsible for flow-independent behaviour. The interstitial fluid flowing through the porous matrix is responsible for flow-dependent behaviour. Biphasic theory, developed by Mow et al. in 1980 brings these components together, assuming a linearly elastic solid matrix with viscous properties and an incompressible viscous fluid. This determined that the frictional drag between the two phases was primarily responsible for the viscoelastic properties of cartilage in tension, compression and indentation [119, 136, 137].

In 1987, Mak then considered the effects of matrix permeability and inherent viscoelasticity of the solid matrix in developing the biphasic poroviscoelastic (BVPE) theory [119]. This theory was then tested experimentally by Setton et al. in 1993 including investigations of the role of the surface zone. Their findings showed that in intact cartilage, the flow-dependent behaviour dominates the dissipation of energy. Contrastingly, with increasing tissue permeability, seen following removal of the surface region that could represent fibrillation of the articular surface in OA, the viscoelasticity of the solid matrix was found to significantly change the energy dissipation properties of the tissue [196]. This also showed how the surface region of cartilage is critical to maintaining fluid pressurisa-

tion in the bulk tissue. Thus far, the simple solid-fluid interactions and behaviours had been considered but the effects of swelling had not. Lai et al introduced a third, ionic, phase to consider the fixed charge density of the proteoglycan network in various ionic solutions which is referred to as triphasic theory [102].

The viscoelastic creep response in cartilage is governed by fluid exudation. As a load is applied, fluid moves out of the tissue. Cartilage has been reported to take between 4-16 h to reach creep equilibrium where no further fluid is removed, so strain no longer increases with constant loading. As such, dynamic mechanical analysis is a useful technique to determine the viscoelastic properties of cartilage, with much shorter time constants. It also enables investigations into the frequency dependent properties of tissues.

1.6 Hydrogels in cartilage tissue engineering

Due to their high water content, hydrogels have been used as 3D ECM mimics for decades [70, 84]. They show great potential to improve the current treatments for cartilage defects as they enable the replication of a 3D ECM that has been shown to be able to be remodelled by embedded chondrocytes [71]. 3D scaffolds have been shown to be of high importance in chondrocyte culture as they can recover and maintain the native Col II phenotype that is lost in monolayer or 2D culture.

Hydrogels can be produced from a number of materials. Polysaccharides used in cartilage engineering include: agarose, alginate, chitosan, CS, gellan and hyaluronic acid as well as blends of these [16, 101]. Proteins used include: collagen, fibrin and silk. Lastly, synthetic hydrogels such as PEGDA have been used as scaffolds for chondrocytes and for MSCs to differentiate into chondrocytes and to produce cartilage-like ECM. Of these different hydrogels, and blends of multiple hydrogels, alginate has shown wide success in maintaining chondrocyte phenotype and allowing the production of cartilage matrix.

1.6.1 Alginate

Alginate (or alginic acid) is a linear polysaccharide derived from brown algae, formed of D-mannuronic acid (M) and L-guluronic acid (G) residues (Figure 1.13). Upon dissolution in water alginate forms a hydrocolloid which can then be gelled upon the introduction of multivalent cations such as Ca^{2+}, Sr^{2+} and Ba^{2+} [108]. These cations form electrostatic interactions with the carboxyl groups of G residues, to form an 'egg-box' structure as shown in Figure 1.14. Therefore, the ratio and pattern of M and G residues has a large impact on the properties of alginate gels, as does the type of multivalent cation used [108]. The ratio and pattern of residues depends on the source of the raw material so the simplest way to tailor the gel properties are with the concentration of alginate and crosslinking cation used. Alginate has been investigated for use in cartilage engineering since the 1980s [39, 39, 70].

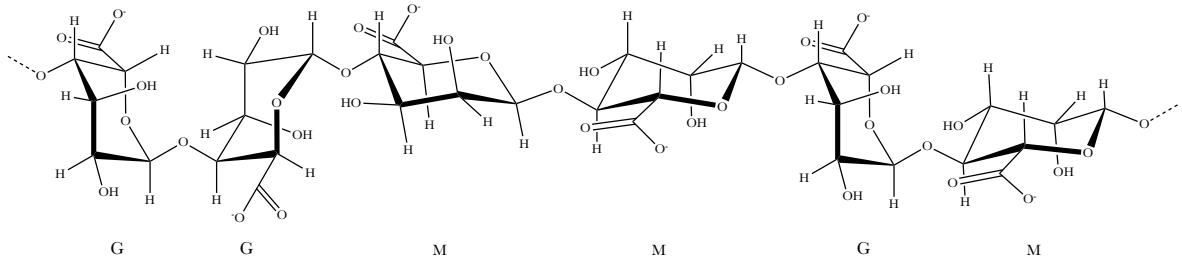

Figure 1.13: Chemical structure of a unit of an alginate chain showing guluronic acid (G) and mannuronic acid (M) groups.

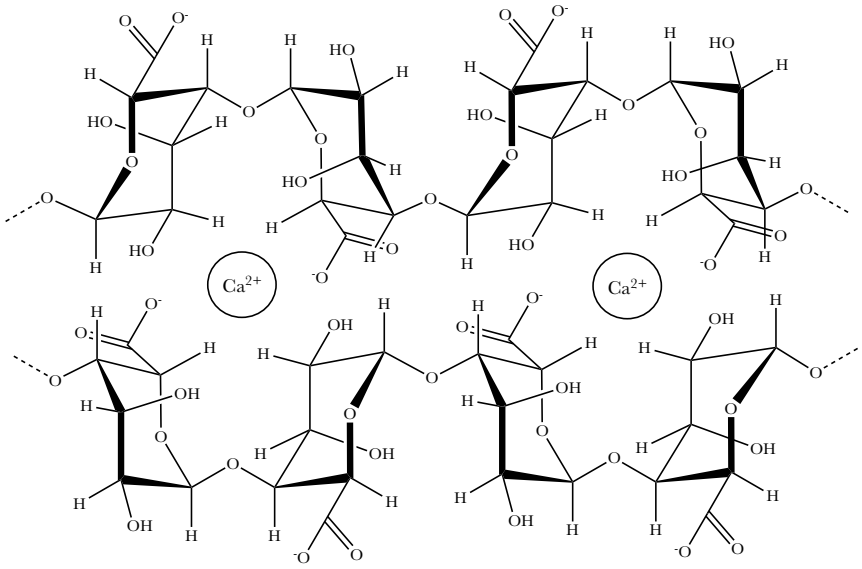

Figure 1.14: Chemical structures of the egg box structure formed between guluronic acid groups upon crosslinking with divalent cations such as calcium (Ca^{2+}).

1.6.2 Gellan gum

Gellan gum is a linear polysaccharide produced by the bacteria *Sphingomonas elodea*. Its primary structure has tetrasaccharide repeating units containing β-D-glucose, β-D-guluronic acid and α-L-rhamnose in a 2:1:1 ratio as shown in Figure 1.15. Gellan is available, and will form gels, in both acetylated and deacetylated forms, as well as varying degrees of acetylation. Highly acetylated gellan undergoes thermogelation at around 42℃, which makes it suitable for cell culture applications. Upon dissolution in heated water, gellan exists as a coiled polymer solution (Figure 1.16). Upon cooling, it forms coiled coils and with the addition of divalent cations, ionic bonds can form between these coiled coils to form a stiffer, but no longer thermoreversible gel (Figure 1.16) [50]. Gellan gum is FDA

approved for use as a food additive and has been investigated for both food and biomedical applications, including as cartilage and bone engineering scaffolds [50, 88, 151, 163].

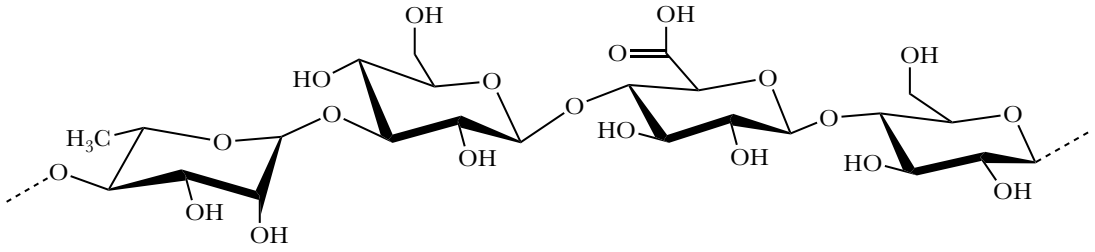

Figure 1.15: Chemical structure of the repeat unit of low acyl gellan gum showing from left-right the structures of β-D-glucose, β-D-guluronic acid, β-D-glucose and α-L-rhamnose.

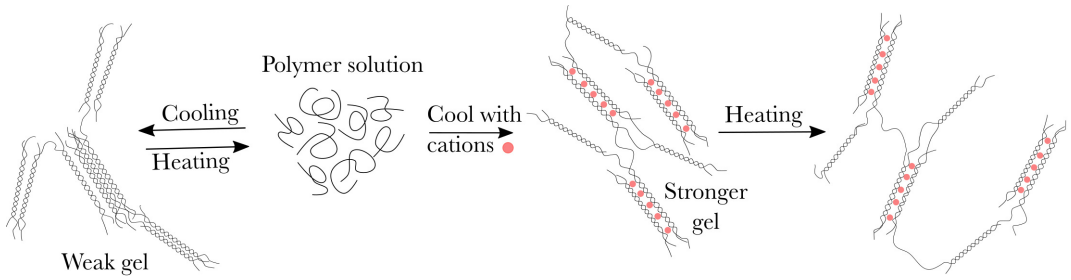

Figure 1.16: Gellan gum structure upon thermal and ionic crosslinking.

1.6.3 Fluid gels

The properties of materials can be precisely controlled by the way in which they are processed and also the way in which they are structured [26, 147]. Fluid gels have long been used in the food and cosmetics industries but research into their use in biomedical applications is relatively new [148].

Fluid gels are produced by introducing shearing forces during their gelation resulting in a network of entangled polymer particles as shown in Figure 1.17B. The key property of these materials is that they exhibit solid, weak-gel like properties at rest but upon application of shear they exhibit liquid-like flowable properties. Depending on the polymer used, the rate of shear applied and the method of inducing shear, the particle morphology and size can be controlled as shown in Figure 1.18. These morphological differences

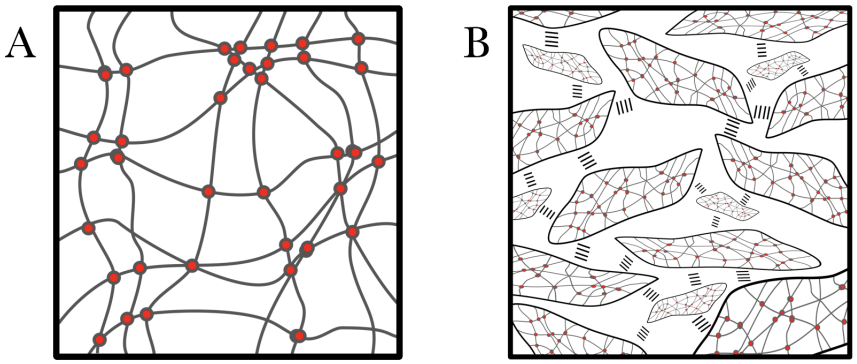

Figure 1.17: Schematic of polymer networks following A) quiescent gelation and B) sheared gelation to produce a fluid gel, from Cooke et al. [26].

have been shown to infer differing mechanical properties, particularly in the solid-like behaviour of the gel [42]. In this instance, the fluid gel produced with a pin stirrer, with a 'hairy particle' morphology (Figure 1.18B) showed a higher yield stress (defined as a 5% deviation from the LVR) than the one produced in a rheometer (Figure 1.18A) [147]. This is likely due to stronger interaction between the extensions of the hairy particles compared to the more spherical ones. Tuning these parameters can give rise to unique rheological properties for the potential delivery of therapeutics, cells and other material.

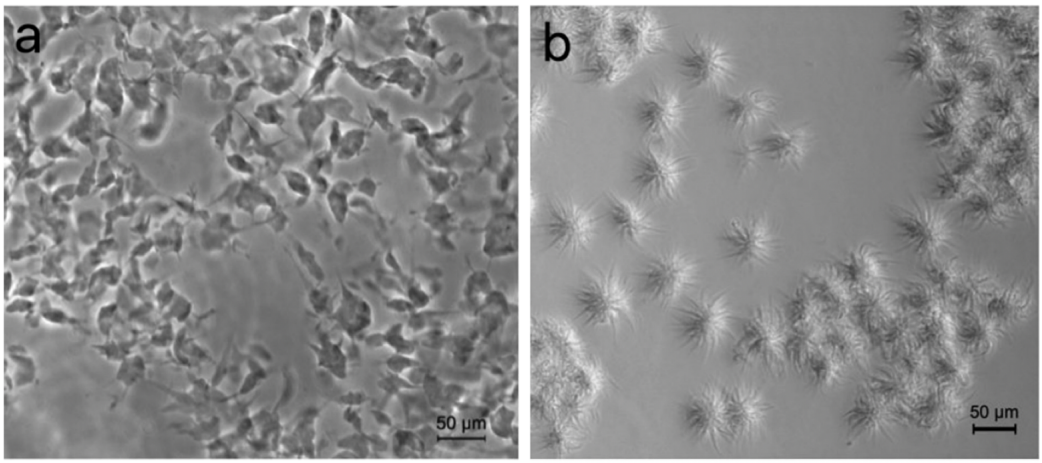

Figure 1.18: Morphology of agar fluid gel particles produced either in a) a rheometer or b) a pin stirrer; reproduced from [42].

1.7 Bioprinting and biofabrication

Biofabrication is a term that has been loosely for many years since the start of 3D printing of biological components but recently a consortium of leaders in the field developed the following definition:

> " The automated generation of biologically functional products with structural organization from living cells, bioactive molecules, biomaterials, cell aggregates such as micro-tissues, or hybrid cell-material constructs, through Bioprinting or Bioassembly and subsequent tissue maturation processes." [65]

This clarifies the process as a way to produce biologically relevant structures from cell-biomaterial mixtures, deposited in a specific way that are then matured into tissues. The material that is extruded or deposited during this process is commonly referred to as a bioink. Again, there was a lot of discussion in the field surrounding the exact definition of a bioink and as such the following has been developed:

> " Formulation of material(s) and biological molecules or cells processed using bioprinting technologies." [134]

There are many parameters to consider during the printing phase of biofabrication that affect the fidelity of the print and the capability of the seeded cells to behave as intended. These are summarised in Figure 1.19.

1.7.1 Methods of bioprinting and bioassembly

There are a number techniques for the printing of soft materials to act as cell scaffolds. Some of these focus on the production of a rigid support for cells (or a cell-seeded hydrogel) to adhere to [100]. While this is an appropriate solution for some applications, other tissues are not suited to rigid scaffolds, even when they are degradable. As such, different techniques have been developed and adapted for printing of soft materials and some of the common ones are detailed.

Electrospinning was originally used in the textile industry but now has been adopted in the fields of tissue engineering and regenerative medicine as a support for 3D cell culture

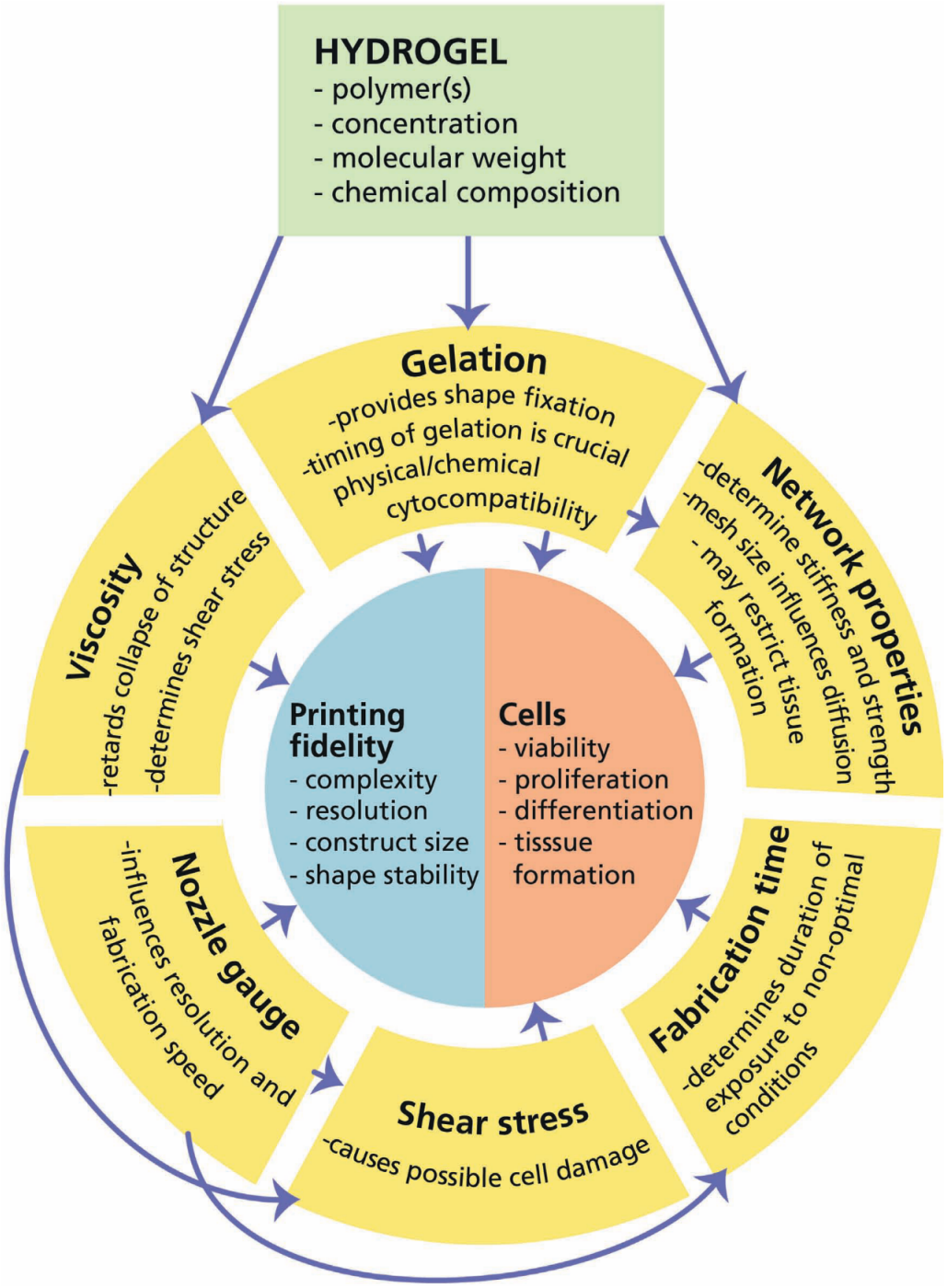

Figure 1.19: Considerations for printing technique; reproduced from Malda et al. [120].

[238]. It can be used to produce large sheets of fibres produced from soluble polymers, with fibre diameters ranging from a few microns down to the nanoscale [64]. The two main features are aligned and random fibres, with the former allowing for control over cellular behaviour with alignment along fibres [240]. A key limitation in electrospinning is production of thick sheets of material, however, the development of melt electrostatic writing (MEW) bridges the gap between electrospinning and fused deposition modelling (FDM). By matching or exceeding the speed of filament extrusion with the speed of the collector, highly ordered single fibre deposition can be achieved [18, 31, 124]. These structures are limited to 2-3mm in height, but by applying a voltage to the nozzle during extrusion the polymer jet is stabilised such that the fibres can be stacked without large deposits of material that are seen when the jet is not stable. Using this approach, MEW can be used to print structures up to 7mm in height [237]. These fabricated structures have been used to reinforce hydrogel cultures of human chondrocytes, giving them similar compressive mechanical properties to human articular cartilage. They were then capable of withstanding a physiologically relevant loading regime and a cartilage-like matrix was produced [224].

Ink-jet, or drop-on-demand, printing acts by depositing very small (1-100 picoliter) droplets of liquid onto a print bed, close enough for them to then coalesce to form fibres, without forming bulges [36, 207]. This can be used to produce structures containing proteins and live cells [35, 190]. To produce 3D cell-seeded constructs by inkjet deposition, Boland et al. deposited cell-seeded $CaCl_2$ into a sodium alginate bath to produce sheets of crosslinked microspheres with endothelial cells encapsulated in the voids [15]. This approach has also been used to print microvasculature-like networks from fibrin gels and HMVECs [29]. Further, cylinders of 4 mm height were printed from PEGDA with human chondrocytes, demonstrating the capability of this technique to produce distinct zones by simultaneous printing and photo-polymerisation of the PEGDA droplets [30]. A key limitation of this technique, is the number of bioinks available as they must have very low viscosity to produce picoliter droplets.

One technique that removes the need for hydrogel scaffolds is the production of organoids (or spheroids) that are then assembled to fuse into larger structures. Organoids are grown using suspension culture, where a mass of cells is grown in a droplet of media. They are then usually assembled on needle arrays and allowed to mature to form a larger scaffold [128]. This technique was been used in the fabrication of hollow constructs for tracheal replacement and verified in a rat model [211]. Recently, the concept of truly scaffold-free, label-free and nozzle-free fabrication has been demonstrated by the fusion of spheroids of chondrocytes (chondrospheres) into millimetre-scale tissue constructs using magnetic levitation [157]. In this study, the needle array usually required for assembly is removed and instead, a paramagnetic solution of cell culture media and 50 mM gadolinium was used in conjunction with a heterogeneous magnetic field with a central void (the levitation point) which allowed the clustering of tissue spheroids for fusion. The resulting fused construct had imperfections and voids, but cell viability was very good [157]. Overall this technique shows a fascinating technological development to overcome many of the limitations in biofabrication.

To enable the production of larger constructs, FDM has been used to print thermolabile polymers. FDM has been used for a long time in rapid prototyping using spool fed polymer filament. The extrusion nozzle is heated, such that the material is liquefied for deposition but quickly cools and solidifies on the print bed [242]. Multi-layer structures that are large in the z-direction can be produced. FDM has been used to produce PCL/CaP scaffolds that were capable of allowing the culture and osteogenic differentiation of MSCs seeded onto them with a fibrin glue [191]. Many studies have employed PCL to print biodegradable scaffolds, with the intention that they can be implanted and resorbed as newly regenerated tissue matrix is laid down. Atala et al. developed a system to print rigid, but biodegradable, PCL lattices along with cell-seeded hydrogels for the production of large-volume tissue constructs [94]. This system was used to print scaffolds for mandible and calvarial bone as well as cartilage and skeletal muscle [94].

Bioplotting, or direct-writing, uses a similar technique to FDM, but the rigid scaffold

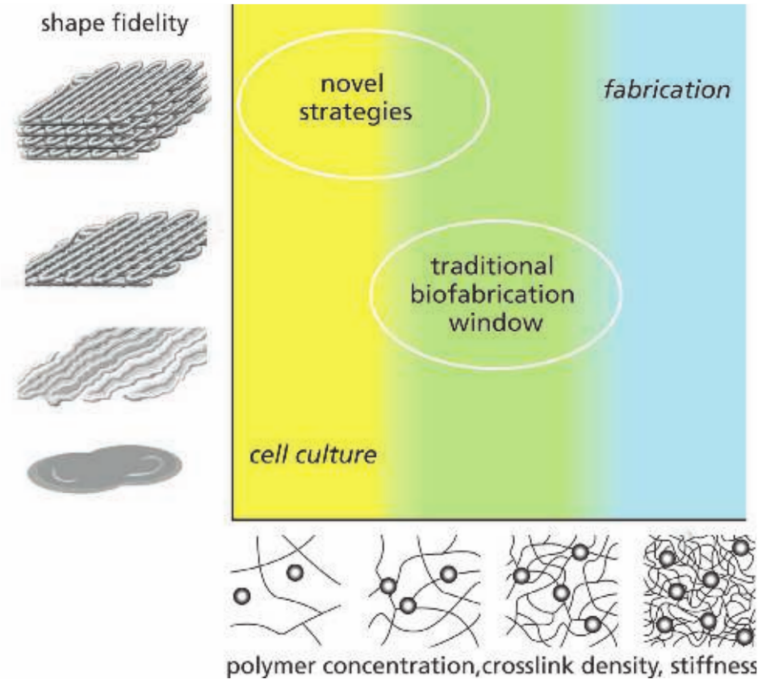

Figure 1.20: A consideration of the biofabrication window regarding hydrogel stiffness and geometry complexity. Softer gels which allow for cell migration and offer high cytocompatibility are of too low viscosity for traditional techniques and so novel techniques are required to overcome this limitation. Reproduced from Malda et al. [120].

is no longer required as the cell-seeded hydrogel is printed directly [11]. This is becoming a widely used technique and has led to the development of many novel hydrogels to enable direct extrusion. Methacrylated gelatin (GelMA) is a commonly used bioink for direct printing of structures for cartilage tissue engineering and has been modified with HA, PEG, PEGDA and graphene oxide to enhance its print properties [144, 195, 244]. Another material that has been modified for printability is hyaluronic acid. Another application of methacrylation of established hydrogels for tissue engineering was achieved by Burdick's group; using methacrylated (and further modified) hyaluronic acid, they were able to produce multi-layer constructs by direct bioplotting [153]. They developed a system to 'in-situ' crosslink these formulations such that they gelled upon arrival on the collector so there was very well controlled deposition of fibres to produce a lattice structure [154].

Many hydrocolloid solutions commonly utilised in 3D cell culture by casting into

moulds are of low viscosity prior to crosslinking into rigid hydrogel structures. A key challenge in printing intricate structures from these materials is avoiding the inherent instabilities of liquids; surface tension forces sharp features towards spherical shapes and gravity causes sagging and buckling of printed lines. To overcome this, some bioplotting strategies have used co-extrusion, where the hydrocolloid solution and crosslinker are printed simultaneously for rapid solidification. Other techniques with photocrosslinkable bioinks can also be directly crosslinked upon extrusion. These strategies are not suitable for all bioinks, particularly those with longer crosslinking times such as collagen. These limitations are summarised in Figure 1.20, in that the softer, lower viscosity gels which show very good cytocompatibility are generally challenging to print into large geometries with high shape fidelity [120]. As many of these softer materials are well established as tissue engineering scaffolds, novel strategies are being developed to overcome these limitations.

1.7.2 Embedded printing

Embedded printing describes a group of techniques that can be used to produce hydrogel constructs of greater complexity or shape-specificity without limitation over build direction, supports or overhangs. Embedded techniques were first published in 2011 and all have a similar theme in that they use 3D support matrices in place of the traditional 2D print bed for bioplotting. These matrices vary from viscous liquids through particulate gel systems to solid gels with embedded phases, and some of the published techniques are summarised in Table 1.2. One of the first embedded printing methods was 'EMB3D', developed by Lewis et al. in 2011 to print perfusable vascular networks in blocks of Pluronic F127 [236]. Using a fugitive, unmodified Pluronic F127, a vascular network was printed inside a liquid reservoir of modified Pluronic F127 that was subsequently photocrosslinked. Simple liquification at 4℃ under vacuum allowed removal of the fugitive phase leaving an embedded perfusable network. This group then developed the technique to print strain sensors within stretchable elastomers for wearable strain sensing devices [142] and soft

autonomous robots [228]. More recently, this group has used PDMS as a viscoplastic matrix to further characterise the effects of the support matrix on the extruded material around the nozzle [66]. The key features of EMB3D are the production of multi-phase components by the embedding of one phase within another fixed one. In this technique the support matrix forms the final part, whereas more commonly, the support matrix is sacrificial.

An example of this is a method that uses a hydrophobic fluid bath, developed by Fischer et al. in 2012. Perfluorotributylamine is, like many fluorocarbons, highly hydrophobic and has a density of 1.9 g cm^{-1} so can mechanically support the printing of a water-based hydrogel [40]. This technique has been used to support printed constructs for 6 months, shows high levels of cell viability, and was also used to direct osteogenic and adipogenic differentiation by changing the mechanical and physicochemical properties of the printed hydrogels [40, 41].

Table 1.2: A summary of embedded printing methods used for bioprinting. 'Matrix' refers to the sacrificial or support phase whilst 'Ink' refers to the material used for printing.

Method	**Matrix**	**Ink**	**Ref.**
EMB3D	1. Pluronic F127 2. PDMS blend	Pluronic F127	1.[236] 2.[66]
Submerged printing	Fluorocarbons	Agarose, Collagen, Agarose - Collagen, Agarose - Chitosan	[40, 41]
GHost writing	HA modified with adamantane and β-cyclodextrin	Modified HA including methacrylation	[78]
Granular gel writing	Carbopol	PS microspheres, PDMS, PVA	[13]
FRESH	Gelatin slurry	Alginate, Collagen, Fibrinogen	[79]
FRE	Carbopol	PDMS	[80]

In 2015, three distinct methods for embedded printing based on different sacrificial matrices were published. Highley, Burdick et al. developed a Guest-Host (GHost)

writing print system in which supramolecular hydrogels (modified hyaluronic acid) were printed into a second a hydrogel matrix of the same material in differing ratios [78]. The hydrogels used for both the bioink and the support material have non-covalent reversible bonds, which are broken during shearing and rapidly reform when the stress is removed. The bioink and matrix materials were also modified by methacrylation to enable covalent crosslinking using UV light. Using this system they were able to print freeform geometries including helices and embedded, perfusable vascular networks whilst achieving cell viability of over 90% [78].

In the same year, a study utilised Carbopol as a granular gel media for embedded printing [12]. Carbopol is a highly hydrophilic polymer that enables high resolution printing of hydrophobic inks such as PS, PVA and PDMS. In this study, the authors showed the possibility of printing polystyrene microspheres with features as small as 100 μm as well as printing human aortic endothelial cells (HAECs) directly into the gel. In order to retrieve printed constructs from the gel, they were produced in PVA before the Carbopol was washed away with water.

Freeform reversible embedding of suspended hydrogels (FRESH) is a technique developed by Feinberg et al. where the support matrix is a gelatin slurry [79]. The slurry support was produced by first thermogelling a solution of gelatin before adding further liquid and blending the gel into small (around 55 μm) particles. This material behaved like a Bingham plastic and enabled the printing of alginate, fibrinogen and collagen using a modified desktop FDM printer. Using this technique, alginate filaments of between 160-250 μm were extruded and helical structures were produced to show that the process was truly freeform. The reversible aspect of this printing technique exists in the way that the gelatin slurry can be liquified by heating to 37°C and the printed part removed before washing to remove residual gelatin. In a further study by this group, carbopol was used as the support matrix to print PDMS. Using this method, they were able to print perfusable bifurcating structures. To release the printed structure, the carbopol was again washed away with aqueous solution [80].

1.8 Thesis overview

General methods and techniques are described in Chapter 2 while specific methods are presented in each of the data chapters. As a result, Chapters 3, 4 and 5 can be interpreted as single chapters as they are based on three separate published papers. Finally, a summary of the findings, limitations of the studies and directions for future investigations are discussed in Chapter 6.

CHAPTER 2

GENERAL TECHNIQUES

This chapter presents and describes the techniques used, specific methodologies are included in the relevant data chapters.

2.1 Ethical approval

Ethical approval for the use of human tissues was granted by the University of Birmingham and the United Kingdom National Ethics Research Committees:

- Chapter 3: Nottingham Research Ethics Committee (05/Q2403/24) and Derby Research Ethics Committee (11/H0405/2).
- Chapter 4: East of Scotland Research Ethics Service (11/ES/1044).
- Chapter 5: Hertfordshire Research Ethics Committee (12/ EE/0136).

All patients, their families or next of kin provided consent for the use of these tissues.

2.1.1 Tissue preparation

Human joint tissue samples were donated by OA patients following total hip replacement (THR) or total knee replacement (TKR) and were transported to the laboratory immediately after surgery, immersed in unsupplemented culture media. They were then stored at

4℃ overnight to enable replicable processing times between samples. Post-mortem samples, from patients with no history of joint disease, were retrieved by Kingsmill Hospital pathology service before being transferred to the laboratory, and were stored in the same way prior to processing.

Cartilage was excised from the subchondral bone using a scalpel; care was taken to ensure that full thickness cartilage was obtained. Cylindrical explants of varying diameters were prepared from cartilage pieces using cork borers. Bone chips of 3-4 mm^3 were removed from the subchondral trabecular bone using bone scissors, and care was taken to ensure that cortical bone was not included in the bone chips.

2.2 Material preparation

2.2.1 Hydrogel preparation

Alginate preparation

Alginate solutions were prepared by the addition of medium viscosity sodium alginate (M/G ratio: 1.56, Mw: 80,000 - 120,000, Sigma Aldrich, UK) to dH_2O and heating to 85℃ for 1 h. The solution was then allowed to cool to room temperature.

Gellan gum preparation

Gellan gum solutions were prepared similarly; low acyl gellan gum (Special Ingredients, UK) was added to dH_2O and stirred at 85℃ for 1 h whilst stirring. Solutions were stored in a water bath at 50℃ until use.

All hydrogel solutions prepared for cell culture were sterilised by autoclaving for 30 min at 121℃ and 1 bar.

Fluid gel preparation

Fluid gels were produced by the introduction of shear during crosslinking which can be achieved using a rheometer, magnetic stirring or overhead mixing. For alginate, a 1.5%

w/v solution was prepared as above and then added to a cup geometry in an AR-G2 rheometer (TA Instruments, USA). The solution was sheared using a vane geometry at a shear rate of 500 s^{-1}, whilst 10% w/v 200 mM calcium chloride was added drop-wise over a period of 3 min. The solution was then equilibrated for 30 min at 20℃.

Agarose solutions were prepared by heating a 0.5% w/v low EEO agarose (Sigma) in dH_2O to 90℃. To form a fluid gel, this solution was then allowed to cool to room temperature (20℃) whilst constant shear was applied at 700 rpm on a magnetic stirrer.

2.2.2 Nanocrystalline hydroxyapatite preparation

Nanocrystalline hydroxyapatite (nanoHAp) was prepared by the precipitation method reported by Mobasherpour et al. [133]. 350 mL of 290 mM calcium nitrate tetrahydrate (Sigma) solution was raised to pH 10 by the drop-wise addition of ammonium hydroxide (NH_4OH, 28-30% NH_3, Sigma). 250 mL of 240 mM ammonium phosphate dibasic (Sigma) was then added to the stirring calcium nitrate drop-wise using a burette, whilst maintaining a pH between 9-11 with the addition of NH_4OH. The resulting solution was left stirring overnight before being centrifuged at 2000 x g for 5 min. The supernatant was removed and the precipitate was washed with dH_2O with agitation before centrifuging again. This was repeated a further four times to remove residual ammonium. The mineral content in solution was found to be 12% w/v by drying in an oven at 65℃ for 6 h.

2.3 Mechanical

2.3.1 Dynamic mechanical analysis

Both the solid-like and liquid-like components of viscoelasticity in cartilage were determined at a range of frequencies using dynamic mechanical analysis (DMA). Unlike stress relaxation and creep which have long time constants, DMA allowed for the investigation of short term loading effects using the phase lag (δ) between load and displacement.

A sinusoidal load was applied to the material and the displacement response was measured as in Figure 2.1. A Fourier analysis was then performed of the load and displacement waves. From this analysis, the magnitudes of the load (F^*) and displacement (d^*), were obtained as well as the angular frequency (ω, by equation 2.1) and time lag (T_δ) [105, 125]. The complex stiffness (k^*) was then calculated as equation 2.2.

$$\omega = 2\pi(Hz) \tag{2.1}$$

$$k^* = \frac{F^*}{d^*} \tag{2.2}$$

The phase lag (δ) was calculated from the fundamental frequency waves determined in the Fourier analysis using equation 2.3. In perfectly elastic materials, $\delta = 0°$ while in perfectly viscous materials $\delta = 90°$.

$$\delta = \omega T_\delta \tag{2.3}$$

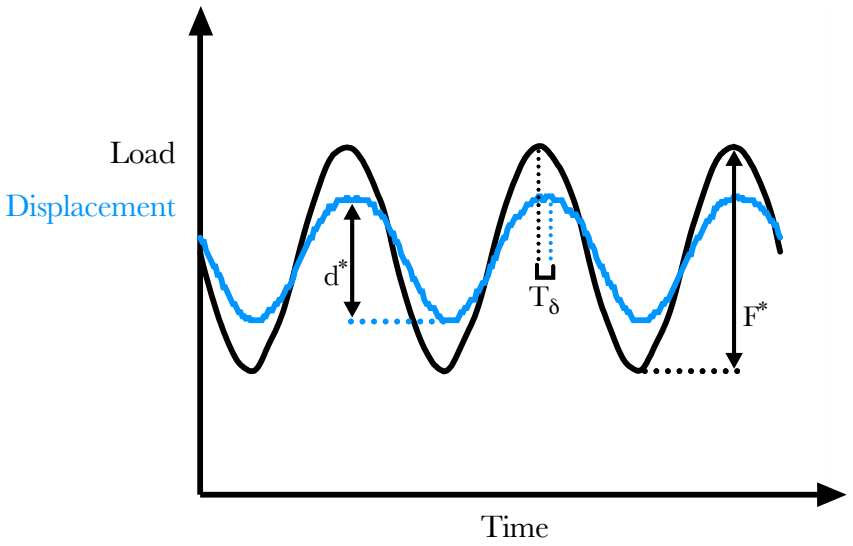

Figure 2.1: Example trace of out-of-phase load and displacement behaviour during cyclic testing of a viscoelastic material. d^* magnitude of displacement; T_δ time lag; F^* magnitude of force.

With these values of complex stiffness (k^*) and phase lag (δ), storage (k') and loss

stiffness (k") were calculated using equations 2.4 and 2.5. These were then be further converted to storage (E') and loss (E") modulus by dividing by a shape factor (SF), determined by the dimensions of the sample (equation 2.6 refers to a cylindrical sample of diameter, d, and thickness, t).

$$k' = k^* cos\delta \tag{2.4}$$

$$k'' = k^* sin\delta \tag{2.5}$$

$$SF = \frac{\pi d^2}{4t} \tag{2.6}$$

$$E' = \frac{k'}{SF} \tag{2.7}$$

$$E'' = \frac{k"}{SF} \tag{2.8}$$

Cartilage DMA

The viscoelastic properties of healthy and OA cartilage specimens were quantified using a Bose ElectroForce 3200 testing machine and the accompanying WinTest 4.1 DMA software (TA Instruments, USA). Prior to testing, cartilage specimens were fully hydrated in Ringer's solution (720 mg NaCl, 37 mg KCl, 170 mg $CaCl_2$ in 100 mL dH_2O, filtered through a 0.22 μm filter) for 30 min before being removed from the solution for testing. Cartilage specimens were placed on an aluminium base plate mounted on a 200 N load cell and were loaded using a 20 mm cylindrical compression platen that made contact with the articulating surface (Figure 2.2). Similar to previous cartilage studies, a sinusoidal compressive force of 16 to 36 N was applied to each specimen [43, 55, 161, 212]. As the cartilage specimens were 5.2 mm in diameter, the peak load of 36 N induced a

peak stress of 1.7 MPa which is similar to the estimated physiological peak stress during walking [241]. Before applying a frequency sweep, each specimen was preloaded to 3 N to avoid initial slipping and subjected to two preconditioning cycles. 1500 and 3000 cycles at 25 and 50 Hz respectively were applied, with 60 s between them, to achieve a dynamic 'steady-state' which has been stated to occur after around 1200 to 4500 cycles for *ex vivo* cartilage [55, 125, 220]. Following preconditioning, eight different physiologically-relevant sinusoidal frequencies (1, 8, 10, 12, 29, 49, 71 and 88 Hz) were applied to each cartilage specimen in order of increasing frequency [55].

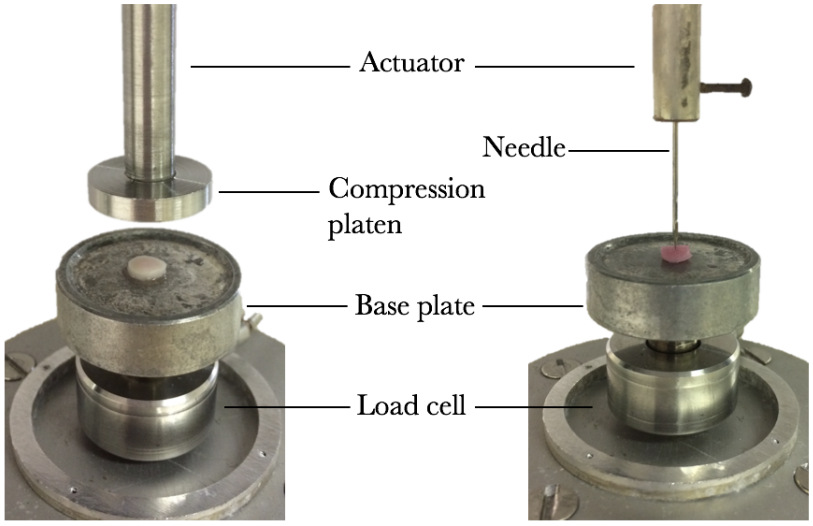

Figure 2.2: Mechanical testing set up for cartilage. Left: Aluminium compression platen mounted for DMA tests. Right: Sharp needle attached for thickness measurements.

Specimen thickness

The thickness of each cartilage specimen was measured, for conversion of DMA stiffness data to moduli, using a needle thickness test. A sharp needle was attached to the machine's displacement transducer (1 μm resolution, Figure 2.2 right) and the needle was pushed through the full thickness of the cartilage specimen. The displacement of the needle from initial contact with the cartilage (Figure 2.3 (a)) to contact with the base plate (Figure 2.3 (c)) was calculated as the cartilage thickness.

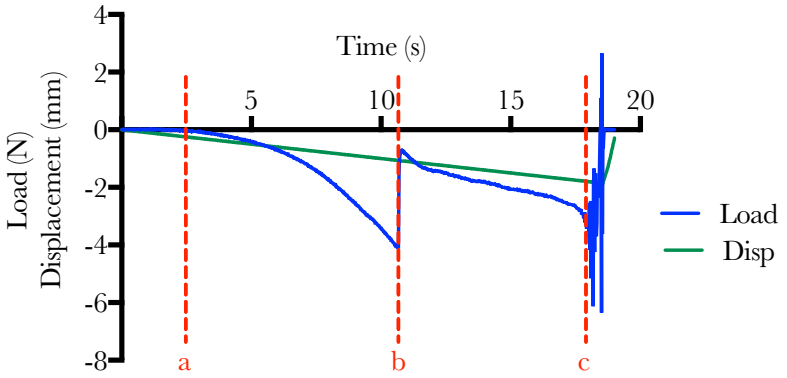

Figure 2.3: Thickness test displacement and load trace. a) initial contact between needle and cartilage, b) point at which the needle overcomes the surface tension and breaks through the surface, c) point at which the needle reaches the aluminium base plate. Thickness is calculated as the displacement between points a and c.

2.3.2 Stress relaxation

Stress relaxation was measured using a Bose Electroforce 5500 (TA Instruments). Each cylindrical hydrogel sample was displaced to 20% strain and the displacement was maintained for 5 min whilst the change in load (N) was measured using a 22 N load cell. Sample dimensions (length, L) were measured using a vernier caliper (10 μm resolution). Stress (σ) and strain (ϵ) were calculated by equations 2.9 and 2.10 respectively.

$$\sigma = \frac{Force}{Area} \tag{2.9}$$

$$\epsilon = \frac{L_0 - L_1}{L_0} \tag{2.10}$$

2.3.3 Rheology

Rheology is a branch of mechanical characterisation that considers the deformation and flow of materials, especially the non-Newtonian flow of liquids and the plastic flow of solids. Oscillation was applied at a range of shear rates and frequencies and the resistance to flow of the material was measured. The shear storage modulus and loss modulus were determined similarly to in DMA by calculating the out-of-phase displacement of the stress

and strain amplitudes.

From the shear storage (G') and shear loss (G'') modulus the complex shear modulus (G^*), phase angle (δ) and complex viscosity (η^*) were determined using equations 2.11, 2.12 and 2.13 respectively. Angular frequency (ω) was calculated as equation 2.1.

$$G^* = \sqrt{G' + G''} \tag{2.11}$$

$$tan\delta = \frac{G''}{G'} \tag{2.12}$$

$$\eta^* = \frac{G^*}{\omega} \tag{2.13}$$

All rheological characterisation was performed using an AR-G2 rheometer (TA instruments, USA). Fluid gels were tested using 40 mm sandblasted parallel plates with a 350 μm gap, while quiescent gels were tested using serrated plates with a 1000 μm gap. In all rheological characterisation, an initial stress sweep was performed to determine the region in which the viscoelastic behaviour was constant (linear viscoelastic region, LVR). Frequency sweeps were then performed at a constant strain to determine the frequency dependent moduli. Shear thinning behaviour was investigated by ramping the shear rate and measuring the change in viscosity. Specific rheological methods are detailed in the relevant chapters.

2.4 Physicochemical and Imaging

2.4.1 Thermogravimetric analysis

Thermogravimetric analysis (TGA) uses a very precise (1 μg resolution) balance to measure mass change in relation to temperature in order to collect information about physical phenomena such as phase transitions. Due to its high measurement accuracy, it can be

used to determine the specific temperatures at which these transitions occur.

The mass change relating to water loss in healthy and OA cartilage samples was measured using TGA in air. Cartilage explants were heated from 25-250℃ at a rate of 1 K.min^{-1} and gas flow rate of 30 ml.min^{-1} using a TG209 F1 (Netzsch, Germany) in aluminium oxide crucibles with lids (Netzsch, Germany). A background correction of the crucible environment was performed prior to testing cartilage samples. The mass was measured continually during heating and the change in mass plotted. The rate of mass change was calculated by the accompanying Netzsh TA4 software (Netzsch, Germany).

2.4.2 Micro X-ray fluorescence spectrometry

X-ray fluorescence spectrometry (μXRF) provides information about the spatial distribution of elements in a sample. X-rays produced by the instrument displace electrons of the inner shells of an atom. This induces an instability in the atom which is immediately corrected by movement of an electron from the next outer shell to fill the valency. Electrons closer to the nucleus have a lower binding energy than those further away, so transition to fill a valency results in a loss of energy. This energy is emitted as a K_α x-ray which is then detected by the instrument. The energy of the emitted x-ray is unique to the element as the distance between orbital shells is specific to each element.

Benchtop μXRF mapping was performed using an M4 Tornado and accompanying software (Bruker, Nano Gmbh, Berlin, Germany). The x-ray tube voltage was set to 50 kV and the tube current set to 500 μA with a pressure of 200 mbar to enable the detection of low K_α elements. For cartilage, 30 μm sections (see 2.5.1) on glass slides were scanned with a pixel size of 20 x 20 μm by the beam rastering across the sample at a scanning rate of 100 ms/px. Following data acquisition the maximum pixel intensity for each element was normalised across all sections.

2.4.3 White light interferometry

White light interferometry (WLI) is used to measure surface profiles and is commonly used to image electronic circuitry. An incident beam of white light is split to divide it between a reference plane and the test object. The reflection of white light from the reference and sample cause changes in the optical interference. This is detected by the CCD of the interferometer and processed to build a 3D profile which can then be analysed.

A MicroXAM Interferometer (KLA Tencor, UK) was used to map and quantify surface roughness (Sa) of healthy and OA cartilage explants both untested and after DMA testing. For each 5.2 mm diameter cartilage explant, 9 216 x 198 μm regions were imaged. The surface roughness (Sa) was then calculated using Scanning Probe Image Processor software (Image Metrology, Denmark).

2.4.4 Scanning electron microscopy

Scanning electron microscopy (SEM) uses a focused beam of electrons to image a sample. The interaction of electrons with atoms in the surface causes secondary electrons (SE) to be emitted, which are then detected to produce topographical information about the sample. The high focus of the beam gives a large depth of field resulting in an image with a 3D appearance.

Hydrogel samples were frozen at -20℃ before being dried under vacuum at -56℃ for 48 h (Mini Lablyo, Frozen in Time, Ltd., York, UK). They were then mounted onto conductive carbon tape for imaging. SEM was performed using a TM3030Plus benchtop instrument and accompanying software (Hitatchi, USA) with a beam acceleration voltage of 15 kV.

2.4.5 Micro computed tomography

Computed tomography uses x-rays and the relative attenuation of the sample is measured by the detector. In μCT, the sample is mounted on a rotating stage that moves in steps

of fractions of degrees to produce a series of images. These are then reconstructed to produce a vertical stack that can be visualised as 3D volumes.

μCT was performed using a Skyscan 1172 and accompanying software (Bruker, Germany). Scan parameters were specific for the material being analysed but all scanning was performed as 180° scans with 3 frame averaging. Prior to scanning, a flat-field correction was done to remove background artefacts such as the container in which samples were scanned. Following scanning, data was reconstructed in NRecon (Bruker) to build a 3D volume. Alignment adjustments and 2D measurements (e.g. cartilage thickness) were performed in DataViewer (Bruker). Further 2D and 3D analyses of the reconstructed data were performed in CTAn (Bruker). Regions of interest were defined and then data was thresholded to remove non-sample objects before morphological operations, such as despeckling, erosion and dilation as necessary before analysis. 3D volumes were visualised in CTVox (Bruker).

2.4.6 Phase contrast microscopy

Phase contrast microscopy uses slight variations in refractive index to image transparent samples. A phase ring blocks a large amount of light coming from the source, but when a sample is inserted, it scatters part of the light which is then refocused on the detector so that an image can be produced. Phase contrast microscopy for the visualisation of fluid gel structures was performed using a Leica DM 6000B.

2.4.7 Confocal laser scanning microscopy

Confocal microscopy enables imaging of a single focal plane, by passing a laser beam through a small aperture which is then reflected off a dichromatic mirror and focused by an objective lens. By rastering across the sample, a single plane image can be produced. Z-stacks are produced by scanning sequential layers of a sample which can then be reconstructed as a 3D image. Confocal microscopy of fluorescently labelled samples was performed using an FV1000 (Olympus, Germany) and 3D z-stacks were produced using

Imaris software (Bitplane, UK).

2.4.8 Cell tracking

Cell tracking was used to determine the level of entrapment provided by hydrogel matrices. Chondrocytes seeded in fluid and quiescent alginate were imaged every 5 min at 3 z-positions in each well over 20 h using a Cell-iQ and accompanying software Cell-iQ Imagen and Cell-iQ Analyser (Chip-Man Technologies, Tampere, Finland).

Cell movement was quantified by tracking individual cells frame-by-frame using Cell-iQ analyser (Chip-Man Technologies). The trajectories were mapped, and the movement in 2D was normalised from gel drift (caused by contraction) by tracking a reference point in each frame.

2.5 Biological

2.5.1 Cryosectioning

Cartilage tissue samples were snap-frozen in liquid nitrogen and embedded in TissueTek OCT (optimal cutting temperature) compound (Sakura, Finetek, USA) for sectioning using an OFT5000 cryostat (Bright Instruments Ltd, UK). Sections were prepared at thicknesses suitable for the intended analysis, attached to glass slides (SuperFrost, ThermoFisher) and stored at -20℃ until staining or analysis.

2.5.2 Alcian blue staining

Alcian blue stains acidic polysaccharides so is suitable for the staining of glycosaminoglycans in cartilage. 10 μm thick sections were prepared as above. Firstly, residual OCT was removed by washing in dH_2O for 5 min before Alcian blue solution was added. After 30 min it was rinsed with running water. Sections were then dehydrated by the addition of increasing concentrations of ethanol from 70-95% before sections were cleared with xylene

and mounted with distyrene, plasticiser and xylene resin (DPX). A coverslip was added and the DPX was allowed to cure for 30 min prior to imaging with an Eclipse E400 optical microscope (Nikon, Japan).

2.5.3 Cell isolation and culture

Chondrocytes

For the isolation of primary human articular chondrocytes (hAC), cartilage was diced into 1-2 mm^3 pieces using a scalpel and digested in sterile-filtered 2 mg/ml collagenase Clostridium Histolyticum, Type IA (0.5-3.0 FALGPA units/mg, Sigma Aldrich, USA) for 3 h at 37℃ under agitation. Following digestion, the solution was passed through a 70 μm cell strainer to remove any remaining fragments of tissue. The filtrate was then centrifuged at 400 x G for 7 min before removing the supernatant and resuspending the cell pellet in basal chondrocyte media:

- Dulbecco's Modified Eagle medium (DMEM) - high (4500 mg/L) glucose with L-Glutamine (D5796, Sigma, USA)
- 10% Fetal Bovine Serum (FBS) - South American origin (Sigma)
- 100 units/mL Penicillin-Streptomycin (Gibco, UK)
- 1% Non-Essential Amino Acids (NEAA) (Sigma)

Following initial isolation, hACs were cultured in a humidified incubator at 37℃ and 5% CO_2. Media was changed twice weekly. When cultures reached 70-80% confluence, they were passaged. Chondrocytes were washed with sterile phosphate buffered saline (PBS) and then 2x Trypsin-EDTA (Sigma, in PBS) was added and incubated at 37℃ and 5% CO_2 for 7-10 min to allow detachment of cells. Trypsin was inactivated by adding chondrocyte growth media. The cell-trypsin-media solution was centrifuged at 400 x g for 7 min and then the supernatant removed. Cells were then either passaged further, used experimentally or cryogenically stored. A human chondrocyte cell line, TC28 (gifted by

AstraZeneca) was also used for some experiments. The culturing and passaging technique for these cells was the same as hACs.

Osteoblasts

Bone chips isolated from joint tissue were washed 3 times in PBS and then 3-4 chips were added to a T25 flask with osteogenic media:

- Dulbecco's Modified Eagle medium (DMEM) - high (4500 mg/L) glucose with L-Glutamine (D5796, Sigma)
- 10% Fetal Bovine Serum (FBS) - South American origin (Sigma)
- 100 units/mL Penicillin-Streptomycin (Gibco)
- 1% Non-Essential Amino Acids (NEAA) (Sigma)
- 2 mM β-glycerophosphate disodium salt hydrate (Sigma, USA)
- 50 μg/mL L-ascorbic acid (Sigma, USA)
- 10 nM dexamethasome (Sigma, USA)

Bone chips were cultured in a humidified incubator at 37℃ and 5% CO_2. Initially, media was changed after 5 days and then every 3 days. After 10-14 days, osteoblasts reached around 30% confluence and bone chips were removed. When cultures reached 70-80% confluence, they were passaged. Osteoblasts were washed with sterile PBS and then 0.05% Trypsin-EDTA (with phenol red, Gibco) was added and incubated at 37℃ and 5% CO_2 for 7-10 min to allow detachment of cells. Trypsin was inactivated by adding osteoblast growth media. The cell-trypsin-media solution was centrifuged at 300 x g for 5 min and then the supernatant removed. Cells were then either passaged further, used experimentally or cryogenically stored.

Cryogenic cell storage

Chondrocytes and osteoblasts were passaged and then resuspended at 1 x 10^6 cells/mL in freezing media (FBS with 10% DMSO). They were then placed in a Mr Frosty (Nalgene, Thermo Scientific, USA) and stored at -80℃ for 24 h before being transferred to liquid nitrogen for longer storage.

Cell counting

Prior to seeding and experiments, cells were counted using a Countess II automated cell counter (Thermo Fisher) with Trypan blue correction. Passaged cells were centrifuged and the pellet resuspended in 1 mL growth media. 10 μL cell suspension was then mixed with 10 μL Trypan Blue solution. 10 μL solution was added to either side of a cell counting slide and automatically counted. Parameters for counting of each cell type are shown in Table 2.1. For encapsulation in hydrogel matrices a seeding density of 1 x 10^6 cells/mL was used throughout.

Table 2.1: Parameters for automated cell counting using Countess II (Thermo Fisher)

Cell type	Light	Focus
TC28	7	2659
Primary chondrocyte	7	2650
Primary osteoblast	7	2660

2.5.4 Live/Dead staining

Cell viability and morphology in monolayer cultures as well as in hydrogel scaffolds were determined using a calcein AM/ethidium homodimer-1 LIVE/DEAD assay (Invitrogen, USA). Calcein AM is cell-permeable and is hydrolysed to green fluorescent calcein by interaction with intra-cellular enzymes; cell-impermeable ethidium homodimer-1 binds to DNA and fluoresces red, and so, binds to the DNA of dead/dying cells with compromised cell membranes.

Culture media was removed and cells in monolayer or hydrogel constructs were washed with PBS. A solution of 2 μM calcein AM and 4 μM ethidium homodimer-1 was prepared in PBS and added to the cell cultures. After 20 min incubation at 37℃ away from direct light, cells were imaged using confocal microscopy (see 2.4.7). The images were then overlaid to view both live and dead cell populations in a single image.

2.5.5 RNA isolation

RNA was isolated from monolayer and hydrogel scaffold cultures using TRIzol reagent (Invitrogen). For cells in monolayer, culture media was removed before 1 mL TRIzol reagent was added for 3 min to lyse the cells. For hydrogel cultures, 1 mL TRIzol was added and the scaffold was then mechanically homogenised using a TissueRuptor (Qiagen). TRIzol and lysate from either preparation was then transferred to a lo-bind microtube (Eppendorf, Sigma). 200 μL chloroform (Fisher Scientific, molecular biology grade, RNAse free) was then added to each sample and they were shaken vigorously by hand for 15 s. Samples were then left on ice for 3 min before centrifugation for 15 min at 12,000 x g at 4℃ for the phase separation of RNA, DNA and protein. The aqueous, RNA-containing phase was aspirated and transferred to a new microtube. The protein and DNA phase were stored at -80℃ if required for further analysis or discarded. 500 μL isopropanol (Sigma, molecular biology grade, RNAse-free) was added to the aspirated RNA phase and RNA was left to precipitate at -20℃ overnight. The precipitate was isolated by centrifugation for 10 min at 12,000 x g at 4℃ before the supernatant was removed and discarded. The pellet was washed with 75% ethanol (Sigma, molecular biology grade, diluted RNAse-free molecular grade water), shaken by hand, and then centrifuged again for 5 min at 7,600 x g at 4℃. The supernatant was discarded and the pellet was dried in a vacuum desiccator for 5-10 min. Finally, the pellet was resuspended in 50 μL RNAse-free H_2O (HyClone, Fisher Scientific). RNA was stored at -80℃ until use in qRT-PCR.

RNA Quality and Concentration

RNA purity and concentration were determined using a NanoDrop 2000 UV-Vis spectrophotometer (Thermo Scientific, USA). 1 μL of RNA was added to the sample stage and the absorbance read at A260 and A280. Only samples with A260/280 ratios of more than 1.7 were used for qRT-PCR.

2.5.6 Quantitative real time polymerase chain reaction (qRT-PCR)

SYBR green chemistry was used for all qRT-PCR; custom forward and reverse primer sequences are listed in Table 2.2. These were used in combination with PrecisionPLUS OneStep SYBR Green master mix (PrimerDesign, UK) and alongside a housekeeping gene (PrimerDesign). The amplification protocol was performed using 5 μL reactions in frosted 384-well plates on a BioRad CFX384 thermocycler. The first step was reverse transcription for 10 min at 55℃ before enzyme activation at 95℃ for 2 min. Denaturation was performed at 95℃ for 10 s followed by 60 s of data collection at 60℃; this was cycled 40 times. Finally, a melt curve was run by the thermocycler. Relative gene expression was determined by ddCT, normalized to the housekeeping gene.

Table 2.2: Primer sequences used in qRT-PCR. Housekeeping primer sequences were not made available by the manufacturers.

Gene	**Accession No.**	**Forward**	**Reverse**
ACAN	NM 001135	CCAACCAGCCTGACA ACTTT	GTGAAGGGGAGGTGG TAATTG
COL1A1	NM 000088	AGACAGTGATTGAAT ACAAAACCA	GGAGTTTACAGGAAG CAGACA
COL2A1	NM 001844	ATGGCTGACCTGACC TGAT	GACAATAAATAAATA GAACACCGAGAT
Sox9	NM 000346	GGACCAGTACCCGCA CTTG	AATCCGGGTGGTCCT TCTTG

2.5.7 1,9-Dimethyl-methylene blue (DMMB) assay

Sulphated glycosaminoglycan (sGAG) release into the supernatant from chondrocyte-alginate cultures was measured using a 1,9-dimethyl-methylene blue (DMMB) assay [46]. DMMB binds to polyanionic substrates (such as sGAG) and undergoes a colour change from blue to violet [243].

The assay colour reagent was prepared by adding 1.6 mg DMMB, 0.304 g glycine, 0.237 g sodium chloride and 9.5 mL 0.1 M hydrochloric acid (HCl) into dH_2O to produce a total volume of 100 mL. The pH was then adjusted to pH 3 using HCl. Supernatant samples (50 μl) at 3, 7, 10, 14, 17, 21, 24, 27 and 30 days and standards of shark chondroitin sulphate were added to 200 μl DMMB colour reagent at pH 3. Alginate alone served as a control to remove the effect of interference of uronic acid groups in alginate. The absorbance was read immediately at A_{540} using a BioTek EL808 plate reader.

2.5.8 Immunohistochemistry

For immunohistochemistry, cell-seeded constructs were fixed with 4% paraformaldehyde for 10 min before blocking in vehicle (0.1 M PBS, 10% goat serum, 0.3% Triton-X-100). Aggrecan was detected using a mouse anti-aggrecan primary antibody (1:200, ThermoFisher, AHP0012) and incubated overnight at 4℃ under agitation. After washing in ice cold vehicle, Alexa-488 goat anti-mouse secondary antibody (1:500, Invitrogen A-21121) was used. Nuclei were counterstained with DAPI (1:5000, Sigma Aldrich). ProLong diamond antifade mountant (Thermo Fisher) was then added to each section before a coverslip was placed over the section and sealed using nail varnish.

2.5.9 Cytokine stimulation

Chondrocytes were seeded into gellan at $1x10^6$ cells/mL and 100 μL volume constructs were printed. Chondrocytes were also seeded into 48 well plates at 1 x 10^5 cells/well to match the seeding density of the printed constructs. Cells were allowed to adhere

overnight before the addition of recombinant IL-1β (from E. Coli, Sigma Aldrich) at 0.1, 0.3, 1, 3, 10 and 30 ng/mL in chondrocyte media. After 4 and 24 h, supernatants were removed and stored at -20℃ prior to analysis by enzyme linked immunosorbent assay (ELISA).

2.5.10 Enzyme-linked immunosorbent assay (ELISA)

Concentrations of IL-6 produced by chondrocytes were determined by solid-phase sandwich ELISA (DuoSet, R&D systems). Briefly, nunc plates (ThermoFisher) were coated with capture antibody (diluted in PBS) and incubated overnight at room temperature (RT) before being washed 3 times with wash buffer (0.05% Tween20 in PBS). Plates were then blocked using 0.1% bovine serum albumin (BSA, Fisher Chemical) in PBS for 2 h at RT. Samples were diluted 1:5 with culture media and IL-6 standards were serially diluted in PBS. 50 μL of sample or standard was added to the plate and incubated for a further 2 h at RT. The plate was then washed again before the detection antibody was added. After a further 2 h incubation and wash, 50 μL Strepdavin-HRP was added to each well and incubated in the dark for 20 min. After a final wash, Tetramethylbenzidine (TMB) solution was added and incubated for 20 min away from light. Stop solution was added before the plate was shaken and the absorbance read at A_{450} and A_{570} on a BioTek EL808 plate reader.

CHAPTER 3

CHANGES TO THE VISCOELASTIC RESPONSE IN OSTEOARTHRITIC CARTILAGE

Data in this chapter is also presented in the published article: *Matrix degradation in osteoarthritis primes the superficial region of cartilage for mechanical damage.* Acta Biomaterialia (2018)[1] [2]

Osteoarthritis (OA) is a degenerative disease that affects 25% of the world's population over fifty years of age. It is a chronic disease of the synovial joints, primarily the hip and knee. The main pathologies are degradation of the articular cartilage and changes to the subchondral bone, as a result of both mechanical wear and a locally elevated inflammatory state. This study compares the viscoelastic properties of cartilage that represents the biochemical changes in OA and age-matched healthy tissue. Further, the mechanical damage induced by this compressive loading cycle was characterised and the mechanism for it was investigated. The storage modulus of OA cartilage was shown to be significantly lower than that of healthy cartilage whilst having a higher capacity to hold water. Following mechanical testing, there was a significant increase in the surface roughness of OA cartilage. This change in surface structure occurred following a reduction in sulphated glycosaminoglycan content of the superficial region in OA, as seen by alcian blue staining and quantified by micro x-ray fluorescence. These findings are important in understanding how the chemical changes to cartilage matrix in OA influence its dynamic mechanical properties and structural integrity.

[1] DOI: 10.1016/j.actbio.2018.07.037

[2] All research was conceived, performed, analysed and written by MEC; co-authors on the published article provided assistance with equipment, proof-reading or supervision of the work.

3.1 Introduction

Mechanically, cartilage provides both a low-friction surface for articulation of the joint and acts to transmit compressive loading forces to the underlying subchondral bone. Similar to many other tissues in the body, it exhibits time-dependent viscous and elastic behaviour in both compression and tension [159]. The superficial region consists of Col II fibres oriented parallel to the articulating surface giving local tensile strength. This collagen network becomes more disordered in the middle region and in the deep zone and through the tidemark, fibres are aligned perpendicular to the articulating surface. In OA, the Col II network deteriorates, starting from the articulating surface in early OA and progressing through the tissue with increasing OA severity, as measured by Hollander et al., using Mankin grading [81]. Aggrecan, the most common proteoglycan in cartilage, is found at highest concentrations in the middle and deep zones. It is the second most abundant protein in cartilage following Col II and it sits along a hyaluronic acid backbone. Individual aggrecan molecules have sulphated glycosaminoglycan (sGAG) chains (keratan and chondroitin sulphate) coming from the aggrecan core protein that form a bottle-brush structure. These sGAG chains have a negative charge resulting in a high binding affinity to water.

The binding of water to proteoglycans is partly responsible for the compressive mechanical properties of cartilage. The carboxyl and sulphate groups of chondroitin sulphate and sulphate group of keratan sulphate provide fixed charge density (FCD) to the tissue, which, in combination with repulsion between neighbouring negatively charged chains results in a high osmotic pressure [74]. In healthy cartilage this pressure is compensated by the Col II network which restricts over-swelling and allows the tissue to resist compressive forces [74]. In OA an increase in matrix metalloproteins (MMPs) and aggrecanases, particularly members of the ADAMTS (A Disintegrin and Metalloproteinase with Thrombospondin motifs) family, have been identified as primary factors in the catabolism of articular cartilage matrix proteins including aggrecan and Col II [23, 81]. Changes in these matrix components have been shown to affect the mechanical properties

of human cartilage [181] and the dynamic mechanical properties of canine tissue with destabilisation-induced OA [68].

The viscoelastic properties of a material can be quantified by numerous methods including creep, stress relaxation and dynamic mechanical analysis (DMA). Unlike creep and stress relaxation which usually have long time constants, DMA is a dynamic testing method. By applying an oscillating force to a specimen and analysis of the out-of-phase displacement response, the frequency-dependent storage and loss moduli can be calculated. The storage modulus (E') describes a material's ability to store energy for elastic recoil while the loss modulus (E") characterises the material's ability to dissipate energy [126]. Studies have examined articular cartilage at low strain rates [51, 92, 136, 137, 196] and others have used DMA to assess frequency-dependency of the viscoelastic properties of cartilage in bovine and human specimens [106]. From these investigations, biphasic theory and BPVE theory were developed [119, 136]. However, the effects of OA on the dynamic, viscoelastic properties of human cartilage have so far been limited to the use of femoral head cartilage, where the direction and magnitude of loading is harder to define, or by indentation methods [178, 182, 196].

Changes to both the mechanical and physicochemical properties of cartilage are of interest in OA, and physical techniques for tissue analysis are becoming more commonly utilised. As such, quantitative mapping of chemical elements present in tissues is now possible using micro x-ray fluorescence spectroscopy (μXRF). This gives good spatial resolution of elements and has been used in a number of tissues including cartilage [83, 234, 245]. Other quantitative techniques that are traditionally used in materials science, but not in biological contexts, such as thermogravimetric analysis, are also being transferred to better understand the chemical structure of tissues and biomaterials. Cartilage is interesting thermogravimetrically due to its high water content, which has implications for its mechanical properties. As such, an accurate quantification of cartilage hydration can be helpful in understanding matrix changes in different disease states [201]. In OA, there is an observed change in the cartilage surface as it becomes fibrillated. White light

interferometry (WLI) is a commonly used technique in the analysis of surface features but as yet its use in characterising biological surfaces is infrequent. These techniques can all be used to enhance the knowledge and understanding of biological tissues.

Varus knee alignment as measured by the femorotibial angle has been shown to be a key factor for development and progression of OA [17]. In this position, the medial aspect of the knee joint experiences more damaging mechanical loading, as seen by a larger reduction in cartilage thickness [138]. However, the local inflammatory environment affects both aspects of the joint equally as the synovial fluid fills the joint space. In this study we have used human cartilage from the lateral aspect of the femoral condyles (Figure 3.1) of OA subjects. This tissue is exposed to the same chemical environment but is macroscopically undamaged. As yet, no one has studied the association between the early viscoelastic and chemical changes that occur in human OA cartilage. Therefore, the aim of this study was to determine the dynamic mechanical properties at a wide range of physiological frequencies and undertake a detailed chemical analysis to understand the differences observed in less structurally degraded, OA and healthy cartilage from the same anatomical region.

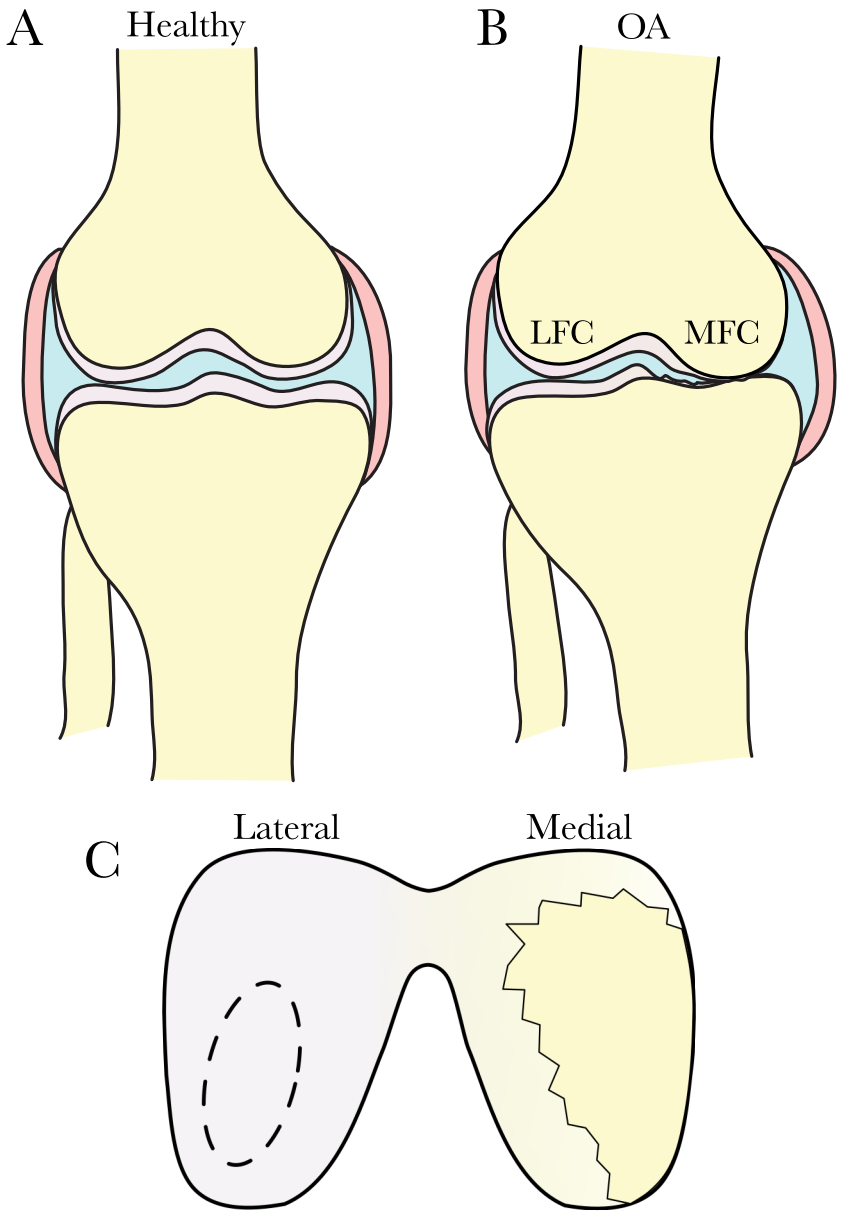

Figure 3.1: Representation of healthy (A) and OA (B,C) joint structures. Varus loading in OA causes a reduced joint space in the medial aspect such that cartilage of the medial aspect including the medial femoral condyle (MFC) undergoes severe mechanical degradation, revealing the underlying subchondral bone. The lateral aspect of the joint maintains a wider joint spacing such that tissue of the lateral femoral condyle (LFC) experiences less mechanical damage. The dashed region in C indicates where cartilage explants were taken for this study.

3.2 Methods

Tissue isolation and preparation

Cartilage explants were isolated from the lateral aspect of the femoral condyle of both OA and age matched post-mortem donors with no history of joint disease, as indicated in Figure 3.1. Cartilage in this region was macroscopically undamaged compared to the medial aspect of the joint, where cartilage had been degraded sufficiently that the subchondral bone was exposed (Figure 3.2). As the synovial fluid fills the joint space, however, the chemical and inflammatory environment is the same across both joint aspects. Tissue from post-mortem subjects is referred to as 'healthy' and tissue from joint replacement is referred to as 'OA'; patient data is presented in Table 3.1.

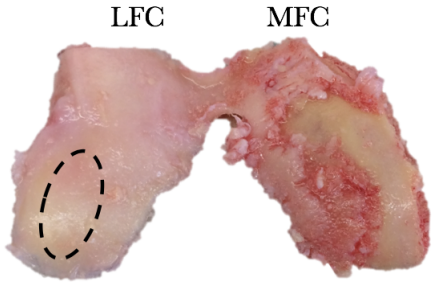

Figure 3.2: Femoral condyles as received in the laboratory from an OA patient following TKR surgery. The dashed region indicates where cartilage explants were taken for this study.

Table 3.1: Age and genders of the 20 patients whose cartilage was studied, n(explants) corresponds to specimens used for DMA.

Tissue	n (explants)	Age	Gender	Thickness (mm)
Healthy	6 (22)	76 (53-87)	M=3	1.465 ± 0.240
OA	14 (37)	71 (56-81)	M=10	1.463 ± 0.206

DMA and thickness testing

Cylindrical cartilage explants were hydrated for 30 min in Ringer's solution before DMA was performed in unconfined cyclic compression. Prior to testing a 3 N preload was

applied to prevent slipping. 1500 and 3000 cycles were then performed at 25 and 50 Hz respectively to achieve a dynamic 'steady state'; this has been shown to occur after between 1200-4500 preconditioning cycles in cartilage [55, 125, 220]. Cartilage samples were then loaded cyclically between 16-36 N at 1, 8, 10, 12, 29, 49, 71 and 88 Hz for 17, 61, 73, 85, 190, 314, 450 and 550 cycles respectively (OA n=37; healthy n=22; total testing time was 6 min 35 s). Cartilage explants of 5.2 mm diameter loaded between 16-36 N, induced a mean stress of 1.22 MPa, peak stress of 1.7 MPa, and 0.95 MPa stress amplitude. Depending on specimen thickness the applied strain was between 1.8-4.8%.

Following viscoelastic testing, the samples were rehydrated in case of any water loss during testing before thickness measurements were performed using a needle thickness test [199]. Samples were then stored at -80°C prior to physicochemical analysis.

Physicochemical characterisation

Firstly TGA was used to determine the absolute water content in the matrix by heating from 25-250°C at 1 K.min^{-1} (n=4). Some explants were then snap-frozen before cryosectioning. μXRF was performed on 30 μm sections to map and quantify element distribution in the sagittal plane of the cartilage, across tested and untested samples (n=3). To visualise the proteoglycan distribution, alcian blue histological staining was performed on 10 μm sections before WLI was used to quantify the areal surface roughness of untested and tested cartilage explants (n=4).

Data analysis and statistical methods

Statistical analyses were performed using Prism 7 (GraphPad, CA, USA). Two-way ANOVA with Tukey's post-hoc testing for multiple comparisons was used for mechanical data. Student's t-tests were used to compare differences between healthy and OA tissues, and also between samples tested and untested by DMA. Results where $p<0.05$ were considered significant. Logarithmic frequency dependent behaviour of the storage (E') and loss (E") moduli were described by equations 3.1 and 3.2 respectively, where (f)

refers to frequency.

$$E' = Aln(f) + B \tag{3.1}$$

$$E'' = Cln(f) + D \tag{3.2}$$

3.3 Results

Viscoelastic properties of OA and healthy cartilage

The frequency dependence of the storage (E') and loss (E") moduli are shown in Figures 3.3A and 3.3B for healthy and OA cartilage respectively. The storage modulus of both healthy and OA cartilage showed logarithmic frequency dependent behaviour which then plateaued from around 50 Hz (Figure 3.3A). Results of two-way ANOVA/Tukey showed that in both the loss and storage modulus, there were significant effects of frequency ($p<0.001$). The effects of disease in relation to frequency were significant in the storage modulus ($p<0.001$) but not in the loss modulus ($p=0.002$). Student's t-tests of the mean moduli values showed that the storage modulus of healthy cartilage was significantly higher ($p<0.05$) than that of OA cartilage at all frequencies with the exception of 88 Hz ($p=0.058$), as shown in Supplementary Table A.1. The loss moduli were also logarithmically frequency dependent and plateaued from around 50 Hz.

Table 3.2 shows the values which satisfy equations 3.1 and 3.2 for both E' and E"; the viscoelastic behaviour was found to be linearly logarithmic. The area inside the hysteresis loops (Figure 3.4) was greater for OA specimens than healthy at low frequencies (OA: 0.068 Nmm; healthy: 0.056 Nmm), and high frequencies (OA: 0.119 Nmm; healthy: 0.084 Nmm), indicating that the healthy specimens had a more elastic response. The mean level of displacement was fairly stable throughout testing showing that there was not a marked change to the height of samples during testing (Supplementary Figure A.1).

Table 3.2: Storage and loss modulus coefficients as equations 3.1 and 3.2 from regression analyses. All coefficients and constants values are MPa, $p<0.05$ indicates that the logarithmic regression was significant.

Sample	**Property**	**A**	**B**	**C**	**D**	**R^2**	**P**
Healthy	E'	2.155	31.79	-	-	0.977	<0.05
OA	E'	1.968	28.07	-	-	0.977	<0.05
Healthy	E"	-	-	0.551	3.576	0.961	<0.05
OA	E"	-	-	0.585	3.166	0.956	<0.05

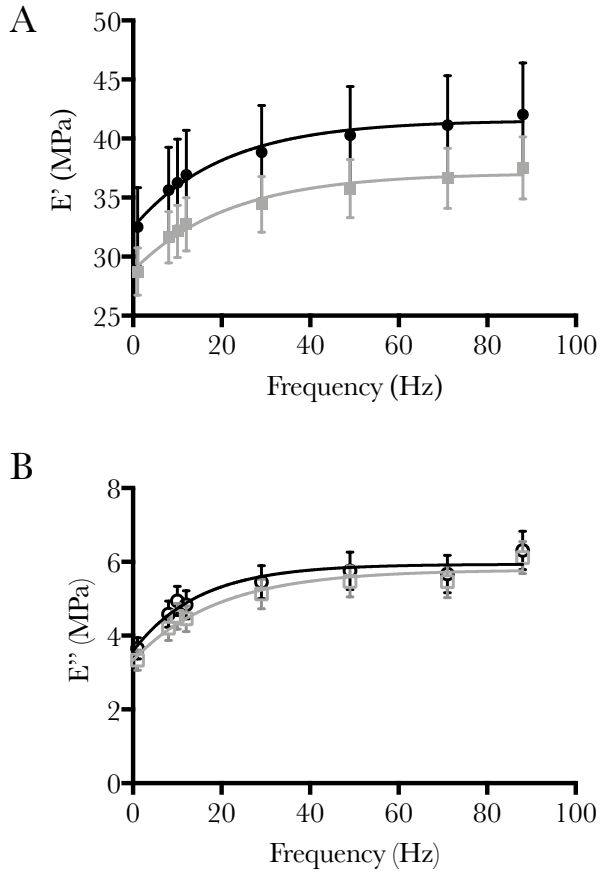

Figure 3.3: A) Storage modulus (E') of healthy (●) and OA (■) cartilage with 95% confidence intervals, B) Loss modulus (E") of healthy (○) and OA (□) cartilage with 95% confidence intervals; H n=22, OA n=37.

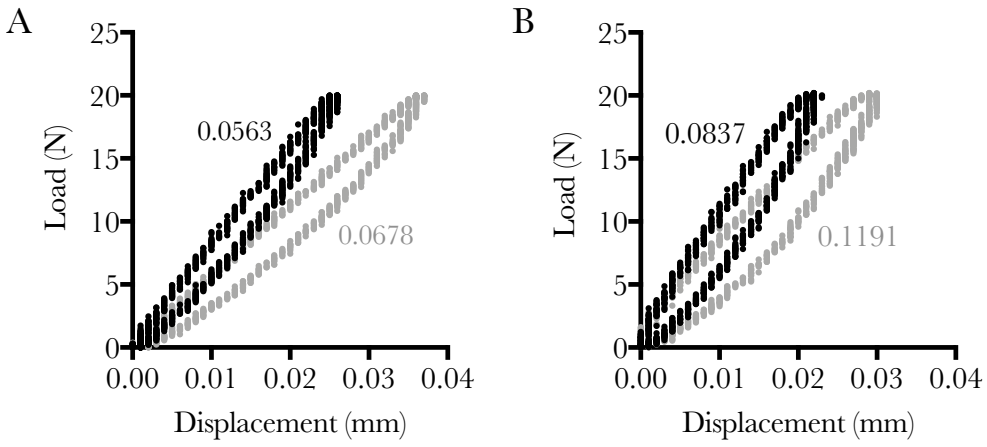

Figure 3.4: Hysteresis loops of healthy (black) and OA (grey) cartilage at A)10 Hz and B) 88 Hz, inset values of hysteresis area (Nmm)

Thermogravimetric analysis of OA and healthy cartilage

The binding of water by the proteoglycan network provides a large contribution to the compressive properties of articular cartilage, so to elucidate the changes seen in Figure 3.3, the amount of water in these samples was accurately measured. TGA was used to quantify the amount of bound water in untested and post-DMA cartilage explants from both healthy and OA subjects. Figure 3.5A shows the change in % mass of OA and healthy cartilage between 25-250°C. Between these temperatures, the loss of water was seen up to around 90°C and a further transition started at around 210°C. The linear region of water loss as stated in Table 3.3 resulted in a larger change in mass in OA specimens compared to healthy (Figure 3.5B). The OA samples showed a significantly larger change in mass by 100°C ($p<0.05$) and a faster peak rate of mass change, as seen by the DTG curve (dashed line). The further change in mass to 250°C was very similar between the healthy and OA samples, -23.76 and -23.08% respectively.

Table 3.3: Thermogravimetric parameters of healthy and OA samples during linear water loss transition, n=4

Sample (N)	**Linear region (°C)**	**DTG peak (°C)**	**DTG peak (%/min)**	**Lin. region mass change**
Healthy (4)	52.30-78.50	69.71	-2.39	-54.22%
OA (4)	53.58-79.99	71.87	-2.74	-60.87%

Mapping and quantification of sulphur in cartilage sections

μXRF was used to quantify the changes in sulphur distribution in OA and healthy tissue which likely corresponds to the aggrecan distribution across cartilage sections. Figure 3.6 shows that in untested samples, healthy cartilage had a consistent gradient across the tissue where sulphur was most abundant in the deep zone and less so in the superficial region. OA cartilage, however, had a less regular gradient towards the surface and visually the superficial region showed minor damage to the surface even in untested samples. Following DMA, the surface of healthy cartilage was slightly deformed along the normal

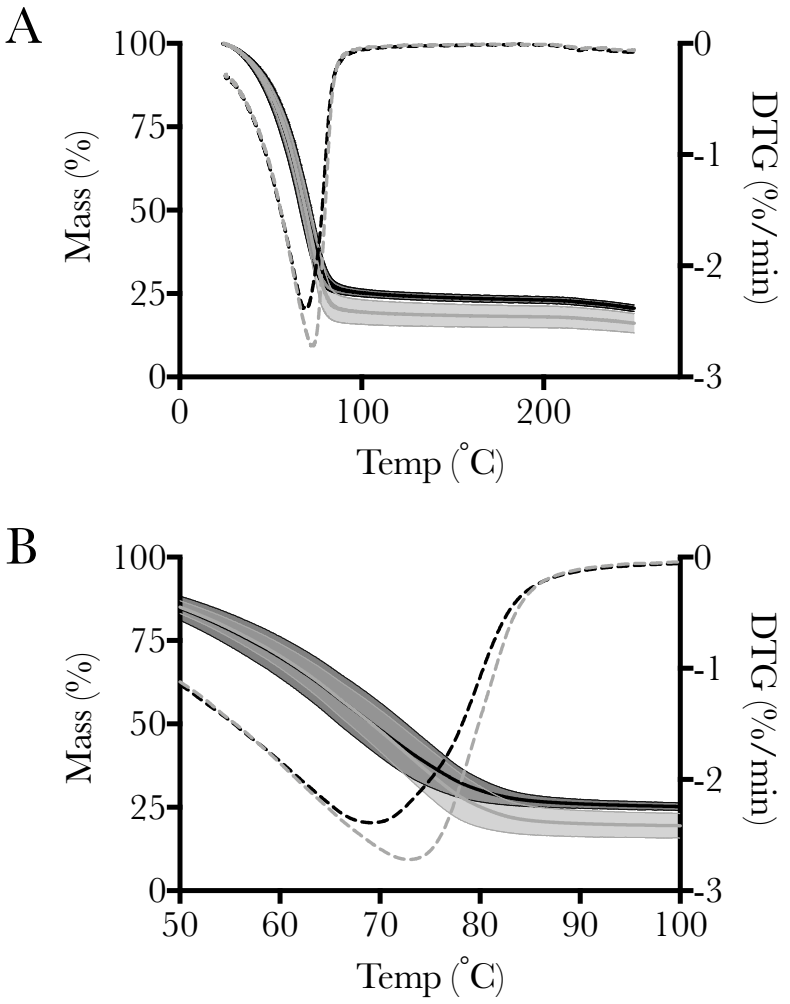

Figure 3.5: Thermogravimetric analysis of OA (grey) and healthy (black) cartilage between (A) 20-250℃. Dashed line indicates kinetics of mass change (DTG). Inset (B) shows the end of the water loss region, n=4.

direction of collagen fibril alignment in this region, but the surface was not macroscopically ruptured as seen in the OA samples. The OA cartilage had severe damage to the articulating surface post-DMA, while the middle and deep regions retained their structure. Figure 3.6B shows the relative quantification of sulphur distribution across the sections. Healthy and OA sections had similar sulphur levels in the deep and middle zones, but the OA samples had lower levels in the superficial zone. Quantification of the post-DMA samples shows that in both OA and healthy samples, mechanical testing reduced the sulphur content, which is likely due to changes in aggrecan proteoglycan organisation.

However, this change was more marked in the superficial region of OA samples compared to healthy. Quantification of the OA samples post-DMA was limited at the articulating surface due to the mechanically-induced damage. In Figure 3.7, co-localisation of calcium and phosphorus was evidence of mineral deposits in the cartilage. These were observed in the middle and superficial zones of OA but not healthy cartilage samples.

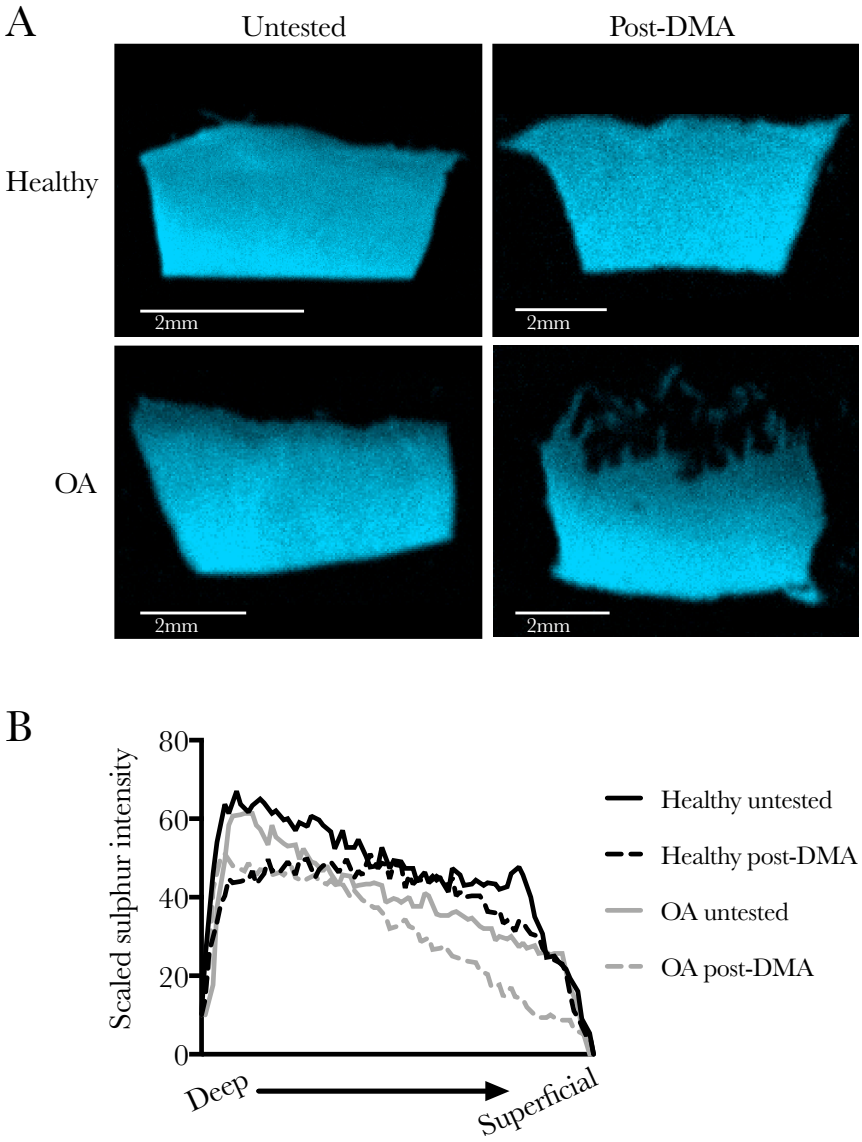

Figure 3.6: μXRF mapping of distribution of sulphur in cartilage sections (sagittal plane), highest intensity is shown by brighter colour, closest to the bone interface at the bottom of each image. B) Relative quantification of sulphur across healthy (black) and OA (grey) cartilage sections that were untested (solid) and post-DMA (dashed) (n=3).

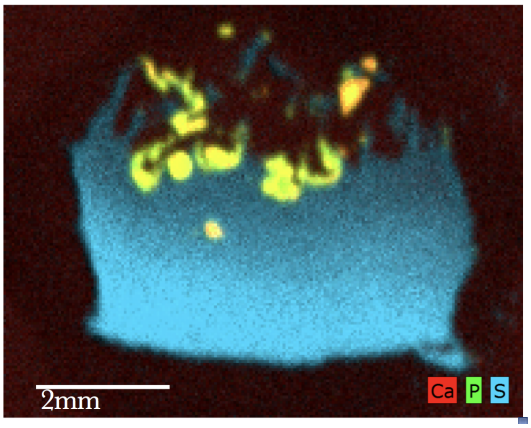

Figure 3.7: μXRF mapping of sulphur, calcium and phosphorus showing evidence of Ca and P localisation in mineral deposits in the middle and superficial regions of OA cartilage.

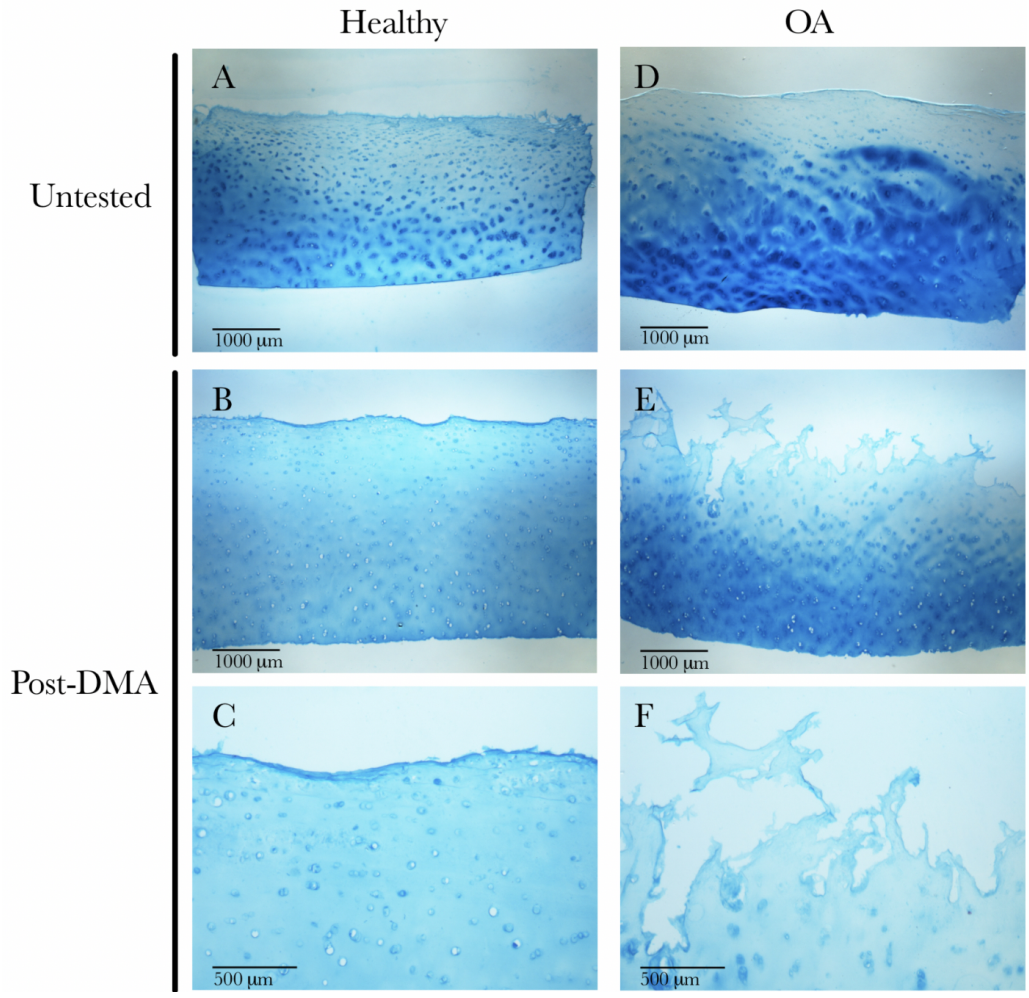

Figure 3.8: Representative alcian blue staining of 10 μm thick cartilage sections from healthy (A-C) and OA (D-F) samples both untested (A, D) and post-DMA (B&C, E&F).

Histological staining

Whilst μXRF was useful for quantifying the changes in element distribution, the resolution was limited. Therefore, in order to better visualise both the proteoglycan distribution and physical changes to the superficial region, alcian blue staining of 10 μm cartilage sections was performed. In healthy cartilage (Figure 3.8A-C), there was a gradient of proteoglycan, with the heaviest staining in the deep region which became progressively lighter towards the superficial region. Following DMA of healthy cartilage, there was no visible difference in the surface structure (Figure 3.8C) from the untested sample (Figure 3.8A) In OA cartilage, the distribution of proteoglycan was less ordered and there was evidence of cell clusters. Further, although there was a gradient, there were also regions of darker staining throughout the middle region (Figure 3.8D). Compared to the healthy tissue, the staining was less even, alongside large cracks in the surface with fragments of tissue detaching from the section (Figure 3.8E, F).

Articulating surface damage

To quantify the damage to the articulating surface following DMA, WLI was used to measure surface roughness. Figure 3.9 shows that there was no difference between healthy specimens that have and have not undergone a dynamic testing protocol. In the OA samples, the surface roughness prior to testing was significantly higher than that of the healthy samples ($p<0.05$) indicating an initial degree of mechanical damage that was not macroscopically visible. Following DMA, the surface roughness of OA specimens was significantly higher than subject-matched samples that have not undergone DMA ($p<0.05$).

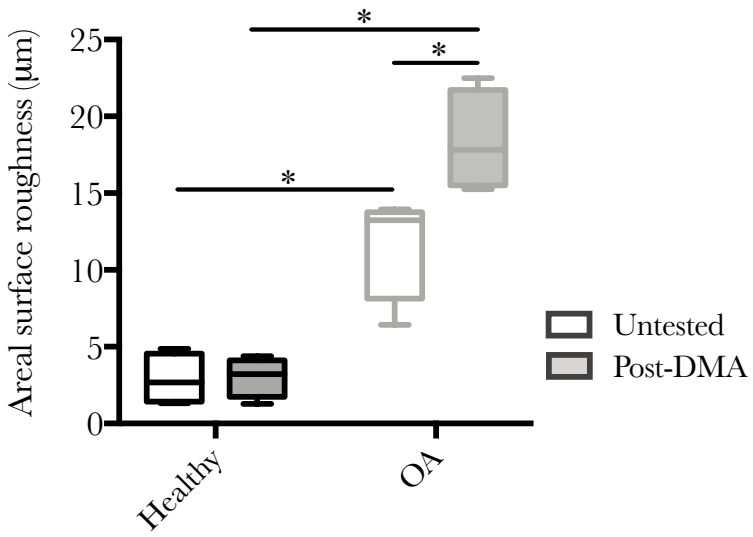

Figure 3.9: Surface roughness of healthy and OA cartilage samples with or without DMA testing as measured by WLI; n=3, * $p<0.05$.

3.4 Discussion

This study aimed to understand the differences in frequency-dependent viscoelastic properties of isolated healthy and OA human articular cartilage and to compare these to the physicochemical changes seen. Tissue was excised from the lateral aspect of the OA joint, which is known to be less exposed to mechanical stresses than the medial aspect, and thus was used to represent cartilage which was not excessively mechanically loaded but was exposed to the same chemical environment.

The first component of this study determined the viscoelastic properties of healthy and OA human cartilage. The logarithmic frequency-dependent behaviour in both the storage and loss modulus was similar to previous findings in human and bovine cartilage [106, 161, 212]. The significant reduction in storage modulus across a range of frequencies in OA specimens is likely to be indicative of disruption to the matrix structure as a result of OA cytokines, MMPs and altered joint loading. The solid matrix components of cartilage, Col II and the aggrecan-rich proteoglycan network, are primarily responsible for the compressive stiffness of cartilage and was shown to be reduced in OA. This difference was statistically significant at all but the highest frequency, 88 Hz (P=0.0581), which has

previously been implicated as a frequency brought about during a rapid heel strike rise time that may predispose subjects to OA [55, 173]. The storage and loss moduli of healthy femoral condyle cartilage were similar to that of 'healthy' human femoral head cartilage (obtained from subjects who had experienced a traumatic fracture of the femoral neck) and follow the same logarithmic trends [212]. The viscoelastic response in cartilage is caused by a combination of fluid-dependent and fluid-independent behaviour [136, 137]. In healthy intact cartilage, the fluid dependent behaviour likely dominates the energy dissipation characteristics. However, in the OA samples where the superficial region is compromised, increasing the tissue permeability, the inherent viscoelasticity of the solid matrix components will have a larger effect on the energy dissipation of the tissue [196].

Cartilage is comprised of more than 70% water, and the binding of water to proteoglycans provides high osmotic pressure, which is a key factor in the compressive properties of the tissue [74]. Therefore, the amount of water in each sample was measured by measuring the change in mass as a function of temperature. The higher water content of OA cartilage compared to healthy was shown thermogravimetrically by Sohar et al. [201]. However, their study showed the end of the water TG step at higher temperatures than seen in this study (102.25°C and 104.60°C compared to 78.50°C and 79.99°C for healthy and OA tissue respectively), which is likely due to the faster rate of heating used in their study (5K.min^{-1}). The increased water content in OA samples is a result of an increased ability for the tissue to swell. This change in swelling capacity is due to breakdown of the Col II network associated with matrix catabolism in OA as measured by Bank et al. They found that an increased swelling percentage correlated with an increased percentage of degraded collagen in human samples from OA femoral head cartilage [8]. This reduced the elastic restraint on the tissue, meaning more extra-fibrillar water can be held [9, 201]. This reduction in restraint is likely to progressively increase during testing of the OA samples as the superficial region becomes damaged and tissue permeability increases [196]. The increase in area of hysteresis between 10 and 88 Hz in both healthy and OA samples is likely caused by the effect of superficial matrix disruption.

Cartilage swelling as a result of changes to the matrix composition has been shown previously using delayed gadolinium enhanced magnetic resonance imaging (dGEMRI), where a correlation between increased cartilage thickness and decreased GAG content was shown in the medial compartment of the knee [28]. The increased water content observed in OA samples may contribute to the similarities in loss modulus seen between healthy and OA tissue. The peak rate of mass change in the water TG step was higher in the OA samples and the peak was shifted to a higher temperature. The faster peak mass change was likely due to the increased water content, whilst the shifted peak suggests a higher binding strength of water to the PG network.

The gradient distribution of matrix components Col II and aggrecan are known to be critical to the proper mechanical functioning of cartilage. As water and its binding to PG is so important in the load-bearing capacity of cartilage, the distribution of the PG network was mapped. Benchtop μXRF was used to elementally map cartilage sections and was a simple and effective way to quantify the differences in sulphur content, corresponding to sGAG and aggrecan content in tissue samples. It is well known that the GAG content at the superficial region is lower than that of the middle and deep zones [160]. Here, however, seen by less bright pixels and quantified by line gradients from the deep to superficial zones, we saw a further reduction in the superficial region in OA cartilage. The reason for this may be proximity and contact with the synovial fluid, which, in the inflamed state of OA has a higher concentration of catabolic MMPs and cytokines [166]. Further, the identification of mineral-like deposits near the cartilage surface of OA cartilage suggests that mineralisation in OA may occur prior to visible mechanical damage to the superficial region. Tissue mineralisation of cartilage and meniscus are common in end-stage OA, usually seen as deposits of HAp and calcium pyrophosphate dihydrate (CPPD) crystals [54].

These mineral deposits were seen primarily in the upper middle and superficial regions of the cartilage sections; they may have a role in the observed surface damage following DMA. Relatively large (they can be seen radiographically), hard particles in a

soft tissue could act as stress concentrations for cracks in cartilage to form, similar to the cracks that form following a traumatic insult to the cartilage surface [184]. Changes in surface roughness were measured using WLI, a technique commonly used in electronics for profiling surfaces. It enabled the quantification of the surface damage by analysing the peaks and valleys in the cartilage surface to quantify surface roughness. The significant increase in surface roughness following DMA in the OA subjects indicated that the superficial region was more susceptible to damage as has been shown previously in bovine tissue [25, 116]. Further, the difference in Sa between healthy and OA samples observed was similar to the profile surface roughness (Ra) seen by Graindorge et al. between healthy (Ra=1.06) and emery-roughened (Ra=23.2) samples [62]. Whilst there was evidence of deformation of the superficial region of healthy tissue under μXRF, the superficial region of OA cartilage showed severe rupturing of the cartilage surface. Disruption to the matrix composition was likely responsible for this; as mentioned, there is a change in the collagen network originating at the articulating surface [81, 143, 145]. This will reduce the tensile strength of the cartilage surface which reduces its ability to resist deformation.

Age-related changes to the proteoglycan content of the superficial layer of cartilage have been identified previously [74]. This effect is enhanced when the biochemical balance shifts in states such as trauma and OA causing increases in catabolic cytokines such as interleukin-1 (IL-1) and tumour necrosis factor alpha (TNFa). Guilak et al. have discussed how physiological joint loading has protective mechanisms for regulating cytokine levels [67, 69, 189]. The balance between protective and damaging joint loading is likely key in the progression of OA. Another factor shown to increase the severity of OA symptoms is obesity; there is a combined effect of increased loading on the joints due to higher body mass alongside elevated production of adipose-derived cytokines (adipokines) [58, 67, 165]. These adipokines have been shown to increase production of many pro-inflammatory cytokines and catabolic matrix proteases. Leptin, a well characterised adipokine, is increased in OA synovial fluid and has been shown to increase MMP-1 and MMP-13 production in human primary chondrocytes and to mediate greater IL-6 secretion from OA synovial

fibroblasts [162, 166]. Importantly in this study, while the joint loading of the OA subjects is focused in the medial compartment of the joint, the use of tissue from the lateral compartment demonstrates the effects of the inflammatory OA environment on cartilage tissue.

Limitations: The use of human tissue samples is limiting in the number available, particularly the numbers of post mortem samples. Firstly, this means that following a power analysis, an effect size of 0.31 should be expected for the presented number of samples and an effect size of 0.48 for the 22 patients that samples were retrieved from. Secondly, due to the limited number of human samples, the testing protocols for DMA were all performed in the same order, so the loading history may affect the viscoelastic measurements. Future studies could investigate whether the loading history affects the viscoelastic response by randomising the order of frequencies during testing. Further, as the cartilage surface is semi-translucent, white light interferometry values are solely relative to surfaces with similar optical properties to cartilage.

3.5 Conclusions

For the first time, we have linked the local changes in chemistry and structure to the dynamic mechanical properties of OA and healthy cartilage, isolated from the same anatomical region in human donors. There is a significant reduction in the storage moduli of cartilage from OA compared to age-matched healthy subjects, indicating that in OA the elastic response of cartilage deteriorates. This reduction in storage modulus is likely due to a disruption to the collagen network as OA tissues showed a higher capacity to swell and bind water. Visible changes to the cartilage surface following DMA were investigated and an increased surface roughness was observed in OA but not healthy tissue. Finally, the mechanism for this disruption was investigated using histological staining and μXRF mapping to determine and quantify the proteoglycan distribution in both healthy and OA tissue.

CHAPTER 4

THE EFFECT OF GEOMETRIC CONFINEMENT ON CHONDROCYTE PHENOTYPE IN 3D CULTURE

Data in this chapter is also presented in the published article: *Geometric Confinement is required for recovery and maintenance of chondrocyte phenotype in alginate.* APL Bioengineering 1 (2017)[1] [2]

Human articular chondrocytes lose their native phenotype when expanded in traditional monolayer cultures. As a consequence, hydrogel encapsulation has been investigated as a means to maintain natural phenotype. Alginate has been widely used for cartilage engineering as it has been shown to enable the recovery of a native collagen type II expressing chondrocyte phenotype. This study has evaluated whether the capacity of the materials to maintain/revert phenotype is due to the composition of the material or the physical entrapment provided by the gel. To achieve this, an alginate fluid gel (a shear-thinning structured gel system) was produced of identical chemistry to a traditionally gelled alginate structure. Both were seeded with passaged primary human articular chondrocytes. Chondrocytes in quiescent alginate showed recovery of the native phenotype and a spherical morphology. Chondrocytes in alginate fluid gel were unable to maintain a recovered phenotype despite having spherical morphology and were shown to have a lower level of entrapment than those in quiescent alginate. These findings indicate that geometric entrapment is essential to maintenance of a recovered chondrocyte phenotype in alginate.

[1] DOI: 10.1063/1.5006752

[2] All research was conceived, performed, analysed and written by MEC; co-authors on the published article provided assistance with equipment, proof-reading or supervision of the work.

4.1 Introduction

An alternative to the pharmacological approaches being investigated to prevent OA progression is the surgical repair of focal defects in cartilage tissue in patients with early-stage OA, via autologous chondrocyte implantation (ACI) [129]. This repair strategy is dependent on the expansion of chondrocytes *in vitro* before re-implantation into the defect site [109]. Critically, expansion in 2D monolayer culture causes chondrocytes to rapidly de-differentiate, with a marked loss in their expression of Col II and aggrecan, and an associated increase in the expression of Col I [6, 152, 192]. This loss of chondrogenicity leads to the formation of an inferior hyaline cartilage, rich in Col I, which has been reported to be functionally similar to the fibro-cartilage that is formed following micro-fracture surgery [218]. Consequently, this means that the ACI process has been of limited clinical success. There is therefore a need to develop an improved method for the expansion of chondrocytes *in vitro*, which can maintain the chondrocyte phenotype and thus promote regeneration of functional articular cartilage.

Hydrogels have been thoroughly investigated in regenerative medicine to act as ECM mimics due to their high water content and high degree of tunability [38, 63]. One such hydrogel is alginate, a linear, un-branched polysaccharide derived from brown algae that has been used in drug delivery, wound healing, and tissue regeneration [38, 108, 158]. Containing b-D-mannuronic acid (M) and a-L-guluronic acid (G) residues arranged either in blocks (GGG/MMM) or alternating sequences (GMGMGM) [108], alginate undergoes ionotropic gelation upon introduction of divalent cations to form crosslinks between G residues resulting in an egg-box structure [84, 110, 208].

Previously, alginate has been shown to maintain adult chondrocyte phenotype and to drive bone marrow derived mesenchymal stem cells towards a chondrogenic phenotype [1, 7, 16, 127]. Whether this is due to the physical entrapment of the chondrocytes in a 3D scaffold or due to the chemical influence of alginate is relatively unknown. The formation of a cartilage matrix by the encapsulation of allogenic chondrocytes is a promising approach to produce cartilage for surgical implantation.

In this chapter, the influence of the physical entrapment of alginate on the embedded chondrocytes has been investigated by comparing markers of cartilage matrix formation when chondrocytes are entrapped in an normal, quiescent alginate gel matrix and also between the particles that are formed in an alginate fluid gel. Fluid hydrogels are produced through the introduction of shear during gelation, resulting in the production of microparticles of gel with short-range interactions [47, 49, 72, 148]. Fluid gels exhibit solid-like behaviour in the absence of external shear stresses, but flow like liquids under shear, and hence could be utilized in an injectable therapeutic solution for the delivery of chondrocytes to defects in the cartilage surface. The cells dispersed within this structure are not physically entrapped as they would be in a normal, quiescently gelled structure; instead, they are suspended between fragments of crosslinked alginate. They are, however, exposed to the same chemical stimuli. The aim of this study was therefore to determine the effect of different levels of encapsulation on chondrocyte viability, morphology, and phenotype by comparing quiescent and fluid alginate.

4.2 Methods

Alginate preparation and characterisation

Fluid (sheared) and quiescent (traditional statically crosslinked) alginate matrices were produced of identical chemistry (1.5% w/v alginate with 10% 0.2 M $CaCl_2$). Fluid alginate was produced by shearing a sodium alginate solution at 500 s^{-1} using a vane geometry on a rheometer while $CaCl_2$ was added drop-wise. The mechanical properties of both matrices were characterised using oscillatory rheology. Initial stress sweeps from 0.1-1000 Pa were performed to determine the linear viscoelastic region (LVR) before frequency sweeps from 0.1-100 Hz at 0.5% strain, to determine the effect of frequency on the viscoelastic properties. Further, the shear rate was ramped from 0.1-500 s^{-1} to determine the shear thinning behaviour of these materials. To model fluid gel response to shearing through a needle or pipette, the shear rate was ramped from 0.1-500-0.1-500-0.1 s^{-1} at constant strain. The bulk architecture of the fluid gel was then investigated; PEG and fluid alginate were mixed in a 4:1 ratio and imaged using phase contrast microscopy. The polymer microarchitectures were then investigated by freeze drying and imaging with SEM.

Encapsulation of chondrocytes in alginate

Primary human chondrocytes, isolated from cartilage of the femoral condyles of OA patients, and immortalised chondrocytes were cultured in monolayer as described in Chapter 2. For quiescent gels, chondrocytes were mixed with 1.5% w/v alginate to a concentration of $1x10^6$ cells/ml and seeded into the wells of a 96-well plate containing 0.2 M $CaCl_2$. The quiescent gel was then incubated for 20 min at 37°C to allow cross-linking to occur. Cell-seeded gels were then rinsed twice with PBS, 0.2 ml of chondrocyte growth medium was added, and they were incubated at 37°C for up to 30 days. Alginate fluid gel was simply mixed with $1x10^6$ hACs and pipetted into a 96-well plate. Media was changed twice weekly.

Biological characterisation

Firstly, the level of entrapment provided by the alginate matrices was visualised by monitoring cell motion using Cell-iQ real-time imaging. An image was taken of a defined z-plane in the gel matrix every 5 min for 24 h. The motion of the cells was then tracked over this time and the relative motility quantified. Cell viability was investigated using Calcein-AM/ethidium homodimer-1 assays and imaged using confocal microscopy. To determine cell phenotype, total RNA was isolated from monolayer and hydrogel cultures with TRIzol reagent before the concentration and purity was measured using spectrophotometry. qRT-PCR was performed using primers designed with Primer Express3 and data was normalised to a β-actin reference gene. sGAG production was quantified using a DMMB assay and aggrecan presence was confirmed using fluorescent immunohistochemistry.

Finally, full-thickness cartilage explants from femoral condyle tissue, or media conditioned from these explants, were added to the alginate-chondrocyte cultures to examine whether the secretome of the tissue and media conditioned from it aided recovery of the chondrogenic phenotype. For the generation of conditioned media, cartilage discs (diameter: 4.1 mm, height: 2 mm) were incubated with 250 μL culture media for 24 h before being applied to cultures.

Statistical analysis

Statistical analyses were performed using Prism 7 (GraphPad, CA, USA). Student's t-tests were used in PCR and DMMB analysis. Mean values and standard error of the mean are plotted. Results where $p<0.05$ were considered significant.

4.3 Results

Monolayer and quiescent alginate culture of chondrocytes

Firstly, the effect of monolayer culture on the chondrogenic phenotype of primary hACs was investigated. Freshly isolated (FI) primary hACs were found to express high levels of Col II and lower levels of Col I (Figure 4.1A). After passaging these cells three times, this had reversed and there was a significantly lower Col II expression ($P<0.005$). The expression profile of Col I and Col II in passaged primary hACs was similar to that observed in the chondrocyte TC28 cell line (Figure 4.1B). This change in gene expression of hACs was accompanied by an elongated fibroblast-like morphology, as the natively spherical cells adhered and spread onto the surface of the culture well (Figure 4.1C).

Primary hACs were then cultured in quiescent alginate matrices for 2 weeks before cell viability and phenotype were investigated. Following 14 days of encapsulation, primary hACs showed high levels of cell viability and displayed a flattened morphology at the edge of the constructs and a spherical morphology in the centre (Figure 4.2A and 4.2B). This is similar to chondrocytes in native cartilage, in contrast to the fibroblast-like morphology of primary hACs cultured in monolayer. Analysis of COL2A1 and COL1A1 mRNA expression over 14 days showed that primary hACs encapsulated in quiescent alginate recovered their native Col II phenotype. Further, the human chondrocyte cell line (TC28) showed recovery of a native phenotype with encapsulation in a quiescent alginate matrix (Figure 4.3).

In addition to measurements of collagen expression, proteoglycan production was quantified over a timecourse of 30 days. This assay is sensitive to binding to uronic acids groups which are also present in alginate, so alginate-only controls were used. Relative to acellular alginate controls, scaffolds containing encapsulated primary hACs and TC28s showed a significant sGAG secretion over a period of 30 days, suggesting that alginate encapsulation supported and maintained aggrecan proteoglycan production (Figure 4.4A). The ability of quiescent alginate to support an anabolic chondrocyte phenotype, which

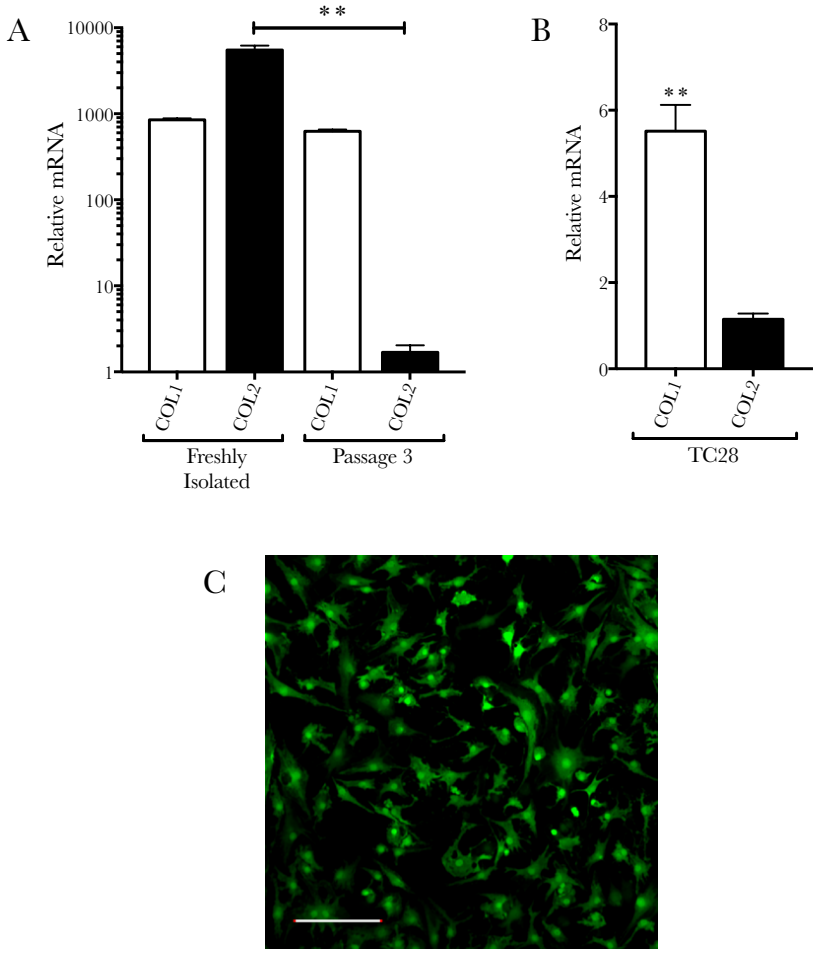

Figure 4.1: Effects of monolayer culture on primary chondrocyte phenotype. A) Relative mRNA expression of Col I and Col II in primary human chondrocytes either directly after isolation from cartilage or following 3 passages in monolayer. B) Relative mRNA expression of Col I and Col II in the TC28 human chondrocyte cell line. C) Passage 3 human chondrocytes exhibiting a fibroblast-like morphology (SB: 200 μm, **P<0.005, n=3.)

produces cartilage extracellular matrix components, was then further validated by histochemical staining of alginate scaffolds. Aggrecan staining was observed in the cytoplasmic region of the chondrocytes (Figure 4.4B).

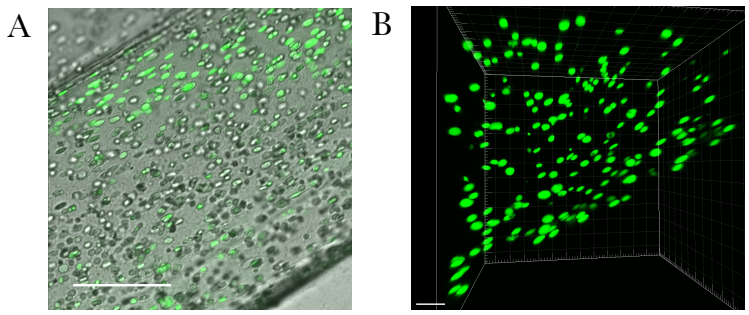

Figure 4.2: A) Primary human chondrocytes encapsulated in quiescent alginate showing flattened morphology at the edge of the construct and spherical morphology in the centre of the construct, SB: 200 μm. B) z-stack demonstrating cell morphology in 3-D, SB: 100 μm.

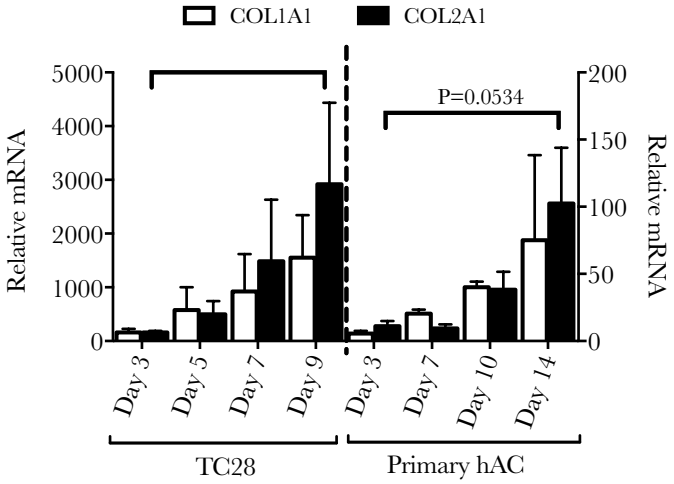

Figure 4.3: Relative expression of Col I and Col II in TC28s and primary human chondrocytes (hAC) throughout 9 and 14 days of culture respectively *: P<0.05, n=3.

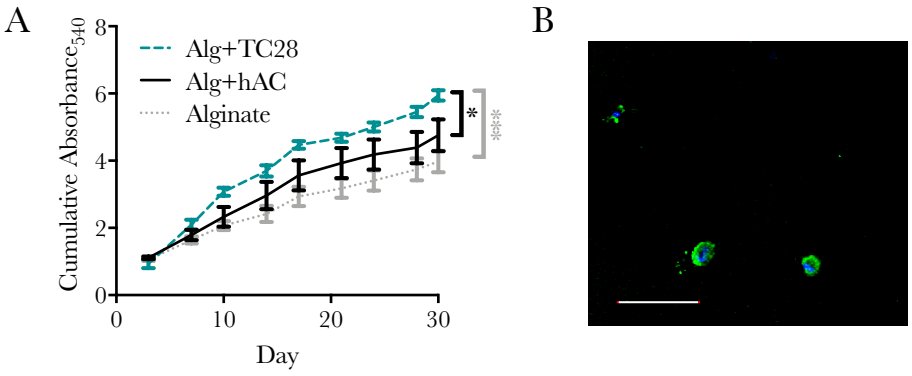

Figure 4.4: A) Cumulative production of sGAGs as detected by DMMB assay at 9 time points over 30 days (n=3) and B) evidence of aggrecan (green) in the cytoplasmic region with nuclei counter stained with DAPI (blue), SB: 200 μm.

Formulation of a deliverable fluid alginate

An alginate fluid gel was produced by drop-wise addition of $CaCl_2$ to sodium alginate solution under shear. The forming of the fluid gel is shown in Figure 4.5A, where the addition of the divalent cation caused a sharp increase in the viscosity of the alginate solution. The viscosity continued to increase until around 6 minutes after which the viscosity dropped slightly and then equilibrated. To ensure that the fluid alginate was deliverable through a needle or cannula, the shear rate was ramped and recovered cyclically between 0.1-500 s^{-1}. There was only evidence of a very small hysteresis loop in Figure 4.5B, indicating that this fluid gel will be stable during manipulation and handling. Figure 4.5C shows the different forms that alginate was produced in. As can be seen on the right hand side of Figure 4.5C, the fluid gel was able to flow like a liquid under shear to then rest as a solid-like material in the absence of shear. The presence of bubbles in the fluid gel shows how the network of entangled polymer chains can reorder around structures.

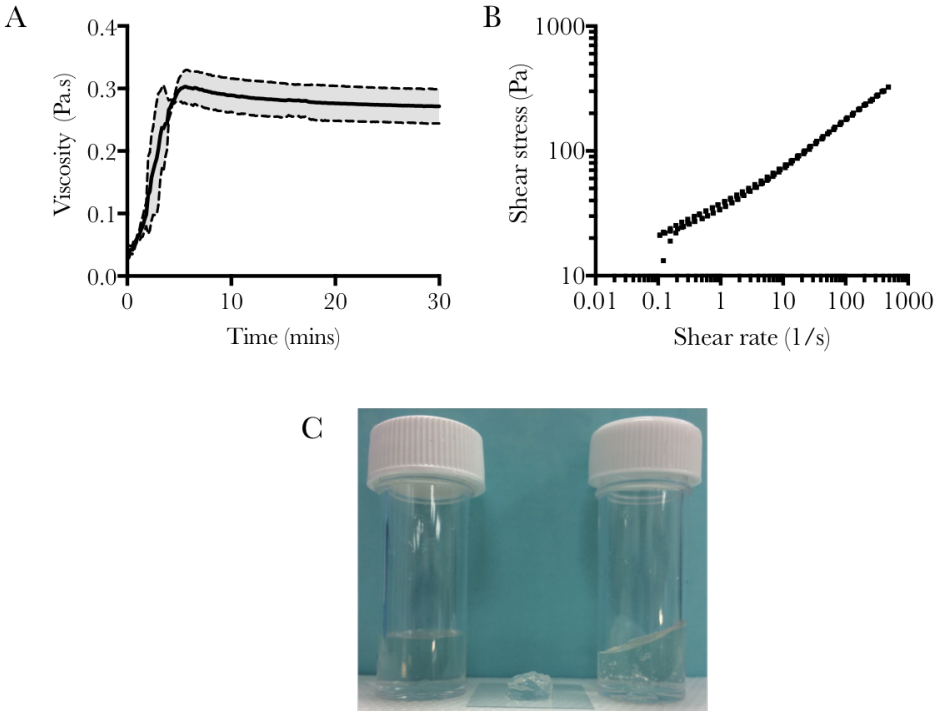

Figure 4.5: Formulation of fluid alginate. A) Viscosity profile during the cross-linking of alginate fluid gels (n=3). B) Change in shear stress with shear rate over ramps of shear rate from 0.1-500-0.1-500^{-1}, sol (left), quiescent (middle) and fluid (right) alginate.

The interesting mechanical properties of fluid gels are partly due to their particulate architectures with short range interactions and entanglements. Figure 4.6A shows the typical architecture of fluid gel fragments connected by ribbon-like structures. Chondrocytes were then seeded between fluid alginate particles and the morphology of all cells was spherical, showing little interaction with the alginate particles. Further there were high levels of cell viability in these cultures (Figure 4.6B and 4.6C).

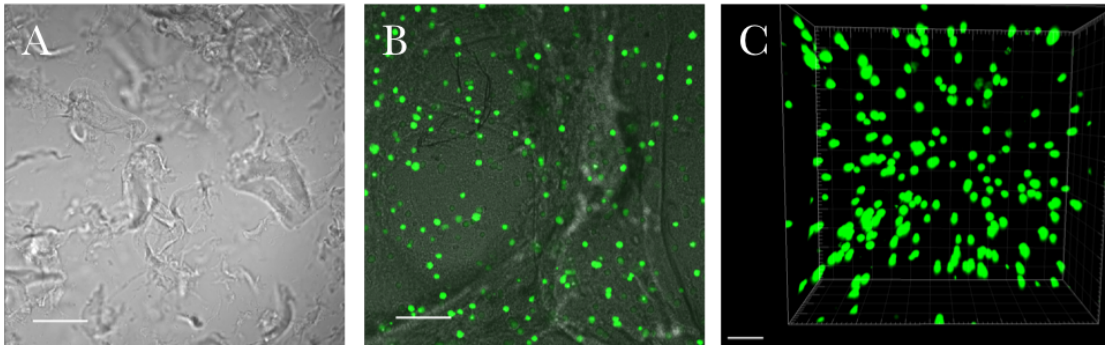

Figure 4.6: Imaging of fluid alginate and seeded chondrocytes. A) Fluid gel architecture (SB: 200 μm), B) fluid gel with chondrocytes showing interaction with alginate fragments and ribbons SB: 100 μm), C) z-stack of chondrocytes in fluid alginate 4 days after seeding, SB: 100 μm

Mechanical characterisation of fluid and quiescent alginate

Dynamic small deformation rheology was performed to determine the viscoelastic properties of both the quiescent and fluid gel systems. Firstly, by applying an increasing oscillatory stress, the LVR of each alginate matrix was determined (Figure 4.7A). The LVR of the fluid gel was shorter than that of the quiescent gel, highlighting the ability of the fluid network to flow under stress. The frequency dependent behaviour of the materials was then probed. The presence of weak interactions and entanglements were confirmed through linear rheology (Figure 4.7B), with the sheared alginate showing solid-like behaviours dependent on frequency, typical of weak gels. Interestingly, the quiescent gel showed a similar mechanical spectrum (at higher G values) inferring structures which mirror each other, complementing data obtained via microscopy shown in Figure 4.8C. Fluid alginate (grey) showed strong shear thinning behaviour

(Figure 4.7C), where increasing the shear to the systems caused reversible breakdown of the entangled polymers. However, this was not seen in the quiescent gel; increasing shear to strains above the LVR caused the gel to fracture (gel fracture points are highlighted in Figure 4.7C using #), resulting in artefacts that resembled thinning profiles.

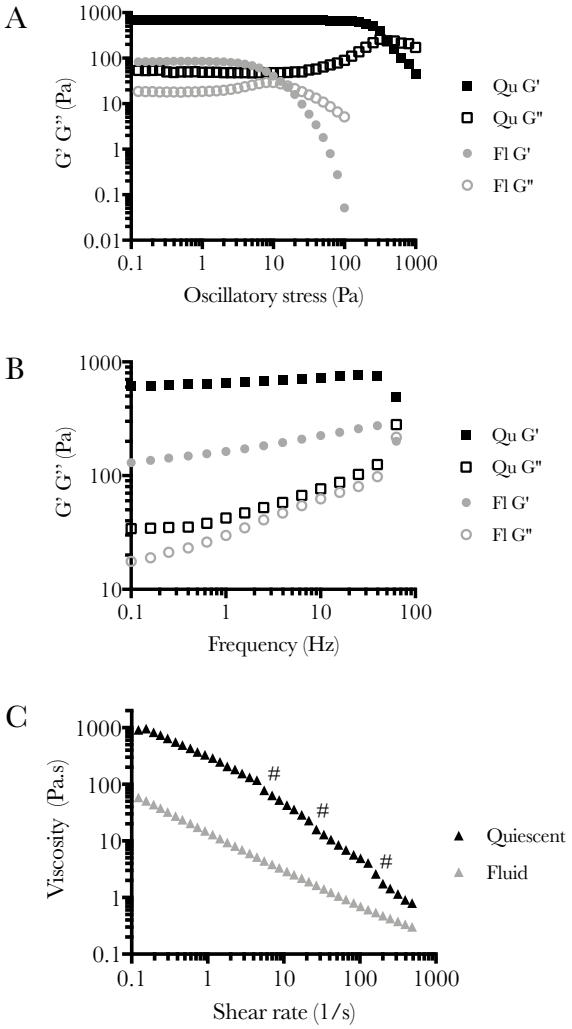

Figure 4.7: Rheological characterisation of quiescent (black) and fluid (grey) alginate. A) Oscillatory stress sweeps (0.1-100 Pa, 1 Hz, 37℃) showing variation in linear viscoelastic region (LVR). B) Mechanical spectra (0.5% strain, 37℃) showing variation in storage modulus (G) and loss modulus (G). C) viscosity sweeps (0.001-100 s^{-1}, 37℃). (G: filled symbols, G: open symbols)

Table 4.1: Storage (G'), loss (G") and complex (G*) moduli of alginates, n=3

	Quiescent			**Fluid**		
Hz/Pa	G'	G"	G*	G'	G"	G*
0.1	615.87	34.45	616.83	146.30	27.84	148.93
1	654.00	42.45	655.38	181.30	33.60	184.39
10	727.13	76.72	731.17	247.30	68.21	256.82

Microstructural observations of fluid and quiescent alginate

To further understand the differences in structure between the two materials, their microstructures were imaged using SEM following freeze drying. At all magnifications, fluid alginate was seen to have a less interconnected pore structure than quiescent alginate. Further, there were large voids observed throughout the fluid alginate structure that were not seen in the quiescent microstructure (Figure 4.8).

Level of cell encapsulation in fluid and quiescent alginate

To understand how the differing gel architectures influenced cell entrapment, chondrocytes were continually imaged in culture over 24 hours. Video 1 [(1)] shows chondrocytes in fluid gel moving laterally across the field of view over a number of hours, as well as downwards through the gel (Screenshots in Figure 4.9A, Video 1). Chondrocytes in quiescent alginate however, did not show as much movement over the same time-course (Figure 4.9B, Video 2). Cell movement was then quantified by frame-by-frame tracking and cells in fluid gel were found to move further per frame than cells in the quiescent alginate, particularly the 25% most motile cells (Figure 4.10A and 4.10B). Overall, this effect was found to be significant between the two gel matrices (Figure 4.10C, $P<0.0001$ by ANOVA).

[1]Videos are available at https://tinyurl.com/yctb9eqm

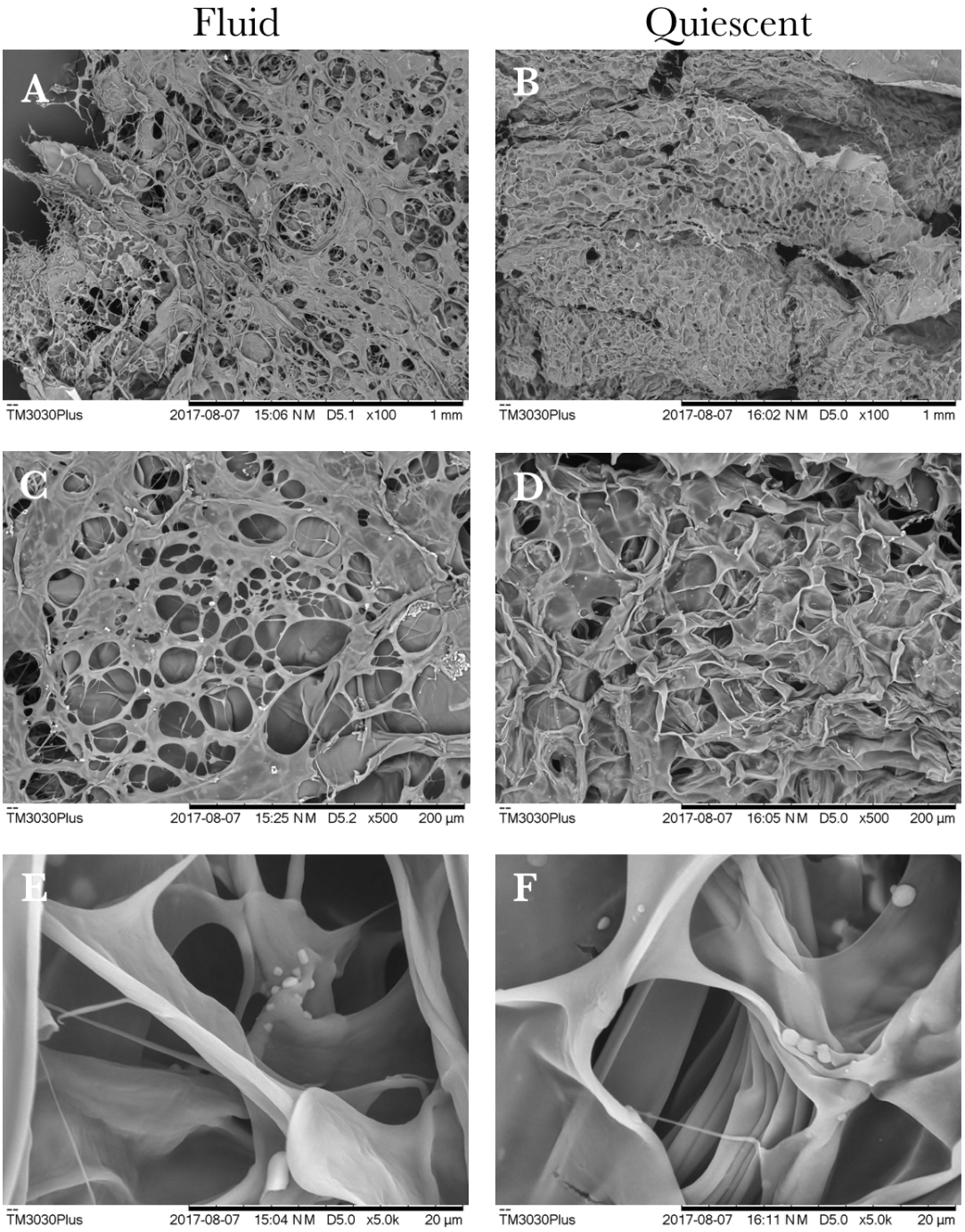

Figure 4.8: SEM images of thin sections of fluid (A, C, E) and quiescent (B, D, F) alginate following freeze drying.

The effect of alginate fluid gel on the phenotype of primary articular chondrocytes

To compare the efficacy of alginate fluid gel with quiescent alginate in recovering and supporting a chondrogenic phenotype, primary hACs were cultured in either alginate fluid gel or in quiescent alginate for a period of 7 days. Following 7 days of culture Col II and aggrecan expression were higher in the quiescent than fluid alginate and Sox9 expression was significantly higher in the quiescent alginate (Figure 4.11).

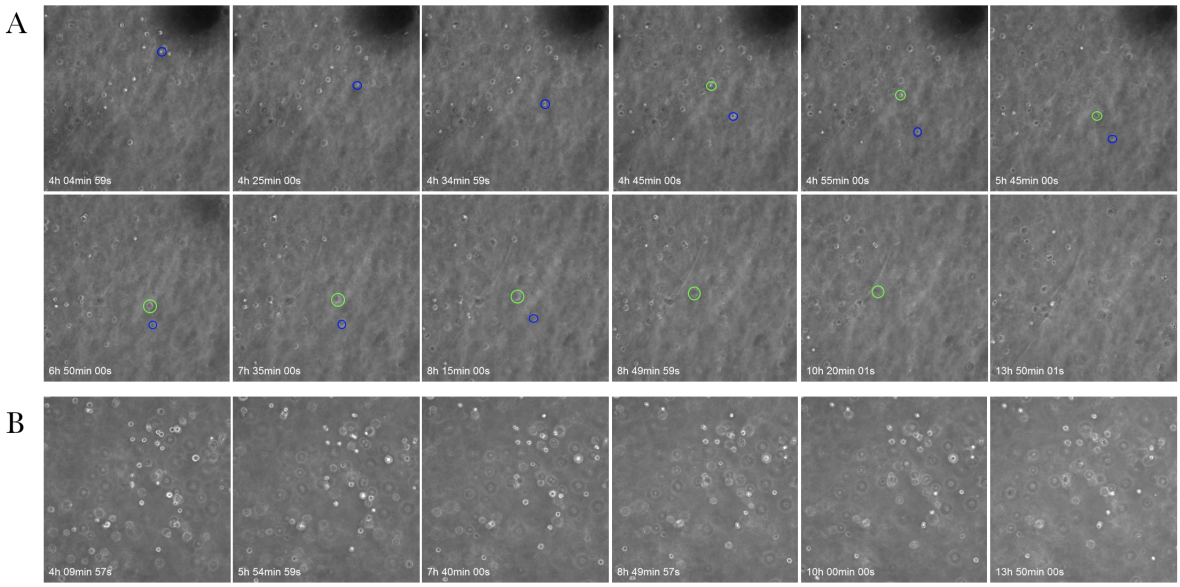

Figure 4.9: Tracking of chondrocytes in (A) fluid and (B) quiescent alginate over 14 hours. Movement of cells is demonstrated by coloured circles. Full videos are available at https://tinyurl.com/yctb9eqm, Videos 1 and 2.

Driving chondrogenic phenotype of primary chondrocytes encapsulated in alginate

Due to the proximity of native cartilage tissue during the ACI repair of cartilage defects, *ex vivo* cartilage tissue and cartilage conditioned media were studied to determine their effect on the efficacy of using fluid and quiescent alginate as chondrocyte delivery matrices. By adding a piece of explanted cartilage tissue, (Figure 4.12A) there was an increase in the expression of COL2A1 in quiescent alginate following 14 days of culture (Figure 4.12).

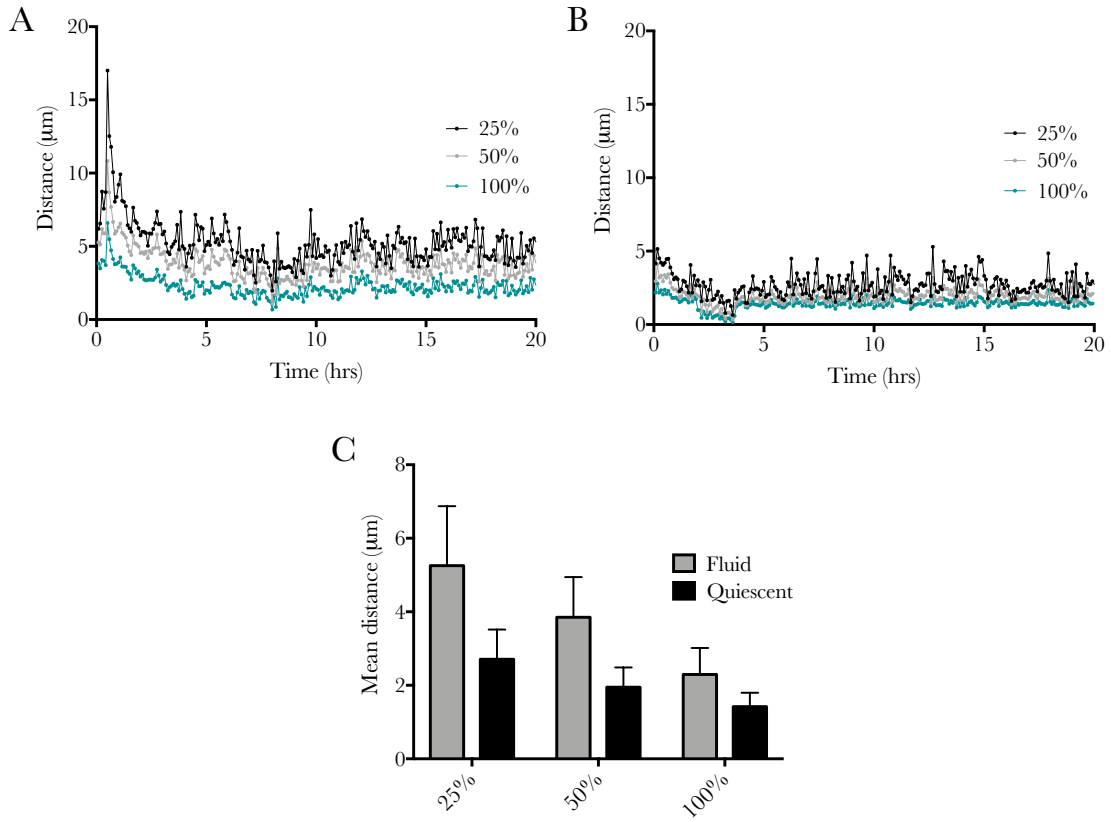

Figure 4.10: Quantitative analysis of cell tracking in A) fluid and B) quiescent alginate matrices. C) shows the mean distance moved by the most motile 25%, 50% and 100% cells in each video. 2-way ANOVA with Tukey post-hoc correction determined the effect of matrix extremely significant over the 241 frames analysed ($P<0.0001$).

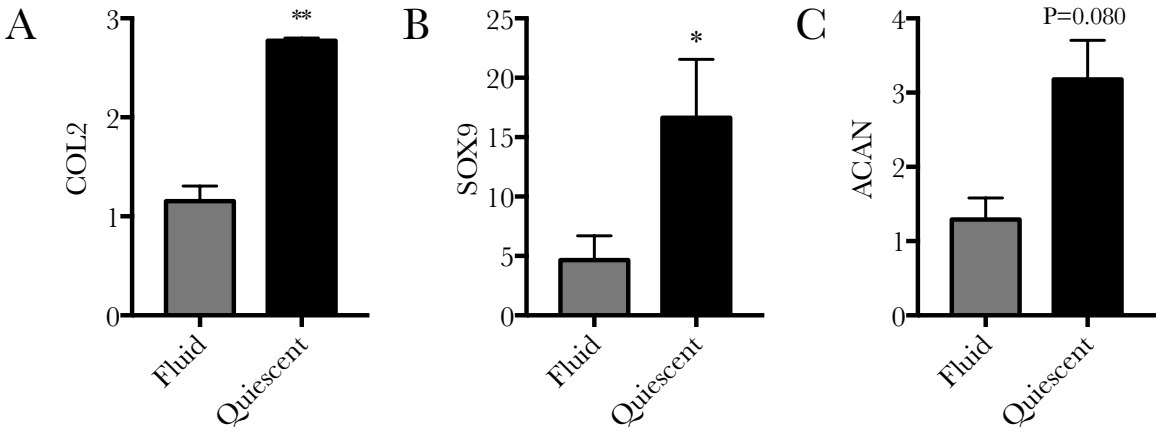

Figure 4.11: Relative mRNA expression of (A) Col II, (B) Sox9 and (C) aggrecan in chondrocytes 7 days after seeding in fluid and quiescent alginate, n=3.

The effect of the physical presence of cartilage tissue was shown to be secondary to the factors released from it (Figure 4.12B), since conditioned cartilage explant media resulted in a greater increase (P=0.0376) in Col II expression than the cartilage tissue itself. This suggests that in the *in vivo* environment, alginate encapsulation of hACs will be even more efficacious in promoting and maintaining the chondrogenic phenotype due to the secretion of endogenous anabolic factors from the surrounding cartilage matrix. This condition was then investigated to determine if it could be used to drive the native alginate phenotype in fluid alginate culture. However, when comparing conditioned and basal media, there was no significant difference between the conditions (P=0.3126, Figure 4.12C); this further supports that physical entrapment of chondrocytes is critical to maintenance of the native Col II phenotype.

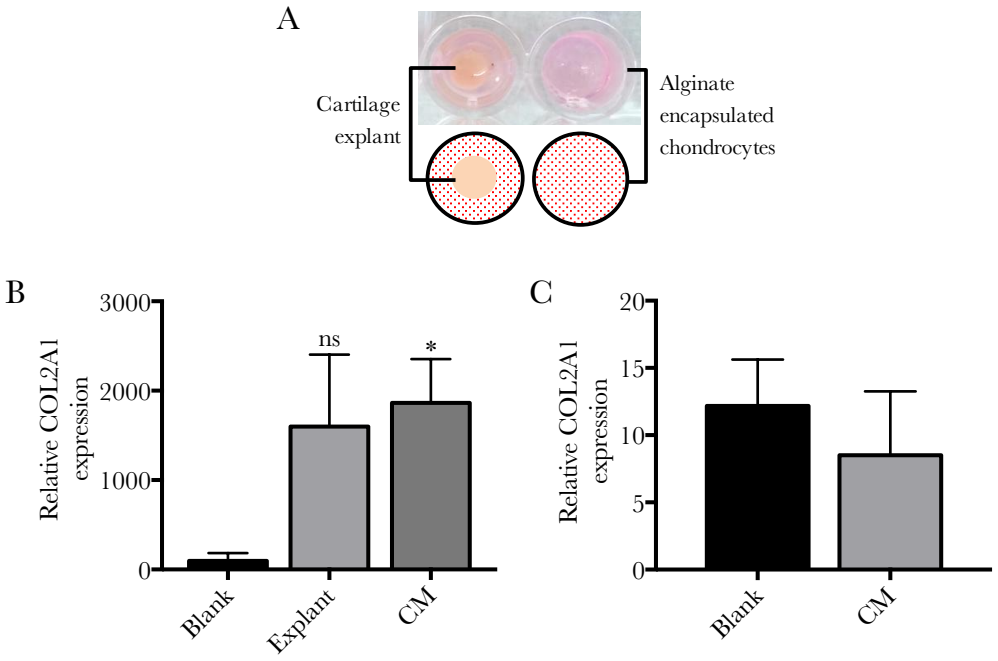

Figure 4.12: A) Experimental set-up for explant (left) and blank/conditioned media (CM) (right). Relative Col II expression in B) quiescent and C) fluid alginate when cultured with basal media (blank), a cartilage explant or conditioned media, n=3.

4.4 Discussion

Alginate has been investigated for cartilage repair and regeneration strategies over the last three decades since it was shown to support the re-differentiation of chondrocytes that had lost their native Col II and proteoglycan-producing phenotype [22, 70, 155]. The mechanism of this effect is relatively unknown but has been attributed to chondrocyte morphology as well as matrix mechanical properties [57, 192]. Here the aim was to resolve the difference between the geometric and chemical influence of alginate matrices.

The findings of this study support previous observations that chondrocytes are not phenotypically stable in 2D culture on untreated tissue culture plastic, with freshly isolated, primary human chondrocytes rapidly losing Col II expression and adopting a fibroblast-like morphology within 3 passages. This is a well-known phenomenon in chondrocyte culture, and has been attributed to the change in morphology when cultured on a stiff substrate [6, 22, 70]. In contrast, when primary chondrocytes were geometrically confined by encapsulation in quiescent alginate they maintained native morphologies depending on the construct region, akin to native chondrocytes in articular cartilage tissue [202]. Additionally, it was found that primary human chondrocytes remained viable for up to 14 days culture in quiescent alginate constructs. Importantly, this data demonstrates that the geometric confinement of human chondrocytes in quiescent alginate promotes a chondrogenic phenotype with maintenance of Col II expression and aggrecan proteoglycan production. These results support the findings of Murphy & Sambanis who showed that the maintenance of spherical chondrocyte morphology is necessary for recovery of the chondrogenic phenotype following monolayer culture [139].

Since use of a quiescent alginate hydrogel construct for the regeneration of articular cartilage would require highly invasive surgery, the use of an alginate fluid gel, which would be suitable for intra-articular injection, was examined to determine if it would exhibit the same chondrogenic phenotype promoting properties. Using the same alginate solution that was used to produce the quiescent constructs, shear was introduced during its gelation with the same concentration of cross-linking cations. This produced a self-supporting

network of gel microparticles referred to as alginate fluid gel [49, 56]. This gelation process was highly reproducible, with little variation between batches. Furthermore, rheological characterization demonstrated that with repeated frequency ramps there was a consistent shear stress. These non-time-dependent shear-thinning properties suggest that alginate fluid-gel could be delivered by intra-articular injection without modification of its structural properties. Mechanically, alginate in its quiescent state was more elastic than fluid alginate and showed a higher complex modulus. The reduction in elastic-like behaviour of the fluid alginate is attributed to the presence of shear during gelation, where mixing prevents a complete network from forming [48]. There were also differences in the liquid-like and frequency dependent properties of the two materials. Both materials were stable at lower frequencies, with the fluid alginate showing a shorter LVR as it can flow when stressed. Such a phenomenon arises through the prevention of a completely gelled network, allowing polymer strands to move freely once the required energy has been met to yield any weak inter-particle interactions or entanglements [47, 48].

Following the investigation into the mechanical properties and the increased loss modulus of fluid alginate compared to quiescent alginate, the level of entrapment provided by the two alginate matrices was investigated. Using cell tracking, it was found that cells in fluid alginate were able to move laterally as well as vertically through the matrix, whereas in quiescent alginate cells were confined to distinct regions. This effect may be due to fluid flow through larger pores and voids in the fluid alginate structure that allowed cells to move laterally through the gel network. This would be also be likely observed in an *in vivo* situation due to joint motion. Further, the difference in microstructure of the alginate may introduce local differences in the stiffness of the gel matrix resulting in changes to cell behaviour.

Despite the success of resuspending chondrocytes in alginate fluid gel and for cell viability to be maintained, this study found that fluid alginate was not as effective at maintaining chondrocyte phenotype as quiescent alginate upon culturing of constructs. This lack of effectiveness of fluid alginate to maintain and promote the chondrogenic phe-

notype of primary chondrocytes was observed despite culturing hydrogels in the presence of explant conditioned growth media. As such, physical entrapment provided by the quiescent alginate gel has been shown to be critical in maintenance of a native chondrocyte phenotype.

4.5 Conclusions

By producing a chemically identical fluid alginate, it has been shown that with a lack of physical entrapment, passaged chondrocytes lose their ability to recover/maintain their phenotype. Even the introduction of growth factors released from *ex vivo* cartilage, which show a significant increase in Col II expression in quiescent alginate, has no effect. Therefore it has been demonstrated that maintenance of a spherical morphology alone is insufficient to recover a native Col II phenotype in passaged adult human chondrocytes. A certain level of geometric confinement for the chondrocytes is also essential.

CHAPTER 5

USING SUSPENDED MANUFACTURE TO MODEL THE OSTEOCHONDRAL UNIT

Data in this chapter is also presented in the published article: *Suspended Manufacture of Biological Structures.* Advanced Materials (2017)[1,2]

In this study we describe a novel method of suspended manufacture for the production of complex soft structures of closely defined morphology, mechanical properties, and chemistry. The process conditions are sufficiently mild that embedded populations of cells maintain high levels of viability and retain phenotype and function. Given the simplicity of the process, it can be used for many existing gel materials without special modification. The method of manufacturing replaces the 2D print bed with a 3D "bed" of gel particles (often referred to as fluid or sheared gels), which behave in bulk as a viscoelastic fluid with rapid elastic recovery, thereby providing support to the complete part. The final structure is formed through the dispersion of a gelling material into the interstices between the supporting fluid gel particles. This enables relatively complex structuring while providing sufficient support to prevent the structure collapsing under its own weight. Once the scaffold structure has been formed the supporting phase may be removed the gentle application of shear. This manufacturing process allows for the use of a wide range of polymeric materials, including many already approved by regulatory bodies. Here we demonstrate the power of this method by manufacturing anisotropic structures with spatially controlled mechanical and chemical properties, which support a co-culture of viable cells.

[1]DOI:10.1002/adma.201605594

[2]The aforementioned paper was published as joint first authorship; data produced by Dr Sam Moxon has been removed and additional research has been undertaken. Further co-authors on the published article provided assistance with equipment, proof-reading or supervision of the work.

5.1 Introduction

Tissues are formed of populations of cells distributed within an extracellular matrix (ECM), which is structured down to the molecular level. Local variations in organization and biochemistry mean that the encapsulated populations of cells are exposed to environments that differ both mechanically and chemically. These environments have been shown to play a strong role in shaping the phenotype of both stem cells and cells of a committed lineage [121, 175, 185, 206]. For some time now researchers have sought to recapitulate tissue structure using a combination of isolated cells and polymeric hydrogels that have a structural resemblance to the ECM [38]. However, often the spatial distribution of biological material within hydrogel scaffolds is uncontrolled and for many applications, the shape and size of the scaffold is important for translation in preclinical and clinical testing.

Biofabrication is a developing field and many printing techniques and bioinks have developed in recent years to enable additive layer manufacturing (ALM) of biological material supported by scaffolds [11, 65, 135]. Tissue constructs with control over the spatial deposition of cells and other biological factors can now be achieved through a number of methods for bioprinting [15]. The majority of soft-solid structures produced by ALM exhibit relatively low complexity and are typically broader at their base than at their peak to reduce the risk of the structure collapsing [15, 94, 99]. A number of research groups are working on the development of novel polymers for ALM, but often the structures they form with these polymers are simplistic, with a self-supporting lattice arrangement frequently being used to build large structures [91, 226]. A limitation of many of these techniques is the printing of low viscosity or slow crosslinking hydrocolloid solutions prior to gelation. Upon extrusion onto a 2D print bed, the capability of traditional methods to build tall or geometrically complex constructs from hydrocolloid solutions is limited without the use of a rigid support structure such as PCL or HAp [27, 94, 238].

Embedded printing describes a sub-set of bioprinting techniques that have been developed as a solution to this limitation and to enable freeform fabrication [12, 40, 78,

79]. They have been used for bioprinting as well as in sensors, soft-robotics and other applications [142, 228, 236]. The principle behind these techniques is that the 2D print bed is replaced by a 3D matrix that acts as a support during the printing of a secondary phase or can have a secondary structure embedded within it. Using this principle, slow crosslinking, low viscosity hydrocolloid solutions and more complex geometries can be printed without the need for rigid support structures [78]. They can then be crosslinked before being recovered from the 3D print matrix for subsequent tissue maturation.

Key properties of the 3D print matrix for embedded bioprinting include:

- Ability to suspend the printed material
- Allow freeform fabrication, unlimited by broad-based bottom-up printing
- Exhibit rapid recovery to prevent voids forming due to shear induced by needle or bioink movement through the matrix
- Ability to remove printed part
- Non-cytotoxicity

Fluid gels fulfil these requirements as support materials for bioprinting. They are formed by introducing shear during the sol-gel transition of hydrogels and result in an entangled microparticulate network [49]. They have unique mechanical properties in that at low shear stresses they behave like weak gels whilst at higher shear stresses they act like liquids [26]. Agarose is a thermally crosslinking polysaccharide that is stable at both room temperature and cell culture conditions. Further, in its use as a 3D matrix for osteochondral tissue engineering, it has been shown to have low cytotoxicity [198].

The development of *in vitro* tissue and organ models are of growing interest as they can be useful tools in modelling biological systems *in vitro* as well as for initial screening of therapeutics prior to use in preclinical animal models [186, 188]. Such models have the potential to refine, reduce and replace the use of animals in early preclinical testing as they could provide more robust *in vitro* testing platforms than commonly used 2D monolayer cultures. In modelling the osteochondral region, recapitulating the continuous interface between the two tissues of distinct chemical and mechanical properties is important [76, 90,

223]. Physical integration of materials with differing mechanical and chemical properties can be challenging, particularly when solid precursor layers are used as they may be prone to delamination. However it has been shown that by using liquid precursors and then allowing for controlled diffusion prior to solidification, a gradient interface can be produced [76].

In this chapter, a novel method of embedded printing is used to replace the traditional 2D print bed with a 3D fluid gel matrix. This allows the extrusion of a secondary hydrogel phase without mixing and supports the printed phase prior to crosslinking. Termed suspended manufacture, this process supports the fragile construct as it is formed, in a similar manner to the way amniotic fluid suspends the developing foetus. Liquid precursors are used to produce bi-layered cell seeded constructs that recapitulate the osteochondral unit, with distinct chemical and mechanical environments.

5.2 Methods

Preparation and characterisation of the agarose fluid gel

In this study, an agarose fluid gel was used as the print bed. A solution of 0.5% w/v agarose was produced on a magnetic stirrer at 90℃ which was then cooled to 20℃ whilst stirring at 700 rpm. The introduction of shear prevented the formation of a traditional quiescent gel structure and instead produced a fluid or 'sheared' gel. The structure of the gel was imaged by mixing the gel with PEG in a 1:4 ratio and imaging using phase contrast microscopy. The mechanical properties under shear were then investigated using oscillatory rheology. An oscillatory stress sweep was performed from 0.1-100 Pa to determine the LVR before a frequency sweep from 0.1-100 Hz at 0.1% strain. To investigate the recovery of viscosity, the shear rate was alternated between 0.1 and 100 s^{-1}, holding for 120 s at each point. The recovery of elasticity was investigated by an initial 60 s at 1 Hz and 0.5% strain before a 60 s hold at 100 s^{-1}. Elasticity was then measured again at 1 Hz and 0.5% strain for 30 s, sampling every 2.5 s.

The printing process

A low-cost FDM printer (Wanhao duplicator i3) was modified by re-wiring the extruder to power a screw-driven syringe extrusion unit. This unit was printed in PLA by an unmodified Wanhao duplicator i3. The design and slicing of 3D models was performed using open source software. 3D models were designed using Fusion 360 software (Autodesk). They were then converted to stereolithography (stl) files and sliced using Cura software (Ultimaker, Netherlands) to produce RepRap flavour g-code.

Figure 5.1 shows the printing process. Firstly, (1) the agarose fluid gel was placed in a petri dish which was secured to the print bed to prevent any movement during printing. At this stage, human cells were seeded into the bioink at 1 x10^6 cells/mL. Secondly (2) the bioink was extruded into the fluid gel as programmed by the g-code produced during slicing. Following printing (3) the crosslinker ($CaCl_2$) was introduced and left for 20 min.

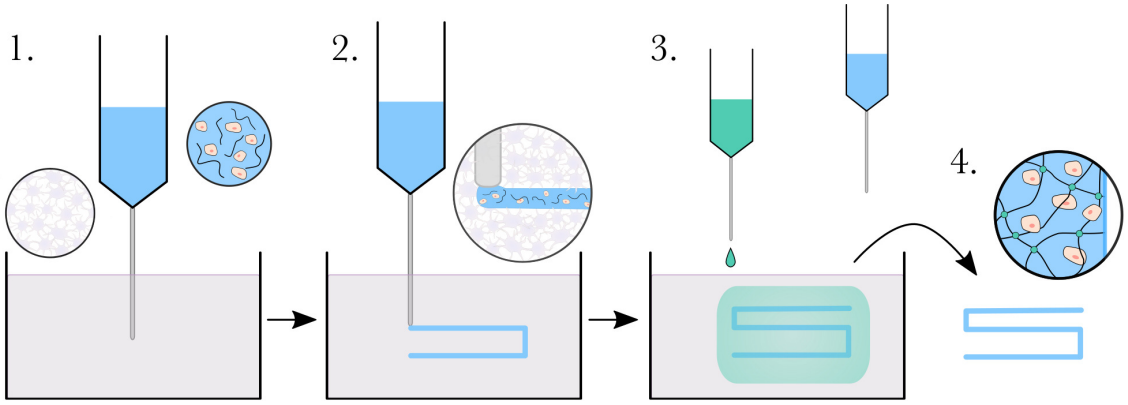

Figure 5.1: The suspended manufacturing print process: 1. Agarose fluid gel and cell-seeded bioink (alginate or gellan gum) produced. 2. Bioink extruded into the fluid gel support matrix 3. Bioink crosslinked 4. Gelled part removed from fluid gel.

In cell seeded constructs, after the first 5 min, culture media was added to the print bath. Finally (4), the crosslinked construct was removed from the agarose print bed and any residual fluid gel was removed by gentle shear and washing with PBS before culture or further analysis. For all experiments, printing was performed at a print speed of 15 mm/s with 0.4 mm layers and 100 % infill density to prevent inclusion of agarose particles.

Determining print resolution and diffusion limitations

To determine printing resolution, 3-layer prints were produced with different needles and immediately imaged optically. The were then recoloured to greyscale in ImageJ and the profile tool was used to measure the width of the printed section. To measure diffusion, a series of walls of 1 mm height and width were printed with 2 mm gaps. They were printed from dyes of differing molecular weight (Mw) and charge: Alcian Blue (1299 $g.mol^{-1}$, cationic) and Fast Green FCF (808 $g.mol^{-1}$, anionic), and then imaged over 2 hrs to measure diffusion of the dye across the gap. They were analysed as above, using ImageJ.

Recapitulation of the osteochondral region

Human femoral condyle tissue from the 'unaffected' region of the joint was washed in PBS to remove residual fat or blood before a cylindrical core was drilled and removed

from the centre using a diamond coated drill bit (10 mm outer diameter) and surgical saw. Primary chondrocytes and osteoblasts were isolated from the tissue of the core and expanded in monolayer. The remaining tissue was scanned using μCT, whilst immersed in culture media to maintain hydration, before being incubated during the expansion of the cell populations. The following μCT parameters were used: 0.5 mm Al filter, 80 kV, 100 μA, 27.05 μm pixels, 670 ms exposure time, 0.6° rotation step, 3 frame averaging. The expanded cells were mixed with hydrogel solutions in preparation for printing. The cartilage-like region used 1.5% w/v gellan gum and the bone-like region used 1.5% w/v gellan gum with 0.6% w/v nanoHAp from solution.

Bilayered structures were printed by extruding the first (non-mineralised) layer and then swapping the syringe to print the second (mineralised) layer; the print geometry was defined by the results of μCT scanning following coring to produce an exact fit for the plug. The whole structure was then ionically crosslinked to gel the two layers into a single structure. For imaging, acellular constructs were sectioned and freeze-dried prior to attaching to 25 mm aluminium conductive SEM stubs using adhesive carbon discs. μCT was used to visualise the mineral inclusion in the scaffolds; the following parameters were used: 30 kV, 70 μA, 6.76 μm pixels, 1000 ms exposure time, 0.3° rotation step, 4 frame averaging. For mechanical characterisation of the influence of the mineral component, constructs were printed solely of either gellan or gellan-mineral before crosslinking and removal of the part.

Biological characterisation of the osteochondral model

Following printing, cell viability was measured using a LIVE/DEAD assay within 2 h. Bilayered constructs were re-implanted into the defect sites in the *ex vivo* tissue that they were isolated from and cultured for 28 days. Following 28 days culture, n=3 constructs were partitioned into cartilage, interface and bone regions before being homogenised for qRT-PCR while some were used for immunohistochemical imaging.

To verify that cells were still functional following following suspended printing, they

were exposed to increasing doses of IL-1β and the resultant production of IL-6 was measured using solid phase sandwich ELISA. The same protocol was applied to chondrocytes in monolayer as a control.

Statistical analysis

Statistical analyses were performed using Prism 7 (GraphPad, CA, USA). Student's t-tests were used in PCR analysis. Data are presented as mean ± standard deviation (SD) with the exception of qRT-PCR data which is presented as mean ± standard error of the mean (SEM). Results where $p<0.05$ were considered significant.

5.3 Results

Characterisation of the agarose fluid bed

Agarose fluid gel was produced by introducing shear as the hydrocolloid solution was cooled. This resulted in the formation of an entangled microparticulate gel network as can be seen in Figure 5.2 using phase contrast microscopy. Individual tadpole-shaped particles were formed (as indicated by arrow in Figure 5.2A) which then appeared to interact from the head-regions to form larger aggregate particles of between 150-200 μm in diameter. The shape of the particles prior to agglomeration was likely due to the way that shear was applied during gelation. The hypothesised production of these particles is shown in Figure 5.2D. The high shear in the column above the stirrer (region marked (1) within dashed lines) may cause the formation of elongated gel particles and the toroidal motion of the bulk gel in 3D forces these individual particles into regions of lower shear. This would allow for the agglomeration and entanglement of these particles. In a bulk,

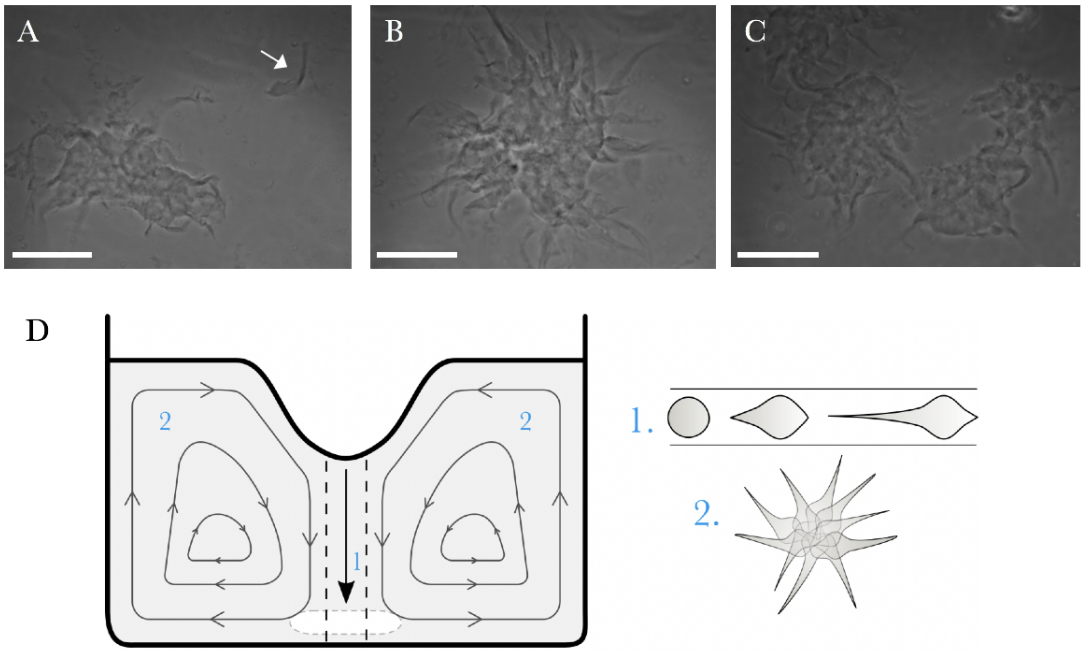

Figure 5.2: Phase contrast imaging of fluid agarose particles showing A) individual units indicated by arrow B) characteristic 'hairy' aggregates and C) interaction of aggregates. D) Schematic hypothesis of formation of individual particles and aggregates at high (1) and low (2) shear regions respectively. SB=150 μm

as seen in Figure 5.2C, the aggregates interact and entangle by the tails which project from the core. These weak entanglements are likely responsible for the unique mechanical properties of fluid gels.

Rheological investigations were performed to investigate the properties of agarose fluid gel under shear. Firstly a stress sweep was performed; the LVR was found to be fairly short with a cross-over between G' and G" at 32 Pa. A frequency sweep was then performed at 1% strain which showed a higher G' than G" ($\tan\delta = 0.17 \pm 0.013$), and slight frequency dependence indicating weak gel, or structured liquid, behaviour (Figure 5.3 A, B). The shear rate was alternated between 0.1 and 100 s^{-1} to investigate the recovery of viscosity. As expected, the fluid gel was highly shear thinning and the recovery of viscosity was very fast (Figure 5.3C). Finally, a high shear rate (100 s^{-1}) was applied and then removed to determine the recovery of elasticity in the agarose matrix. Figure 5.3D shows that there was a rapid increase in shear storage modulus immediately following shearing, although the recovery to the original elasticity takes longer than 30 s.

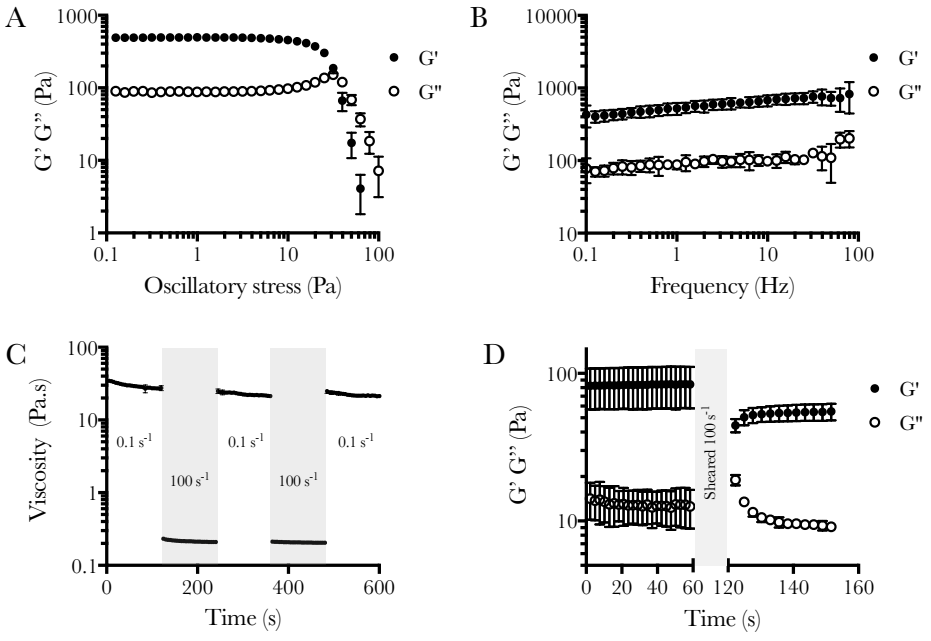

Figure 5.3: Rheological characterisation of 0.5 w/v% agarose fluid gel A) Stress sweep from 0.1-100 Pa B) Frequency sweep from 0.1-100 Hz at 0.1% strain C) Recovery of viscosity between shear rates of 0.1 and 100 s^{-1} D) Recovery of elasticity at 1 Hz and 0.5 % strain following a 60 s peak hold at 100 s^{-1}. Data plotted are mean ±SD, (n=3).

Suspended printing resolution and diffusion limits

Printing into a particulate fluid system restricted the resolution of print geometries to features that were larger than the interstices between gel particles. By printing a dye with a similar viscosity to water, the movement of material through the continuous phase into the interstices between fluid gel particles was visualised (Figure 5.4A-F). The achieved resolution decreased as the inner diameter of the needle increased (and Birmingham gauge number decreased) (Figure 5.4, $R^2 = 0.9846$). There was also larger variability of the printed wall width when a larger needle was used.

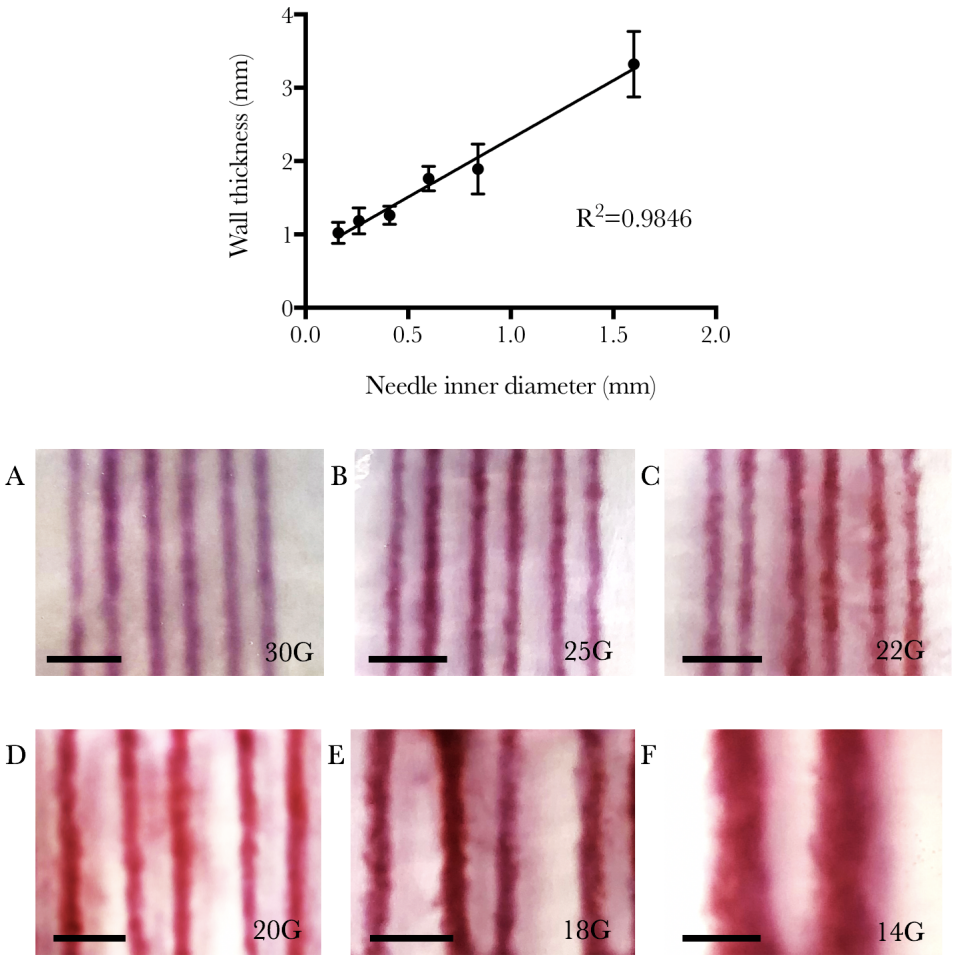

Figure 5.4: Resolution capabilities of 0.5 w/v% fluid agarose print bed with increasing needle diameter (decreasing gauge) A-F. SB: 5 mm; data are presented as mean ± SD, n=18.

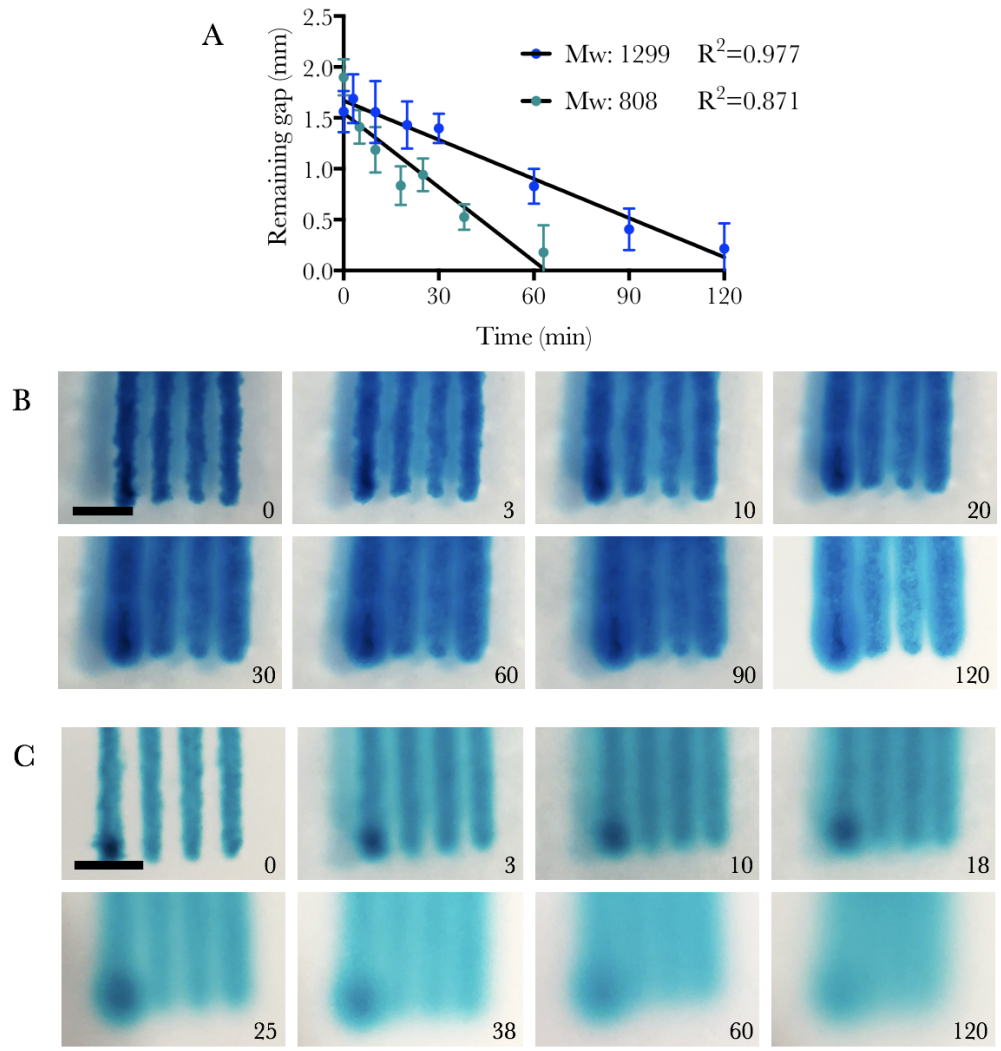

Figure 5.5: Diffusion of low viscosity dyes of varying molecular weight across a 2mm gap following printing. A) Diffusion data over time, B and C) Optical images of diffusion over 120 min in B) Alcian Blue solution of 1299 g.mol^{-1} and C) Fast Green FCF solution of 808 g.mol^{-1}. SB: 5 mm, bottom right = time (min); data are presented as mean ± SD, n=9.

Further, whilst low viscosity solutions could be printed and supported, there was a limitation of diffusion through the particulate gel matrix. This resulted in a finite crosslinking time before printed features were lost. Figure 5.5 shows the time-dependent diffusion of dye solutions of different molecular weight (Mw) across 2 mm gaps. The diffusion of the dye as it filled the gap was imaged over 2 h as shown in Figures 5.5 B and C. The dye with a lower Mw (Fast Green FCF, Figure 5.5C) showed significantly faster diffusion than the higher Mw dye (Alcian Blue, Figure 5.5B)) (P=0.0063).

Bioprinting of low viscosity solutions into complex geometries

To demonstrate that this technique allows for freeform fabrication, a number of structures were printed. Printing of helical structures with overhangs showed the capability of the agarose fluid bed to support a suspended low viscosity gel prior to crosslinking (Figure 5.6D and video 3 [(1)]). In more practical applications, the printing of tubular structures and perfusable bifurcations were also possible using this technique (Figure 5.6).

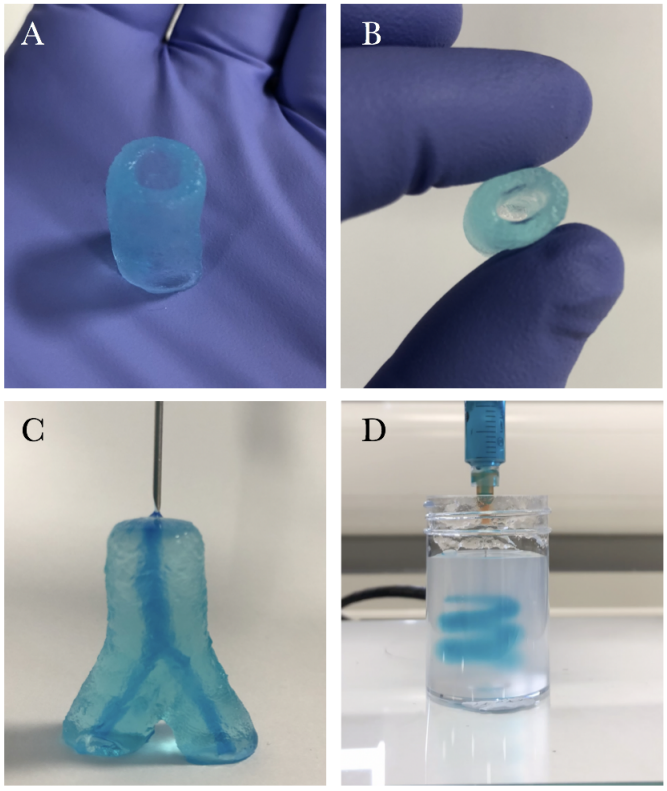

Figure 5.6: Examples of geometries that can be printed from 1% w/v alginate (with food dye for visualisation) using suspended manufacture including hollow (A,B) and hollow bifurcating (C) structures. D) is a snapshot of Video 3, showing the printing of a helical structure with overhangs without the need for additional support structures.

Bioprinting of bi-layered constructs and subsequent characterisation

To produce constructs that model the OCU, mineralised and non-mineralised regions were required. As such, HAp was combined with gellan gum and printed into gellan/gellan-

[1]Video available at https://tinyurl.com/yctb9eqm

mineral constructs with continuous interfaces. This was observed visually in Figure 5.7A, as the addition of mineral increased the opacity of the gel construct. Mineral is highly attenuating so its distribution in the whole construct was investigated using μCT as in Figure 5.7B. The interaction of HAp with the gellan polymer network can be seen in Figure 5.7 C, as it coated the polymer throughout in individual particles but also formed aggregates, as indicated by the arrow. Finally, inclusion of HAp resulted in faster relaxation behaviour following loading to 20% strain (Figure 5.7D).

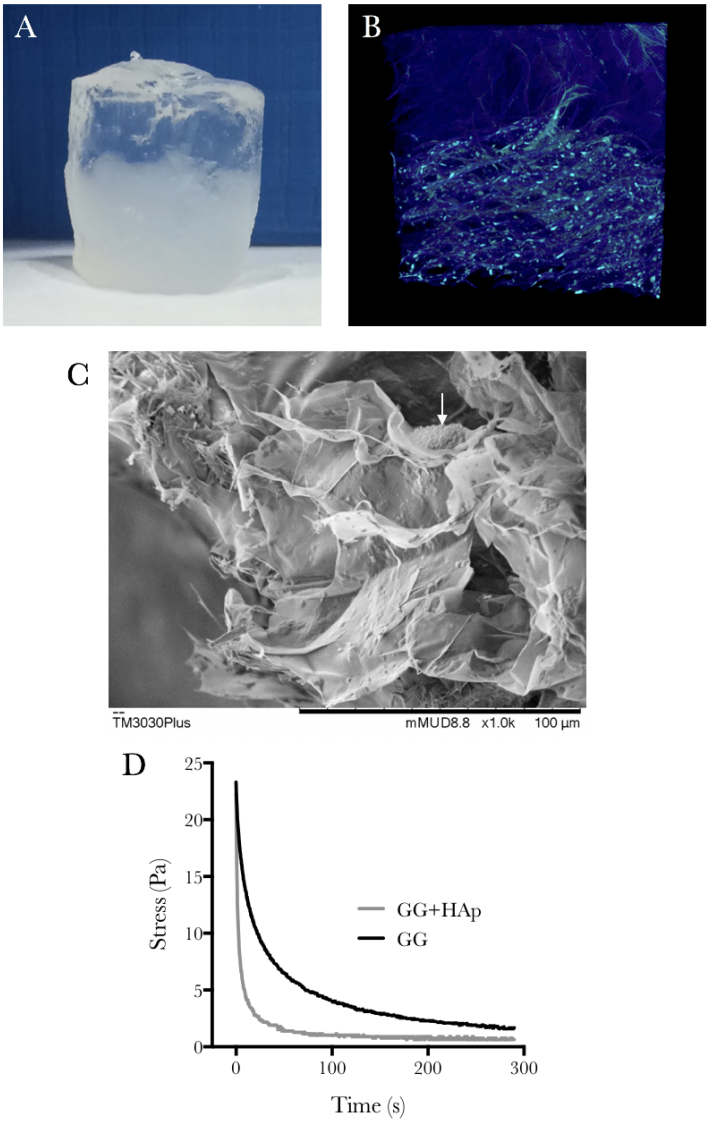

Figure 5.7: Introduction of mineral for production of bi-layered constructs. A) Gellan/Gellan-HAp construct. B) μCT reconstruction of a bi-layered construct. C) SEM of HAp integrated into gellan structure, arrow indicates aggregated HAp. D) Stress relaxation behaviour of gellan (GG) and GG-HAp constructs.

Characterisation of embedded printed cell populations

Human osteoblasts and chondrocytes were isolated and cultured prior to printing into a bi-layered construct. The printing process showed very good cell viability (Figure 5.8) with very few dead cells. qRT-PCR was used to determine the stability of cell phenotype following printing and 28 day culture of osteochondral plugs. The retrieved constructs were sectioned as shown in Figure 5.9A prior to homogenisation for analysis. Figure 5.9 shows that Col II and aggrecan expression remained highest in the cartilage-like region of the constructs and lowest in the bone-like region. Col I characterisation showed the opposite, with the highest expression in the bone-like region.

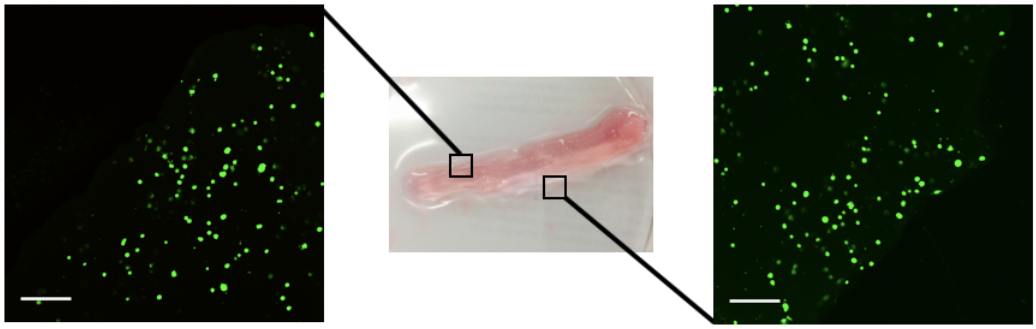

Figure 5.8: Viability of TC28 cells directly after printing SB: 200 μm

For the development of tissue models, it is important that the embedded cell populations maintain their ability to produce cartilage matrix and maintain functional responses to stimulation. Production of aggrecan (ACAN) by chondrocytes following SusMan was investigated using IHC; Figure 5.10A shows strong evidence of aggrecan in the peripheral regions of cells and some evidence of aggrecan in the extracellular regions. The response of chondrocytes to inflammatory stimuli in printed constructs was evaluated by measuring the production of IL-6 as a function of IL-1β dosage. Figure 5.10B shows this response at 4 and 24 h. In the 3D printed (SusMan) group, the peak response was delayed and seen to occur at a higher IL-1β concentration than in the monolayer group. The increase between 4 and 24 h in both groups was similar however.

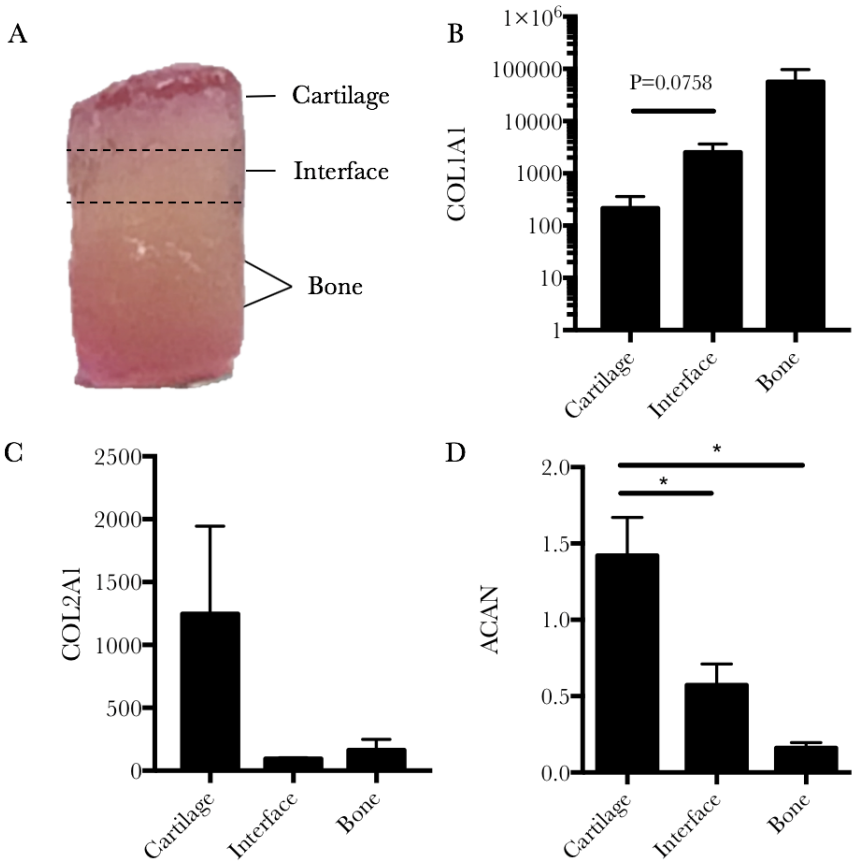

Figure 5.9: qRT-PCR of partitioned constructs following 28 days culture. A) Retrieved construct after culture in an *ex vivo* defect B) COL1A1, C) COL2A1 and D)ACAN expression relative to 18S. Data are shown as mean + SEM, n=3.

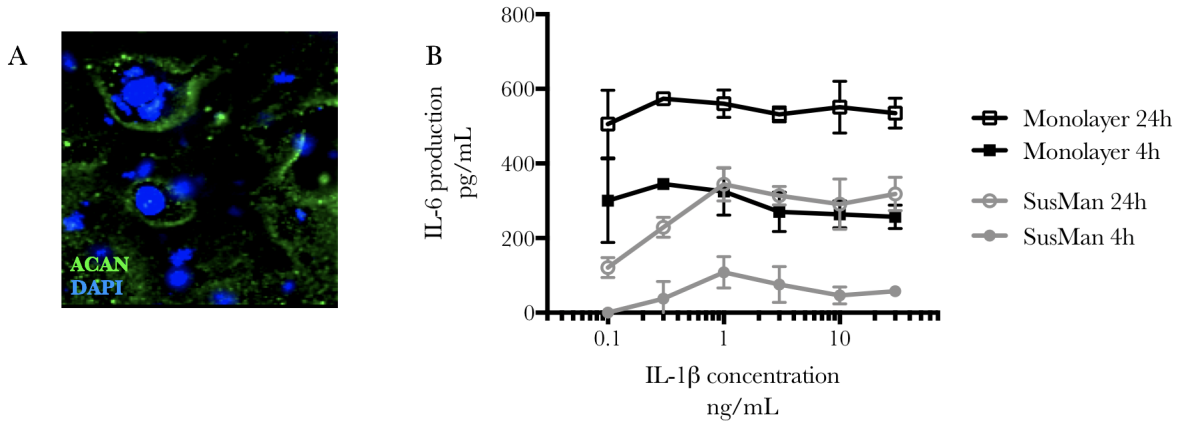

Figure 5.10: Functional characterisation of SusMan constructs A) Aggrecan staining in cartilage-like region. B)IL-6 production as a result of IL-1β stimulation at varying doses in both monolayer culture and SusMan produced constructs. Data are shown as mean $\pm$ SD, n=4.

5.4 Discussion

Bioprinting is a growing field and has already enabled the production of cell-seeded tissue constructs with high degrees of control over both the spatial deposition of both biological material and support materials [94]. The development of embedded printing has allowed for more complex geometries to be produced and from a wider pool of bioinks [13, 79]. In this study, the aim was to use a novel technique for embedded printing to produce functional cell-seeded models of the OCU.

Using this technique, the traditional 2D print bed was replaced by a 3D fluid gel support matrix. The agarose fluid gel showed hairy particle morphology similar to that seen by Ellis et al. in the production of an agar fluid gel in a pin stirrer [42]. The hypothesised method of formation of these fluid gel particles is based on the toroidal fluid motion seen in vortex flow generated by a magnetic stirrer [73]. As the hydrocolloid solution undergoes sol-gel transition, the central, vertical shear forces cause elongation of a spherical particle into a tadpole-like morphology. These then entangle to form aggregates, which are presumed to take a largely spherical morphology based on their circular appearance in 2D by phase contrast microscopy.

The entanglements between neighbouring particles are responsible for their rheological properties; in the absence of shear, particles are highly entangled and exhibit weak-gel behaviour. However, these are weak entanglements, such that upon the application of low shear (30-40 Pa) they are easily disrupted, allowing the particles to move past each other in a fluid-like motion [132]. During printing, the movement of the needle through the gel, as well as extrusion of the bioink into the gel, displaces the fluid gel. When the local forces involved in printing are removed, the matrix quickly restructures as shown by the fast viscous recovery of the fluid gel after shearing. Increasing the needle diameter resulted in thicker walls being printed and also more variability which is likely due to both the increased volume of material that was extruded and also because the needle itself was larger, so induced greater shear forces on the surrounding fluid gel.

The use of fluid gel as the support matrix draws similarities with some other tech-

niques that have been employed for embedded printing. The FRESH method, developed by Hinton et al., uses a gelatin slurry, produced by blending crosslinked gelatin into microparticles, that polysaccharide and protein-based bioinks can be printed into [79]. Following printing, the gelatin slurry matrix is heated to liquefy it and it is then removed. This was also possible in agarose fluid gels as they are thermogelling, however, fluid gels could also be removed by the gentle application of shear using sterile instruments or shear from washing. Another technique with similarities has also been investigated by Hinton but was first developed by Bhattacharjee et al.; 'Writing in the granular gel medium', employs carbopol, a highly hydrophilic granular polymer of 7 μm particles, into which hydrophobic inks can be printed with high (100 μm) resolution [12, 80].

In SusMan, the combination of the fluid gel particles and residual phase of partially gelled material (the continuous phase), limited the print resolution and allows diffusion of liquid material through the matrix. Increasing the Mw of the bioink reduced the rate of diffusion, enabling longer times for crosslinking before feature resolution was lost. In this study, dyes of Mw from 808-1299 with viscosities close to that of water were used to study resolution and diffusion. Using low viscosity solutions represents the worst-case scenario for diffusion as the movement of liquid into the interstices between fluid gel particles will be at its highest. A number of polysaccharide and protein-based bioinks have been printed using SusMan, including collagen which has a crosslinking time of between 0.5-2 h depending on the protein concentration (Senior, Cooke et al. *In preparation*).

In this study, a 1% w/v alginate solution was shown to be suitable for producing complex geometries by SusMan; tubular constructs of up to 30 mm in height as well as perfusable bifurcating structures were printed, crosslinked and removed from the fluid gel matrix. For cell-seeded constructs, gellan gum was used; gellan has previously been shown to be suitable for cell culture and can be easily modified by the introduction of HAp to alter its chemical and mechanical properties [88, 118]. Here, bi-layered gellan/gellan-mineral constructs were produced. The use of sol-HAp ensured that the mineral was fairly evenly distributed in the polymer, with a few larger aggregates. The interface between the

mineralised and non-mineralised regions appears to be continuous optically and by μCT; upon removal of the construct following the culture period, the structure was still intact. The addition of nanoHAp was also shown to increase the rate of stress relaxation, which has previously been shown to favour mineralisation in culture [24]. The process conditions applied to the cells during printing were sufficiently mild that very good viability was seen in chondrocytes after printing.

Primary human chondrocytes and osteoblasts were isolated and cultured in printed scaffolds for 28 days. The expression of Col II and Col I changed gradually throughout the structure inline with what would be expected with the native tissue region. This indicated that while the two sections of the osteochondral scaffold were well integrated, the embedded cell population retained their native phenotype. As in chapter 4, quiescently gelled polysaccharide matrices restricted cell migration. The production of aggrean shown by IHC, indicated that the embedded chondrocytes were still metabolically active and capable of laying down matrix, as has been seen previously in chondrocyte culture in gellan [150]. Further, their functional response to stimuli was confirmed by the production of IL-6 in response to IL-1β stimulation. The response was delayed, compared to chondrocytes in monolayer, in relation to both timing and dosage. The level of cytokine production at 4 h in monolayer was not seen in the printed constructs until 24 h. This delayed response may be due to the diffusion of both the IL-1β into the construct and IL-6 out of the gellan matrix. Further, the peak response in printed constructs was at 1 ng/mL compared to 0.3 ng/mL in monolayer culture. This may be due to reduced proliferation in the 3D matrix compared to in monolayer, although this was not quantified.

The use of ALM to produce functional tissue constructs has two potential applications: 1) to replace damaged or defective tissue and 2) to produce *in vitro* models. These models may be used for the testing of novel therapeutics prior to preclinical animal models as well as developing a better understanding of *in vivo* processes [187, 188]. It is widely accepted that osteochondral cell behaviour in 3D culture is much closer to that of the *in vivo* environment than 2D culture [38]. Therefore, development of 3D models as

platforms for drug profiling may enable better *in vitro* testing of potential therapeutics to reduce the number of animals used in preclinical studies. Further, by integrating multiple cell types, the mode of action of therapeutics on both the bone and cartilage aspects of the joint may be assessed simultaneously.

5.5 Conclusions

In this study, a new method of embedded printing was used to manufacture comparatively complex soft-solid structures by extruding a hydrocolloid solution into a supporting fluid gel matrix. The fluid gel matrix was characterised and a hypothesis for the morphology of the gel particles was presented. The resolution and diffusion of low viscosity solutions were measured to determine the limits of the technique. The method allowed the structuring of soft-solid materials into geometries not possible by traditional bioplotting techniques. It was shown that suspended manufacture could recapitulate the structure of the osteochondral region as defined by CT scanning. The printed structure maintained its morphology and mechanical robustness over a period of four weeks of culture during which the encapsulated cells retained their phenotype. Further, the embedded cell population was responsive to inflammatory stimuli showing that cells maintain their functional response such that this model could be developed into a testing platform for novel therapeutics.

CHAPTER 6

CONCLUSIONS AND FUTURE WORK

6.1 General overview

The osteochondral unit is a highly specialised structure that serves many functions. In OA and traumatic cartilage injuries, there are both clinically detectable and clinically silent changes in remodelling of cartilage, bone and other joint tissues. As the prevalence of OA and other degenerative diseases continues to increase with the world's ageing and increasingly obese population, developing a better understanding of the changes is highly important in order to develop better and more effective treatment strategies.

In this thesis, new findings about the clinically silent changes that occur in the OA joint have been presented by utilising techniques that are established in the fields of engineering and material science but are infrequently used to study biological systems. Further, unanswered questions about the phenotypic changes commonly reported in chondrocyte culture in 3D have been investigated alongside development of new methods for delivery of cell populations by structuring hydrogels. Finally, by utilising these hydrogel structuring methods, a novel bioprinting method was developed to overcome some of the limitations in traditional bioprinting. This enabled the production of bioprinted models of the osteochondral unit that could maintain cell phenotype and function whilst providing distinct chemical and mechanical environments.

6.2 Limitations and future investigations

6.2.1 Mechanical and physicochemical analysis of cartilage

The early, clinically silent changes that occur in OA prior to mechanical cartilage damage are clinically important, as interventions at this stage may help to slow or prevent degenerative OA. In chapter 3, methods more commonly seen in materials science were used to investigate the changing matrix properties of OA cartilage.

Cartilage has long been known to be a viscoelastic tissue, and here the frequency-dependent viscoelastic behaviour of human OA and healthy cartilage was compared for the first time. Due to the use of human tissue, the sample number was limited; particularly the number of 'healthy' post mortem samples available. As such, all mechanical testing was performed in the same order of increasing frequency. It is likely that during testing, some fluid was pushed out of the cartilage explant as they were tested in unconfined compression. Therefore, there will be small and gradual decreases in the level of hydration during testing. To investigate this, future studies should consider randomising the order in which the frequencies are applied or test in a hydrated system. Further, in this study a wide range of frequencies were measured to investigate both typical and atypical heel strike rise times. It would be interesting to look more closely at the viscoelastic behaviour at the lower frequencies, as they are more commonly experienced in normal loading.

Regarding the physicochemical characterisation of cartilage samples, it would be interesting to further investigate the mineral identified in cartilage sections from OA subjects. Determining whether this was HAp (the most common mineral found in bone) or calcium pyrophosphate dihydrate (CPPD) may help identify the mechanism of formation or deposition. This could be achieved by investigating the Ca:P ratio in inclusions from quantitative μXRF data. The use of TGA allowed for a very accurate quantification of the amount of water present in OA and healthy tissues but could also be used to gather more information about the changing cartilage matrix. TGA has been used previously to identify the amount of organic material in bone, both between species and also between

disease states in humans so could provide interesting information about the state of the cartilage matrix in healthy and OA samples [131].

Another interesting observation that could be achieved in future studies is the depth dependence of the dynamic mechanical properties reported. As the structure and chemistry of cartilage varies through the different zones of cartilage, the difference in properties in OA could be further elucidated; as was seen in this study, the superficial region was susceptible to damage whilst the middle and deep zones were undamaged in this loading regime. This further study could be achieved by performing DMA at sufficiently low frequencies that none of the tissues were damaged, then removing a defined depth of tissue using a microtome and re-testing (following full recovery). For this investigation, it would be important to maintain the cartilage on the subchondral bone to ensure that the full depth of cartilage was being tested.

6.2.2 Geometric confinement of chondrocytes

Cartilage was one of the first tissues that researchers sought to regenerate and to model *in vitro*, with its seemingly simple composition and structural organisation. However, this was not to be the case and after over 30 years of research, tissue engineered hyaline cartilage has still not reached clinical use. This can be attributed to many reasons. Cartilage is formed during early development and matures into a tissue with very low matrix turnover in adult life. Therefore, adult chondrocytes exhibit low anabolic capacity for matrix production. Many strategies have investigated the use of stem cells, and embryonic stem cells have shown great potential for cartilage (and other) tissue engineering strategies. However, the ethics surrounding their use are difficult to navigate. Over decades of cartilage engineering research, alginate has consistently been shown to promote chondrocyte phenotype and matrix production.

In chapter 4, alginate matrices of identical chemistry but different structures were produced and seeded with human chondrocytes. In fluid alginate, chondrocytes were able to migrate laterally and vertically through the gel matrix compared to the quiescent

matrix where they were static. Reducing the level of confinement reduced the capacity of the chondrocytes to redifferentiate following monolayer expansion. Work by Lee, Mooney and Chaudhuri, that was published a week prior to the work presented in this thesis, showed very similar results [107]. Using alginate matrices of differing stress relaxation times they showed that more elastic hydrogels, with faster relaxation times, caused a larger upregulation of expression of Coll II and aggrecan. They also showed that in the slower relaxing gels, there was upregulation of IL-1β, MMP-13 and ADAMTS-4, which are all markers of cartilage matrix breakdown [107].

In this study, fluid gel matrices were shown to be unsuitable for chondrocyte culture regarding the maintenance of phenotype. However, they support cell viability and also allow migration of cells so may show potential in culture and delivery of other cell types. As the alginate particles produced during shear are on the range of 10-20x the size of chondrocytes, it is hypothetically possible to produce an alginate fluid gel with chondrocytes entrapped within the gel, which would provide the level of confinement required. The limitation here however would be cell viability as the introduction of high shear during gelation would likely cause cell death. Another avenue for chondrocyte culture in fluid gels is to modify the alginate chains to introduce cell-binding ligands; this may act to constrict their movement or stimulate the mechanosensory pathways that are active in entrapped cells. Generally, future investigations into the use of fluid gels for unconfined 3D cell culture should focus on cell types which require a soft substrate (or are non-adherent) and those for the investigation of cell migration in 3D.

6.2.3 Biofabrication of osteochondral tissue models

Embedded printing shows great potential to produce bioprinted constructs of greater complexity without gravitational limitations typically seen in ALM of hydrogels. In chapter 5, a novel method for embedded printing was presented and utilised for the production of bilayered scaffolds to recapitulate the osteochondral unit. The same concept of introducing shear during gelation as demonstrated in chapter 4 was used to produce a support

matrix for low viscosity materials in bioprinting. The agarose fluid gel was shown to be a suitable support matrix for the printing of materials with low viscosity - even water could be printed into the fluid gel matrices. There are, however, limitations surrounding the use of particulate print matrices. These were investigated *via* the diffusion of dyes of different Mw. Further investigations into the diffusion of hydrocolloid solutions through the matrix would be valuable in developing a fuller understanding of the diffusion limitations in polysaccharide, protein and synthetic bioinks. Regarding the resolution limitation investigated, the use of smaller needles and hardware with increased print resolution may reduce the size of features that can be printed. Developing a more complete understanding of the continuous phase of partially gelled material within the fluid gel would also help these investigations.

To advance the presented osteochondral model as an *in vitro* model of OA, a potential study could explore the co-culture of osteoblasts and chondrocytes from different cohorts of patients and investigating cellular crosstalk. By using chondrocytes from OA patients and osteoblasts from 'healthy' patients (and *vice versa*), cross-talk between the healthy and OA groups could help to better understand the sequence of events that occur. Further, co-cultures of cells isolated from OA patients of differing BMI classifications could be used to probe the effects of adipokines on inflammation-based drivers of OA progression. In this context, adipose tissue-conditioned media could be an efficient way to deliver adipokines. As the hydrogel constructs can be easily divided into regions for analysis, these bioprinted co-culture systems are simple to section for analysis compared to having mixed cell populations in a single-layered 3D scaffold. When a co-culture is well established, the validation of potential therapeutic targets should be performed. These could be therapeutics that aim to dampen the inflammatory response and also those that aim to recover normal production of cartilage matrix.

To develop this model further in the future, increasing the number of cell types used in co-culture would enable the production of a construct that more closely modelled the whole joint environment. This, however, would present greater challenges in designing

bioinks to promote native phenotype and production of extracellular matrix in more cell types, in a single culture media. This would likely involve employing different base bioinks, prior to additives, in different regions. This has been achieved from a materials aspect (Senior, Cooke et al. *In preparation*), but the integration of cells and further biological material would be critical for the development of a more sophisticated model. An elegant demonstration of the ability to modify cell phenotype could be achieved by the seeding of a single stem cell population into materials of different mechanical properties and chemistry within the same construct, and measuring the potential for differentiation directed by the scaffold rather than growth factors in culture media.

Finally, this printing technique is not limited to producing models of the osteochondral unit. One example is the modelling of a blood vessel lumen. As shown, tubular structures can be printed of complex and bifurcating geometries that can then be perfused. By integrating smooth muscle cells into the bioink, they could be printed into tubular structures, before seeding endothelial cells onto the inner surface. Following establishment of the cell populations, the effects of different flow regimes on the endothelial and muscle cell populations could be investigated. Suspended manufacture is a flexible and inexpensive way to bioprint complex and physiologically-sized constructs from materials that support cell culture but are not 'printable' by other methods. There is potential for this technique to be used in the production of both *in vitro* models and potentially implantable *in vivo* constructs for tissue regeneration.

6.3 Overall summary

The three studies presented in this thesis answer novel questions and provide potential solutions surrounding the changes to the cartilage extracellular matrix in osteoarthritis and cartilage injuries. By structuring hydrogels in a unique way, materials which have been well characterised for use in TE have new usability. Further investigations into components of each of these studies should be sought to continue their development.

LIST OF REFERENCES

[1] S. Ab-Rahim, L. Selvaratnam, H. R. B. Raghavendran, and T. Kamarul. Chondrocyte-alginate constructs with or without TGF-beta 1 produces superior extracellular matrix expression than monolayer cultures. *Molecular and Cellular Biochemistry*, 376(1-2):11–20, 2013. doi: 10.1007/s11010-012-1543-0.

[2] I. Afara, I. Prasadam, R. Crawford, Y. Xiao, and A. Oloyede. Non-destructive evaluation of articular cartilage defects using near-infrared (NIR) spectroscopy in osteoarthritic rat models and its direct relation to Mankin score. *Osteoarthritis and Cartilage*, 20(11):1367–1373, 2012. ISSN 10634584. doi: 10.1016/j.joca.2012.07.007.

[3] M. R. Allen and D. B. Burr. Bone Modeling and Remodeling. In *Basic and Applied Bone Biology*, pages 75–90. Academic Press, jan 2013. ISBN 9780124160156. doi: 10.1016/B978-0-12-416015-6.00004-6.

[4] ARUK. Osteoarthritis in general practice - Data and Perspectives - Arthritis Research UK. *The Medical press*, 222:253–258, 2013.

[5] K. A. Athanasiou, E. M. Darling, G. D. DuRaine, J. C. Hu, and A. H. Reddi. *Articular Cartilage*. 2017. ISBN 978-1-4987-0622-3.

[6] A. L. Aulthouse, M. Beck, E. Griffey, J. Sanford, K. Arden, M. A. Machado, and W. A. Horton. Expression of the human chondrocyte phenotype in vitro. *In Vitro Cellular and Developmental Biology - Animal*, 25(7):659–668, 1989. ISSN 08838364. doi: 10.1007/BF02623638.

[7] H. A. Awad, M. Q. Wickham, H. A. Leddy, J. M. Gimble, and F. Guilak. Chondrogenic differentiation of adipose-derived adult stem cells in agarose, alginate, and gelatin scaffolds. *Biomaterials*, 25(16):3211–3222, 2004. ISSN 01429612. doi: 10.1016/j.biomaterials.2003.10.045.

[8] R. A. Bank, M. Soudry, A. Maroudas, J. Mizrahi, and J. M. Tekoppele. The increased swelling and instantaneous deformation of osteoarthritic cartilage is highly

correlated with collagen degradation. *Arthritis and Rheumatism*, 43(10):2202–2210, 2000. ISSN 00043591. doi: 10.1002/1529-0131(200010)43:10.

[9] P. J. Basser, R. Schneiderman, R. A. Bank, E. Wachtel, and A. Maroudas. Mechanical properties of the collagen network in human articular cartilage as measured by osmotic stress technique. *Archives of Biochemistry and Biophysics*, 351(2):207–219, 1998. ISSN 00039861. doi: 10.1006/abbi.1997.0507.

[10] T. Beno, Y. J. Yoon, S. C. Cowin, and S. P. Fritton. Estimation of bone permeability using accurate microstructural measurements. *Journal of Biomechanics*, 39(13): 2378–2387, 2006. ISSN 00219290. doi: 10.1016/j.jbiomech.2005.08.005.

[11] L. E. Bertassoni, J. C. Cardoso, V. Manoharan, A. L. Cristino, N. S. Bhise, W. A. Araujo, P. Zorlutuna, N. E. Vrana, A. M. Ghaemmaghami, M. R. Dokmeci, and A. Khademhosseini. Direct-write bioprinting of cell-laden methacrylated gelatin hydrogels. *Biofabrication*, 6(2), 2014. ISSN 17585090. doi: 10.1088/1758-5082/6/2/024105.

[12] M. Bhattacharjee, J. Coburn, M. Centola, S. Murab, A. Barbero, D. L. Kaplan, I. Martin, and S. Ghosh. Tissue engineering strategies to study cartilage development, degeneration and regeneration. *Adv Drug Deliv Rev*, 84:107–122, 2015. doi: 10.1016/j.addr.2014.08.010.

[13] T. Bhattacharjee, S. M. Zehnder, K. G. Rowe, S. Jain, R. M. Nixon, W. G. Sawyer, and T. E. Angelini. Writing in the granular gel medium. *Science Advances*, 1(8): 4–10, 2015. ISSN 23752548. doi: 10.1126/sciadv.1500655.

[14] H. Blain, P. Chavassieux, N. Portero-Muzy, F. Bonnel, F. Canovas, M. Chammas, P. Maury, and P. D. Delmas. Cortical and trabecular bone distribution in the femoral neck in osteoporosis and osteoarthritis. *Bone*, 43(5):862–868, 2008. ISSN 87563282. doi: 10.1016/j.bone.2008.07.236.

[15] T. Boland, X. Tao, B. J. Damon, B. Manley, P. Kesari, S. Jalota, and S. Bhaduri. Drop-on-demand printing of cells and materials for designer tissue constructs. *Materials Science and Engineering C*, 27(3):372–376, 2007. ISSN 09284931. doi: 10.1016/j.msec.2006.05.047.

[16] D. Bosnakovski, M. Mizuno, G. Kim, S. Takagi, M. Okumura, and T. Fujinaga. Chondrogenic differentiation of bovine bone marrow mesenchymal stem cells (MSCs) in different hydrogels: Influence of collagen type II extracellular matrix on MSC chondrogenesis. *Biotechnology and Bioengineering*, 93:1152–1163, 2006. ISSN 00063592. doi: 10.1002/bit.20828.

[17] G. M. Brouwer, A. W. Van Tol, A. P. Bergink, J. N. Belo, R. M. Bernsen, M. Reijman, H. A. Pols, and S. M. Bierma-Zeinstra. Association between valgus and varus alignment and the development and progression of radiographic osteoarthritis of the knee. *Arthritis and Rheumatism*, 56(4):1204–1211, 2007. ISSN 00043591. doi: 10.1002/art.22515.

[18] T. D. Brown, P. D. Dalton, and D. W. Hutmacher. Direct writing by way of melt electrospinning. *Advanced Materials*, 23(47):5651–5657, 2011. ISSN 09359648. doi: 10.1002/adma.201103482.

[19] L. V. Burgin, L. Edelsten, and R. M. Aspden. The mechanical and material properties of elderly human articular cartilage subject to impact and slow loading. *Medical Engineering and Physics*, 36(2):226–232, 2014. ISSN 13504533. doi: 10.1016/j.medengphy.2013.11.002.

[20] D. B. Burr and M. A. Gallant. Bone remodelling in osteoarthritis. *Nature Reviews Rheumatology*, 8(11):665–673, 2012. ISSN 17594790. doi: 10.1038/nrrheum.2012.130.

[21] E. Calvo, I. Palacios, E. Delgado, O. Sanchez-Pernaute, R. Largo, J. Egido, and G. Herrero-Beaumont. Histopathological correlation of cartilage swelling detected by magnetic resonance imaging in early experimental osteoarthritis. *Osteoarthritis and Cartilage*, 12(11):878–886, 2004. ISSN 10634584. doi: 10.1016/j.joca.2004.07.007.

[22] M. M. J. Caron, P. J. Emans, M. M. E. Coolsen, L. Voss, D. A. M. Surtel, A. Cremers, L. W. van Rhijn, and T. J. M. Welting. Redifferentiation of dedifferentiated human articular chondrocytes: Comparison of 2D and 3D cultures. *Osteoarthritis and Cartilage*, 20(10):1170–1178, 2012. ISSN 10634584. doi: 10.1016/j.joca.2012.06.016.

[23] B. Caterson, C. R. Flannery, C. E. Hughes, and C. B. Little. Mechanisms involved in cartilage proteoglycan catabolism. *Matrix Biology*, 19(4):333–344, 2000. ISSN 0945053X. doi: 10.1016/S0945-053X(00)00078-0.

[24] O. Chaudhuri, L. Gu, D. Klumpers, M. Darnell, S. A. Bencherif, J. C. Weaver, N. Huebsch, H.-P. Lee, E. Lippens, G. N. Duda, and D. J. Mooney. Hydrogels with tunable stress relaxation regulate stem cell fate and activity. *Nature materials*, 15: 326–333, 2015. ISSN 1476-1122. doi: 10.1038/nmat4489.

[25] C. T. Chen, M. Bhargava, P. M. Lin, and P. A. Torzilli. Time, stress, and location dependent chondrocyte death and collagen damage in cyclically loaded articular

cartilage. *Journal of Orthopaedic Research*, 21(5):888–898, 2003. ISSN 07360266. doi: 10.1016/S0736-0266(03)00050-0.

[26] M. E. Cooke, S. W. Jones, B. ter Horst, N. Moiemen, M. Snow, G. Chouhan, L. J. Hill, M. Esmaeli, R. J. Moakes, J. Holton, R. Nandra, R. L. Williams, A. M. Smith, and L. M. Grover. Structuring of Hydrogels across Multiple Length Scales for Biomedical Applications. *Advanced Materials*, 30(14), 2018. ISSN 15214095. doi: 10.1002/adma.201705013.

[27] P. F. Costa, C. Vaquette, J. Baldwin, M. Chhaya, M. E. Gomes, R. L. Reis, C. Theodoropoulos, and D. W. Hutmacher. Biofabrication of customized bone grafts by combination of additive manufacturing and bioreactor knowhow. *Biofabrication*, 6(3):035006, 2014. ISSN 17585090. doi: 10.1088/1758-5082/6/3/035006.

[28] M. D. Crema, D. J. Hunter, D. Burnstein, F. W. Roemer, L. Li, F. Eckstein, N. Krishnan, M.-P. H. Le-Graverand, and A. Guermazi. Association of changes in delayed gadolinium-enhanced MRI of cartilage (dGEMRIC) with changes in cartilage thickness in the medial tibiofemoral compartment of the knee: a 2 year follow-up study using 3.0 T MRI. *Annals of the rheumatic diseases*, 73(11):1935–1941, 2014. ISSN 14682060. doi: 10.1136/annrheumdis-2012-203083.

[29] X. Cui and T. Boland. Human microvasculature fabrication using thermal inkjet printing technology. *Biomaterials*, 30(31):6221–6227, 2009. ISSN 01429612. doi: 10.1016/j.biomaterials.2009.07.056.

[30] X. Cui, G. Gao, T. Yonezawa, and G. Dai. Human Cartilage Tissue Fabrication Using Three-dimensional Inkjet Printing Technology. *Journal of Visualized Experiments*, (88):1–5, 2014. ISSN 1940-087X. doi: 10.3791/51294.

[31] P. D. Dalton. Melt electrowriting with additive manufacturing principles. *Current Opinion in Biomedical Engineering*, 2:49–57, 2017. ISSN 24684511. doi: 10.1016/j.cobme.2017.05.007.

[32] E. M. Darling and K. A. Athanasiou. Growth factor impact on articular cartilage subpopulations. *Cell and Tissue Research*, 322(3):463–473, 2005. ISSN 0302766X. doi: 10.1007/s00441-005-0020-4.

[33] B. De Crombrugghe, V. Lefebvre, R. R. Behringer, W. Bi, S. Murakami, and W. Huang. Transcriptional mechanisms of chondrocyte differentiation. *Matrix Biology*, 19(5):389–394, 2000. ISSN 0945053X. doi: 10.1016/S0945-053X(00)00094-9.

[34] B. Decker, W. F. McGuckin, B. F. McKenzie, and C. H. Slocumb. Concentration of hyaluronic acid in synovial fluid. *Clinical chemistry*, 5:465–469, 1959. ISSN 00099147.

[35] B. Derby. Bioprinting: Inkjet printing proteins and hybrid cell-containing materials and structures. *Journal of Materials Chemistry*, 18(47):5717–5721, 2008. ISSN 09599428. doi: 10.1039/b807560c.

[36] B. Derby. Inkjet Printing of Functional and Structural Materials: Fluid Property Requirements, Feature Stability, and Resolution. *Annual Review of Materials Research*, 40(1):395–414, 2010. ISSN 1531-7331. doi: 10.1146/annurev-matsci-070909-104502.

[37] I. M. K. Driesang and E. B. Hunziker. Delamination rates of tissue flaps used in articular cartilage repair. *Journal of Orthopaedic Research*, 18(6):909–911, 2000. ISSN 07360266. doi: 10.1002/jor.1100180609.

[38] J. L. Drury and D. J. Mooney. Hydrogels for tissue engineering: Scaffold design variables and applications. *Biomaterials*, 24(24):4337–4351, 2003. ISSN 01429612. doi: 10.1016/S0142-9612(03)00340-5.

[39] J. L. Drury, R. G. Dennis, and D. J. Mooney. The tensile properties of alginate hydrogels. *Biomaterials*, 25(16):3187–3199, 2004. doi: 10.1016/j.biomaterials.2003.10.002.

[40] D. F. Duarte Campos, A. Blaeser, M. Weber, J. Jäkel, S. Neuss, W. Jahnen-Dechent, and H. Fischer. Three-dimensional printing of stem cell-laden hydrogels submerged in a hydrophobic high-density fluid. *Biofabrication*, 5(1):015003, 2013. ISSN 17585082. doi: 10.1088/1758-5082/5/1/015003.

[41] D. F. Duarte Campos, A. Blaeser, A. Korsten, S. Neuss, J. Jäkel, M. Vogt, and H. Fischer. The Stiffness and Structure of Three-Dimensional Printed Hydrogels Direct the Differentiation of Mesenchymal Stromal Cells Toward Adipogenic and Osteogenic Lineages. *Tissue Engineering Part A*, 21(3-4):740–756, 2015. ISSN 1937-3341. doi: 10.1089/ten.tea.2014.0231.

[42] A. L. Ellis, A. B. Norton, T. B. Mills, and I. T. Norton. Stabilisation of foams by agar gel particles. *Food Hydrocolloids*, 73:222–228, 2017. ISSN 0268005X. doi: 10.1016/j.foodhyd.2017.06.038.

[43] D. M. Espino, D. E. T. Shepherd, and D. W. L. Hukins. Viscoelastic properties of bovine knee joint articular cartilage: dependency on thickness and loading frequency. *BMC Musculoskeletal Disorders*, 15(1):205, 2014. ISSN 1471-2474. doi: 10.1186/1471-2474-15-205.

[44] D. Eyre. Collagen of articular cartilage. *Arthritis Research*, 4(1), 2002. doi: 10.1186/ar380.

[45] M. Fakhry, E. Hamade, B. Badran, R. Buchet, and D. Magne. Molecular mechanisms of mesenchymal stem cell differentiation towards osteoblasts. *World journal of stem cells*, 5(4):136–48, 2013. ISSN 1948-0210. doi: 10.4252/wjsc.v5.i4.136.

[46] R. W. Farndale, D. J. Buttle, and A. J. Barrett. Improved Quantitation and Discrimination of Sulfated Glycosaminoglycans by Use of Dimethylmethylene Blue. *Biochimica Et Biophysica Acta*, 883(2):173–177, 1986. doi: Doi 10.1016/0304-4165(86)90306-5.

[47] I. Fernandez Farres and I. T. Norton. Formation kinetics and rheology of alginate fluid gels produced by in-situ calcium release. *Food Hydrocolloids*, 40:76–84, 2014. ISSN 0268005X. doi: 10.1016/j.foodhyd.2014.02.005.

[48] I. Fernandez Farres, M. Douaire, and I. T. Norton. Rheology and tribological properties of Ca-alginate fluid gels produced by diffusion-controlled method. *Food Hydrocolloids*, 32(1):115–122, 2013. ISSN 0268005X. doi: 10.1016/j.foodhyd.2012.12.009.

[49] I. Fernandez Farres, R. Moakes, and I. Norton. Designing biopolymer fluid gels: A microstructural approach. *Food Hydrocolloids*, 42:362–372, 2014. doi: 10.1016/j.foodhyd.2014.03.014.

[50] C. J. Ferris, K. J. Gilmore, G. G. Wallace, M. In, and H. Panhuis. Modified gellan gum hydrogels for tissue engineering applications. *Soft Matter*, (9):3705–3711, 2013. doi: 10.1039/c3sm27389j.

[51] J. M. Fick. How the structural integrity of the matrix can influence the microstructural response of articular cartilage to compression. *Connective tissue research*, 54 (2):83–93, 2013. ISSN 1607-8438. doi: 10.3109/03008207.2012.746321.

[52] R. Florencio-Silva, G. R. d. S. Sasso, E. Sasso-Cerri, M. J. Simões, and P. S. Cerri. Biology of Bone Tissue: Structure, Function, and Factors That Influence Bone Cells. *Biomed Research International*, 2015, 2015. ISSN 23146141. doi: 10.1155/2015/421746.

[53] A. J. Fosang and F. Beier. Emerging Frontiers in cartilage and chondrocyte biology. *Best Practice and Research: Clinical Rheumatology*, 25(6):751–766, 2011. ISSN 15216942. doi: 10.1016/j.berh.2011.11.010.

[54] M. Fuerst, O. Niggemeyer, L. Lammers, F. Schäfer, C. Lohmann, and W. Rüther. Articular cartilage mineralization in osteoarthritis of the hip. *BMC Musculoskeletal Disorders*, 10(1):166, 2009. ISSN 14712474. doi: 10.1186/1471-2474-10-166.

[55] G. R. Fulcher, D. W. L. Hukins, and D. E. T. Shepherd. Viscoelastic properties of bovine articular cartilage attached to subchondral bone at high frequencies. *BMC Musculoskeletal Disorders*, 10(1), 2009. ISSN 14712474. doi: 10.1186/1471-2474-10-61.

[56] A. Gabriele, F. Sypyropoulos, and I. T. Norton. Kinetic study of fluid gel formation and viscoelastic response with kappa-carrageenan. *Food Hydrocolloids*, 23(8):2054–2061, 2009. doi: 10.1016/j.foodhyd.2009.03.018.

[57] N. G. Genes, J. A. Rowley, D. J. Mooney, and L. J. Bonassar. Effect of substrate mechanics on chondrocyte adhesion to modified alginate surfaces. *Archives of Biochemistry and Biophysics*, 422(2):161–167, 2004. ISSN 00039861. doi: 10.1016/j.abb.2003.11.023.

[58] M. B. Goldring. Osteoarthritis and cartilage: the role of cytokines. *Curr Rheumatol Rep*, 2(6):459–465, 2000.

[59] M. B. Goldring and S. R. Goldring. Articular cartilage and subchondral bone in the pathogenesis of osteoarthritis. *Annals of the New York Academy of Sciences*, 1192(1):230–237, apr 2010. ISSN 00778923. doi: 10.1111/j.1749-6632.2009.05240.x.

[60] M. B. Goldring and M. Otero. Inflammation in osteoarthritis. *Curr Opin Rheumatol*, 23(5):471–478, 2011. doi: 10.1097/BOR.0b013e328349c2b1.

[61] S. R. Goldring and M. B. Goldring. Changes in the osteochondral unit during osteoarthritis: Structure, function and cartilage bone crosstalk, 2016. ISSN 17594804.

[62] S. Graindorge, W. Ferrandez, E. Ingham, Z. Jin, P. Twigg, and J. Fisher. The role of the surface amorphous layer of articular cartilage in joint lubrication. *Proceedings of the Institution of Mechanical Engineers, Part H: Journal of Engineering in Medicine*, 220(5):597–607, 2006. ISSN 09544119. doi: 10.1243/09544119JEIM122.

[63] J. J. Green and J. H. Elisseeff. Mimicking biological functionality with polymers for biomedical applications. *Nature*, 540(7633):386–394, 2016. ISSN 0028-0836. doi: 10.1038/nature21005.

[64] A. Greiner and J. H. Wendorff. Electrospinning: A fascinating method for the preparation of ultrathin fibers. *Angewandte Chemie - International Edition*, 46 (30):5670–5703, 2007. ISSN 14337851. doi: 10.1002/anie.200604646.

[65] J. Groll, T. Boland, T. Blunk, J. A. Burdick, D. W. Cho, P. D. Dalton, B. Derby, G. Forgacs, Q. Li, V. A. Mironov, L. Moroni, M. Nakamura, W. Shu, S. Takeuchi, G. Vozzi, T. B. Woodfield, T. Xu, J. J. Yoo, and J. Malda. Biofabrication: Reappraising the definition of an evolving field. *Biofabrication*, 8(1), 2016. ISSN 17585090. doi: 10.1088/1758-5090/8/1/013001.

[66] A. K. Grosskopf, R. L. Truby, H. Kim, A. Perazzo, J. A. Lewis, and H. A. Stone. Viscoplastic Matrix Materials for Embedded 3D Printing. *ACS Applied Materials and Interfaces*, 10(27):23353–23361, 2018. ISSN 19448252. doi: 10.1021/acsami.7b19818.

[67] F. Guilak. Biomechanical factors in osteoarthritis. *Best Practice and Research: Clinical Rheumatology*, 25(6):815–823, 2011. ISSN 15216942. doi: 10.1016/j.berh.2011.11.013.

[68] F. Guilak, A. Ratcliffe, N. Lane, M. P. Rosenwasser, and V. C. Mow. Mechanical and biochemical changes in the superficial zone of articular cartilage in canine experimental osteoarthritis. *Journal of Orthopaedic Research*, 12(4):474–484, 1994. ISSN 1554527X. doi: 10.1002/jor.1100120404.

[69] F. Guilak, B. Fermor, F. J. Keefe, V. B. Kraus, S. A. Olson, D. S. Pisetsky, L. A. Setton, and J. B. Weinberg. The Role of Biomechanics and Inflammation in Cartilage Injury and Repair. *Clinical orthopaedics and related research*, (423):17–26, 2004. doi: 10.1097/01.blo.0000131233.83640.91.

[70] J. Guo, G. W. Jourdian, and D. K. Maccallum. Culture and growth characteristics of chondrocytes encapsulated in alginate beads. *Connective Tissue Research*, 19 (2-4):277–297, 1989. ISSN 03008207. doi: 10.3109/03008208909043901.

[71] Q. Guo and J. H. Elisseeff. Cartilage Tissue Engineering. *Principles of Regenerative Medicine*, 1340:981–995, 2011. ISSN 1064-3745. doi: 10.1016/B978-0-12-381422-7.10053-7.

[72] M. Guvendiren, H. D. Lu, and J. A. Burdick. Shear-thinning hydrogels for biomedical applications. *Soft Matter*, 8(2):260–272, 2012. ISSN 1744-683X. doi: 10.1039/C1SM06513K.

[73] G. Halász, B. Gyüre, I. M. Jánosi, K. G. Szabó, T. Tél, G. Halasz, B. Gyure, I. M. Janosi, K. G. Szabo, and T. Tel. Vortex flow generated by a magnetic stirrer. *American Journal of Physics*, 75(12):1–8, 2007. ISSN 00029505. doi: 10.1119/1.2772287.

[74] E. Han, S. S. Chen, S. M. Klisch, and R. L. Sah. Contribution of proteoglycan osmotic swelling pressure to the compressive properties of articular cartilage. *Biophysical Journal*, 101(4):916–924, 2011. ISSN 00063495. doi: 10.1016/j.bpj.2011.07.006.

[75] L. Hangody and P. Fules. Autologous osteochondral mosaicplasty for the treatment of full-thickness defects of weight-bearing joints: ten years of experimental and clinical experience. *J Bone Joint Surg Am*, 85-A Suppl:25–32, 2003.

[76] B. A. Harley, A. K. Lynn, Z. Wissner-Gross, W. Bonfield, I. V. Yannas, and L. J. Gibson. Design of a multiphase osteochondral scaffold III: Fabrication of layered scaffolds with continuous interfaces. *Journal of Biomedical Materials Research - Part A*, 92(3):1078–1093, 2010. ISSN 15493296. doi: 10.1002/jbm.a.32387.

[77] D. Heinegård and T. Saxne. The role of the cartilage matrix in osteoarthritis. *Nature Reviews Rheumatology*, 7(1):50–56, 2011. ISSN 17594790. doi: 10.1038/nrrheum.2010.198.

[78] C. B. Highley, C. B. Rodell, and J. A. Burdick. Direct 3D Printing of Shear-Thinning Hydrogels into Self-Healing Hydrogels. *Advanced Materials*, 27(34):5075–5079, 2015. ISSN 15214095. doi: 10.1002/adma.201501234.

[79] T. J. Hinton, Q. Jallerat, R. N. Palchesko, J. H. Park, M. S. Grodzicki, H.-J. H.-J. Shue, M. H. Ramadan, A. R. Hudson, and A. W. Feinberg. Three-dimensional printing of complex biological structures by freeform reversible embedding of suspended hydrogels. *Science Advances*, 1(9):e1500758–e1500758, 2015. ISSN 2375-2548. doi: 10.1126/sciadv.1500758.

[80] T. J. Hinton, A. Hudson, K. Pusch, A. Lee, and A. W. Feinberg. 3D Printing PDMS Elastomer in a Hydrophilic Support Bath via Freeform Reversible Embedding. *ACS Biomaterials Science and Engineering*, 2(10):1781–1786, 2016. ISSN 23739878. doi: 10.1021/acsbiomaterials.6b00170.

[81] A. P. Hollander, I. Pidoux, A. Reiner, C. Rorabeck, R. Bourne, and A. R. Poole. Damage to type II collagen in aging and osteoarthritis starts at the articular surface, originates around chondrocytes, and extends into the cartilage with progressive degeneration. *Journal of Clinical Investigation*, 96(6):2859–2869, 1995. ISSN 00219738. doi: 10.1172/JCI118357.

[82] M. J. Hubbard. Articular debridement versus washout for degeneration of the medial femoral condyle. A five-year study. *The Journal of bone and joint surgery. British volume*, 78(2):217–219, 1996. ISSN 0301-620X.

[83] E. A. Hughes, S. C. Cox, M. E. Cooke, O. G. Davies, R. L. Williams, T. J. Hall, and L. M. Grover. Interfacial Mineral Fusion and Tubule Entanglement as a Means to Harden a Bone Augmentation Material. *Advanced Healthcare Materials*, 7(7): 1701166, 2018. ISSN 21922659. doi: 10.1002/adhm.201701166.

[84] N. C. Hunt and L. M. Grover. Cell encapsulation using biopolymer gels for regenerative medicine. *Biotechnology Letters*, 32:733–742, 2010. doi: 10.1007/s10529-010-0221-0.

[85] D. J. Hunter, D. Schofield, and E. Callander. The individual and socioeconomic impact of osteoarthritis. *Nature Reviews Rheumatology*, 10(7):437–441, 2014. ISSN 17594804. doi: 10.1038/nrrheum.2014.44.

[86] D. Ibrahim, A. A. Mostafa, S. Korowash, W. Suchanek, M. Yoshimura, A. Bigi, G. Cojazzi, S. Panzavolta, A. Ripamonti, N. Roveri, M. Romanello, K. N. Suarez, L. Moro, F. Driessens, D. Smith, E. Carlisle, A. Ruys, C. Rey, B. Collins, T. Goehl, I. Dickson, M. Glimcher, R. LeGeros, E. Carlisle, E. Carlisle, E. Carlisle, I. Gibson, J. Huang, S. Best, W. Bonfield, N. Patel, I. Gibson, K. Hing, S. Best, E. Damien, W. R. P. Bonfield, A. Porter, N. Patel, J. Skepper, S. Best, W. Bonfield, A. Porter, N. Patel, J. Skepper, S. Best, W. Bonfield, M. Jarcho, C. Bolen, M. Thomas, J. Bobick, J. Kay, R. Doremus, T. Kokubo, E. Bouyer, F. Gitzhofer, I. Boulos, C. Hammond, S. Koutsopoulos, W. Suchanek, P. Shuk, K. Byrappa, R. Rimana, K. TenHuisen, V. Janas, D. Tadic, F. Peters, M. Epple, A. Fidalgo, L. Iiharco, S. Sprio, A. Tampieri, E. Landi, M. Sandri, S. Martorana, G. Celotti, G. Logroscino, F. Balas, J. Pérez-Pariente, M. Vallet-Regí, X. Tang, X. Xiao, R. Liu, I. Gibson, S. Best, W. Bonfield, L. Boyer, J. Carpena, and J. Lacout. Chemical characterization of some substituted hydroxyapatites. *Chemistry Central Journal*, 5(1):74, 2011. ISSN 1752-153X. doi: 10.1186/1752-153X-5-74.

[87] A. Jackson and W. Gu. Transport Properties of Cartilaginous Tissues. *Current Rheumatology Reviews*, 5(1):40–50, 2009. ISSN 15733971. doi: 10.2174/157339709787315320.

[88] P. Jamshidi, G. Chouhan, R. L. Williams, S. C. Cox, and L. M. Grover. Modification of gellan gum with nanocrystalline hydroxyapatite facilitates cell expansion and spontaneous osteogenesis. *Biotechnology and Bioengineering*, 113(7):1568–1576, 2016. ISSN 10970290. doi: 10.1002/bit.25915.

[89] G. D. Jay and K. A. Waller. The biology of Lubricin: Near frictionless joint motion. *Matrix Biology*, 39:17–24, 2014. ISSN 15691802. doi: 10.1016/j.matbio.2014.08.008.

[90] C. I. Johnson, D. J. Argyle, and D. N. Clements. In vitro models for the study of osteoarthritis. *Veterinary Journal*, 209:40–49, 2016. ISSN 15322971. doi: 10.1016/j.tvjl.2015.07.011.

[91] T. Jungst, W. Smolan, K. Schacht, T. Scheibel, and J. Groll. Strategies and Molecular Design Criteria for 3D Printable Hydrogels. *Chemical Reviews*, 116(3):1496–1539, 2016. ISSN 15206890. doi: 10.1021/acs.chemrev.5b00303.

[92] J. S. Jurvelin, M. D. Buschmann, and E. B. Hunziker. Mechanical aniosotropy of human knee articular cartilage in compression. *Trans Orthop Res Soc*, 217:215–219, 1996.

[93] K. E. Kadler, D. F. Holmes, J. A. Trotter, and J. A. Chapman. Collagen fibril formation. *Journal of Biochemistry*, 316(Pt 1):1–11, 1996. ISSN 0264-6021. doi: 10.1042/bj3160001.

[94] H. W. Kang, S. J. Lee, I. K. Ko, C. Kengla, J. J. Yoo, and A. Atala. A 3D bioprinting system to produce human-scale tissue constructs with structural integrity. *Nat Biotechnol*, 34(3):312–319, 2016. doi: 10.1038/nbt.3413.

[95] A. Karim and A. C. Hall. Chondrocyte Morphology in Stiff and Soft Agarose Gels and the Influence of Fetal Calf Serum. *Journal of Cellular Physiology*, (July), 2016. ISSN 10974652. doi: 10.1002/jcp.25507.

[96] E. Kavanagh and D. E. Ashhurst. Development and aging of the articular cartilage of the rabbit knee joint: Distribution of biglycan, decorin, and matrilin-1. *Journal of Histochemistry and Cytochemistry*, 47(12):1603–1615, 1999. ISSN 00221554. doi: 10.1177/002215549904701212.

[97] G. Kempson. Relationship between the tensile properties of articular cartilage from the human knee and age. *Annals of the Rheumatic Diseases*, 41:508–511, 1982.

[98] G. E. Kempson, C. J. Spivey, S. A. V. Swanson, and M. A. R. Freeman. Patterns of cartilage stiffness on normal and degenerate human femoral heads. *Journal of Biomechanics*, 4(6):597–609, 1971. ISSN 00219290. doi: 10.1016/0021-9290(71)90049-2.

[99] M. Kesti, C. Eberhardt, G. Pagliccia, D. Kenkel, D. Grande, A. Boss, and M. Zenobi-Wong. Bioprinting Complex Cartilaginous Structures with Clinically

Compliant Biomaterials. *Advanced Functional Materials*, 25(48):7406–7417, 2015. ISSN 16163028. doi: 10.1002/adfm.201503423.

[100] T. J. Klein, J. Malda, R. L. Sah, and D. W. Hutmacher. Tissue engineering of articular cartilage with biomimetic zones. *Tissue Eng Part B Rev*, 15(2):143–157, 2009. doi: 10.1089/ten.TEB.2008.0563.

[101] L. Kock, C. C. Van Donkelaar, and K. Ito. Tissue engineering of functional articular cartilage: The current status. *Cell and Tissue Research*, 347:613–627, 2012. ISSN 0302766X. doi: 10.1007/s00441-011-1243-1.

[102] W. M. Lai, J. S. Hou, and V. C. Mow. A Triphasic Theory for the Swelling and Deformation Behaviors of Articular Cartilage. *Journal of Biomechanical Engineering*, 113(3):245, 1991. ISSN 01480731. doi: 10.1115/1.2894880.

[103] K. Lampropoulou-Adamidou, P. Lelovas, E. V. Karadimas, C. Liakou, I. K. Triantafillopoulos, I. Dontas, and N. A. Papaioannou. Useful animal models for the research of osteoarthritis. *European Journal of Orthopaedic Surgery and Traumatology*, 24(3):263–271, 2014. ISSN 14321068. doi: 10.1007/s00590-013-1205-2.

[104] J. M. Lane and C. Weiss. Review of articular cartilage collagen research. *Arthritis & Rheumatism*, 18(6):553–562, 1975. ISSN 15290131. doi: 10.1002/art.1780180605.

[105] B. M. Lawless, S. C. Barnes, D. M. Espino, and D. E. Shepherd. Viscoelastic properties of a spinal posterior dynamic stabilisation device. *Journal of the Mechanical Behavior of Biomedical Materials*, 59:519–526, 2016. ISSN 18780180. doi: 10.1016/j.jmbbm.2016.03.011.

[106] B. M. Lawless, H. Sadeghi, D. K. Temple, H. Dhaliwal, D. M. Espino, and D. W. L. Hukins. Viscoelasticity of articular cartilage: Analysing the effect of induced stress and the restraint of bone in a dynamic environment. *Journal of the Mechanical Behavior of Biomedical Materials*, 75:293–301, 2017. doi: 10.1016/j.jmbbm.2017.07.040.

[107] H. P. Lee, L. Gu, D. J. Mooney, M. E. Levenston, and O. Chaudhuri. Mechanical confinement regulates cartilage matrix formation by chondrocytes. *Nature Materials*, 16(12):1243–1251, 2017. ISSN 14764660. doi: 10.1038/nmat4993.

[108] K. Y. Lee and D. J. Mooney. Alginate: Properties and biomedical applications. *Progress in Polymer Science (Oxford)*, 37(1):106–126, 2012. ISSN 00796700. doi: 10.1016/j.progpolymsci.2011.06.003.

[109] J. C. H. Leijten, N. Georgi, L. Wu, C. A. Van Blitterswijk, and M. Karperien. Cell Sources for Articular Cartilage Repair Strategies: Shifting from Monocultures to Cocultures. *Tissue Engineering Part B-Reviews*, 19(1):31–40, 2013. doi: 10.1089/ten.teb.2012.0273.

[110] M. A. LeRoux, F. Guilak, and L. A. Setton. Compressive and shear properties of alginate gel: Effects of sodium ions and alginate concentration. *Journal of Biomedical Materials Research*, 47(1):46–53, 1999. doi: 10.1002/(SICI)1097-4636(199910)47.

[111] G. Li, J. Yin, J. Gao, T. S. Cheng, N. J. Pavlos, C. Zhang, and M. H. Zheng. Subchondral bone in osteoarthritis: Insight into risk factors and microstructural changes. *Arthritis Research and Therapy*, 15(6), 2013. ISSN 14786354. doi: 10.1186/ar4405.

[112] R. Liu-Bryan, K. Pritzker, G. S. Firestein, and R. Terkeltaub. TLR2 Signaling in Chondrocytes Drives Calcium Pyrophosphate Dihydrate and Monosodium Urate Crystal-Induced Nitric Oxide Generation. *The Journal of Immunology*, 174(8): 5016–5023, 2005. ISSN 0022-1767. doi: 10.4049/jimmunol.174.8.5016.

[113] R. F. Loeser, S. R. Goldring, C. R. Scanzello, and M. B. Goldring. Osteoarthritis: A disease of the joint as an organ. *Arthritis and Rheumatism*, 64(6):1697–1707, 2012. ISSN 00043591. doi: 10.1002/art.34453.

[114] L. S. Lohmander, L. A. Hoerrner, and M. W. Lark. Metalloproteinases, tissue inhibitor, and proteoglycan fragments in knee synovial fluid in human osteoarthritis. *Arthritis & Rheumatism*, 36(2):181–189, 1993. ISSN 15290131. doi: 10.1002/art.1780360207.

[115] P. Lorenzo, P. Neame, Y. Sommarin, and D. Heinegård. Cloning and deduced amino acid sequence of a novel cartilage protein (CILP) identifies a proform including a nucleotide pyrophosphohydrolase. *Journal of Biological Chemistry*, 273(36):23469–23475, 1998. ISSN 00219258. doi: 10.1074/jbc.273.36.23469.

[116] E. Lucchinetti, C. S. Adams, W. E. Horton, and P. A. Torzilli. Cartilage viability after repetitive loading: A preliminary report. *Osteoarthritis and Cartilage*, 10(1): 71–81, 2002. ISSN 10634584. doi: 10.1053/joca.2001.0483.

[117] M.A. MacConail. The movements of Bones and Joints. *The Journal of bone and joint surgery*, 33B:251–257, 1951. ISSN 2049-4394, 2049-4408. doi: 10.1148/radiology.215.2.r00ma01497.

[118] T. Majumdar, M. E. Cooke, B. M. Lawless, F. Bellier, E. A. Hughes, L. M. Grover, S. W. Jones, and S. C. Cox. Formulation and viscoelasticity of mineralised hydrogels for use in bone-cartilage interfacial reconstruction. *Journal of the Mechanical Behavior of Biomedical Materials*, 80:33–41, 2018. ISSN 18780180. doi: 10.1016/j.jmbbm.2018.01.016.

[119] A. F. Mak, W. M. Lai, and V. C. Mow. Biphasic indentation of articular cartilage-I. Theoretical analysis. *Journal of Biomechanics*, 20(7):703–714, 1987. ISSN 00219290. doi: 10.1016/0021-9290(87)90036-4.

[120] J. Malda, J. Visser, F. P. Melchels, T. Jüngst, W. E. Hennink, W. J. Dhert, J. Groll, and D. W. Hutmacher. 25th anniversary article: Engineering hydrogels for biofabrication. *Advanced Materials*, 25(36):5011–5028, 2013. ISSN 09359648. doi: 10.1002/adma.201302042.

[121] A. S. Mao, J.-W. Shin, and D. J. Mooney. Effects of substrate stiffness and cell-cell contact on mesenchymal stem cell differentiation. *Biomaterials*, 98:184–191, 2016. ISSN 01429612. doi: 10.1016/j.biomaterials.2016.05.004.

[122] A. Maroudas, H. Muir, and J. Wingham. The correlation of fixed negative charge with glycosaminoglycan content of human articular cartilage. *BBA - General Subjects*, 177(3):492–500, 1969. ISSN 03044165. doi: 10.1016/0304-4165(69)90311-0.

[123] Y. Matsusue, T. Yamamuro, and H. Hama. Arthroscopic multiple osteochondral transplantation to the chondral defect in the knee associated with anterior cruciate ligament disruption. *Arthroscopy*, 9(3):318–321, 1993. ISSN 07498063. doi: 10.1016/S0749-8063(05)80428-1.

[124] E. McColl, J. Groll, T. Jungst, and P. D. Dalton. Design and fabrication of melt electrowritten tubes using intuitive software. *Materials and Design*, 155:46–58, 2018. ISSN 18734197. doi: 10.1016/j.matdes.2018.05.036.

[125] T. McCormack and J. M. Mansour. Reduction in tensile strength of cartilage precedes surface damage under repeated compressive loading in vitro. *Journal of Biomechanics*, 31(1):55–61, 1998. ISSN 0021-9290.

[126] K. P. Menard. *Dynamic Mechanical Analysis: A Practical Introduction*. CRC press, Taylor & Francis Group, Boca Raton, 2nd edition, 2008. ISBN 978-1-4200-5312-8.

[127] R. Mhanna, A. Kashyap, G. Palazzolo, Q. Vallmajo-Martin, J. Becher, S. Moller, M. Schnabelrauch, and M. Zenobi-Wong. Chondrocyte culture in three dimensional alginate sulfate hydrogels promotes proliferation while maintaining expres-

sion of chondrogenic markers. *Tissue Eng Part A*, 20(9-10):1454–1464, 2014. doi: 10.1089/ten.TEA.2013.0544.

[128] V. Mironov, R. P. Visconti, V. Kasyanov, G. Forgacs, C. J. Drake, and R. R. Markwald. Organ printing: Tissue spheroids as building blocks. *Biomaterials*, 30 (12):2164–2174, 2009. ISSN 01429612. doi: 10.1016/j.biomaterials.2008.12.084.

[129] H. Mistry, M. Connock, J. Pink, D. Shyangdan, C. Clar, P. Royle, R. Court, L. C. Biant, A. Metcalfe, and N. Waugh. Autologous chondrocyte implantation in the knee: Systematic review and economic evaluation. *Health Technology Assessment*, 21(6):V–160, 2017. ISSN 20464924. doi: 10.3310/hta21060.

[130] K. Mithoefer, R. J. Williams 3rd, R. F. Warren, H. G. Potter, C. R. Spock, E. C. Jones, T. L. Wickiewicz, and R. G. Marx. The microfracture technique for the treatment of articular cartilage lesions in the knee. A prospective cohort study. *J Bone Joint Surg Am*, 87(9):1911–1920, 2005. doi: 10.2106/JBJS.D.02846.

[131] L. D. Mkukuma, J. M. Skakle, I. R. Gibson, C. T. Imrie, R. M. Aspden, and D. W. Hukins. Effect of the proportion of organic material in bone on thermal decomposition of bone mineral: An investigation of a variety of bones from different species using thermogravimetric analysis coupled to mass spectrometry, high-temperature X-ray diffraction,. *Calcified Tissue International*, 75(4):321–328, 2004. ISSN 0171967X. doi: 10.1007/s00223-004-0199-5.

[132] R. J. Moakes, A. Sullo, and I. T. Norton. Preparation and characterisation of whey protein fluid gels: The effects of shear and thermal history. *Food Hydrocolloids*, 45: 227–235, 2015. ISSN 0268005X. doi: 10.1016/j.foodhyd.2014.11.024.

[133] I. Mobasherpour, M. S. Heshajin, A. Kazemzadeh, and M. Zakeri. Synthesis of nanocrystalline hydroxyapatite by using precipitation method. *Journal of Alloys and Compounds*, 430(1-2):330–333, 2007. ISSN 09258388. doi: 10.1016/j.jallcom.2006.05.018.

[134] L. Moroni, T. Boland, J. A. Burdick, C. De Maria, B. Derby, G. Forgacs, J. Groll, Q. Li, J. Malda, V. A. Mironov, C. Mota, M. Nakamura, W. Shu, S. Takeuchi, T. B. Woodfield, T. Xu, J. J. Yoo, and G. Vozzi. Biofabrication: A Guide to Technology and Terminology. *Trends in Biotechnology*, 36(4):384–402, 2018. ISSN 18793096. doi: 10.1016/j.tibtech.2017.10.015.

[135] L. Moroni, J. A. Burdick, C. Highley, S. J. Lee, Y. Morimoto, S. Takeuchi, and J. J. Yoo. Biofabrication strategies for 3D in vitro models and regenerative medicine.

Nature Reviews Materials, 3(5):21–37, 2018. ISSN 20588437. doi: 10.1038/s41578-018-0006-y.

[136] V. C. Mow, S. C. Kuei, W. M. Lai, and C. G. Armstrong. Biphasic Creep and Stress Relaxation of Articular Cartilage in Compression: Theory and Experiments. *Journal of Biomechanical Engineering*, 102(1):73, feb 1980. ISSN 01480731. doi: 10.1115/1.3138202.

[137] V. C. Mow, M. H. Holmes, and W. Michael Lai. Fluid transport and mechanical properties of articular cartilage: A review. *Journal of Biomechanics*, 17(5):377–394, 1984. ISSN 00219290. doi: 10.1016/0021-9290(84)90031-9.

[138] R. Moyer, W. Wirth, J. Duryea, and F. Eckstein. Anatomical alignment, but not goniometry, predicts femorotibial cartilage loss as well as mechanical alignment: Data from the Osteoarthritis Initiative. *Osteoarthritis and Cartilage*, 24(2):254–261, 2016. ISSN 15229653. doi: 10.1016/j.joca.2015.08.016.

[139] C. L. Murphy and A. Sambanis. Effect of oxygen tension and alginate encapsulation on restoration of the differentiated phenotype of passaged chondrocytes. *Tissue Engineering*, 7(6):791–803, 2001. doi: Doi 10.1089/107632701753337735.

[140] C. J. L. Murray, T. Vos, R. Lozano, M. Naghavi, A. D. Flaxman, C. Michaud, M. Ezzati, K. Shibuya, J. A. Salomon, and A. D. Lopez. Disability-adjusted life years (DALYs) for 291 diseases and injuries in 21 regions, 19902010: a systematic analysis for the Global Burden of Disease Study 2010. *The Lancet*, 380(9859):2197–2223, 2012. ISSN 0140-6736. doi: 10.1016/S0140-6736(12)61689-4.

[141] E. Musacchio, R. Ramonda, E. Perissinotto, L. Sartori, R. Hirsch, L. Punzi, S. Zambon, M. C. Corti, G. Baggio, E. Manzato, A. Doria, and G. Crepaldi. The impact of knee and hip chondrocalcinosis on disability in older people: The ProVA Study from northeastern Italy. *Annals of the Rheumatic Diseases*, 70(11):1937–1943, 2011. ISSN 00034967. doi: 10.1136/ard.2011.150508.

[142] J. T. Muth, D. M. Vogt, R. L. Truby, Y. Mengüç, D. B. Kolesky, R. J. Wood, and J. A. Lewis. Embedded 3D printing of strain sensors within highly stretchable elastomers. *Advanced Materials*, 26(36):6307–6312, 2014. ISSN 15214095. doi: 10.1002/adma.201400334.

[143] F. Nelson, L. Dahlberg, S. Laverty, A. Reiner, I. Pidoux, M. Ionescu, G. L. Fraser, E. Brooks, M. Tanzer, L. C. Rosenberg, P. Dieppe, and A. Robin Poole. Evidence for altered synthesis of type II collagen in patients with osteoarthritis. *Journal of Clinical Investigation*, 102(12):2115–2125, 1998. ISSN 0021-9738. doi: 10.1172/JCI4853.

[144] C. L. Nemeth, K. Janebodin, A. E. Yuan, J. E. Dennis, M. Reyes, and D.-H. Kim. Enhanced Chondrogenic Differentiation of Dental Pulp Stem Cells Using Nanopatterned PEG-GelMA-HA Hydrogels. *Tissue Engineering Part A*, 20(21-22): 2817–2829, 2014. ISSN 1937-3341. doi: 10.1089/ten.tea.2013.0614.

[145] M. Nickien, A. Thambyah, and N. D. Broom. How a decreased fibrillar interconnectivity influences stiffness and swelling properties during early cartilage degeneration. *Journal of the Mechanical Behavior of Biomedical Materials*, 75:390–398, 2017. ISSN 18780180. doi: 10.1016/j.jmbbm.2017.07.042.

[146] T. L. Norman, D. Vashishth, and D. B. Burr. Fracture toughness of human bone under tension. *Journal of Biomechanics*, 28(3), 1995. ISSN 00219290. doi: 10.1016/0021-9290(94)00069-G.

[147] I. T. Norton, D. A. Jarvis, and T. J. Foster. A molecular model for the formation and properties of fluid gels. *Int J Biol Macromol*, 26(4):255–261, 1999.

[148] I. T. Norton, W. J. Frith, and S. Ablett. Fluid gels, mixed fluid gels and satiety. *Food Hydrocolloids*, 20:229–239, 2006. doi: 10.1016/j.foodhyd.2004.03.011.

[149] E. M. Obeid, M. A. Adams, and J. H. Newman. Mechanical properties of articular cartilage in knees with unicompartmental osteoarthritis. *The Journal of Bone and Joint Surgery. British Volume*, 76(2):315–319, 1994. ISSN 0301-620X.

[150] J. T. Oliveira, T. C. Santos, L. Martins, M. A. Silva, A. P. Marques, A. G. Castro, N. M. Neves, and R. L. Reis. Performance of new gellan gum hydrogels combined with human articular chondrocytes for cartilage regeneration when subcutaneously implanted in nude mice. *Journal of Tissue Engineering and Regenerative Medicine*, 3(7):493–500, 2009. ISSN 19326254. doi: 10.1002/term.184.

[151] J. T. Oliveira, T. C. Santos, L. Martins, R. Picciochi, A. P. Marques, A. G. Castro, N. M. Neves, J. F. Mano, and R. L. Reis. Gellan Gum Injectable Hydrogels for Cartilage Tissue Engineering Applications: In Vitro Studies and Preliminary In Vivo Evaluation. *Tissue Engineering Part A*, 16(1):343–353, 2010. ISSN 1937-335X. doi: 10.1089/ten.tea.2009.0117.

[152] M. Otero, M. Favero, C. Dragomir, K. E. Hachem, K. Hashimoto, D. A. Plumb, and M. B. Goldring. Human chondrocyte cultures as models of cartilage-specific gene regulation. *Methods Mol Biol*, 806:301–336, 2012. doi: 10.1007/978-1-61779-367-721.

[153] L. Ouyang, C. B. Highley, C. B. Rodell, W. Sun, and J. A. Burdick. 3D Printing of Shear-Thinning Hyaluronic Acid Hydrogels with Secondary Cross-Linking. *ACS Biomaterials Science and Engineering*, 2(10):1743–1751, 2016. ISSN 23739878. doi: 10.1021/acsbiomaterials.6b00158.

[154] L. Ouyang, C. B. Highley, W. Sun, and J. A. Burdick. A Generalizable Strategy for the 3D Bioprinting of Hydrogels from Nonviscous Photo-crosslinkable Inks. *Advanced Materials*, 29(8), 2017. ISSN 15214095. doi: 10.1002/adma.201604983.

[155] K. T. Paige, L. G. Cima, M. J. Yaremchuk, B. L. Schloo, J. P. Vacanti, and C. A. Vacanti. De Novo Cartilage Generation Using Calcium Alginate-Chondrocyte Constructs. *Plastic & Reconstructive Surgery*, 97(1):168–178, 1996.

[156] C. Palazzo, C. Nguyen, M. M. Lefevre-Colau, F. Rannou, and S. Poiraudeau. Risk factors and burden of osteoarthritis. *Annals of Physical and Rehabilitation Medicine*, 59(3):134–138, 2016. ISSN 18770665. doi: 10.1016/j.rehab.2016.01.006.

[157] V. A. Parfenov, E. V. Koudan, E. A. Bulanova, and P. A. Karalkin. Biofabrication Technology Using Magnetic Levitational Assembly Using Magnetic Levitational Assembly. *Biofabrication*, 10, 2018.

[158] H. Park, S. W. Kang, B. S. Kim, D. J. Mooney, and K. Y. Lee. Shear-reversibly crosslinked alginate hydrogels for tissue engineering. *Macromolecular Bioscience*, 9 (9):895–901, sep 2009. ISSN 16165187. doi: 10.1002/mabi.200800376.

[159] S. Park and G. A. Ateshian. Dynamic response of immature bovine articular cartilage in tension and compression, and nonlinear viscoelastic modeling of the tensile response. *Journal of biomechanical engineering*, 128(4):623–30, 2006. ISSN 0148-0731. doi: 10.1115/1.2206201.

[160] A. D. Pearle, R. F. Warren, and S. A. Rodeo. Basic science of articular cartilage and osteoarthritis. *Clinics in Sports Medicine*, 24(1):1–12, 2005. ISSN 02785919. doi: 10.1016/j.csm.2004.08.007.

[161] B. Pearson and D. M. Espino. Effect of hydration on the frequency-dependent viscoelastic properties of articular cartilage. *Proceedings of the Institution of Mechanical Engineers, Part H: Journal of Engineering in Medicine*, 227(11):1246–1252, 2013. ISSN 09544119. doi: 10.1177/0954411913501294.

[162] M. J. Pearson, D. Herndler-Brandstetter, M. A. Tariq, T. A. Nicholson, A. M. Philp, H. L. Smith, E. T. Davis, S. W. Jones, and J. M. Lord. IL-6 secretion in osteoarthritis patients is mediated by chondrocyte-synovial fibroblast cross-talk and

is enhanced by obesity. *Scientific Reports*, 7(1):3451, 2017. ISSN 20452322. doi: 10.1038/s41598-017-03759-w.

[163] D. R. Pereira, R. F. Canadas, J. Silva-Correia, A. P. Marques, R. L. Reis, and J. M. Oliveira. Gellan Gum-Based Hydrogel Bilayered Scaffolds for Osteochondral Tissue Engineering. *Key Engineering Materials*, 587:255–260, 2013. ISSN 1662-9795. doi: 10.4028/www.scientific.net/KEM.587.255.

[164] A. E. Peters, R. Akhtar, E. J. Comerford, and K. T. Bates. The effect of ageing and osteoarthritis on the mechanical properties of cartilage and bone in the human knee joint. *Scientific Reports*, 8(1):1–13, 2018. ISSN 20452322. doi: 10.1038/s41598-018-24258-6.

[165] A. M. Philp, R. L. Collier, L. M. Grover, E. T. Davis, and S. W. Jones. Resistin promotes the abnormal Type I collagen phenotype of subchondral bone in obese patients with end stage hip osteoarthritis. *Scientific Reports*, 7(1):4042, 2017. ISSN 20452322. doi: 10.1038/s41598-017-04119-4.

[166] A. M. Philp, E. T. Davis, and S. W. Jones. Developing anti-inflammatory therapeutics for patients with osteoarthritis. *Rheumatology (Oxford, England)*, 56:869–891, 2017. doi: 10.1093/rheumatology/kew278.

[167] C. A. Poole, M. H. Flint, and B. W. Beaumont. Chondrons extracted from canine tibial cartilage: Preliminary report on their isolation and structure. *Journal of Orthopaedic Research*, 6(3):408–419, 1988. ISSN 1554527X. doi: 10.1002/jor.1100060312.

[168] C. A. Poole, T. T. Glant, and J. R. Schofield. Chondrons from articular cartilage. (IV) Immunolocalization of proteoglycan epitopes in isolated canine tibial chondrons. *Journal of Histochemistry and Cytochemistry*, 39(9):1175–1187, 1991. ISSN 00221554. doi: 10.1177/39.9.1717545.

[169] C. A. Poole, R. T. Gilbert, D. Herbage, and D. J. Hartmann. Immunolocalization of type IX collagen in normal and spontaneously osteoarthritic canine tibial cartilage and isolated chondrons. *Osteoarthritis and Cartilage*, 5(3):191–204, 1997. ISSN 10634584. doi: 10.1016/S1063-4584(97)80014-3.

[170] N. Presle, P. Pottie, H. Dumond, C. Guillaume, F. Lapicque, S. Pallu, D. Mainard, P. Netter, and B. Terlain. Differential distribution of adipokines between serum and synovial fluid in patients with osteoarthritis. Contribution of joint tissues to their articular production. *Osteoarthritis and Cartilage*, 14(7):690–695, 2006. ISSN 10634584. doi: 10.1016/j.joca.2006.01.009.

[171] M. Racila and J. M. Crolet. Nano and macro structure of cortical bone: Numerical investigations. *Mechanics of Advanced Materials and Structures*, 14(8):655–663, 2007. ISSN 15376494. doi: 10.1080/15376490701673193.

[172] L. Rackwitz, F. Djouad, S. Janjanin, U. Nöth, and R. S. Tuan. Functional cartilage repair capacity of de-differentiated, chondrocyte- and mesenchymal stem cell-laden hydrogels in vitro. *Osteoarthritis and Cartilage*, 22(8):1148–1157, 2014. ISSN 15229653. doi: 10.1016/j.joca.2014.05.019.

[173] E. Radin, K. Yang, C. Riegger, V. Kish, and J. O'Connor. Relationship between lower limb dynamics and knee joint pain. *Journal of Orthopaedic Research*, 9:398–405, 1991.

[174] R. A. Rahman, M. A. A. Radzi, N. M. Sukri, N. M. Nazir, and M. Sha'ban. Tissue engineering of articular cartilage: From bench to bed-side. *Tissue Engineering and Regenerative Medicine*, 12(1):1–11, 2014. ISSN 22125469. doi: 10.1007/s13770-014-9044-8.

[175] X. Ren, V. Tu, D. Bischoff, D. W. Weisgerber, M. S. Lewis, D. T. Yamaguchi, T. A. Miller, B. A. Harley, and J. C. Lee. Nanoparticulate mineralized collagen scaffolds induce in vivo bone regeneration independent of progenitor cell loading or exogenous growth factor stimulation. *Biomaterials*, 89:67–78, 2016. ISSN 18785905. doi: 10.1016/j.biomaterials.2016.02.020.

[176] N. Reznikov, R. Shahar, and S. Weiner. Three-dimensional structure of human lamellar bone: the presence of two different materials and new insights into the hierarchical organization. *Bone*, 59:93–104, 2014.

[177] N. Reznikov, R. Shahar, and S. Weiner. Bone hierarchical structure in three dimensions. In *Acta Biomaterialia*, number 10, pages 3815–3826, 2014. ISBN 1742-7061. doi: 10.1016/j.actbio.2014.05.024.

[178] F. Richard, M. Villars, and S. Thibaud. Viscoelastic modeling and quantitative experimental characterization of normal and osteoarthritic human articular cartilage using indentation. *Journal of the Mechanical Behavior of Biomedical Materials*, 24: 41–52, 2013. ISSN 17516161. doi: 10.1016/j.jmbbm.2013.04.012.

[179] S. Roberts, B. Weightman, J. Urban, and D. Chappell. Mechanical and biochemical properties of human articular cartilage in osteoarthritic femoral heads and in autopsy specimens. *Clinical Biomechanics*, 1(4):233, 1986. ISSN 02680033. doi: 10.1016/0268-0033(86)90152-X.

[180] S. Roberts, J. Menage, L. J. Sandell, E. H. Evans, and J. B. Richardson. Immunohistochemical study of collagen types I and II and procollagen IIA in human cartilage repair tissue following autologous chondrocyte implantation. *Knee*, 16(5): 398–404, 2009. ISSN 09680160. doi: 10.1016/j.knee.2009.02.004.

[181] D. L. Robinson, M. E. Kersh, N. C. Walsh, D. C. Ackland, R. N. de Steiger, and M. G. Pandy. Mechanical properties of normal and osteoarthritic human articular cartilage. *Journal of the Mechanical Behavior of Biomedical Materials*, 61:96–109, 2016. ISSN 17516161. doi: 10.1016/j.jmbbm.2016.01.015.

[182] S. Ronken, M. P. Arnold, H. Ardura García, A. Jeger, A. U. Daniels, and D. Wirz. A comparison of healthy human and swine articular cartilage dynamic indentation mechanics. *Biomechanics and Modeling in Mechanobiology*, 11(5):631–639, 2012. ISSN 16177959. doi: 10.1007/s10237-011-0338-7.

[183] H. H. Roseberry, A. B. Hastings, and J. K. Morse. X-ray analysis of bone and teeth. *Journal of Biological Chemistry*, 90(2):395–407, 1931. ISSN 0021-9258.

[184] H. Sadeghi, B. Lawless, D. Espino, and D. Shepherd. Effect of frequency on crack growth in articular cartilage. *Journal of the Mechanical Behavior of Biomedical Materials*, 77:40–46, 2018. ISSN 17516161. doi: 10.1016/j.jmbbm.2017.08.036.

[185] K. Saha, J. F. Pollock, D. V. Schaffer, and K. E. Healy. Designing synthetic materials to control stem cell phenotype. *Current Opinion in Chemical Biology*, 11(4):381–387, 2007. ISSN 13675931. doi: 10.1016/j.cbpa.2007.05.030.

[186] S. Samavedi and N. Joy. 3D printing for the development of in vitro cancer models. *Current Opinion in Biomedical Engineering*, 2:35–42, 2017. ISSN 24684511. doi: 10.1016/j.cobme.2017.06.003.

[187] S. Samavedi, P. Diaz-Rodriguez, J. D. Erndt-Marino, and M. Hahn. A 3D chondrocyte-macrophage co-culture system to probe inflammation in experimental osteoarthritis. *Tissue Engineering Part A*, page ten.TEA.2016.0007, 2016. ISSN 1937-3341. doi: 10.1089/ten.TEA.2016.0007.

[188] S. Samavedi, P. Diaz-Rodriguez, J. D. Erndt-Marino, and M. S. Hahn. A Three-Dimensional Chondrocyte-Macrophage Coculture System to Probe Inflammation in Experimental Osteoarthritis. *Tissue Engineering Part A*, 23(3-4):101–114, 2017. ISSN 1937-3341. doi: 10.1089/ten.tea.2016.0007.

[189] J. Sanchez-Adams, H. A. Leddy, A. L. McNulty, C. J. O'Conor, and F. Guilak. The mechanobiology of articular cartilage: bearing the burden of osteoarthritis. *Current*

rheumatology reports, 16(10):451, 2014. ISSN 15346307. doi: 10.1007/s11926-014-0451-6.

[190] R. E. Saunders, J. E. Gough, and B. Derby. Delivery of human fibroblast cells by piezoelectric drop-on-demand inkjet printing. *Biomaterials*, 29(2):193–203, 2008. ISSN 01429612. doi: 10.1016/j.biomaterials.2007.09.032.

[191] J. T. Schantz, A. Brandwood, D. W. Hutmacher, H. L. Khor, and K. Bittner. Osteogenic differentiation of mesenchymal progenitor cells in computer designed fibrin-polymer-ceramic scaffolds manufactured by fused deposition modeling. *Journal of Materials Science: Materials in Medicine*, 16(9):807–819, 2005. ISSN 09574530. doi: 10.1007/s10856-005-3584-3.

[192] E. Schuh, S. Hofmann, K. Stok, H. Notbohm, R. Müller, and N. Rotter. Chondrocyte redifferentiation in 3D: The effect of adhesion site density and substrate elasticity. *Journal of Biomedical Materials Research - Part A*, 100 A(1):38–47, 2012. ISSN 15493296. doi: 10.1002/jbm.a.33226.

[193] B. L. Schumacher, J. A. Block, T. M. Schmid, M. B. Aydelotte, and K. E. Kuettner. A novel proteoglycan synthesized and secreted by chondrocytes of the superficial zone of articular cartilage. *Archives of Biochemistry and Biophysics*, 311(1):144–152, 1994. ISSN 00039861. doi: 10.1006/abbi.1994.1219.

[194] B. L. Schumacher, C. E. Hughes, K. E. Kuettner, B. Caterson, and M. B. Aydelotte. Immunodetection and partial cDNA sequence of the proteoglycan, superficial zone protein, synthesized by cells lining synovial joints. *Journal of Orthopaedic Research*, 17(1):110–120, 1999. ISSN 07360266. doi: 10.1002/jor.1100170117.

[195] W. Schuurman, P. A. Levett, M. W. Pot, P. R. van Weeren, W. J. Dhert, D. W. Hutmacher, F. P. Melchels, T. J. Klein, and J. Malda. Gelatin-methacrylamide hydrogels as potential biomaterials for fabrication of tissue-engineered cartilage constructs. *Macromolecular Bioscience*, 13(5):551–561, 2013. ISSN 16165187. doi: 10.1002/mabi.201200471.

[196] L. A. Setton, W. Zhu, and V. C. Mow. The biphasic poroviscoelastic behavior of articular cartilage: Role of the surface zone in governing the compressive behavior. *Journal of Biomechanics*, 26(4-5):581–592, 1993. ISSN 00219290. doi: 10.1016/0021-9290(93)90019-B.

[197] L. A. Setton, D. M. Elliott, and V. C. Mow. Altered mechanics of cartilage with osteoarthritis: Human osteoarthritis and an experimental model of joint de-

generation. *Osteoarthritis and Cartilage*, 7(1):2–14, 1999. ISSN 10634584. doi: 10.1053/joca.1998.0170.

[198] E. J. Sheehy, T. Vinardell, C. T. Buckley, and D. J. Kelly. Engineering osteochondral constructs through spatial regulation of endochondral ossification. *Acta Biomaterialia*, 9(3):5484–5492, 2013. ISSN 17427061. doi: 10.1016/j.actbio.2012.11.008.

[199] D. E. T. Shepherd and B. B. Seedhom. Thickness of human articular cartilage in joints of the lower limb. *Annals of the Rheumatic Diseases*, 58(1):27–34, 1999. ISSN 0003-4967. doi: 10.1136/ard.58.1.27.

[200] G. D. Smith, G. Knutsen, and J. B. Richardson. A clinical review of cartilage repair techniques. *J Bone Joint Surg Am.*, 87(4):715–24., 2005. ISSN 0301-620X. doi: 10.1302/0301-620X.87B4.15971.

[201] G. Sohár, E. Pallagi, P. Szabó-Révész, and K. Tóth. New thermogravimetric protocol for the investigation of normal and damaged human hyaline cartilage. *Journal of Thermal Analysis and Calorimetry*, 89(3):853–856, 2007. ISSN 13886150. doi: 10.1007/s10973-007-8256-8.

[202] A. J. Sophia Fox, A. Bedi, and S. A. Rodeo. The basic science of articular cartilage: structure, composition, and function. *Sports Health*, 1(6):461–468, 2009. doi: 10.1177/1941738109350438.

[203] A. Spyropoulou, K. Karamesinis, and E. K. Basdra. Mechanotransduction pathways in bone pathobiology. *Biochimica et biophysica acta*, 1852(9):1700–1708, 2015. ISSN 0006-3002. doi: 10.1016/j.bbadis.2015.05.010.

[204] J. R. Steadman, W. G. Rodkey, S. B. Singleton, and K. K. Briggs. Microfracture technique for full-thickness chondral defects: Technique and clinical results. *Operative Techniques in Orthopaedics*, 7(4):300–304, 1997. ISSN 10486666. doi: 10.1016/S1048-6666(97)80033-X.

[205] D. G. C. A. B. Steele and D. G. C. A. B. Steele. *The Anatomy and Biology of the Human Skeleton*. Texas A & M University Press, 1988. ISBN 0-89096-300-2.

[206] J. P. Stegemann, H. Hong, R. M. Nerem, P. Jan, and R. M. N. Mechanical. Mechanical , biochemical , and extracellular matrix effects on vascular smooth muscle cell phenotype. *J Appl Physiol*, 98:2321–2327, 2005. doi: 10.1152/japplphysiol.01114.2004.

[207] J. Stringer and B. Derby. Formation and stability of lines produced by inkjet printing. *Langmuir*, 26(12):10365–10372, 2010. ISSN 07437463. doi: 10.1021/la101296e.

[208] J. Sun and H. Tan. Alginate-based biomaterials for regenerative medicine applications. *Materials*, 6(4):1285–1309, 2013. ISSN 19961944. doi: 10.3390/ma6041285.

[209] N. SundarRaj, D. Fite, S. Ledbetter, S. Chakravarti, and J. R. Hassell. Perlecan is a component of cartilage matrix and promotes chondrocyte attachment. *Journal of cell science*, 108:2663–2672, 1995. ISSN 0021-9533. doi: 10.1038/2151376A0.

[210] E. Tamjid, M. Rezaei, Y. Akhtari, A. Ehsandoost, and B. Samavati. A Review on Total Hip Joint Arthroplasty : Prosthesis Design and Clinical Trials. *Journal of Applied Tissue Engineering*, 5(2), 2018.

[211] D. Taniguchi, K. Matsumoto, T. Tsuchiya, R. MacHino, Y. Takeoka, A. Elgalad, K. Gunge, K. Takagi, Y. Taura, G. Hatachi, N. Matsuo, N. Yamasaki, K. Nakayama, and T. Nagayasu. Scaffold-free trachea regeneration by tissue engineering with bio-3D printing. *Interactive Cardiovascular and Thoracic Surgery*, 26(5):745–752, 2018. ISSN 15699285. doi: 10.1093/icvts/ivx444.

[212] D. K. Temple, A. A. Cederlund, B. M. Lawless, R. M. Aspden, and D. M. Espino. Viscoelastic properties of human and bovine articular cartilage: a comparison of frequency-dependent trends. *BMC Musculoskeletal Disorders*, 17;419, 2016. doi: 10.1186/s12891-016-1279-1.

[213] J. T. Thomas, S. Ayad, and M. E. Grant. Cartilage collagens: Strategies for the study of their organisation and expression in the extracellular matrix. *Annals of the Rheumatic Diseases*, 53(8):488–496, 1994. ISSN 00034967. doi: 10.1136/ard.53.8.488.

[214] D. P. Tonge, M. J. Pearson, and S. W. Jones. The hallmarks of osteoarthritis and the potential to develop personalised disease-modifying pharmacological therapeutics. *Osteoarthritis and Cartilage*, 22(5):609–621, 2014. ISSN 15229653. doi: 10.1016/j.joca.2014.03.004.

[215] P. A. Torzilli. Effects of temperature, concentration and articular surface removal on transient solute diffusion in articular cartilage. *Medical & biological engineering & computing*, pages S93–8, 1993. ISSN 0140-0118. doi: 10.1007/BF02446656.

[216] K. Tóth, G. Sohár, E. Pallagi, and P. Szabó-Révész. Further characterization of degenerated human cartilage with differential scanning calorimetry. *Thermochimica Acta*, 464(1-2):75–77, 2007. ISSN 00406031. doi: 10.1016/j.tca.2007.07.013.

[217] M. H. van den Bosch. Inflammation in osteoarthritis: is it time to dampen the alarm-in this debilitating disease? *Clinical & Experimental Immunology*, 2018. ISSN 00099104. doi: 10.1111/cei.13237.

[218] H. Vasiliadis and J. Wasiak. Autologous chondrocyte implantation for full thickness articular cartilage defects of the knee. *Cochrane Database of Systemic Reviews*, (10): 1–61, 2011. doi: 10.1002/14651858.CD003323.

[219] B. M. Vertel. The ins and outs of aggrecan. *Trends in Cell Biology*, 5(12):458–464, 1995. ISSN 09628924. doi: 10.1016/S0962-8924(00)89115-1.

[220] A. Verteramo and B. B. Seedhom. Effect of a single impact loading on the structure and mechanical properties of articular cartilage. *Journal of Biomechanics*, 40(16): 3580–3589, 2007. ISSN 00219290.

[221] A. Vidal-Lesso, E. Ledesma-Orozco, L. Daza-Benítez, and R. Lesso-Arroyo. Mechanical Characterization of Femoral Cartilage Under Unicompartimental Osteoarthritis. *Ingenieria mechanica technologia y desarrollo*, 4(6):239–246, 2014. ISSN 1665-7381.

[222] C. A. Vilela, C. Correia, J. M. Oliveira, R. A. Sousa, J. Espregueira-Mendes, and R. L. Reis. Cartilage Repair Using Hydrogels: A Critical Review of in Vivo Experimental Designs. *ACS Biomaterials Science & Engineering*, 1(9):726–739, 2015. ISSN 2373-9878. doi: 10.1021/acsbiomaterials.5b00245.

[223] R. A. Vindas Bolaños, S. M. Cokelaere, J. M. Estrada McDermott, K. E. Benders, U. Gbureck, S. G. Plomp, H. Weinans, J. Groll, P. R. van Weeren, and J. Malda. The use of a cartilage decellularized matrix scaffold for the repair of osteochondral defects: the importance of long-term studies in a large animal model. *Osteoarthritis and Cartilage*, 25(3):413–420, 2017. ISSN 15229653. doi: 10.1016/j.joca.2016.08.005.

[224] J. Visser, P. A. Levett, N. C. te Moller, J. Besems, K. W. Boere, M. H. van Rijen, J. C. de Grauw, W. J. Dhert, P. R. van Weeren, and J. Malda. Crosslinkable hydrogels derived from cartilage, meniscus, and tendon tissue. *Tissue Eng Part A*, 21(7-8):1195–1206, 2015. doi: 10.1089/ten.TEA.2014.0362.

[225] T. Vos, A. D. Flaxman, M. Naghavi, R. Lozano, C. Michaud, M. Ezzati, K. Shibuya, J. A. Salomon, A. D. Lopez, and C. J. Murray. Years lived with disability (YLDs) for 1160 sequelae of 289 diseases and injuries 19902010: a systematic analysis for the Global Burden of Disease Study 2010. *The Lancet*, 380(9859):2163–2196, 2012. ISSN 0140-6736. doi: 10.1016/S0140-6736(12)61729-2.

[226] S. Wang, J. M. Lee, and W. Y. Yeong. Smart hydrogels for 3D bioprinting. Smart hydrogels for 3D bioprinting. *International Journal of Bioprinting*, 1(1):3–14, 2015. doi: 10.18063/IJB.2015.01.005.

[227] U. G. Wegst, H. Bai, E. Saiz, A. P. Tomsia, and R. O. Ritchie. Bioinspired structural materials. *Nature Materials*, 14(1):23–36, 2015. ISSN 14764660. doi: 10.1038/nmat4089.

[228] M. Wehner, R. L. Truby, D. J. Fitzgerald, B. Mosadegh, G. M. Whitesides, J. A. Lewis, and R. J. Wood. An integrated design and fabrication strategy for entirely soft, autonomous robots. *Nature*, 536(7617):451–455, 2016. ISSN 14764687. doi: 10.1038/nature19100.

[229] S. Weiner and H. D. Wagner. THE MATERIAL BONE: Structure-Mechanical Function Relations. *Annual Review of Materials Science*, 28(1):271–298, 1998. ISSN 0084-6600. doi: 10.1146/annurev.matsci.28.1.271.

[230] S. Weiner, W. Traub, and H. D. Wagner. Lamellar bone: Structure-function relations. *Journal of Structural Biology*, 126(3):241–255, 1999. ISSN 10478477. doi: 10.1006/jsbi.1999.4107.

[231] A. M. Weinstein, B. N. Rome, W. M. Reichmann, J. E. Collins, S. A. Burbine, T. S. Thornhill, J. Wright, J. N. Katz, and E. Losina. Estimating the Burden of Total Knee Replacement in the United States. *The Journal of Bone and Joint Surgery-American Volume*, 95(5):385–392, 2013. ISSN 0021-9355. doi: 10.2106/JBJS.L.00206.

[232] R. E. Wilusz, L. E. DeFrate, and F. Guilak. A biomechanical role for perlecan in the pericellular matrix of articular cartilage. *Matrix Biology*, 31(6):320–327, 2012. ISSN 0945053X. doi: 10.1016/j.matbio.2012.05.002.

[233] R. E. Wilusz, J. Sanchez-Adams, and F. Guilak. The structure and function of the pericellular matrix of articular cartilage. *Matrix Biology*, 39:25–32, 2014. ISSN 15691802. doi: 10.1016/j.matbio.2014.08.009.

[234] P. M. Wrobel, S. Bała, M. Czyzycki, M. Golasik, T. Librowski, B. Ostachowicz, W. Piekoszewski, A. Surïwka, and M. Lankosz. Combined micro-XRF and TXRF methodology for quantitative elemental imaging of tissue samples. *Talanta*, 162: 654–659, 2017. ISSN 00399140. doi: 10.1016/j.talanta.2016.10.043.

[235] W. Wu, R. C. Billinghurst, I. Pidoux, J. Antoniou, D. Zukor, M. Tanzer, and A. R. Poole. Sites of collagenase cleavage and denaturation of type II collagen in aging and

osteoarthritic articular cartilage and their relationship to the distribution of matrix metalloproteinase 1 and matrix metalloproteinase 13. *Arthritis and Rheumatism*, 46(8):2087–2094, 2002. ISSN 00043591. doi: 10.1002/art.10428.

[236] W. Wu, A. Deconinck, and J. A. Lewis. Omnidirectional printing of 3D microvascular networks. *Advanced Materials*, 23(24):178–183, 2011. ISSN 09359648. doi: 10.1002/adma.201004625.

[237] F. M. Wunner, M. L. Wille, T. G. Noonan, O. Bas, P. D. Dalton, E. M. De-Juan-Pardo, and D. W. Hutmacher. Melt Electrospinning Writing of Highly Ordered Large Volume Scaffold Architectures. *Advanced Materials*, 30(20):1–6, 2018. ISSN 15214095. doi: 10.1002/adma.201706570.

[238] T. Xu, K. W. Binder, M. Z. Albanna, D. Dice, W. Zhao, J. J. Yoo, and A. Atala. Hybrid printing of mechanically and biologically improved constructs for cartilage tissue engineering applications. *Biofabrication*, 5(1), 2013. ISSN 17585082. doi: 10.1088/1758-5082/5/1/015001.

[239] L.-P. Yan, J. M. Oliveira, A. L. Oliveira, and R. L. Reis. Current Concepts and Challenges in Osteochondral Tissue Engineering and Regenerative Medicine. *ACS Biomaterials Science & Engineering*, page 150220124046001, 2015. ISSN 2373-9878. doi: 10.1021/ab500038y.

[240] F. Yang, R. Murugan, S. Wang, and S. Ramakrishna. Electrospinning of nano/micro scale poly(l-lactic acid) aligned fibers and their potential in neural tissue engineering. *Biomaterials*, 26(15):2603–2610, 2005. ISSN 01429612. doi: 10.1016/j.biomaterials.2004.06.051.

[241] J. Q. Yao and B. B. Seedhom. Mechanical Conditioning of Articular Cartilage To Prevalent Stresses. *British Journal of Rheumatology*, 32:956–965, 1993.

[242] I. Zein, D. W. Hutmacher, K. C. Tan, and S. H. Teoh. Fused deposition modeling of novel scaffold architectures for tissue engineering applications. *Biomaterials*, 23 (4):1169–1185, 2002. ISSN 01429612. doi: 10.1016/S0142-9612(01)00232-0.

[243] C. H. Zheng and M. E. Levenston. Fact versus artifact: Avoiding erroneous estimates of sulfated glycosaminoglycan content using the dimethylmethylene blue colorimetric assay for tissue-engineered constructs. *European Cells and Materials*, 29:224–236, 2015. ISSN 14732262. doi: 10.22203/eCM.v029a17.

[244] X. Zhou, M. Nowicki, H. Cui, W. Zhu, X. Fang, S. Miao, S. J. Lee, M. Keidar, and L. G. Zhang. 3D bioprinted graphene oxide-incorporated matrix for promoting chondrogenic differentiation of human bone marrow mesenchymal stem cells. *Carbon*, 116:615–624, 2017. ISSN 00086223. doi: 10.1016/j.carbon.2017.02.049.

[245] N. Zoeger, P. Roschger, J. G. Hofstaetter, C. Jokubonis, G. Pepponi, G. Falkenberg, P. Fratzl, A. Berzlanovich, W. Osterode, C. Streli, and P. Wobrauschek. Lead accumulation in tidemark of articular cartilage. *Osteoarthritis and Cartilage*, 14(9): 906–913, 2006. ISSN 10634584. doi: 10.1016/j.joca.2006.03.001.

APPENDIX A

CHAPTER 3 SUPPLEMENTARY MATERIAL

Frequency (Hz)	**Healthy n=22**	**OA n=37**	**p**
1	32.50 ±1.60	28.74 ±0.98	0.039
8	35.63 ±1.74	31.63 ±1.08	0.043
10	36.26 ±1.77	32.13 ±1.09	0.040
12	36.93 ±1.82	32.74 ±1.11	0.041
29	38.84 ±1.91	34.42 ±1.16	0.040
49	40.29 ±1.99	35.76 ±1.21	0.043
71	41.13 ±2.01	36.63 ±1.25	0.050
88	42.03 ±2.10	37.52 ±1.30	0.058

Table A.1: Storage modulus mean ±SD and p-values

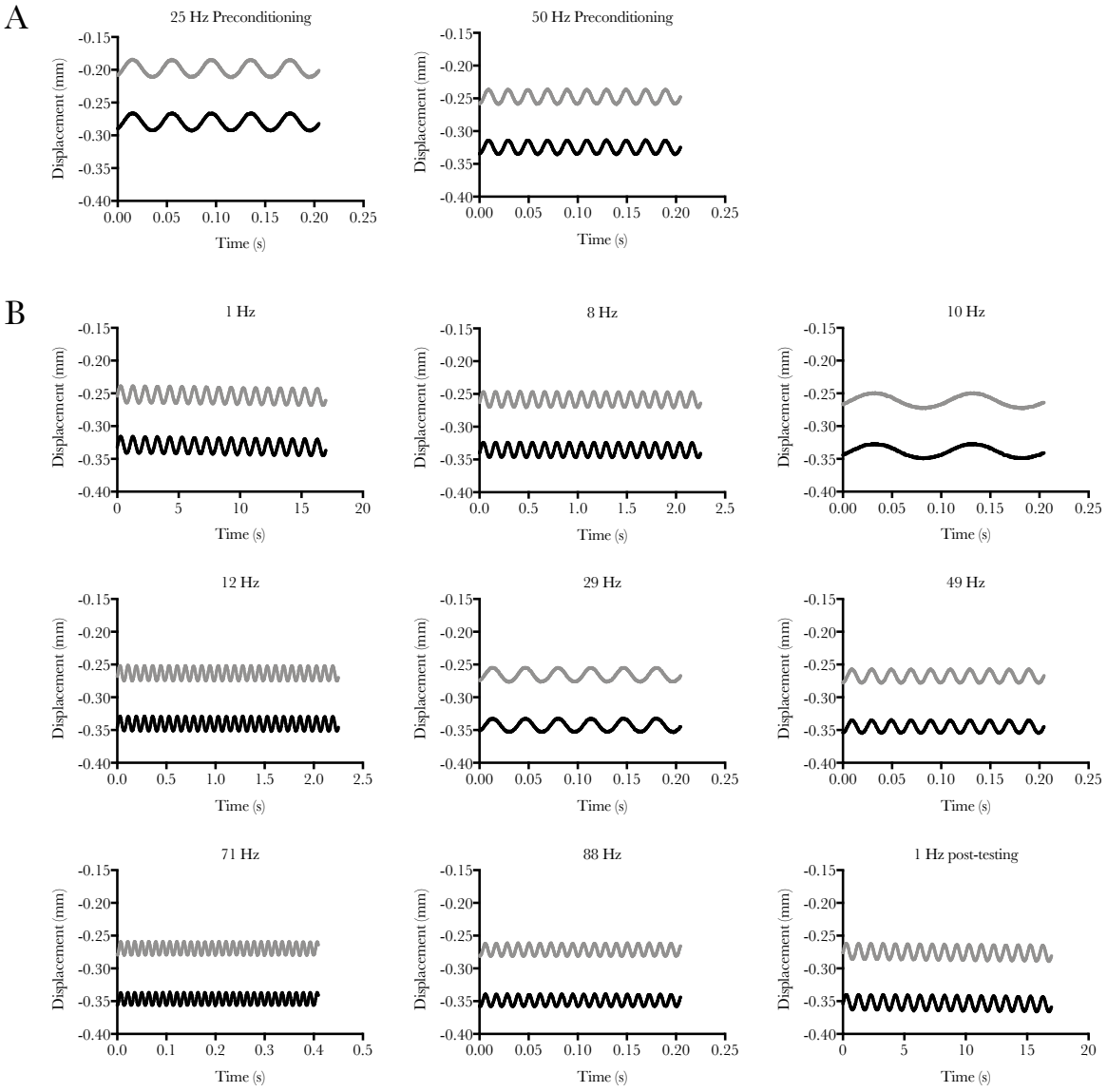

Figure A.1: Temporal displacement of OA (grey) and healthy (black) cartilage during A) preconditioning cycles and B) testing frequencies. For a representative healthy specimen, the displacement amplitude for 1 Hz at the beginning of cycling was 0.025 mm and for 1 Hz at the end of the testing was 0.022 mm. In this OA specimen, the displacement amplitude for 1 Hz was 0.024 mm at both the start and end of the testing protocol.

APPENDIX B

PUBLISHED PAPERS

ADVANCED MATERIALS
www.advmat.de

Structuring of Hydrogels across Multiple Length Scales for Biomedical Applications

*Megan E. Cooke, Simon W. Jones, Britt ter Horst, Naiem Moiemen, Martyn Snow, Gurpreet Chouhan, Lisa J. Hill, Maryam Esmaeli, Richard J. A. Moakes, James Holton, Rajpal Nandra, Richard L. Williams, Alan M. Smith, and Liam M. Grover**

The development of new materials for clinical use is limited by an onerous regulatory framework, which means that taking a completely new material into the clinic can make translation economically unfeasible. One way to get around this issue is to structure materials that are already approved by the regulator, such that they exhibit very distinct physical properties and can be used in a broader range of clinical applications. Here, the focus is on the structuring of soft materials at multiple length scales by modifying processing conditions. By applying shear to newly forming materials, it is possible to trigger molecular reorganization of polymer chains, such that they aggregate to form particles and ribbon-like structures. These structures then weakly interact at zero shear forming a solid-like material. The resulting self-healing network is of particular use for a range of different biomedical applications. How these materials are used to allow the delivery of therapeutic entities (cells and proteins) and as a support for additive layer manufacturing of larger-scale tissue constructs is discussed. This technology enables the development of a range of novel materials and structures for tissue augmentation and regeneration.

1. Introduction

Hydrogels are extensively used in regenerative medicine research as a consequence of their high-water content, meaning that they can be placed into a biological system without compromising viability.[1–3] Furthermore, given that they are formed from large, organic molecules, there is considerable scope for customizing the materials through modifications in the chemistry of the polymer backbone (the introduction of cell adhesion moieties, etc.), or by manipulating the gel cross-linking process.[4,5] The first application of encapsulation to protect mammalian cells was in the 1980s, to enable the delivery of pancreatic islets as a treatment for diabetes.[3] This has ultimately spawned a very active research field, where gels are often used for the delivery of cells or other therapeutics.[6–8] In the last ten years, gels have been used widely to study how cells are able to respond to their local environments, enabling ground-breaking work that not only starts to reveal how cell fate can be determined by tailoring stiffness,[9,10] the geometry of moieties distributed around the cells,[11,12] and the viscoelasticity of cell attachments/environments,[13] but can be exploited to synthesize unique delivery systems.[14,15] All of this points to the fact that there should be a panapoly of novel gel-based materials that are making their way to clinical application. Despite all of this progress, however, this is not the case and one of the major reasons for this is that new medical materials must pass a very large number of biological safety tests before they are used. In addition, materials to be used in clinical trials or for sale on the market must be supplied via a manufacturing process that is developed, validated, and operated in accordance with Good Manufacturing Practice (GMP). This requires engagement with appropriate GMP-licensed pharmaceutical/medical device manufacturing facilities. The use of bespoke chemistries and formulation conditions can preclude the use of processing methods and equipment that are standard to the pharmaceutical/medical device

M. E. Cooke, Dr. B. ter Horst, Prof. M. Snow, Dr. G. Chouhan, Dr. R. J. A. Moakes, Dr. J. Holton, Dr. R. Nandra, Dr. R. L. Williams, Prof. L. M. Grover
School of Chemical Engineering
University of Birmingham
Edgbaston, Birmingham B15 2TT, UK
E-mail: l.M.Grover@bham.ac.uk

M. E. Cooke, Dr. S. W. Jones
Institute of Inflammation and Ageing
MRC Musculoskeletal Ageing Centre
QE Hospital
University of Birmingham
Edgbaston, Birmingham B15 2TT, UK

Dr. B. ter Horst, Prof. N. Moiemen
Scar Free Foundation Centre for Burns Research
QE Hospital
University of Birmingham
Edgbaston, Birmingham B15 2TT, UK

Dr. L. J. Hill, M. Esmaeli
Institute of Inflammation and Ageing
University of Birmingham
Edgbaston, Birmingham B15 2TT, UK

Dr. A. M. Smith
Department of Pharmacy
University of Huddersfield
Queensgate, Huddersfield HD1 3DH, UK

DOI: 10.1002/adma.201705013

manufacturing industry. Thus, this furthers the increasing level of innovation required to develop a finished product. In many cases, this means that it is not economically viable to move these materials to the point of clinical trial and so clinical researchers tend to stick with a very small number of materials, which they use to deliver a multitude of therapeutic entities. In an attempt to take a much more rational approach to the use of hydrogels in clinical applications, we have pushed forward research on the structuring of materials that have already secured MHRA/EMA/FDA approval so that they can exhibit distinct physical properties. We have done this by modifying gelation conditions through the application of shear and by the absorption of reactive molecules into the gel structure in order to enable the formation of third phases within and between the gel particles. Although not completely void of the substantial costs required to deliver new therapeutic molecules, which require significant investment in toxicological and safety testing, the significant reduction gained from previously obtained data sets allows a more direct route to translation, which may result in higher degrees of adoption. Therefore, this paper summarizes the work that we have done in this area in the past few years and suggests areas for further research and development opportunities in the coming years.

2. Structuring Hydrogels by Shear—Formation of Fluid Gels

The diverse and controllable characteristics of gels, in particular hydrogels (water-based gels), have initiated great interest across a multitude of industries and applications. Within the field of biomedical research, many FDA/MHRA/EMA-approved synthetic polymers have been studied for their ability to form gelled networks.[16] However, more recently, there has been a push toward more natural biopolymers such as polysaccharides and sugar-based hydrogelators[17] for both their ready availability and frequent similarity to the extracellular matrix (ECM). It is of no surprise therefore, that polysaccharide hydrogels have become widely used in the field of tissue engineering: predominately used as scaffolds, presenting a mimetic of ECM with the intrinsic ability to stimulate growth and the formation of new tissue.[18]

Their key ability to structure large volumes while creating an elastic system arises through the material microstructure; where coupling of long, structurally regular chains forms intermolecular junction zones that pack in a fashion comparable to those of solid-state materials.[19] However, to better understand the origins of the macroscopic properties, it is necessary to consider structure–property relationships from the molecular level. It is common to distinguish protein structures at multiple levels of organization.[20] These descriptions are also apt for polysaccharides: the primary structure detailing the sugar chain sequence, secondary structure defining geometric arrangement (helices and ribbons), and tertiary structure highlighting the 3D association of secondary structures.[21] This structuring across the polymer chains leads to varying levels of chain associations during the disorder–order transition upon gelation. For example, in the case of carrageenan (a galactopyranose polymer), domains of linked helices (tertiary structures) are formed through intermolecular association, but further require ionic-mediation to develop a continuous gel structure (**Figure 1**ai).[22] Therefore, inevitably, the number and density of junctions formed in this way between polymer chains is a direct function of the final gel strength and elasticity.[23]

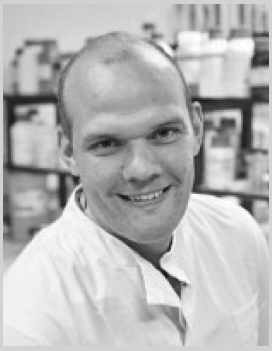

Liam M. Grover is the Director of the Healthcare Technology Research Institute at the University of Birmingham. He is a materials scientist by training and his research focuses on the interactions between materials and biological systems. He has a particular interest in controlling the assembly of the extracellular matrix as a means to enhance regeneration, prevent scarring and inhibit the pathological formation of bone. His group currently works on developing treatments for these conditions and translating these technologies to clinical settings.

This results in an array of material behaviors varying from strong gels, with relatively large moduli independent across a large range of frequencies, indicative of self-supporting structures, to weak maleable gels, where weakly associated chains lead to high-frequency sensitive systems with comparatively low moduli (Figure 1b).[24] However, the reliance on molecular configuration to achieve certain properties is a major problem, since when implanted or formed in situ the large number of other molecules that are present in the in vivo milieu interfere with these processes and can make them unpredictable. Such unpredictability is a significant barrier to clinical translation.

In an effort to produce more predictable systems, microgel suspensions known as "fluid" or "sheared" gels are being employed for their unique flow behaviors,[25] engineering the ability to self-structure post-shearing.[26–28] This presents a much more dynamic scaffold, which can be prepared exogenously for potential injection into the body.[29,30] Patented in 1990 as a system of microgels for use in food and cosmetics, derived upon shearing throughout gelation, fluid gels are substantially less rigid than their quiescently formed counterparts.[30] Shearing during the sol–gel transition results in networks of weakly flocculated, discrete gel entities (Figure 1aii), whereby particle sizes become dependent on the applied shear, and suspension rheology based on particle volume fractions.[31,32] However, in reality, such systems are more complicated, as interactions between particles on a mesoscopic level (structuring between particles) effectively dictate the bulk rheology of the systems. The particulate nature of these networks engenders a level of self-healing following manipulation, which is a key property that can be exploited in a number of biomedical applications.

The differences between quiescent gels and the properties of the microgels formed on shearing again lie in the microstructural changes upon gelation. One such example is the significantly reduced enthalpies of melting in carrageenan fluid

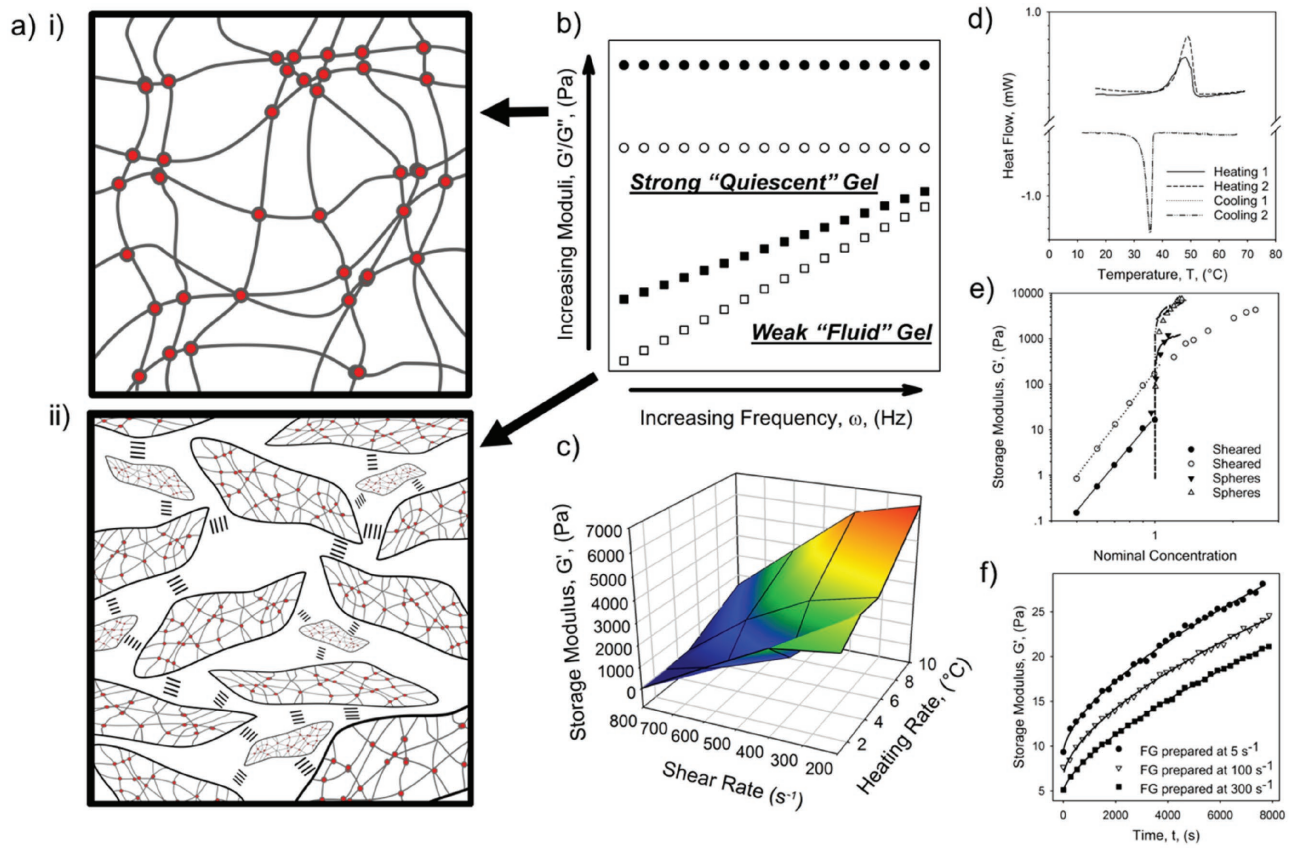

Figure 1. a) i) Schematic showing a typical gelled network where polymers interconnect to form junction zones (highlighted using red dots). ii) Diagram of a fluid/sheared gel system, where anisotropic gelled particles interact to form a weak continuous network. b) Idealized mechanical spectra showing G' and G'' dependency on frequency for both a strong "quiescent" and weak "fluid" gel system. c) 3D plot depicting the effects of processing on resulting suspension elastic response for protein fluid-gel particles. d) Differential scanning calorimetry (DSC) curves for carrageenan fluid gels. Note the change in peak height for the first and second melts, showing a change in degree of ordering between the fluid gel in the first heat and quiescent gel in the second heat. Adapted with permission.[34] Copyright 2012, Elsevier Ltd. e) Comparison of elastic moduli for sheared and spherical microgel systems: (●) 0.75% agar sheared gel, (○) 1.75% agar sheared gel, (▼) 2% agar microgel spheres, and (△) 5% agar microgel spheres. Trend lines show both power and Hertz fits to sheared and spherical systems respectively. Adapted with permission.[25] Copyright 2000, the Royal Society of Chemistry. f) Structuring as a function of time for carrageenan fluid gels (FG) prepared at various shear rates: (●) 5 s^{-1}, (▽) 100 s^{-1}, and (■) 300 s^{-1}. Reproduced with permission.[27] Copyright 2009, Elsevier Ltd.

gels when compared to their quiescent form (Figure 1d). Such data infers a heterogeneous polymer density across the gelled entities, with fewer ordered helices toward the particle peripheries.[33] This is not true for all polysaccharides however, as agar systems do not show such disparities.[32] Here, rapid gelation kinetics result in more uniform helical domains across the particles.[34,35] This suggests a mechanistic change in the microgel formation, driven by competition between two major factors: gelation kinetics and shear separation time/length scale (Figure 1c). Particle morphology also demonstrates a dependency on the competition between the two phenomena. In systems where gelation kinetics "k" greatly outweighs the time scale of separation "γ" ($k > \gamma$), rapid aggregation followed by subsequent shear breakdown develops large anisotropic morphologies. Whereas, in the counter case, $k < \gamma$, large shear forces confine growth, leading to more regular particles.[27] The consequential effects of such changes in particle morphology upon the aforementioned mesoscopic structuring have been clearly identified for both linear and nonlinear rheological properties. In the case of spherical particles, suspensions agree with Hertzian models resulting in elastic moduli arising through particle deformation, as systems become closely packed (Figure 1e).[25,36] Elastic response for anisotropic particles however, occurs at much lower volume fractions.[25] This is also reflected in the nonlinear measurements, with particles enhancing viscosities at volume fractions as low as $\Phi = 0.2$.[37] In these cases, large effective hydrodynamic volumes associated with anisotropic morphologies allow a vast degree of continuous phase to become structured by very few particles.[37–41]

Although some of the literature highlights the differences between quiescent and fluid gels, projecting the design rules in which to engineer systems with specific intrinsic properties, the actual nature of the interstitial space between particles is yet to be adequately defined. One theory proposes that disordered "hairy-like" polymers at the particle interfaces interlink to form a weak network between particles.[32] This may be the case for closely packed particles, where the interstitial layer is of the order of several hundred nanometers. However, an alternative explanation proposed here would be a combination of entropically driven structuring,[40,41] resulting in steric

confinement of particles, and/or weak electrostatic bridging between microgel interfaces at smaller length scales. Such a theory would encompass hysteretic effects, where self-structuring postshearing through entropic interweaving and electrostatic bridging, results in the observed recovery of an elastic network (Figure 1f).[26–28]

3. The Delivery of Biological Therapeutics Using Hydrogels

Many hydrogel materials have been used for the encapsulation and culture of cells in vitro, both for continued immunoisolation[42,43] and for the controlled delivery of biotherapeutics (both cells and proteins).[44–48] With the use of traditional "quiescently" gelled materials this can be very challenging, since gelation in a complex biological environment rich in ions and proteins can modify the kinetics of the gelation process and result in a material that gels unpredictably or behaves unpredictably following the gelation process – something that is completely unacceptable in a clinical environment. Up until relatively recently, there was also little consideration to how the local environment has a strong influence on the dynamic mechanical properties of these materials. Alginate, for example, is now known to lose mechanical integrity when placed into a physiological environment,[49,50] due to ion exchange of the divalent cations that enable the formation of "egg-box" junctions for monovalent ions such as sodium.[51] This causes the dispersion of the polymeric material and a loss of its ability to structure the surrounding liquid. This unpredictable behavior may explain why immunoisolation using polymers like alginate has proven ineffective when applied clinically, unless other polymers are incorporated as mechanically protective and permselective coatings.[42] What is also becoming very clear is that the materials are not "biologically inert", but rather provide subtle environmental cues that strongly drive cellular behavior. Initially, this was thought to be principally a consequence of the modulus of the materials,[9,10] but more recently reports have suggested that this can be modified by changing the distribution of grafted adhesion moieties and the nature of the interactions that may be formed with the polymer chain.[4,11,12] It has become clear that the level of entrapment that can be provided by the relatively stiff quiescently gelled matrix can have a significant influence on biological properties, including the capacity of cells to proliferate, maintain specific phenotypes or even secrete functional protein molecules as shown in **Figure 2**.[52–54]

3.1. Sheared/Fluid Gels as Delivery Agents

The shear processing of gels offers an additional degree of freedom for the production of cell and protein-delivery devices. From the perspective of handling, the reversible structural properties of fluid gels allow it to liquefy upon the application of shear, but may also be combined with biological fluids such as platelet-rich plasma or bone marrow aspirate and still thicken/solidify in situ. This is often very difficult to achieve with injectable hydrogels that solidify through a process of cross-linking, in situ. As such, fluid gels have the capacity to act as delivery agents for a great number of different cell and protein products (**Figure 3**).

Mesenchymal stem cells alone have been proposed to have beneficial effects in patients suffering a multitude of pathologies across body systems, including: the lungs,[55] brain,[56] musculoskeletal system,[57,58] peripheral nervous system,[59] skin,[60] and the heart.[61] Although some have reported that direct injection of these cells into the affected tissues can have beneficial therapeutic effects, the level of engraftment of the cells to the site of application typically ranges between only 1% and 10%,[62–65] and has been proposed to be as low as 0.001%.[66] As a result, the number of cells that are typically used in these therapies tend to be very large, ultimately creating the potential for carcinogenesis and other negative outcomes. The cost of such a treatment is, of course, considerable and as has been shown with autologous chondrocyte implantation (ACI), the clinical outcome and patient benefit over standard of care is unclear.[67,68] There are a number of ways to overcome these issues, which include the retention of the cells at the site of the implant within a material or through the use of cheaper autologous therapies. These are classified as minimal interventions by the regulator.

We have been able to develop materials for the repair and regeneration of cartilage, the cornea, and the skin that can be delivered in a way that is amenable to eventual clinical application. Through careful formulation, we have been able to produce materials that may be delivered using a range of different applicator technologies already used by clinicians, including cannulas/needles, sprays, and eyedroppers. Below, is a brief description of how we have used fluid gels to produce these therapeutics along with our progress in taking these to the point of clinical application. Furthermore, we have outlined major challenges that still need to be overcome in order to enable transition to the clinic. For each example, we have also outlined the clinical problems that we are attempting to address in order to place the technologies in context.

3.1.1. Cell Delivery for Cartilage Regeneration

Articular cartilage is a specialized avascular connective tissue layer covering the ends of bones that come together to form joints. It provides a smooth lubricated surface to minimize friction between the contact areas of the bones, and facilitates efficient load distribution through to the subchondral hard tissue. Chondrocytes, the sole cell type within cartilage, are sparsely distributed within a dense extracellular matrix that is mainly composed of collagen, water, proteoglycans, and glycoproteins. The high concentrations of hyaluronan and proteoglycan aggrecans allow for large volumes of aqueous medium to be entrapped within the matrix, and for covalent binding to other structural proteins, respectively, providing articular cartilage with its shock-absorbing properties.[69] Collagen organization, as well as relative matrix composition, cell density, and cell morphology, vary as a function of depth from the articular surface and act collectively to resist the range of forces experienced by the joint.

The avascular nature of cartilage and the low number of cells that are found within articular cartilage matrix result in a tissue

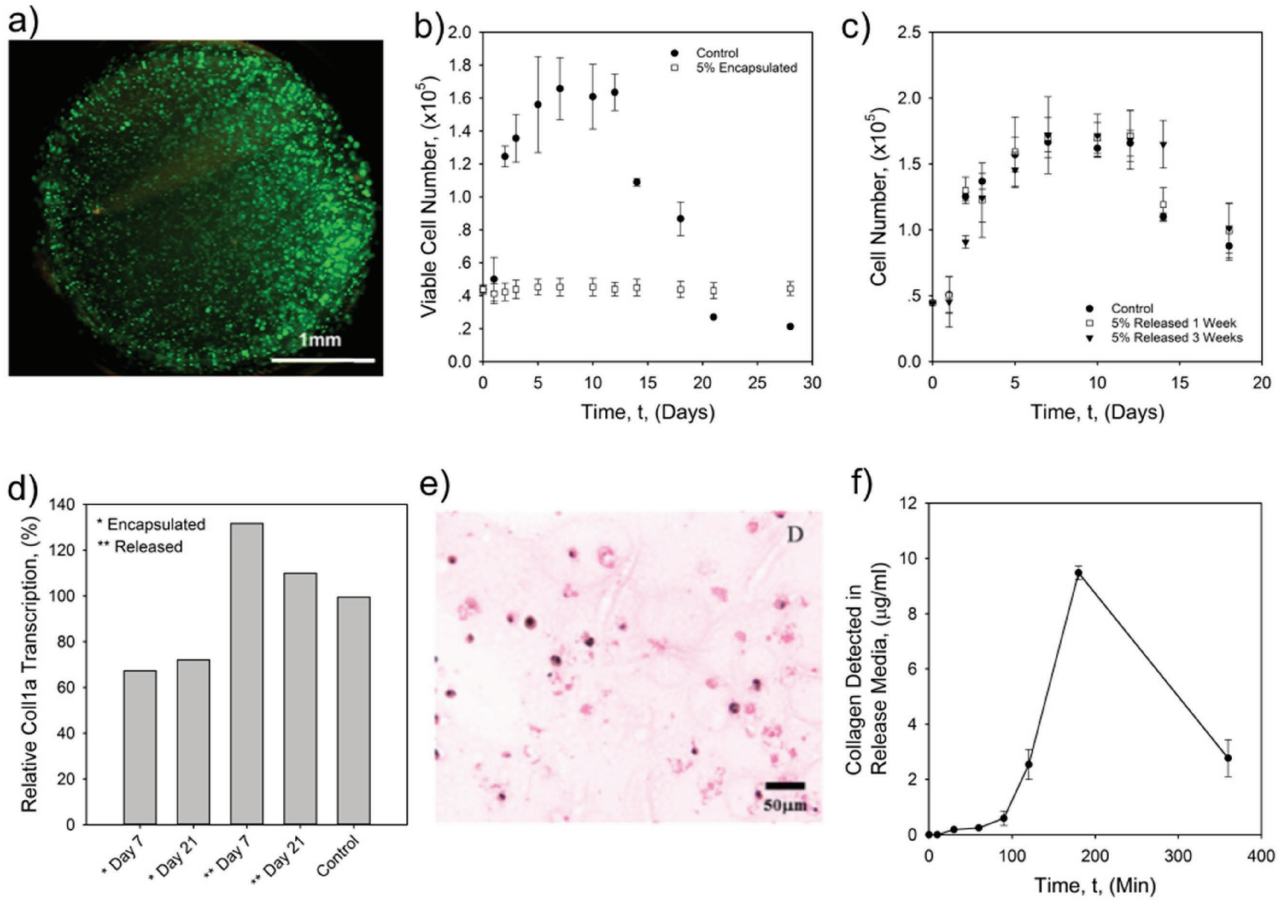

Figure 2. Effect of entrapment on cellular activity. a) Live/dead staining of encapsulated fibroblasts 4 d postencapsulation in 5% w/v alginate quiescent gel. Live cells stain green and dead cells stain red. b) Growth curves of the encapsulated 3T3 fibroblasts shown in (a), compared with nonencapsulated 3T3s (control). The encapsulated fibroblasts remain at a constant viable cell number up to 33 d postencapsulation, rather than exhibiting the normal bell-shaped growth curve seen with monolayer cultured fibroblasts. c) Fibroblasts released from encapsulation in 5% w/v alginate quiescent gel display normal growth in monolayer culture after both 1 and 3 weeks encapsulation. Adapted with permission.[52] Copyright 2009, Elsevier Ltd. d) Relative transcription of Coll1a by 3T3 fibroblasts encapsulated in 2% w/v Ca–alginate quiescent hydrogel for 7 and 21 d. Expression is shown for encapsulated cells and those that are released and grown as monolayers for 48 h and control fibroblasts, grown as monolayers having never been encapsulated. Col1a transcription was found to be only approximately 25–30% lower than before encapsulation. e) Despite the relatively high Col1a transcription levels while encapsulated, Haematoxylin Van Gieson (HVG) staining of the samples revealed very little collagen matrix had been produced by the encapsulated cells even after 3 weeks. f) However, soluble collagen was detected within the alginate structures and could be released into physiological media. Overall, this suggested that while the alginate gel system allowed for the passage of essential collagen precursor molecules and their assembly into soluble collagen, it sterically hindered collagen fibrillization. Adapted with permission.[53] Copyright 2012, the American Chemical Society.

with poor regenerative capacity following damage. Articular cartilage is one of the most challenging tissues to engineer or mimic synthetically due to the complex transitions in composition and ultrastructure, which are vital to its overall mechanical function. Consequently, most therapies for the repair of damaged cartilage involve tissue grafts or exploiting the local biology to facilitate new tissue formation. The current gold standard treatments in the repair of focal cartilage defects are microfracture or mosaicplasty. Microfracture involves removing the damaged cartilage and making a series of small holes in the subchondral plate causing bleeding from the marrow, and the formation of a clot that fills the focal defect. The aim here is to introduce and retain progenitor cells (present in marrow) into the defect site, a fraction of which have the potential to develop into chondrocytes and facilitate new cartilage formation. In mosaicplasty, small portions of cartilage are transplanted from nonarticulating regions of the affected joint into the cartilage defect site. This approach enables the engraftment of an already fully developed native cartilage structure. A common drawback with both methods is the formation of a fibrocartilaginous matrix as opposed to hyaline cartilage.[70,71] Fibrocartilage does not exhibit the same specialized surface structure as hyaline cartilage. As a consequence, the new tissue is mechanically inferior to the surrounding intact cartilage (particularly in resisting shear forces), which increases the risk of failure. A range of cell-based therapies, such as ACI, have been developed for the production of a native articular cartilage. To date, none of these methods have been able to surpass microfracture as the method of choice for orthopedic surgeons. Although there has been some success with the use of bone-derived mesenchymal stem cells for cartilage regeneration, there is a recognized need for culture and delivery systems that successfully maintain the

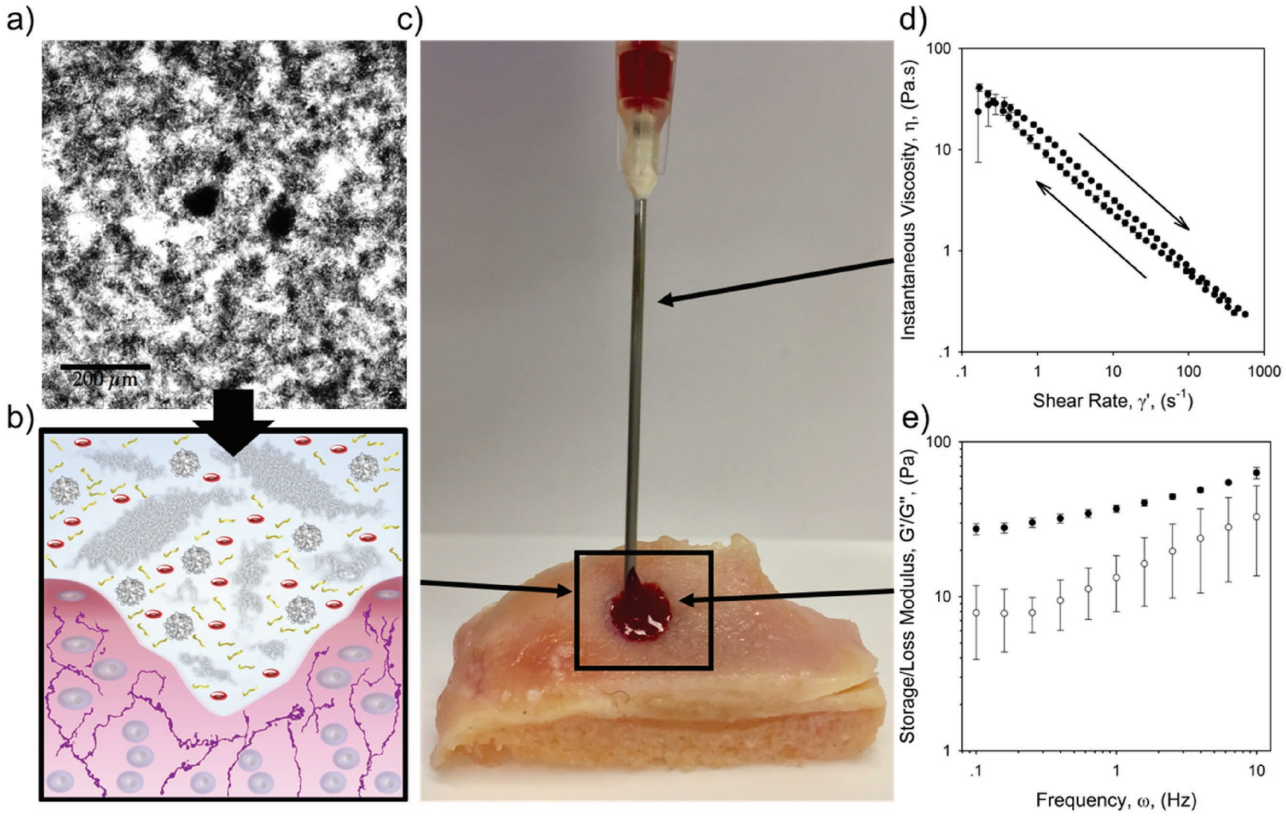

Figure 3. a) Optical microscopic image of diluted alginate fluid gel negatively stained with blood. Red blood cells (black) become sterically localized by the sheared alginate gel (white). Scale bar represents 200 μm. b) Schematic diagram depicting the stabilization of PRP (platelet rich plasma) via fluid-gel particles for in situ cartilage repair. c) Section of a tibial plateau with defect plugged using alginate/BMAC (bone marrow aspirate concentrate) fluid gel using a syringe. d) Flow profile obtained for 10% blood serum in 1% alginate fluid gel. The plot shows data for both increasing and decreasing shear, highlighting its reversible shear thinning behavior, crucial for application via syringe. e) Frequency sweep obtained for the same sample showing the typical weak solid-like structure exhibited by fluid gels under static conditions.

required chondrogenic phenotype during culture expansion in the lab, and upon implantation – especially for maintaining chondrogenic phenotype during the healing process. Alginate-based gels have been used as a biomaterial in chondrocyte culture since the 1980s as demonstrated by Guo et al. in 1989.[72] The general popularity of alginates in bioengineering stems from their good biocompatibility/tolerance with a range of tissues, low cost, and ease of gelation using divalent ions (many of which are endogenous to the human body). However, it is the similarility between the ultrastructure of gelled alginates and that of native extracellular matrix that has made alginates favorable for use in research and development into chondrocyte culture.[51,73] The 3D structure of the gels is thought to help the chondrocytes exhibit more in vivo-like behavior.[74] Furthermore, the ability to form 3D structures with tunable bulk mechanical properties, incorporate cell binding moieties, and allow the diffusion of soluble factors have proven to be important features in supporting chondrogenesis and maintaining chondrogenic phenoptype. Thus, their regenerative potential is maximized.[51,75] Hwang et al. demonstrated that the porosity in a gel system can be tuned by the addition of gelatin microbeads as a means of enhancing the mass transport of oxygen, nutrients, secreted biomolecules, and waste products.[76] Promising human cell-based models have also been developed with good medium to long-term cell viability. Choi et al. successfully cultured human articular chondrocytes in alginate beads over 15 d, and Loeser et al. successfully cultured human articular chondrocytes in alginate exposed to the chondrogenic growth factor insulin-like growth factor-1 and reported 95% survival at 21 d.[77,78]

Beyond the successful culture of chondrocytes in a lab, a major issue is the delivery and retention of chondrocytes into a focal defect using a non-invasive approach. Many have attempted to form in situ gelling materials that are capable of solidifying in the focal defect, and there are clinical products on the market that form a polymerized biological scaffold within the defect (BST-CarGel, Smith & Nephew; GelrinC, Regents Biomaterials; Chondron, RMS Regrow). We have demonstrated that it is possible to use "sheared" or "fluid" gels as vehicles to deliver and retain populations of chondrocyte cells. These materials can be injected into an aqueous medium and will retain their mechanical integrity over a period of 21 d of ageing (**Figure 4**). Importantly, the material can be injected through a narrow gauge needle while maintaining the viability of the incorporated cell population (Figure 3). Once injected into a defect, unlike gel systems that are gelled in situ or before implantation, the cells are able to move within the structure of the fluid gel and can migrate down into the bottom of the tissue

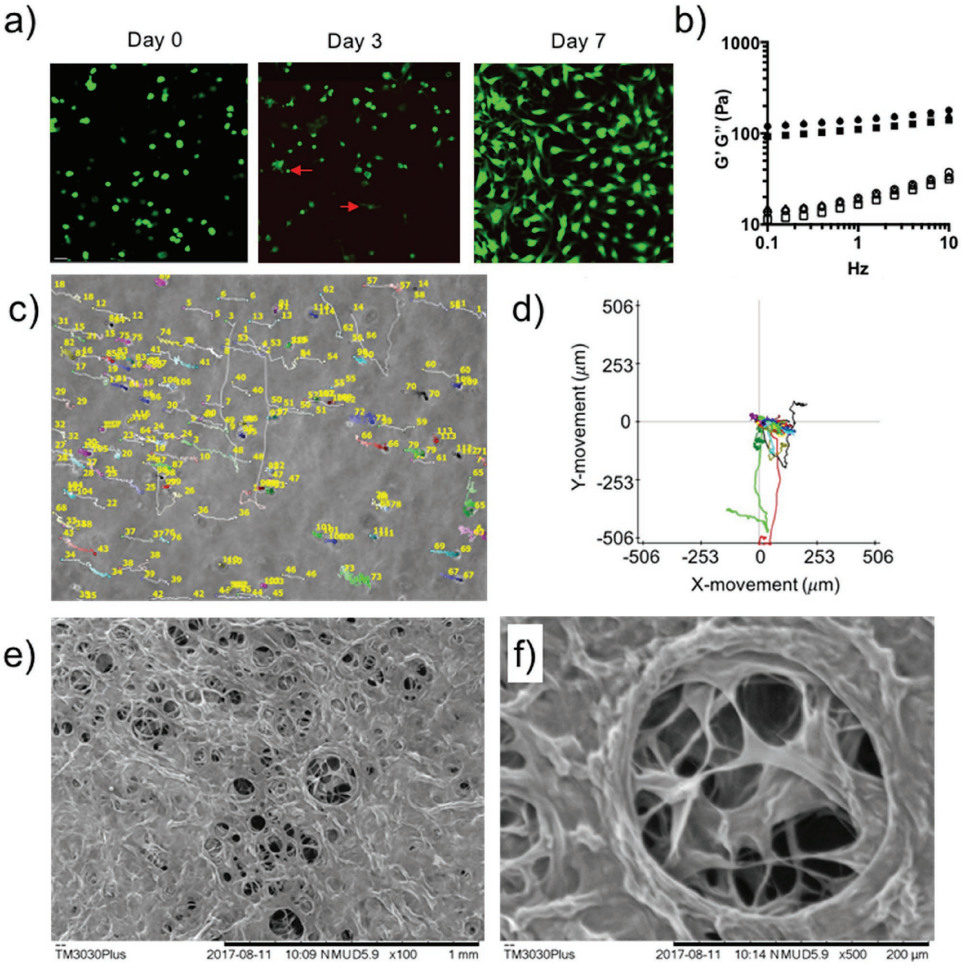

Figure 4. a) Sedminentation of cells through a fluid-gel network over 7 d. b) Mechanical stability of fluid alginate over 3 weeks (day 7: circles; day 14: squares; day 21: triangles; G': closed symbols; G'': open symbols). c) Cell tracking showing lateral movement of cells through fluid alginate. d) Quantification of the cell movement in the x–y plane. e) Fluid alginate architecture showing voidage regions in the polymer network.

defect (Figure 4). However, recent work within our group has also suggested that the lack of physical entrapment of the cells can result in the dedifferentiation of the encapsulated cells into a fibroblastic phenotype. While this lack of physical entrapment may ultimately hinder the use of fluid gels for the delivery of differentiated chondrocyte cells, we have demonstrated that fluid gels are effective in the delivery of other biological agents, such as platelet rich plasma and bone marrow aspirate concentrate, and their stabilization within a model joint defect. Our current work aims to translate this technology into a usable minimal intervention for cartilage augmentation (Figure 3). The ability of fluid gels to facilitate cell migration can actually be an advantage when designing therapies for other tissue applications. In the case of the skin, the ability for cells to migrate through the surface of the material would enable a topically applied cell population to fully colonize the wound bed.

3.1.2. Skin—Keratinocyte Delivery to Aid Wound Closure

Skin exhibits a multilayered structure with the uppermost layer of the epidermis consisting of layered keratinocytes that differentiate from the basal lamina over a period of several weeks.[79] The layer below the epidermis, known as the dermis, consists of a population of fibroblast cells that play a role in secreting extracellular matrix molecules such as collagen types I and IV and glycosaminoglycans.[80]

Serious damage to the epidermal and dermal layers break this fragile interplay until healing occurs and the wound is closed. In the case of large and deep burns, wound healing without intervention can take several weeks, wherein a patient is likely to develop acute systemic dysfunction with high risk of death through systemic infection and dehydration.[81] In order to speed the process of conventional skin grafting, it is possible to grow a multilayer sheet of keratinocytes in the laboratory in a period of up to 3 weeks.[82–85] These cells may then be applied to the surface of the wound. The keratinocytes then accelerate the closure of the wound by secreting factors that are able to stimulate collagen deposition (TGF-β1) and differentiation of the cells in the wound bed into myofibroblasts, which are able to fully close the wound. Although this process was pioneered in the 1970s and has found use in the clinic, the cost of the treatment, in addition to the amount of time it takes to generate sufficient cells, limits utility.[86] Poor outcomes in terms

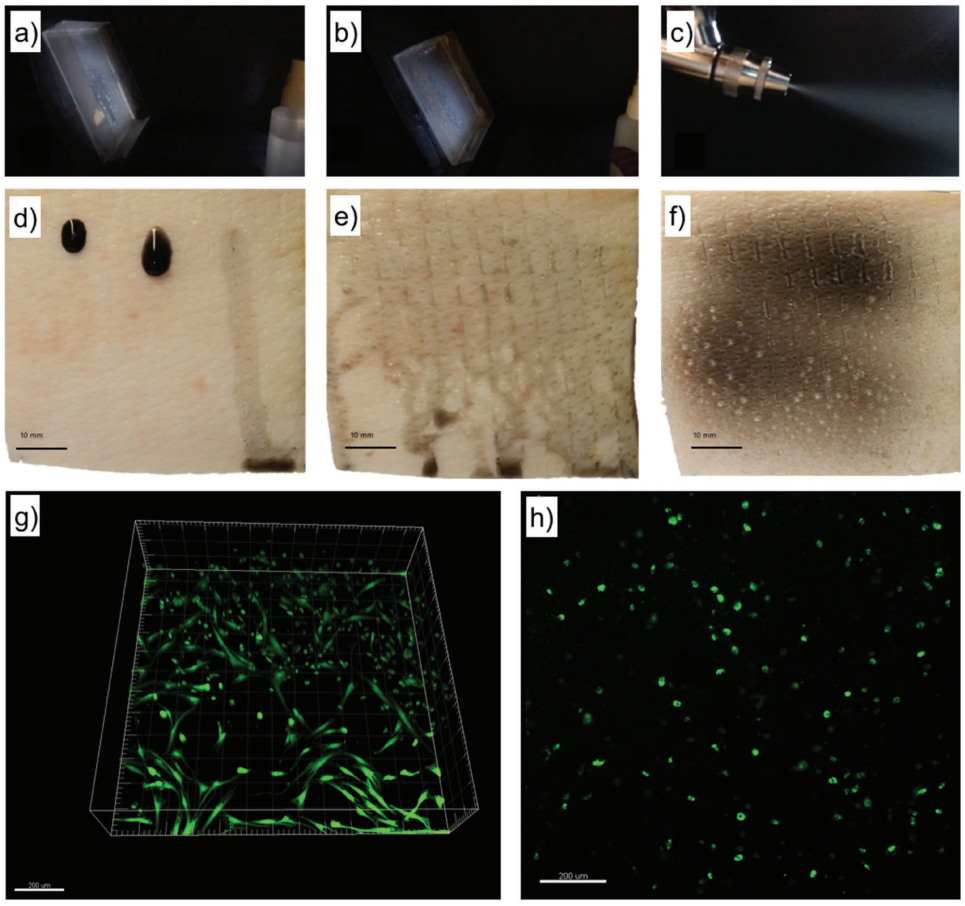

Figure 5. Cell encapsulation and spray deposition of gellan gum fluid gel. Video of a) spray delivery with handheld spray pump of material to tilted gelatin substrate demonstrated poor adherence of water b) compared to gellan gum fluid gel. c) Airbrush spray delivery system was used to standardize air pressure at delivery (15 PSI) and nozzle size (0.75 mm). d) Comparison of dyed gellan fluid gel (left), quiescent gellan gel (middle) and sodium chloride (right) droplets to porcine skin indicates a low rate of spreading of the gellan explained by the higher viscosity and structural stability of the material. e) Airbrush spray delivery of dyed sodium chloride to porcine skin showed rapid run-off with pooling of material at the bottom of the substrate, f) whereas uniform distribution without run-off was achieved by gellan fluid-gel spray delivery. g) Fluorescence cell viability assay of human dermal fibroblasts (HDF) 7 d after encapsulation in gellan fluid gel (live cells green, dead cell red), cells are viable and attach to the bottom of the well and seem to migrate out of the gel. h) High viability of cells at day 1 following spraying of encapsulated HDFs in gellan fluid gel.

of graft take, formation of bullae (blisters), poor handling due to fragility of sheets, and wound contraction have been reported. More recently, spray technologies have been used to deliver autologous and allogenic keratinocytes to the surface of wounded skin. Preconfluent cells have demonstrated utility in regenerating the skin and require a similar culture period of approximately 2–3 weeks.[87–89] Consequently, there is now a drive to develop allogeneic therapies from immunogenically privileged neonatal foreskin fibroblasts and keratinocytes.[90] However, a phase 3 clinical trial in nonhealing wounds was stopped prematurely due to low efficacy.[91] There are also products available that eliminate the in vitro culturing step by separating epithelial cells from patient biopsies in the clinical setting, and these cells may then be dispersed and sprayed onto the wound surface in a single procedure.[92,93] Although these technologies have been available for some time, there are as yet few clinical trials that show a conclusive benefit for using this approach.[94,95] One potential reason for this is that the cells themselves are delivered using a low-viscosity spraying system and anecdotally the level of "run-off" from the wound surface following spraying is high.[86] Although some products now try to remedy this using fibrin glue as an adjunct, the technology has yet to find strong traction in the clinic.[96,97] One of the major advantages of using a fluid gel system for the delivery of keratinocytes is that the material itself shear-thins considerably under the rapid shear forces experienced in a spraying system. We have utilized fluid-gel systems that are formed from a polysaccharide called gellan gum. Populations of cells may be incorporated into this system and can then be sprayed through a nozzle and deposited onto a surface as shown in **Figure 5**a–c. The soft solid then rapidly structures as it impacts on the skin, where the cells are retained on the surface, rather than running off, maintaining high-levels of viability. Importantly, the structure of the fluid gel allows cell movement within it, and we have shown that the viscosity of the material can be tailored to allow sedimentation of cells onto the upper surface of the tissue. In addition to being sprayed onto the surface of the skin, the gellan fluid gel may also be used to spread cells

across a surface, yet be retained in place once the spreading process has been completed. Figure 5d–f demonstrates how the material is retained on the surface of the skin. The material is compared against sodium chloride and a gellan quiescent gel. When the surface of the skin was inclined, the fluid gel was retained on the surface of the skin in exactly the same way as the gellan quiescent gel. It is worth noting that in order to get the quiescently gelled gellan to spread and then reset on the surface of the skin, the material was heated to around 50 °C before being allowed to cool, which would not have been conducive to cell survival. Shear structuring of the material was a successful way to enhance functionality without compromising cell viability (Figure 5g–h). The next challenge with this material will be to develop a manufacturing and packaging process that will not compromise the properties of the finished product. At present, the delicate structure tends to breakdown when exposed to doses of gamma irradiation considered low by industry standards. The development of non traditional sterilization methods may prove essential in the transit of these materials to the clinic. Although autoclaving is a possibility without causing a significant change in the properties of the final product, this method is unsuitable for the delivery of delicate therapeutic proteins that may be required to enhance the regenerative capacity of the tissue.

3.1.3. Cornea—Scar Prevention

The cornea is a layered structure exhibiting very high levels of organization in order to both protect the inside of the eye and provide the majority of the eye's refractive power.[98] The cornea is composed of five layers, with the anterior surface of the cornea consisting of epithelial cell layers that overlay a tough collagenous layer (Bowman's layer), mostly consisting of tightly woven collagen type I meshworks. The corneal stroma is an optically transparent layer composed of heterotypic collagen type I and V fibrils of around 30 nm in diameter, embedded within a proteoglycan matrix.[98,99] The stroma makes up 90% of the overall corneal thickness and is maintained by resident keratinocytes.[98] The collagen fibrils are arranged in flattened tightly spaced bands called lamellae that traverse the diameter of the cornea and are superimposed over one another making up most of the stromal thickness.[100] Further structuring occurs from the interlacing of the lamellae, which is most prominent within the anterior and mid-stromal layers and less so in the posterior stroma, where they are stacked in a similar fashion to layers in plywood.[98] The posterior stromal region, particularly in the central corneal region, is more hydrated than the rest of the stroma and thus the corneal stroma overall is akin to a highly structurual and mechanical anistotropic hydrogel system. The predominant collagen orientation within the stroma also varies as a function of depth. In the anterior region, the collagen does not exhibit any preferred orientation, whereas the mid- and posterior regions demonstrate preferred orthogonal arrangement of collagen along the nasal-temporal and superinferior directions.[101] The key structural factors of the cornea, leading to high optical transparency, are the uniformity of the collagen fibril diameters and tight regulation of the distances between adjacent collagen fibrils.[98,99,102,103] The fourth layer of the cornea, Descemet's membrane, is composed of a thin layer of collagen type IV and is designed to support the corneal endothelium layer that makes up the posterior surface of the cornea. When the corneal surface is damaged, it is typically capable of healing itself. However, in the case of infection (e.g., microbial keratitis), a significant inflammatory process is triggered, resulting in the upregulation of growth factors such as TGF-β1, which is a potent fibrogenic factor leading to disorganized deposition of collagen and extracellular matrix within the stroma.[104] Dysregulated collagen and ECM deposition prevents light transmission through the cornea and ultimately leads to blindness.[105] Treatment of diseases such as microbial keratitis may result in a corneal transplant if standard treatments with antibiotics and steroid fail.[106] Therapeutic proteins such as decorin have been shown to regulate the deposition of collagen by binding the inflammatory cytokine TGFβ-1.[107] This prevents collagen upregulation as well as the differentiation of keratocytes to the myofibroblastic phenotype that causes wound contraction and ECM deposition.[108] Topical delivery of therapeutic proteins/molecules to the surface of the eye has previously been attempted, however with limited success.[109–112] Gellan fluid-gel based eyedrops allow for the initial retention and then tailored release of the therapeutic agents onto the surface of the eye over a period of hours, as opposed to seconds/minutes as experienced with the majority of eyedrops (**Figure 6**a–c).[113] Since gellan is optically transparent, a patient's vision would not be compromised by the gellan when placed on the eye. During blinking, the eyelid sweeps over and applies shear to the surface of the gellan eyedrop, causing layers of the material to be removed. The eyedrop is cleared from the surface of the eye over a period of around 2 h. This technology has been exploited to deliver a sustained dose of decorin to the surface of the eye, which we have demonstrated facilitates reepithelialization of the eye surface (Figure 6d,e), both ex vivo in an organ culture model of corneal abrasion and when challenged in an in vivo corneal abrasion model. In addition to delivering the molecule to the surface of the eye over an extended period of time, we believe that the eyedrop will provide some relief to patients with this very painful condition, by lubricating the surface. Indeed, it has previously been reported that fluid gels, if formulated correctly, can be used as an adequate lubricant for surfaces.[114]

4. Bioprinting

In addition to enabling the encapsulation of cells and proteins for in situ delivery, the "self-healing" structure of fluid gels means they have found application as supports for additive layer manufacturing (ALM) of soft material structures, with complexity that is far beyond what has previously been reported. For many years, researchers have sought to replicate tissue structure and composition by using a combination of isolated cells and polymeric hydrogels that have a structural resemblance to ECM, to create an implantable living construct.[115] Most constructs have been fabricated using a gel casting process that provides little control over the microscale geometry of the deposited material, or the local mechanical properties so important to controlling cell fate. Innovation in

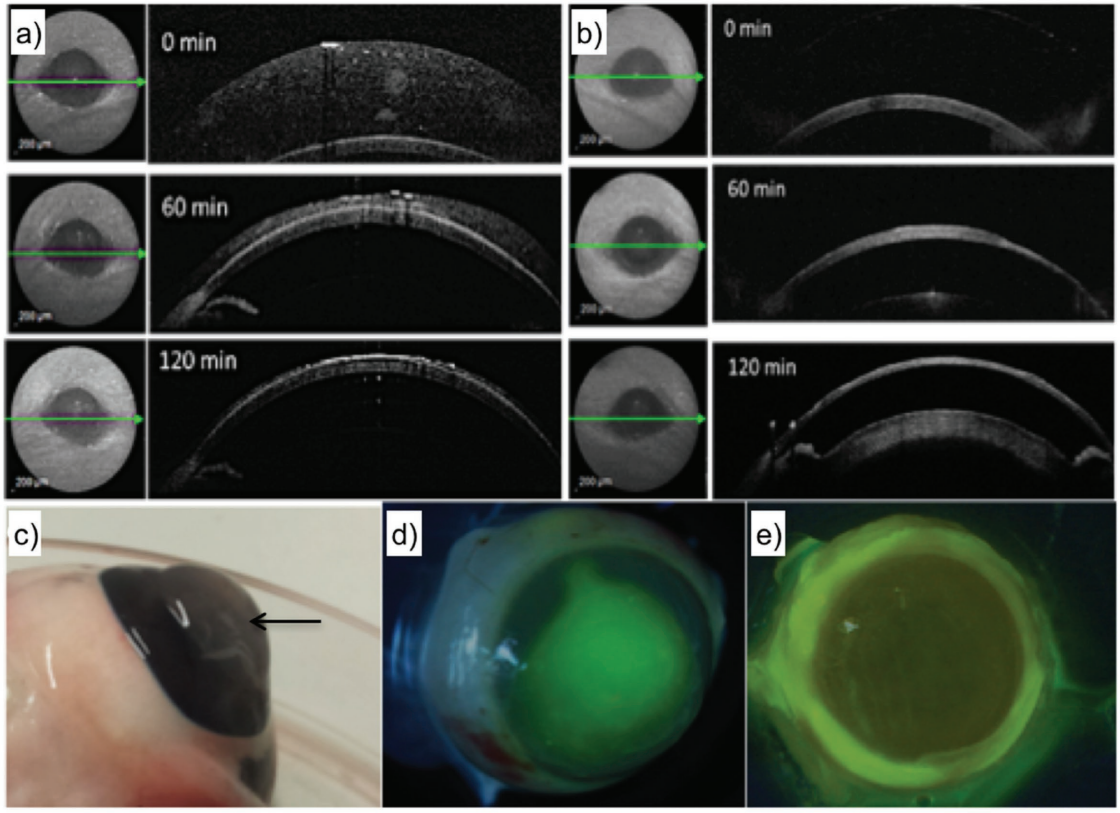

Figure 6. Optical coherance tomography (OCT) images illustrating the flow and clearance rate of fluid-gel eyedrops: a) when compared to PBS drops. b) On the surface of intact rat eyes over a 2-h period, fluid gel remained on the surface of the eye for nearly 60 min and some residue was noticed at 120 min. The PBS drop however cleared within 60 min. Fluid-gel thickens on the surface of freshly enucleated pig eyes, indicated by the black arrow. c) Eyes treated over 4 d with fluid gels containing decorin demonstrated significant reepithelialization in ex vivo organ culture models e) when compared to d) fluid gels without decorin.

this area has been driven largely by the desire to develop therapies that come close to offering the same key advantages as auto- and allografts, in that they are structurally and biologically the same as the surrounding tissue, while moving away from harvesting graft material itself. This is because the grafts are only suitable for relatively small defects and the graft approach in general is unlikely to be able to meet future clinical demand.

3D bioprinting using ALM has become a useful approach for creating structures with a greater level of complexity than traditional processing methods, such as casting, with some degree of control over the distribution of biological material throughout the structure.[116] While ALM of hard materials is relatively mature and adopted by a number of industries, ALM of soft mateials remains challenging. One of the major challenges for 3D bioprinting is the lack of suitable materials that are both able to replicate tissue material behavior and compatible with current 3D printing technologies. The advantage of biopolymer materials for tissue engineering applications is their similarity to native ECM. However, controlling their physical properties to be optimal for both the tissue engineering application and the mechanics of the printing process is more difficult than of synthetic materials. Biopolymers used for tissue engineering tend to have relatively low viscosities in the pregelled state that facilitates mixing with cells. Furthermore, many of these materials exhibit pseudoplastic (shear thinning) flow behavior that also can be advantageous for extrusion, when fabricating scaffolds. Unfortunately, low-viscosity materials can be problematic when 3D bioprinting, as the printed structure can collapse and lose its shape before solidification can be initiated.[117] Another problem when 3D printing biopolymer hydrogels is the inability to integrate multiple layers of material once gelled, preventing the production of integrated gels with regional variations in mechanical behavior. To overcome these problems, researchers often incorporate highly viscous materials to maintain a 3D shape after deposition,[117–119] which is not ideal as highly viscous materials can impede homogeneous cell mixing and often require increased extrusion pressure in order to print. This can lead to reduced cell viability as a result of the shear stresses inflicted on cells and has therefore limited their use in 3D bioprinting.[120]

We recently developed a technique that overcomes some of the issues associated with additive layer manufacturing when using low-viscosity materials, allowing them to be used as a bioink to create relatively complex soft-solid structures.[116] This was achieved by extruding a gelling biopolymer solution into a self-healing fluid-gel matrix, which suspends the fragile printed construct in the liquid state to prevent flow and thus retaining the deposited morphology. Additionally, as the printed construct remained in the liquid state, it was possible to build the construct layer by layer and interface two different materials

with dissimilar mechanical properties, creating a structure with distinct regions of anisotropic physical behavior. To demonstrate the potential for clinical application of the technique, we created a structure that recapitulated the osteochondral region as directed by microcomputed tomography (CT) imaging.[116]

Native osteochondral tissue has a gradually changing microstructure that extends from disordered mineralized collagen in subchondral bone[121] to cartilage, across which there are distinct variations in the relative concentrations of noncollagenous proteins, and orientation of collagen fibers as a function of depth.[122] This graded structure allows applied stress to be distributed across the interface without specific stress localization, helping to prevent delamination from occurring.[123] In our work, femoral condyle tissue was donated from patients following total knee replacement surgery and a full-thickness osteochondral defect was introduced using a surgical drill. The tissue containing the defect was scanned using micro-CT to generate a 3D model. Chondrocytes and osteoblasts were isolated from the tissue samples and, following primary cell culture, were added to 1.5% gellan and 1.5% gellan mixed with 5% nanohydroxyapatite (HA), respectively. Using the 3D model as a guide for accurate dimensions, an osteochondral implant was manufactured with the lower layer loaded with gellan, HA, and osteoblast cells, while the upper layer of the construct was manufactured using gellan gum loaded with chondrocytes. The manufactured cell-laden construct was then implanted into the defect of the ex vivo femoral condyle. After 4 weeks in culture, the construct maintained morphology and the encapsulated cells retained their phenotype within the distinct layers of the manufactured structure.

Our suspended additive layer manufacturing process has since been integrated into a commercially available extrusion-based 3D bioprinter (Cellink, Sweden), adding the ability to manufacture more geometrically intricate structures. To demonstrate the ability to retain the structural integrity of printed low-viscosity materials, an S-hook shaped construct was printed from a G-code file using 1% w/w gellan gum (**Figure 7**a). When printed onto a planar surface, the structure collapsed as the material began to flow under gravitational force (Figure 7b). However, when printed into a fluid-gel bed (prepared from 0.5% agarose), the structure retained the S-hook shape, clearly demonstrating protective support afforded by the surrounding fluid gel on the printed construct (Figure 7c). We then demonstrated the ability of the process to manufacture graded interfaces between soft-solid structures over relatively large length scales. Our model for this was printing conjoined doublet and triplet cuboids from single cuboid units measuring 10 mm × 10 mm × 5 mm, using gellan gum and gellan gum containing an orange dye (Figure 7d–f). Once the first cuboid was printed and remained in the liquid state, a second cuboid was printed with a 1 mm overlap with the first cuboid in the lateral plane to create an interfacial region. Once printed, the structures were crosslinked in situ using 100×10^{-3} M $CaCl_2$ for 30 min, and recovered as a single structure from the suspending particulate gel by gently washing with distilled water. This technique could potentially be used to model diffusion of molecules from one gel system to another, or fabricate discrete molecular reservoirs within a larger structure. Finally, we explored the potential to integrate different materials each with different gelation mechanisms using suspended bioprinting. Figure 7g–i shows the manufacture of cylindrical constructs consisting of a layer of gellan gum and a layer of type 1 collagen (PureCol EZ Gel, Advanced BioMatrix, USA), each layer with dimensions of 5 mm × 5 mm × 2.5 mm. In this example, the fluid gel base was maintained at 37 °C while the gellan cylinder was deposited first and left in the liquid state. The collagen was then deposited at 20 °C and left for 60 min to allow thermal gelation to occur, as the collagen equilibrated to 37 °C temperature of the supporting particulate bed. To initiate gelation of the gellan cylinder, 100×10^{-3} M $CaCl_2$ was added to the construct and left to gel for a further 30 min. Once fully crosslinked, the construct could be removed as one piece (Figure 7h). The finished construct exhibited a clear interfacial region between the two layers, which could not be physically separated, thus suggesting the formation of an interpenetrating polymerized network across the interface (Figure 7i). The order in which the different materials are gelled during fabrication of a construct can strongly influence the stability of the interface between them. Successful integration of collagen and gellan layers required the gelation of the collagen layer before gelation of the gellan layer. This is attributed to a mechanism reported by Gillette et al. when attempting to integrate collagen into crosslinked alginate, whereby the small pore size of the gelled alginate inhibited the formation of a network of collagen fibers within the alginate structure.[124]

In summary, the easily removable physical support offered by the fluid gel bed enables the deposition of biological materials in the liquid phase in 3D, with complex geometries and interfaces, before solidifying into a single construct with graded mechanical, chemical, and structural properties. This approach effectively decouples the viscosity of the starting material from the desired mechanical properties of the final printed construct. Biopolymers can be prepared at the relatively low viscosities required for low-pressure extrusion-based bioprinting, with the final mechanical properties engineered into the materials by gelation postextrustion.

Suspended bioprinting is, therefore, an enabler for a range of soft-solid materials, for which their full potential in tissue engineering is well established but not fully realized to date, to be used in the ALM of implantable biological constructs.

5. Conclusions and Outlook

Soft-solid materials have long been used as basic building blocks in the fields of tissue engineering and regenerative medicine, with certain materials having found use as wound dressings, eyedrops, and for the immunoisolation of cells. Despite extraordinary amounts of innovation around the manipulation of chemistry and local mechanics, which has significantly improved our understanding of how local environments can influence cell behavior, relatively few new so-called "smart materials" have made the transition to full clinical use. One of the reasons for this relative lack of progress is that the costs of taking new compositions to the clinic, through toxicity testing and characterization, is so high as to make it uneconomical. We have focused a large amount of research on modifying material structures by making changes

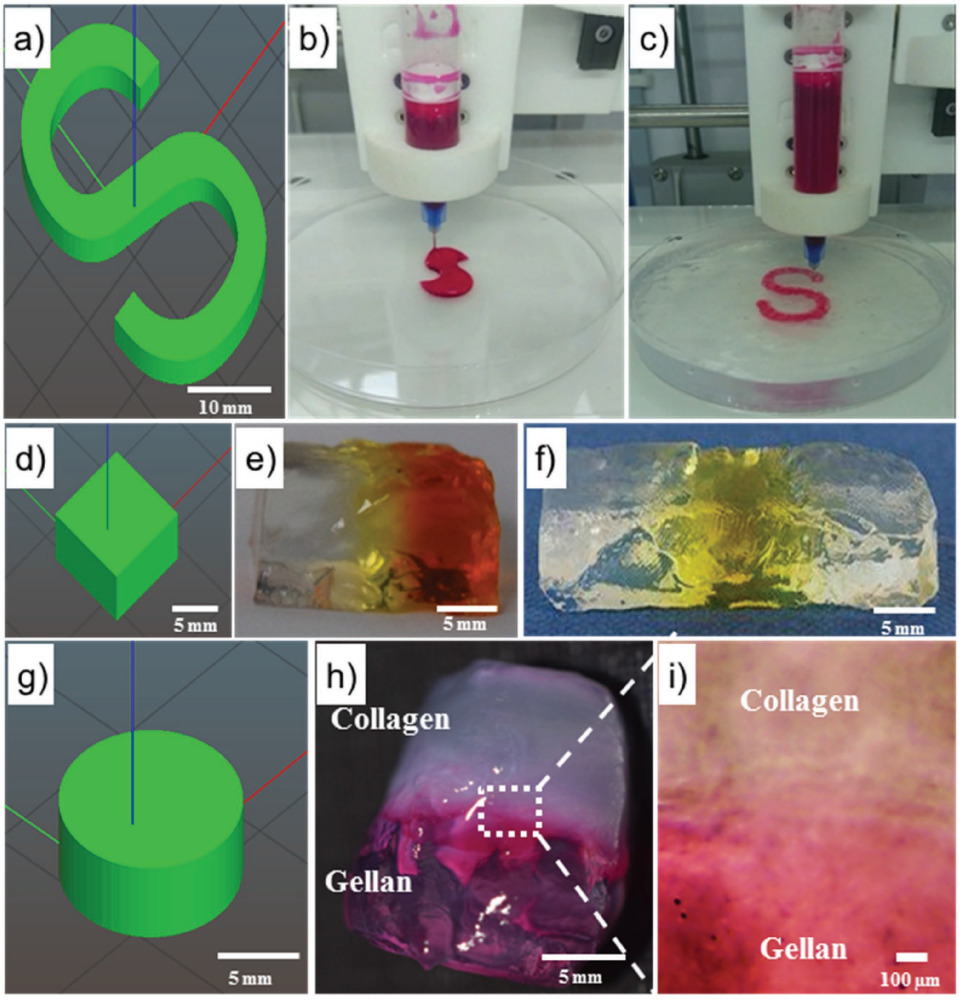

Figure 7. Suspended bioprinting of various biopolymer structures. a,b) G-code image for an S-shape hook with dimensions of 25 mm × 40 mm × 2.5 mm was printed using 1% w/w gellan gum onto a planar surface and imaged at the end of the printing process. c) The same structure printed into a 0.5% w/w agarose particulate gel bed. The construct printed onto the planar surface lost all structural integrity, collapsing under its own weight and flowed across the surface, resulting in a distorted structure. The construct printed within the particulate bed retained accurate dimensional conformation. d–f) Design and manufacture of multilayered constructs using suspended bioprinting. d) G-code file of a 10 mm × 10 mm × 5 mm cuboid. Two cuboids integrated using suspended bioprinting process; one contained a dye highlighting the ability to interface two separate biopolymer structures e) and another incorporating a double interface of gellan/dyed gellan/gellan to illustrate the potential for creating compositional gradients. g–i) Suspended bioprinting of a composite hydrogel cylindrical structure. g) G-code image of the single cylindrical structure with dimensions of 10 mm × 10 mm × 5 mm. h) Composite structure prepared from 1.5% gellan with 0.5% type 1 collagen using the suspended bioprinting process. i) A microscopic image of the interfacial region between the two dissimilar materials. These example constructs illustrate the potential of this approach to 3D bioprinting to manufacture biopolymer constructs with distinct anisotropic chemical and mechanical properties.

to processing conditions, without modifying composition. In the case of hydrogels, this has allowed us to take existing regulator-approved materials, and process them in a manner that allows us to produce structures that exhibit very distinct properties from the conventionally processed materials. Of particular use is the capacity of these materials to self-heal following the application of mechanical shear. This means that the materials are able to be delivered through a narrow aperture, which generates local shear and liquefies the material sufficiently that it may be deposited over a surface, where it solidifies. This has allowed us to produce eyedrops, cell spraying devices, and injectable delivery devices. Importantly, these materials are ready for translation to the clinic having undergone less cumbersome toxicity testing than for a completely new material. We have also used the self healing capacity of these materials to provide support in a new method for the additive layer manufacturing of cell containing soft-solids. This method differs to other soft-solid additive layer manufacturing methods, in that both the support phase and the cell-bearing phase can exhibit exactly the same composition. When the part has been removed from the print-bed, the support material can be dispersed by the application of gentle shear. This enables us to produce complex structures with a supporting medium without the worry of contaminating the implant surface.

These systems are still far from being exploited to their full potential and also still need considerable refinement

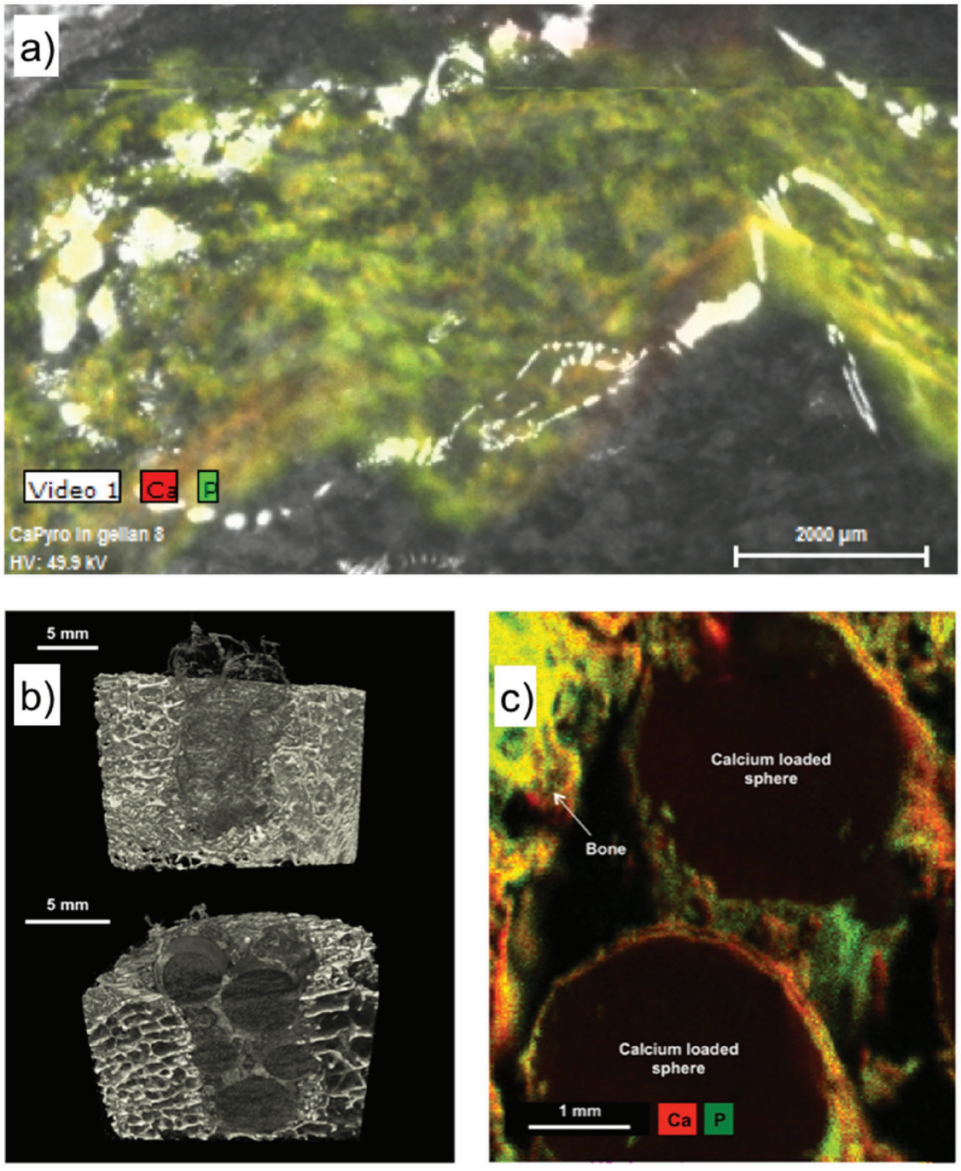

Figure 8. Fluid-gel materials may be loaded with osteogenic ceramics materials and extruded through a syringe, before they thicken upon a surface. a) The ceramic particles remain evenly distributed throughout the process. b,c) It is also possible to deliver the precursors of bone mineral formation within gel materials such that they harden in situ to form a relatively stiff composite matrix, but remain liquid prior to administration. This flexibility enables the tailoring of local environments to create more regenerative localized conditions. b,c) Reproduced with permission.[125] Copyright 2018, Wiley-VCH.

before eventually finding widespread use across medical fields. The polymeric gels are very difficult to sterilize using standard methods, and at present require non-cost effective low-throughput processes that allow for sterile-filling. Future innovations and collaborative work with the regulators should seek to develop new, more gentle sterilization methods, that are not likely to cause destruction of the polymeric material from which the structure is formed. Gamma irridation, ethylene oxide, and high temperatures are all very useful for sterilizing metallic materials, but impart enough energy into hydrated polymer systems to cause significant breakdown, and therefore significantly modify the properties exhibited by the materials. The use of alternative light sources (UV and blue light) and supercritical processing technologies may well provide the answer to this significant problem, but need to be validated and widely accepted by regulators worldwide.

We have also only just begun to explore the potential of these materials for delivering complex, composite structures. The incorporation of secondary materials into the fluid gel, which are capable of inducing osteogenesis in codistributed bone marrow aspirate and other sources of cell populations, has significant potential for shaping the local cellular environment in vivo, thereby enabling superior tissue regeneration (**Figure 8**a). Indeed, providing the reactants to generate a third phase between the polymeric components of the gel, enabling hardening into a comparatively stiff structure has already been achieved with some success (Figure 8b,c).[125]

Acknowledgements

The authors would like to acknowledge Dr. Sam Moxon, Jessica Senior, and Erik Hughes for their contribution to Figures 7 and 8. The authors would also like to acknowledge the EPSRC, MRC, and Wellcome Trust for the provision of funding.

Conflict of Interest

The authors declare no conflict of interest.

Keywords

biomaterials, hydrogels, regenerative medicine, soft materials, structuring

Received: September 2, 2017
Revised: October 20, 2017
Published online:

[1] V. Bisceglie, *Z. Krebsforsch.* **1934**, *40*, 122.
[2] T. M. S. Chang, *Science* **1964**, *146*, 524.
[3] F. Lim, A. Sun, *Science* **1980**, *210*, 908.
[4] J. A. Rowley, D. J. Mooney, *J. Biomed. Mater. Res.* **2002**, *60*, 217.
[5] S. R. Peyton, P. D. Kim, C. M. Ghajar, D. Seliktar, A. J. Putnam, *Biomaterials* **2008**, *29*, 2597.
[6] L. Gasperini, J. F. Mano, R. L. Reis, *J. R. Soc., Interface* **2014**, *11*, 20140817.
[7] J. A. Rowley, G. Madlambayan, D. J. Mooney, *Biomaterials* **1999**, *20*, 45.
[8] N. C. Hunt, L. M. Grover, *Biotechnol. Lett.* **2010**, *32*, 733.
[9] A. J. Engler, S. Sen, H. L. Sweeney, D. E. Discher, *Cell* **2006**, *126*, 677.
[10] J. H. Wen, L. G. Vincent, A. Fuhrmann, Y. S. Choi, K. C. Hribar, H. Taylor-Weiner, S. Chen, A. J. Engler, *Nat. Mater.* **2014**, *13*, 979.
[11] D. Zhang, M. B. Sun, J. Lee, A. A. Abdeen, K. A. Kilian, *J. Biomed. Mater. Res., Part A* **2016**, *104*, 1212.
[12] H. Li, J. J. Cooper-White, *Biomater. Sci.* **2014**, *2*, 1693.
[13] O. Chaudhuri, L. Gu, D. Klumpers, M. Darnell, S. A. Bencherif, J. C. Weaver, N. Huebsch, H. Lee, E. Lippens, G. N. Duda, D. J. Mooney, *Nat. Mater.* **2015**, *15*, 326.
[14] C. T. S. Wong, P. Foo, J. Seok, W. Mulyasasmita, A. Parisi-amon, S. C. Heilshorn, **2009**, *106*, 22067.
[15] B. A. Aguado, W. Mulyasasmita, J. Su, D. Ph, K. J. Lampe, D. Ph, S. C. Heilshorn, D. Ph, **2012**, *18*, 806.
[16] J. L. Drury, D. J. Mooney, *Biomaterials* **2003**, *24*, 4337.
[17] L. A. Estroff, A. D. Hamilton, *Chem. Rev.* **2004**, *104*, 1201.
[18] S. Yang, K.-F. Leong, Z. Du, C.-K. Chua, *Tissue Eng.* **2001**, *7*, 679.
[19] E. R. Morris, D. A. Rees, *Br. Med. Bull.* **1978**, *34*, 49.
[20] L. Römer, T. Scheibel, **2008**, *2*, 154.
[21] D. A. Rees, E. J. Welsh, *Angew. Chem., Int. Ed. English* **1977**, *16*, 214.
[22] E. R. Morris, D. A. Rees, G. Robinson, *J. Mol. Biol.* **1980**, *138*, 349.
[23] P. J. Flory, *Polymer* **1979**, *20*, 1317.
[24] S. B. Ross-Murphy, V. J. Morris, E. R. Morris, *Faraday Symp. Chem. Soc.* **1983**, *18*, 115.
[25] W. J. Frith, X. Garijo, T. J. Foster, I. T. Norton, in *Gums and Stabilisers for the Food Industry 11* (Eds: P. A. Williams, G. O. Phillips), Royal Society of Chemistry, Cambridge, UK **2002**, pp. 95–103.
[26] I. Fernández Farrés, I. T. Norton, *Food Hydrocolloids* **2014**, *40*, 76.
[27] A. Gabriele, F. Spyropoulos, I. T. Norton, *Food Hydrocolloids* **2009**, *23*, 2054.
[28] R. J. A. Moakes, A. Sullo, I. T. Norton, *RSC Adv.* **2015**, *5*, 60786.
[29] M. Spector, T. C. Lim, *Biomed. Mater.* **2016**, *11*, 14110.
[30] M. Liu, X. Zeng, C. Ma, H. Yi, Z. Ali, X. Mou, S. Li, Y. Deng, N. He, *Bone Res.* **2017**, *5*, 17014.
[31] C. R. T. Brown, A. N. Cutler, I. T. Norton, *EP 0355908 A1*, **1990**.
[32] I. T. Norton, D. A. Jarvis, T. J. Foster, *Int. J. Biol. Macromol.* **1999**, *26*, 255.
[33] R. J. A. Moakes, A. Sullo, I. T. Norton, *Food Hydrocolloids* **2015**, *45*, 227.
[34] D. A. Garrec, I. T. Norton, *J. Food Eng.* **2012**, *112*, 175.
[35] I. T. Norton, D. M. Goodall, K. R. J. Austen, E. R. Morris, D. A. Rees, *Biopolymers* **1986**, *25*, 1009.
[36] I. Fernández Farrés, R. J. A. Moakes, I. T. Norton, *Food Hydrocolloids* **2014**, *42*, 362.
[37] D. A. Garrec, B. Guthrie, I. T. Norton, *Food Hydrocolloids* **2013**, *33*, 151.
[38] B. Wolf, R. Scirocco, W. J. Frith, I. T. Norton, *Food Hydrocolloids* **2000**, *14*, 217.
[39] B. Wolf, W. J. Frith, S. Singleton, M. Tassieri, I. T. Norton, *Rheol. Acta* **2001**, *40*, 238.
[40] M. Doi, S. F. Edwards, *The Theory of Polymer Dynamics*, Clarendon Press, Oxford, UK **1990**.
[41] T. A. Witten, *Rev. Mod. Phys.* **1999**, *71*, S367.
[42] E. S. O'Sullivan, A. Vegas, D. G. Anderson, G. C. Weir, *Endocr. Rev.* **2011**, *32*, 827.
[43] H. Uludag, P. De Vos, P. A. Tresco, *Adv. Drug Delivery Rev.* **2000**, *42*, 29.
[44] B. G. Ballios, M. J. Cooke, D. van der Kooy, M. S. Shoichet, *Biomaterials* **2010**, *31*, 2555.
[45] M. J. Caicco, T. Zahir, A. J. Mothe, B. G. Ballios, A. J. Kihm, C. H. Tator, M. S. Shoichet, *J. Biomed. Mater. Res., Part A* **2013**, *101 A*, 1472.
[46] P. B. Malafaya, G. A. Silva, R. L. Reis, *Adv. Drug Delivery Rev.* **2007**, *59*, 207.
[47] P. C. Bessa, M. Casal, R. L. Reis, *J. Tissue Eng. Regener. Med.* **2008**, *2*, 81.
[48] E. A. Silva, D. J. Mooney, *Biomaterials* **2010**, *31*, 1235.
[49] N. C. Hunt, A. M. Smith, U. Gbureck, R. M. Shelton, L. M. Grover, *Acta Biomater.* **2010**, *6*, 3649.
[50] S. H. Jahromi, L. M. Grover, J. Z. Paxton, A. M. Smith, *J. Mech. Behav. Biomed. Mater.* **2011**, *4*, 1157.
[51] K. Y. Lee, D. J. Mooney, *Prog. Polym. Sci.* **2012**, *37*, 106.
[52] N. C. Hunt, R. M. Shelton, L. M. Grover, *Biomaterials* **2009**, *30*, 6435.
[53] A. M. Smith, N. C. Hunt, R. M. Shelton, G. Birdi, L. M. Grover, *Biomacromolecules* **2012**, *13*, 4032.
[54] N. C. Hunt, R. M. Shelton, D. J. Henderson, L. M. Grover, *Tissue Eng., Part A* **2013**, *19*, 905.
[55] J. W. Lee, X. Fang, N. Gupta, V. Serikov, M. A. Matthay, *Proc. Natl. Acad. Sci. USA* **2009**, *106*, 16357.
[56] O. Lindvall, Z. Kokaia, *Nature* **2006**, *441*, 1094.
[57] J. Kiernan, J. E. Davies, W. L. Stanford, *Stem Cells Transl. Med.* **2017**, *6*, 1930.
[58] B. D. Cosgrove, P. M. Gilbert, E. Porpiglia, F. Mourkioti, S. P. Lee, S. Y. Corbel, M. E. Llewellyn, S. L. Delp, H. M. Blau, *Nat. Med.* **2014**, *20*, 255.
[59] M. A. Lopez-Verrilli, F. Picou, F. A. Court, *Glia* **2013**, *61*, 1795.
[60] A. Nuschke, *Organogenesis* **2014**, *10*, 29.
[61] J. C. Garbern, R. T. Lee, *Cell Stem Cell* **2013**, *12*, 689.
[62] X. Li, K. Tamama, X. Xie, J. Guan, *Stem Cells Int.* **2016**, *2016*, 7168797.
[63] G. Caocci, M. Greco, G. La Nasa, *Mediterr. J. Hematol. Infect. Dis.* **2017**, *9*, e2017032.

[64] L. Li, X. Chen, W. E. Wang, C. Zeng, *Stem Cells Int.* **2016**, *2016*, 9682757.
[65] L. M. Marquardt, S. C. Heilshorn, *Curr. Stem Cell Rep.* **2016**, *2*, 207.
[66] S. A. Reed, E. R. Leahy, *J. Anim. Sci.* **2013**, *91*, 59.
[67] National Institute for Health and Care Excellence, *The Use of Autologous Chondrocyte Implantation for the Treatment of Cartilage Defects in the Knee Joints*, National Institute for Health and Care Excellence, London **2005**.
[68] National Institute for Health and Care Excellence, *Appraisal Consultation Document Autologous Chondrocyte Implantation for Repairing Symptomatic Articular Cartilage Defects of the Knee (Including a Review of TA89)*, National Institute for Health and Care Excellence, London **2015**.
[69] U. N. G. Wudebwe, A. Bannerman, P. Goldberg-Oppenheimer, J. Z. Paxton, R. L. Williams, L. M. Grover, *Philos. Trans. R. Soc. London B., Biol. Sci.* **2015**, *370*, 1.
[70] H. S. Vasiliadis, J. Wasiak, *Cochrane Database Syst. Rev.* **2010**, CD003323.
[71] D. Correa, S. A. Lietman, *Semin. Cell Dev. Biol.* **2016**, *62*, 67.
[72] J. F. Guo, G. W. Jourdian, D. K. MacCallum, *Connect. Tissue Res.* **1989**, *19*, 277.
[73] J. Sun, H. Tan, *Materials* **2013**, *6*, 1285.
[74] M. Baghaban Eslaminejad, L. Taghiyar, F. Falahi, *Iran. Biomed. J.* **2009**, *13*, 153.
[75] F. Guilak, D. M. Cohen, B. T. Estes, J. M. Gimble, W. Liedtke, C. S. Chen, *Cell Stem Cell.* **2009**, *5*, 17.
[76] C. M. Hwang, S. Sant, M. Masaeli, N. N. Kachouie, B. Zamanian, S.-H. Lee, A. Khademhosseini, *Biofabrication* **2010**, *2*, 35003.
[77] B. H. Choi, J.-I. I. Woo, B.-H. H. Min, S. R. Park, *J. Biomed. Mater. Res., Part A* **2006**, *79*, 858.
[78] R. F. Loeser, C. A. Pacione, S. Chubinskaya, *Arthritis Rheum.* **2003**, *48*, 2188.
[79] G. D. Weinstein, J. L. McCullough, P. Ross, *J. Invest. Dermatol.* **1984**, *82*, 623.
[80] S. Werner, T. Krieg, H. Smola, *J. Invest. Dermatol.* **2007**, *127*, 998.
[81] M. P. Rowan, L. C. Cancio, E. a Elster, D. M. Burmeister, L. F. Rose, S. Natesan, R. K. Chan, R. J. Christy, K. K. Chung, *Crit. Care* **2015**, *19*, 243.
[82] N. O'Connor, J. Mulliken, S. Banks-Schlegel, O. Kehinde, H. Green, *Lancet* **1981**, *317*, 75.
[83] G. G. Gallico, N. E. O'Connor, C. C. Compton, O. Kehinde, H. Green, *N. Engl. J. Med.* **1984**, *311*, 448.
[84] F. M. Wood, M. L. Kolybaba, P. Allen, *Burns* **2006**, *32*, 538.
[85] R. Sood, D. Roggy, M. Zieger, J. Balledux, S. Chaudhari, D. J. Koumanis, H. S. Mir, A. Cohen, C. Knipe, K. Gabehart, J. J. Coleman, *J. Burn Care Res.* **2010**, *31*, 559.
[86] D. L. Chester, D. S. Balderson, R. P. G. Papini, *J. Burn Care Rehabil.* **2004**, *25*, 266.
[87] B. Hartmann, A. Ekkernkamp, C. Johnen, J. C. Gerlach, C. Belfekroun, M. V. Küntscher, *Ann. Plast. Surg.* **2007**, *58*, 70.
[88] H. Yim, H. T. Yang, Y. S. Cho, C. H. Seo, B. C. Lee, J. H. Ko, I. S. Kwak, D. Kim, J. Hur, J. H. Kim, W. Chun, *Burns* **2011**, *37*, 1067.
[89] H. Lee, *Burns* **2012**, *38*, 931.
[90] R. S. Kirsner, W. A. Marston, R. J. Snyder, T. D. Lee, D. I. Cargill, H. B. Slade, *Lancet* **2012**, *380*, 977.
[91] R. S. Kirsner, W. Vanscheidt, D. H. Keast, J. C. Lantis, C. R. Dove, S. M. Cazzell, M. Vartivarian, M. Augustin, W. A. Marston, N. D. McCoy, D. I. Cargill, T. D. Lee, J. E. Dickerson, H. B. Slade, *Wound Repair Regen.* **2016**, *24*, 894.
[92] G. Gravante, M. C. Di Fede, A. Araco, M. Grimaldi, B. De Angelis, A. Arpino, V. Cervelli, A. Montone, *Burns* **2007**, *33*, 966.
[93] J. C. Gerlach, C. Johnen, E. McCoy, K. Bräutigam, J. Plettig, A. Corcos, *Burns* **2011**, *37*, e19.
[94] R. Sood, D. Roggy, M. Zieger, M. Nazim, B. Hartman, J. Gibbs, *Wounds* **2015**, *27*, 31.
[95] B. ter Horst, G. Chouhan, N. S. Moiemen, L. M. Grover, *Adv. Drug Delivery Rev.* **2018**, *123*, 18.
[96] I. Grant, K. Warwick, J. Marshall, C. Green, R. Martin, *Br. J. Plast. Surg.* **2002**, *55*, 219.
[97] P. Johnstone, J. S. S. Kwei, G. Filobbos, D. Lewis, S. Jeffery, *Burns* **2017**, *43*, e27.
[98] K. M. Meek, C. Knupp, *Prog. Retin. Eye Res.* **2015**, *49*, 1.
[99] G. J. Parfitt, C. Pinali, R. D. Young, A. J. Quantock, C. Knupp, *J. Struct. Biol.* **2010**, *170*, 392.
[100] R. D. Young, C. Knupp, C. Pinali, K. M. Y. Png, J. R. Ralphs, A. J. Bushby, T. Starborg, K. E. Kadler, A. J. Quantock, *Proc. Natl. Acad. Sci. USA* **2014**, *111*, 687.
[101] M. Abahussin, S. Hayes, N. E. K. Cartwright, C. S. Kamma-Lorger, Y. Khan, J. Marshall, K. M. Meek, *Invest. Ophthalmol. Visual Sci.* **2009**, *50*, 5159.
[102] S. D. Hanlon, A. R. Behzad, L. Y. Sakai, A. R. Burns, *Exp. Eye Res.* **2015**, *132*, 198.
[103] S. Chen, M. F. Young, S. Chakravarti, D. E. Birk, *Matrix Biol.* **2014**, *35*, 103.
[104] I. Jiro, K. Kenji, I. Ikuo, K. Masakazu, S. Chie, K. Shigeru, *Prog. Retinal Eye Res.* **2000**, *19*, 113.
[105] S. M. Thomasy, V. K. Raghunathan, M. Winkler, C. M. Reilly, A. R. Sadeli, P. Russell, J. V. Jester, C. J. Murphy, *Acta Biomater.* **2014**, *10*, 785.
[106] T. Bourcier, F. Thomas, V. Borderie, C. Chaumeil, L. Laroche, *Sci. Rep.* **2003**, *87*, 834.
[107] R. R. Mohan, R. Gupta, M. K. Mehan, J. W. Cowden, S. Sinha, *Exp. Eye Res.* **2011**, *91*, 238.
[108] S. S. Chaurasia, R. R. Lim, R. Lakshminarayanan, R. R. Mohan, *J. Funct. Biomater.* **2015**, *6*, 277.
[109] M. Ahuja, A. S. Dhake, S. K. Sharma, D. K. Majumdar, *Am. Assoc. Pharm. Sci.* **2008**, *10*, 229.
[110] S. Sriram, D. J. Gibson, P. Robinson, L. Pi, S. Tuli, A. S. Lewin, G. Schultz, *Exp. Eye Res.* **2014**, *125*, 173.
[111] A. Munin, F. Edwards-lévy, *Phamaceutics* **2011**, *3*, 793.
[112] R. Y. Reins, S. D. Hanlon, S. Magadi, A. M. Mcdermott, *PLoS One* **2016**, *11*, e0152889.
[113] U. Nagaich, N. Jain, *J. Sci. Soc.* **2013**, *40*, 90.
[114] R. Mao, J. Tang, B. G. Swanson, *Carbohydr. Polym.* **2000**, *41*, 331.
[115] M. W. Tibbitt, K. S. Anseth, *Biotechnol. Bioeng.* **2009**, *103*, 655.
[116] S. R. Moxon, M. E. Cooke, S. C. Cox, M. Snow, L. Jeys, S. W. Jones, A. M. Smith, L. M. Grover, *Adv. Mater.* **2017**, *29*, 1605594.
[117] Y. He, F. Yang, H. Zhao, Q. Gao, B. Xia, J. Fu, *Sci. Rep.* **2016**, *6*, 29977.
[118] T. Boland, X. Tao, B. J. Damon, B. Manley, P. Kesari, S. Jalota, S. Bhaduri, *Mater. Sci. Eng. C* **2007**, *27*, 372.
[119] B. Duan, L. A. Hockaday, K. H. Kang, J. T. Butcher, *J. Biomed. Mater. Res., Part A* **2013**, *101 A*, 1255.
[120] R. Chang, J. Nam, W. Sun, *Tissue Eng., Part A* **2008**, *14*, 41.
[121] M. B. Goldring, S. R. Goldring, *Ann. N. Y. Acad. Sci.* **2010**, *1192*, 230.
[122] A. J. Sophia Fox, A. Bedi, S. A. Rodeo, *Sports Health* **2009**, *1*, 461.
[123] S. E. Campbell, V. L. Ferguson, D. C. Hurley, *Acta Biomater.* **2012**, *8*, 4389.
[124] B. M. Gillette, J. a Jensen, B. Tang, G. J. Yang, A. Bazargan-Lari, M. Zhong, S. K. Sia, *Nat. Mater.* **2008**, *7*, 636.
[125] E. A. B. Hughes, S. C. Cox, M. E. Cooke, O. G. Davies, R. L. Williams, T. J. Hall, L. M. Grover, *Adv. Healthcare Mater.* **2018**, https://doi.org/10.1002/adhm.201701166.

Acta Biomaterialia 78 (2018) 320–328

Contents lists available at ScienceDirect

Acta Biomaterialia

journal homepage: www.elsevier.com/locate/actabiomat

Full length article

Matrix degradation in osteoarthritis primes the superficial region of cartilage for mechanical damage

Megan E. Cooke [a,b,*], Bernard M. Lawless [c], Simon W. Jones [b], Liam M. Grover [a]

[a] School of Chemical Engineering, University of Birmingham, Birmingham, UK
[b] MRC ARUK Centre for Musculoskeletal Ageing, QE Hospital, University of Birmingham, Birmingham, UK
[c] Department of Mechanical Engineering, University of Birmingham, Birmingham, UK

ARTICLE INFO

Article history:
Received 21 February 2018
Received in revised form 23 June 2018
Accepted 17 July 2018
Available online 29 July 2018

Keywords:
Osteoarthritis
Viscoelastic
Dynamic mechanical analysis
Cartilage
Thermogravimetric analysis

ABSTRACT

Osteoarthritis (OA) is a degenerative disease that affects 25% of the world's population over fifty years of age. It is a chronic disease of the synovial joints, primarily the hip and knee. The main pathologies are degradation of the articular cartilage and changes to the subchondral bone, as a result of both mechanical wear and a locally elevated inflammatory state. This study compares the viscoelastic properties of cartilage that represents the biochemical changes in OA and age-matched healthy tissue. Further, the mechanical damage induced by this compressive loading cycle was characterised and the mechanism for it was investigated. The storage modulus of OA cartilage was shown to be significantly lower than that of healthy cartilage whilst having a higher capacity to hold water. Following mechanical testing, there was a significant increase in the surface roughness of OA cartilage. This change in surface structure occurred following a reduction in sulphated glycosaminoglycan content of the superficial region in OA, as seen by alcian blue staining and quantified by micro X-ray fluorescence. These findings are important in understanding how the chemical changes to cartilage matrix in OA influence its dynamic mechanical properties and structural integrity.

Statement of significance

Cartilage has a very specialised tissue structure which acts to resist compressive loading. In osteoarthritis (OA), there is both mechanically- and chemically-induced damage to cartilage, resulting in severe degradation of the tissue. In this study we have undertaken a detailed mechanical and chemical analysis of macroscopically undamaged OA and healthy cartilage tissue. We have demonstrated, for the first time in human tissue, that the mechanical degradation of the tissue is attributed to a chemical change across the structure. In macroscopically undamaged OA tissue, there is a reduction in the elastic response of cartilage tissue and an associated destabilisation of the matrix that leaves it susceptible to damage. Understanding this allows us to better understand the progression of OA to design better therapeutic interventions.

1. Introduction

In osteoarthritis (OA), a degenerative disease of synovial joints, there are both mechanical and inflammation-induced processes that result in changes to joint tissues [1–3]. Of these, the most commonly reported is degeneration of hyaline cartilage, whilst there are also pathological changes to the subchondral bone and synovium [4,5]. Cartilage is avascular and therefore has a limited capacity for self-repair, so structural damage to its surface is largely irreversible. It has three main non-water components: chondrocytes, a network of collagen type II (Col II), and proteoglycans. These proteoglycans bind water, which, in turn, makes up between 70–80% of cartilage by weight [6,7]. The distribution and alignment of these three constituents results in a graduated tissue structure which brings about distinct mechanical properties [8].

Mechanically, cartilage provides both a low-friction surface for articulation of the joint and acts to transmit compressive loading forces to the underlying subchondral bone. Similar to many other tissues in the body, it exhibits time-dependent viscous and elastic

* Corresponding author at: School of Chemical Engineering, University of Birmingham, Birmingham, UK
E-mail address: megan.cooke.research@gmail.com (M.E. Cooke).

https://doi.org/10.1016/j.actbio.2018.07.037
1742-7061/

behaviour in both compression and tension [9]. The superficial region consists of Col II fibres oriented parallel to the articulating surface giving local tensile strength. This collagen network becomes more disordered in the middle region and in the deep zone and through the tidemark, fibres are aligned perpendicular to the articulating surface. In OA, the Col II network deteriorates, starting from the articulating surface in early OA and progressing through the tissue with increasing OA severity, as measured by Hollander et al., using Mankin grading [10]. Aggrecan, the most common proteoglycan, is found primarily in the middle and deep zones. It is the second most abundant protein in cartilage following Col II and it sits along a hyaluronic acid backbone. Individual aggrecan molecules have sulphated glycosaminoglycan (sGAG) chains (keratan and chondroitin sulphate) coming from the aggrecan core protein that form a bottle-brush structure. These sGAG chains have a negative charge resulting in a high binding affinity to water.

The binding of water to proteoglycans is partly responsible for the compressive mechanical properties of cartilage. The carboxyl and sulphate groups of chondroitin sulphate and sulphate group of keratan sulphate provide fixed charge density (FCD) to the tissue, which, in combination with repulsion between neighbouring negatively charged chains results in a high osmotic pressure [11]. In healthy cartilage this pressure is compensated by the Col II network which restricts over-swelling and allows the tissue to resist compressive forces [11]. In OA an increase in matrix metalloproteins (MMPs) and aggrecanases, particularly members of the ADAMTS (A Disintegrin and Metalloproteinase with Thrombospondin motifs) family, have been identified as primary factors in the catabolism of articular cartilage matrix proteins including aggrecan and Col II [2,10]. Changes in these matrix components have been shown to affect the mechanical properties of human cartilage [12] and the dynamic mechanical properties of canine tissue with destabilisation-induced OA [13].

The viscoelastic properties of a material can be quantified by numerous methods including creep, stress relaxation and dynamic mechanical analysis (DMA). Unlike creep and stress relaxation which usually have long time constants, DMA is a dynamic testing method. By applying an oscillating force to a specimen and analysis of the out-of-phase displacement response, the frequency-dependent storage and loss moduli can be calculated. The storage modulus (E') describes a material's ability to store energy for elastic recoil while the loss modulus (E'') characterises the material's ability to dissipate energy [14]. Studies have examined articular cartilage at low strain rates [15,16] and others have used DMA to assess frequency-dependency of the viscoelastic properties of cartilage in bovine and human specimens [17]. However, the effects of OA on the viscoelastic properties of human cartilage have so far only been examined using indentation methods and these looked at femoral head cartilage, where the direction and magnitude of loading is harder to define [18].

Changes to both the mechanical and physicochemical properties of cartilage are of interest in osteoarthritis, and physical techniques for tissue analysis are becoming more commonly utilised. As such, quantitative mapping of chemical elements present in tissues is now possible using micro X-ray fluorescence. This gives good spatial resolution of elements and has been used in a number of tissues including cartilage [19–21]. Other quantitative techniques that are traditionally used in materials science but not biological analysis such as thermogravimetric analysis are also being transferred to understand the chemical structure of tissues and biomaterials. Cartilage is interesting thermogravimetrically due to its high water content, and such, the changes in hydration in different disease states and from different anatomical locations are interesting when considering the importance of water on the inherent mechanical properties of cartilage [22]. In OA, there is an observed change in the joint surface as cartilage becomes fibrillated. Interferometry is a commonly used technique in the analysis of surfaces but as yet its use in characterising biological surfaces is infrequent. These techniques can all be used to enhance knowledge and understanding of biological tissues.

Varus knee alignment as measured by the femorotibial angle has been shown to be a key factor for development and progression of OA [23]. In this position, the medial aspect of the knee joint experiences more damaging mechanical loading, as seen by a larger reduction in cartilage thickness [24]. However, the local inflammatory environment affects both aspects of the joint equally as the synovial fluid fills the joint space. In this study we have used human cartilage from the lateral aspect of the femoral condyles (Fig. 1) of OA subjects. This tissue is exposed to the same chemical environment but is macroscopically undamaged. As yet, no one has studied the links between the early mechanical and chemical changes to human OA cartilage. Therefore, the aim of this study was to determine the dynamic mechanical properties at a range of physiological frequencies and undertake a detailed chemical analysis to understand the differences observed in early, less structurally degraded, OA and healthy cartilage from the same anatomical region.

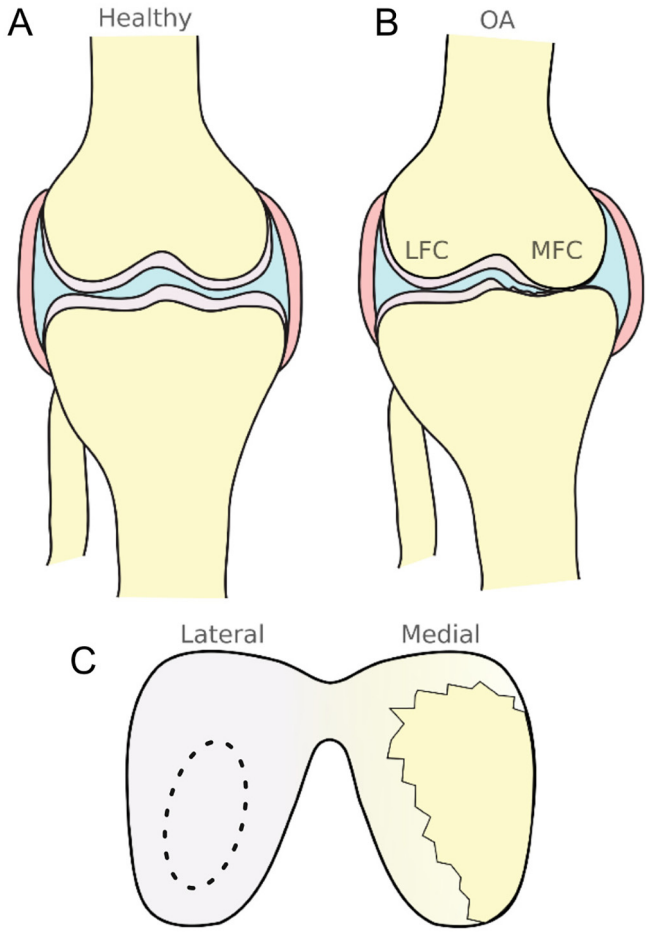

Fig. 1. Representation of healthy (A) and OA (B,C) joint structures. Varus loading in OA causes a reduced joint space in the medial aspect such that cartilage of the medial aspect including the medial femoral condyle (MFC) undergoes severe mechanical degradation, revealing the underlying subchondral bone. The lateral aspect of the joint maintains a wider joint spacing such that tissue of the lateral femoral condyle (LFC) experiences less mechanical damage. The dashed region in C indicates where cartilage explants were taken for this study.

2. Methods

2.1. Materials

All materials listed below were supplied by Sigma Aldrich, Gillingham, UK unless otherwise stated.

2.2. Tissue source and preparation

OA tissue was donated by consenting patients following elective total knee replacement and was approved by the United Kingdom National Research Ethics Service (Nottingham Research Ethics Committee 1 (05/Q2403/24)). Ethical approval was also obtained (Derby Research Ethics Committee 1 (11/H0405/2)) to collect non-OA knee cartilage from post mortem donors (mean ± SEM age: 74 ± 5 years) (Kings Mill Hospital, Sutton in Ashfield, UK) with no history of joint pain or evidence of cartilage fibrillation based on chondropathy assessment. Consent was obtained from all patients or their families.

Medial patellofemoral OA was diagnosed radiographically, by a narrowing of the joint space; healthy tissue was donated post mortem by patients with no history of joint disease and with no gross evidence of OA. 22 healthy cartilage explants were taken from 6 subjects and 37 OA explants were taken from 14 subjects; further details are shown in Table 1.

Full thickness cartilage was excised from the underlying subchondral bone of the lateral femoral condyle using a scalpel, as indicated by the dashed region in Fig. 1. This region has been shown to be less mechanically loaded in OA than the medial side [25]. Cylindrical cartilage explants of 5.2 mm diameter were then produced using a cork borer. Each specimen underwent one freeze–thaw cycle; freezing and thawing has been shown to not alter the dynamic properties of cartilage [26].

2.3. Dynamic mechanical analysis (DMA)

The viscoelastic properties of healthy and OA specimens were quantified using a Bose ElectroForce 3200 testing machine and the accompanying Bose WinTest 4.1 DMA software (TA Instruments, New Castle, DE, USA). Prior to testing, cartilage specimens were fully hydrated in Ringer's solution for 30 min before being removed from the solution for testing. Cartilage specimens were placed on an aluminium base plate and were loaded using a 20 mm cylindrical compression platen that made contact with the articulating surface. Similar to previous cartilage studies, a sinusoidal compressive force of 16 to 36 N was applied to each specimen [27–30]. As the cartilage specimens were 5.2 mm in diameter, the peak load of 36 N induced a peak stress of 1.7 MPa which is similar to the estimated physiological peak stress during walking [31]. The mean applied stress was 1.22 MPa and the amplitude of applied stress was 0.95 MPa; the applied strain was 1.8–4.8% depending on specimen thickness. Before applying a frequency sweep, each specimen was preloaded to 3 N (to avoid initial slipping) and subjected to two preconditioning cycles. 1500 and 3000 cycles at 25 and 50 Hz respectively were applied, with 60 s between them, to achieve a dynamic 'steady-state' which has been stated to occur after around 1200 to 4500 preconditioning cycles for *ex vivo* cartilage [27,32,33]. The shift in mean level of displacement following these cycles is shown in Appendix Fig. A.8A as some excess fluid was removed. Following preconditioning, eight different physiologically-relevant sinusoidal frequencies (1, 8, 10, 12, 29, 49, 71 and 88 Hz for 17, 61, 73, 85, 190, 314, 450 and 555 cycles respectively) were applied to each cartilage specimen in order of increasing frequency [27]. The total testing time for each specimen was limited to 6 min and 35 s to reduce dehydration of the samples. For each frequency, the WinTest DMA software performed Fourier analyses of the sinusoidal force and displacement waves. From this analysis, the magnitudes of the load (F^*) and displacement (d^*), the phase lag (δ) and the frequency were quantified [32,34]. The viscoelastic properties, complex stiffness (k^*), storage stiffness (k') and loss stiffness (k'') were then calculated using:

$$k^* = \frac{F^*}{d^*} \tag{1}$$

$$k' = k^* cos\delta \tag{2}$$

$$k'' = k^* sin\delta \tag{3}$$

The storage (E') and loss (E'') moduli were then calculated, using a shape factor (SF)

$$SF = \frac{\pi d^2}{4t} \tag{4}$$

$$E' = \frac{k'}{SF} \tag{5}$$

$$E'' = \frac{k''}{SF} \tag{6}$$

For Eq. (4), d) is the specimen diameter (5.2 mm) and (t) is the specimen thickness which was measured as below.

2.4. Cartilage thickness

The thickness of each cartilage specimen was measured using a needle thickness test following DMA. Briefly, a sharp needle was attached to the machine's displacement transducer (1 μm resolution) and the needle was pushed through the full thickness of the cartilage specimen. Further details of this technique are described elsewhere [35].

2.5. Thermogravimetric analysis

The mass change relating to water loss in healthy and OA cartilage samples was measured using thermogravimetric analysis (TGA) in air. Cartilage explants were heated from 25–250 °C at a rate of 1 K.min^{-1} and gas flow rate of 30 ml.min^{-1} using a TG209 F1 (Netzsch, Germany) in aluminium oxide crucibles with lids (Netzsch, Germany). A background correction of the crucible environment was performed prior to testing cartilage samples. The mass was measured continually during heating and the change in mass plotted; the rate of mass change was calculated by the accompanying Netzsh TA4 software (Netzsch, Germany).

2.6. Micro-X-ray fluorescence (μXRF)

Elemental maps of cartilage sections were generated using a M4 Tornado μXRF system and accompanying M4 software (Bruker Nano Gmbh, Berlin, Germany). 30 μm cartilage sections were mapped with a pixel size of 20 μm and scanning at 100 ms/px under vacuum of 200 mbar. The distribution of sulphur was imaged and quantified in different regions of OA and healthy

Table 1
Age and genders of the 20 patients whose cartilage was studied, n (explants) corresponds to specimens used for DMA.

Tissue	n (explants)	Age	Gender	Thickness (mm)
Healthy	6 (22)	76 (53–87)	M = 3	1.465 ± 0.240
OA	14 (37)	71 (56–81)	M = 10	1.463 ± 0.206

cartilage without and with mechanical testing protocols applied to it. Absolute quantification was used to compare sulphur content between samples; relative quantification was used to visualise calcium, phosphorus and sulphur content (M4 software).

2.7. Tissue sectioning and histology

Sections were snap-frozen in liquid nitrogen and embedded in TissueTek OCT (optimal cutting temperature) compound (Sakura, Finetek, Torrance, CA, USA) for sectioning using an OFT5000 cryostat (Bright Instruments Ltd, Luton, UK). 10 μm sections were fixed to slides and kept at −20 °C until staining. OCT was washed twice with dH_2O before an alcian blue working solution of (in 3% acetic acid) was added for 10 min. Following staining, sections were dehydrated using 50, 70, 90, 95 and 100% ethanol before clearing with xylene and mounting with DPX (distyrene, plasticiser and xylene) resin (Honeywell-Fluka, NJ, US).

2.8. Interferometry

A MicroXAM Interferometer (KLA Tencor, UK) was used to map and quantify surface roughness of healthy and OA cartilage explants both untested and after DMA testing. For each 5.2 mm diameter cartilage explant, 9 216 x 198 nm regions were imaged, stitched and areal surface roughness (Sa) was calculated using Scanning Probe Image Processor software (Image Metrology, Denmark).

2.9. Data analysis and statistical methods

Statistical analysis was performed using Prism 7 (GraphPad, CA, USA). Two-way ANOVA with Tukey's post hoc testing for multiple comparisons was used for mechanical data. Student's t-tests were used to compare differences between healthy and OA tissues, and also between samples tested and untested by DMA. Results where $p < 0.05$ were considered significant. Logarithmic frequency dependent behaviour was described by Eqs. (7) and (8), where (f) refers to frequency.

$$E' = Aln(f) + B \tag{7}$$

$$E'' = Cln(f) + D \tag{8}$$

3. Results

3.1. Viscoelastic properties of healthy and OA specimens

The frequency dependence of the storage (E') and loss (E'') moduli are shown in Figs. 2A and 2B for healthy and OA cartilage respectively. The storage modulus of both healthy and OA cartilage was logarithmically frequency dependent and the behaviour plateaued from around 50 Hz (Fig. 2A). Results of two-way ANOVA/Tukey showed that in both the loss and storage modulus, there were significant effects of frequency ($p < 0.001$), the effects of disease in relation to frequency were significant in the storage modulus ($p < 0.001$) but not in the loss modulus ($p = 0.002$). Students t-tests of the mean moduli values showed that the storage modulus of healthy cartilage was significantly higher ($p < 0.05$) than that of OA cartilage at all frequencies with the exception of 88 Hz ($p = 0.058$), as shown in Appendix Table A.4. The loss moduli were also logarithmically frequency dependent and plateaued around 50 Hz. Table 2 shows the values which satisfy Eqs. (7) and (8) for both E' and E''; the viscoelastic behaviour was found to be linearly logarithmic. The area inside the hysteresis loops (Fig. 3) was greater for OA specimens than healthy, at both low and high

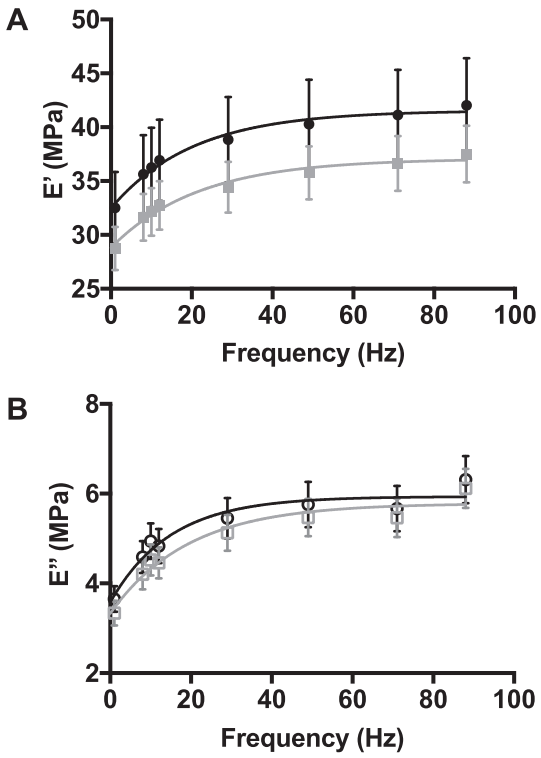

Fig. 2. A) Storage modulus (E') of healthy (•) and OA (■) cartilage with 95% confidence intervals, B) Loss modulus (E'') of healthy (○) and OA (□) cartilage with 95% confidence intervals; H n = 22, OA n = 37.

frequencies, indicating that the healthy specimens had a more elastic response. The mean level of displacement was fairly stable throughout testing (Appendix Fig. A.8B).

3.2. Thermogravimetric analysis of OA and healthy cartilage

The binding of water by the proteoglycan network provides a large contribution to the compressive properties of articular cartilage, so to elucidate the changes seen in Fig. 2, the amount of water in these samples was accurately measured. TGA was used to quantify the amount of bound water in untested and post-DMA cartilage explants from both healthy and OA subjects. Fig. 4A shows the change in % mass of OA and healthy cartilage between 25–250 °C. Between these temperatures, the loss of water was seen up to around 90 °C and a further transition started at around 210 °C. The linear region of water loss as shown in Table 3 resulted in a larger change in mass between the healthy and OA specimens (Fig. 4B). The OA samples showed a significantly larger change in mass by 100°C ($p < 0.05$) and a faster peak rate of mass change, as seen by the DTG curve (dashed line). The further change in mass to 250 °C was very similar between the healthy and OA samples, −23.76 and −23.08% respectively.

3.3. Mapping and quantification of sulphur in cartilage sections

μXRF was used to quantify the changes in aggrecan distribution in OA and healthy tissue by measuring the levels of sulphur across cartilage sections. Fig. 5 shows that in untested samples, healthy cartilage had a consistent gradient across the tissue where sulphur was most abundant in the deep zone and less so in the superficial region. OA cartilage, however, had a less regular gradient towards the surface and visually the superficial region showed minor damage to the surface even in untested samples. Following DMA, the surface of healthy cartilage was slightly deformed along the

Table 2
Storage and loss modulus coefficients as Eqs. (7) and (8) from regression analyses. All coefficients and constants values are MPa, $p < 0.05$ indicates that the logarithmic regression was significant.

Sample	Property	A	B	C	D	R^2	P
Healthy	E′	2.155	31.79	–	–	0.977	<0.05
OA	E′	1.968	28.07	–	–	0.977	<0.05
Healthy	E″	–	–	0.551	3.576	0.961	<0.05
OA	E″	–	–	0.585	3.166	0.956	<0.05

normal direction of collagen fibril alignment in this region. However, the surface was not macroscopically ruptured as seen in the OA samples. The OA cartilage had severe damage to the articulating surface post-DMA, while the middle and deep regions retained their structure. Fig. 5B shows the relative quantification of sulphur distribution across the sections. Healthy and OA sections had similar sulphur levels in the deep and middle zones, but the OA samples had lower levels in the superficial zone. Quantification of the post-DMA samples shows that in both OA and healthy samples, mechanical testing reduced the sulphur content, which is likely due to changes in aggrecan proteoglycan organisation. However, this change was more marked in the superficial region of OA samples compared to healthy. Quantification of the OA samples post-DMA was limited at the articulating surface due to the mechanically-induced damage. In Fig. 5C, co-localisation of calcium and phosphorus was evidence of mineral deposits in the cartilage. These were observed in the OA but not healthy cartilage samples.

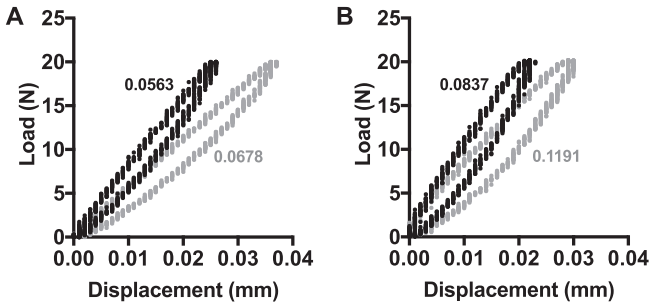

Fig. 3. Hysteresis loops of healthy (black) and OA(grey) cartilage at A)10 Hz and B) 88 Hz, inset values of hysteresis area (Nmm).

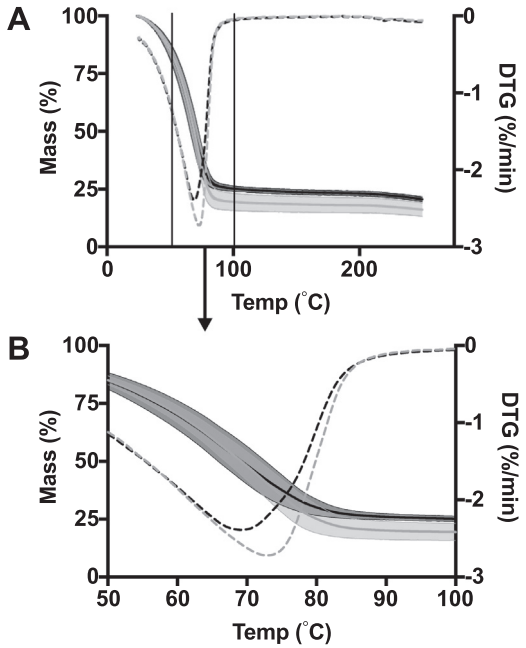

Fig. 4. Thermogravimetric analysis of OA (grey) and healthy (black) cartilage between (A) 20–250 °C. Dashed line indicates kinetics of mass change (DTG). Inset (B) shows the end of the water loss region.

3.4. Histological staining

Whilst μXRF was useful for quantifying the changes in element distribution, the resolution was limited. Therefore, in order to better visualise both the proteoglycan distribution and physical changes to the superficial region, alcian blue staining of 10 μm cartilage sections was performed. In healthy cartilage (Fig. 6A-C), there was a gradient of proteoglycan, with the heaviest staining in the deep region and getting progressively lighter towards the superficial region. Following DMA of healthy cartilage, there was no visible difference in the surface structure (Fig. 6C) from the untested sample (Fig. 6A) In OA cartilage, the distribution of proteoglycan was less ordered and there was evidence of cell clusters. Further, although there was a gradient, there were also regions of darker staining throughout the middle region (Fig. 6D). Compared to the healthy tissue, the staining was less even. There were large cracks visible in the surface with fragments of tissue detaching from the section (Fig. 6E, F).

3.5. Articulating surface damage

Following DMA, the surface region of OA cartilage samples was visibly damaged, and it was also seen in histological sections (Fig. 6). To quantify the damage, interferometry was used to measure surface roughness. Fig. 7A shows that there was no difference between healthy specimens that have and have not undergone a dynamic testing protocol. In the OA samples (Fig. 7B), the surface roughness prior to testing was significantly higher than that of the healthy samples ($p < 0.05$) indicating an initial degree of mechanical damage that was not macroscopically visible. Following DMA, the surface roughness of OA specimens was significantly higher than subject-matched samples that have not undergone DMA ($p < 0.05$).

Table 3
TG parameters of healthy and OA samples during linear water loss transition.

Sample (N)	Linear region (°C)	DTG peak (°C)	DTG peak (%/min)	Linear region mass change
Healthy (4)	52.30–78.50	69.71	−2.39	−54.22%
OA (4)	53.58–79.99	71.87	−2.74	−60.87%

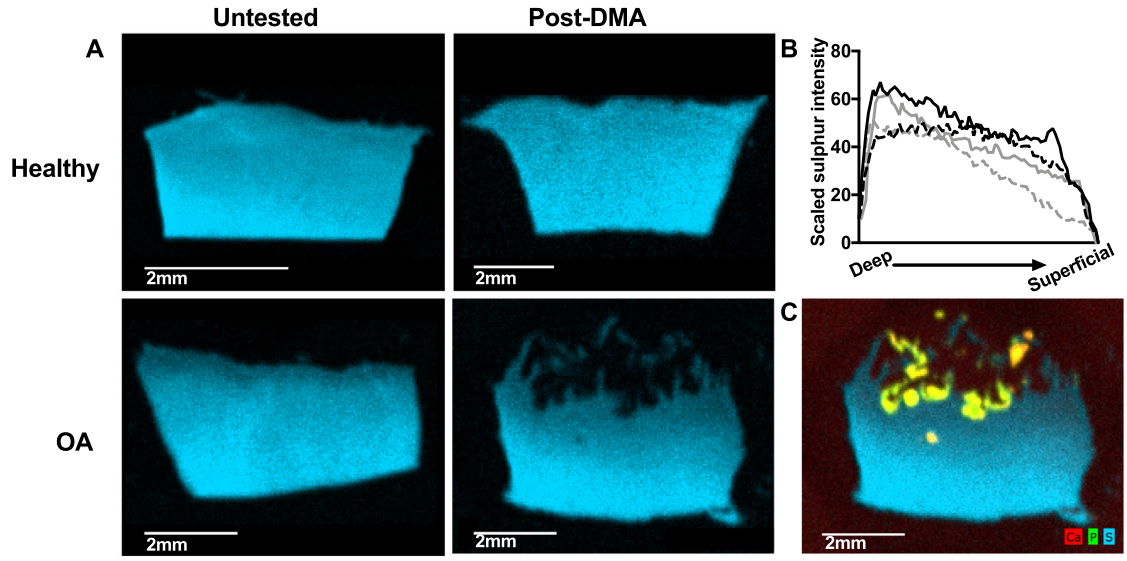

Fig. 5. A) μXRF mapping of distribution of sulphur in cartilage sections, highest intensity depicted by brighter colour closest to the bone interface at the bottom of each image. B) Quantification of sulphur across healthy (black) and OA (grey) cartilage sections that are untested (solid) and post-DMA (dashed) (n = 3). C) Sulphur, calcium and phosphorus map showing evidence of Ca and P localisation in mineral deposits.

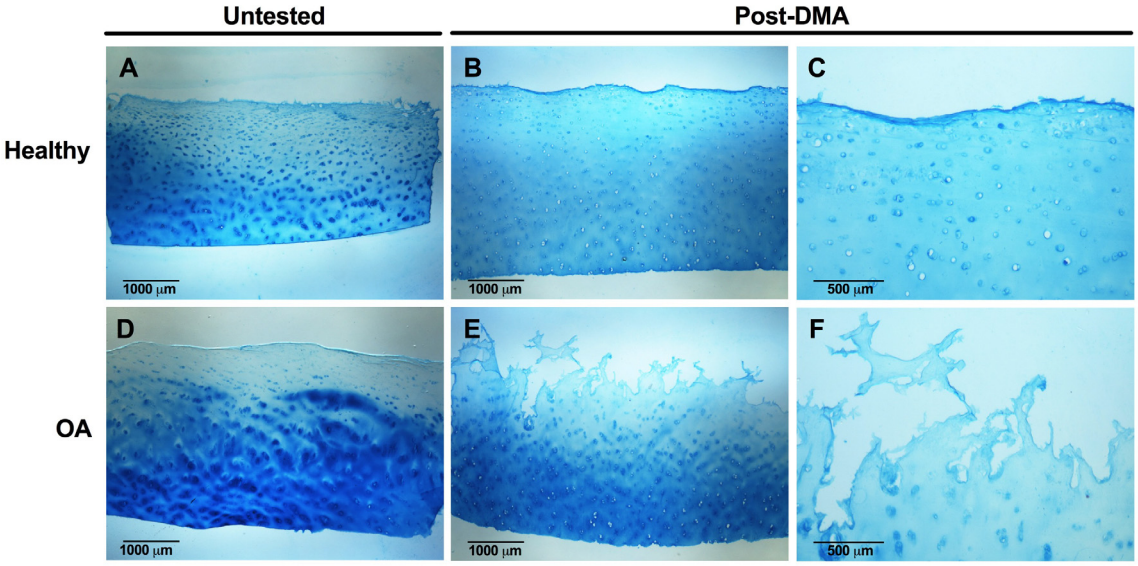

Fig. 6. Representative alcian blue staining of 10 μm thick cartilage sections from healthy (A-C) and OA (D-F) samples both untested (A, D) and post-DMA (B&C, E&F). The radial gradient observed in the lower magnification images is an artefact of the light microscope used to image these sections.

4. Discussion

This study aimed to understand the differences in frequency-dependent viscoelastic properties of isolated healthy and OA human articular cartilage and compare these to the physicochemical changes seen. Tissue was excised from the lateral aspect of the OA joint, which is known to be less exposed to mechanical stresses than the medial aspect, and thus was used to represent cartilage which was not excessively mechanically loaded but was exposed to the same chemical environment.

The first component of this study determined the viscoelastic properties of healthy and OA human cartilage. The logarithmic frequency-dependent behaviour in both the storage and loss modulus was similar to findings in human and bovine cartilage [17,29,30]. The significant reduction in storage modulus across a range of frequencies in OA specimens is likely to be indicative of disruption to the matrix structure as a result of OA cytokines, MMPs and altered joint loading. The solid matrix components of cartilage, Coll II and the aggrecan-rich proteoglycan network, are primarily responsible for the compressive stiffness of cartilage and was shown to be reduced in OA. This difference was statistically significant at all but the highest frequency, 88 Hz ($P = 0.0581$), which has previously been implicated as a frequency brought about during a rapid heel strike rise time that may predispose subjects to OA [27,36]. The storage and loss moduli of healthy femoral condyle cartilage were similar to that of 'healthy' human femoral head cartilage (obtained from subjects who had experienced a traumatic fracture of the femoral neck) and follow the same logarithmic trends [29]. The viscoelastic response in cartilage is caused by a combination of fluid flux and polymer chain

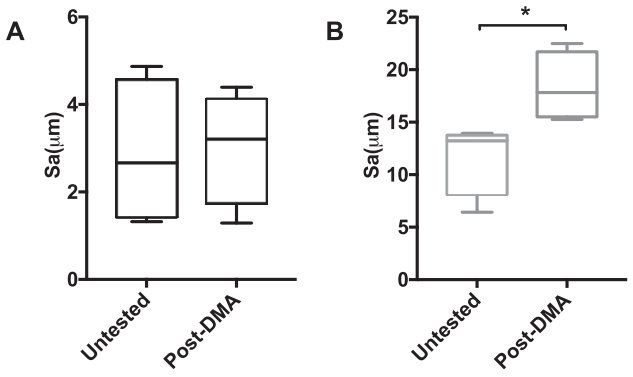

Fig. 7. Surface roughness of A) healthy and B) OA cartilage samples with or without DMA testing; $^{*}p < 0.05$.

sliding. The linear log trends seen in both moduli suggest that the compressive viscoelastic response may be dominated by the solid matrix components involved in polymer chain sliding.

Cartilage is comprised of more than 70% water, and the binding of water to proteoglycans provides high osmotic pressure, which is a key factor in the compressive properties of the tissue [11]. Therefore, the amount of water in each sample was measured by measuring the change in mass as a function of temperature. The higher water content of OA cartilage compared to healthy was shown thermogravimetrically by Sohar et al. [22]. However, their study showed the end of the water TG step at higher temperatures than seen in this study (102.25 °C and 104.60 °C compared to 78.50 °C and 79.99 °C for healthy and OA tissue respectively), which is likely due to the faster rate of heating used in their study (5 $K.min^{-1}$). The increased water content in OA samples is a result of an increased ability for the tissue to swell. This change in swelling capacity is due to breakdown of the Col II network associated with matrix catabolism in OA as measured by Bank et al. They found that an increased swelling percentage correlated with an increased percentage of degraded collagen in human samples from OA femoral head cartilage [37]. This reduces the elastic restraint on the tissue, meaning more extrafibrillar water can be held [22,38]. Cartilage swelling as a result of changes to the matrix composition has been shown previously using delayed gadolinium enhanced magnetic resonance imaging (dGEMRI), where a correlation between increased cartilage thickness and decreased GAG content was shown in the medial compartment of the knee [39]. The increased water content observed in OA samples may contribute to the similarities in loss modulus seen between healthy and OA tissue. The peak rate of mass change in the water TG step was higher in the OA samples and the peak was shifted to a higher temperature. The faster peak mass change was likely due to the increased water content, whilst the shifted peak suggests a higher binding strength of water to the PG network.

The gradient distribution of matrix components Col II and aggrecan are known to be critical to the proper mechanical functioning of cartilage. As water and its binding to PG is so important in the load-bearing capacity of cartilage, the distribution of the PG network was mapped. Benchtop μXRF was used to elementally map cartilage sections and was a simple and effective way to quantify the differences in sulphur content, corresponding to sGAG and aggrecan content in tissue samples. It is well known that the GAG content at the superficial region is lower than that of the middle and deep zones [40]. Here, however, seen by less bright pixels and quantified by line gradients from the deep to superficial zones, we saw a further reduction in the superficial region in OA cartilage. The reason for this may be proximity and contact with the synovial fluid, which, in the inflamed state of OA has a higher concentration of catabolic MMPs and cytokines [1]. Further, the identification of mineral-like deposits near the cartilage surface of OA cartilage suggested that mineralisation in OA may occur prior to visible mechanical damage to the superficial region. Tissue mineralisation of cartilage and meniscus are common in end-stage OA, usually seen as deposits of hydroxyapatite (HAp) and calcium pyrophosphate dihydrate (CPPD) crystals [41].

These mineral deposits were seen primarily in the upper middle and superficial regions of the cartilage sections; they may have a role in the observed surface damage following DMA. Relatively large (they can be seen radiographically), hard particles in a soft tissue could act as stress concentrations for cracks in cartilage to form, similar to the cracks that form following a traumatic insult to the cartilage surface [42]. Measuring the changes in surface roughness was achieved using interferometry, a technique commonly used in electronics for profiling surfaces. It enabled the quantification of the surface damage by analysing the peaks and valleys using light reflectance to quantify surface roughness. The significant increase in surface roughness following DMA in the OA subjects indicated that the superficial region was more susceptible to damage as has been shown previously in bovine tissue [43,44]. Further, the difference in Sa between healthy and OA samples observed was similar to the profile surface roughness (Ra) seen by Graindorge et al. between healthy (Ra = 1.06) and emery-roughened (Ra = 23.2) samples [45]. Whilst there was evidence of deformation of the superficial region of healthy tissue under μXRF, the superficial region of OA cartilage showed severe rupturing of the cartilage surface. Disruption to the matrix composition was likely responsible for this; as mentioned, there is a change in the collagen network originating at the articulating surface [10,46,47]. This reduces the tensile strength of the cartilage surface which reduces its ability to resist deformation.

Age-related changes to the proteoglycan content of the superficial layer of cartilage have been identified previously [11]. This effect is enhanced when the biochemical balance shifts in states such as trauma and OA causing increases in cytokines such as interleukin-1 (IL-1) and tumour necrosis factor alpha (TNFa) which drive matrix catabolism. Guilak et al. discuss the interplay between how physiological joint loading has protective mechanisms for regulating cytokine levels [48–50]. This balance between protective and damaging joint loading is likely key in the progression of OA. Another factor shown to increase the severity of OA symptoms is obesity; the increased loading on the joints due to higher body mass in combination with elevated production of adipose-derived cytokines (adipokines) [51]. These adipokines have been shown to increase production of many pro-inflammatory cytokines. Leptin, a well characterised adipokine, is increased in OA synovial fluid and has been shown to increase MMP-1 and MMP-13 production in human primary chondrocytes and to mediate greater IL-6 secretion from OA synovial fibroblasts [1,52]. Importantly in this study, while the joint loading of the OA subjects is focused in the medial compartment of the joint, the use of tissue from the lateral compartment demonstrates the important effects of the inflammatory OA environment on cartilage tissue.

Limitations: The use of human tissue samples is limiting in the number available, particularly the numbers of post mortem samples. Firstly, this means that following a power analysis, an effect size of 0.31 should be expected for the presented number of samples and an effect size of 0.48 for the 22 patients that samples were retrieved from. Secondly, due to the limited number of human samples, the testing protocols for DMA were all performed in the same order, so the loading history may affect the viscoelastic measurements. Future studies could investigate whether the loading history affects the viscoelastic response by randomising the order of frequencies during testing. Further, as the cartilage surface is semi-translucent, white light interferometry values are solely relative to surfaces with similar optical properties to cartilage.

5. Conclusions

For the first time, we have linked the local changes in chemistry and structure to the dynamic mechanical properties of OA and healthy cartilage, isolated from the same anatomical region in human donors. There is a significant reduction in the storage moduli of cartilage from OA compared to age-matched healthy subjects, indicating that in OA the elastic response of cartilage deteriorates. This reduction in storage modulus was found to be likely due to a disruption to the collagen network as OA tissues showed a higher capacity to swell and bind water. Visible changes to the cartilage surface following DMA were investigated and an increased surface roughness was observed in osteoarthritic but not healthy tissue. Finally, the mechanism for this disruption was investigated using histological staining and μXRF mapping to determine and quantify the proteoglycan distribution in both healthy and OA tissue.

Acknowledgements

MEC gratefully acknowledges funding from the EPSRC Sci-Phy-4-Health Centre for Doctoral Training (EP/ L016346/1); DMA equipment used in this study was funded by Arthritis Research UK (Grant No. H0671). OA tissue was obtained with the help of Prof Ed Davis (Royal Orthopaedic Hospital, Birmingham). The post mortem tissue was obtained with the help of Prof David Walsh (University of Nottingham) and Deborah Wilson (Kings Mill Hospital, Sutton in Ashfield, Nottingham). The authors would like to thank Hamid Sadeghi for assistance during experimentation and Daniel M. Espino for discussion on aspects of this study.

Appendix A

Table A.4
Storage Modulus mean ± SD and *p*-values.

Frequency (Hz)	Healthy n = 22	OA n = 37	p
1	32.50 ± 1.60	28.74 ± 0.98	0.039
8	35.63 ± 1.74	31.63 ± 1.08	0.043
10	36.26 ± 1.77	32.13 ± 1.09	0.040
12	36.93 ± 1.82	32.74 ± 1.11	0.041
29	38.84 ± 1.91	34.42 ± 1.16	0.040
49	40.29 ± 1.99	35.76 ± 1.21	0.043
71	41.13 ± 2.01	36.63 ± 1.25	0.050
88	42.03 ± 2.10	37.52 ± 1.30	0.058

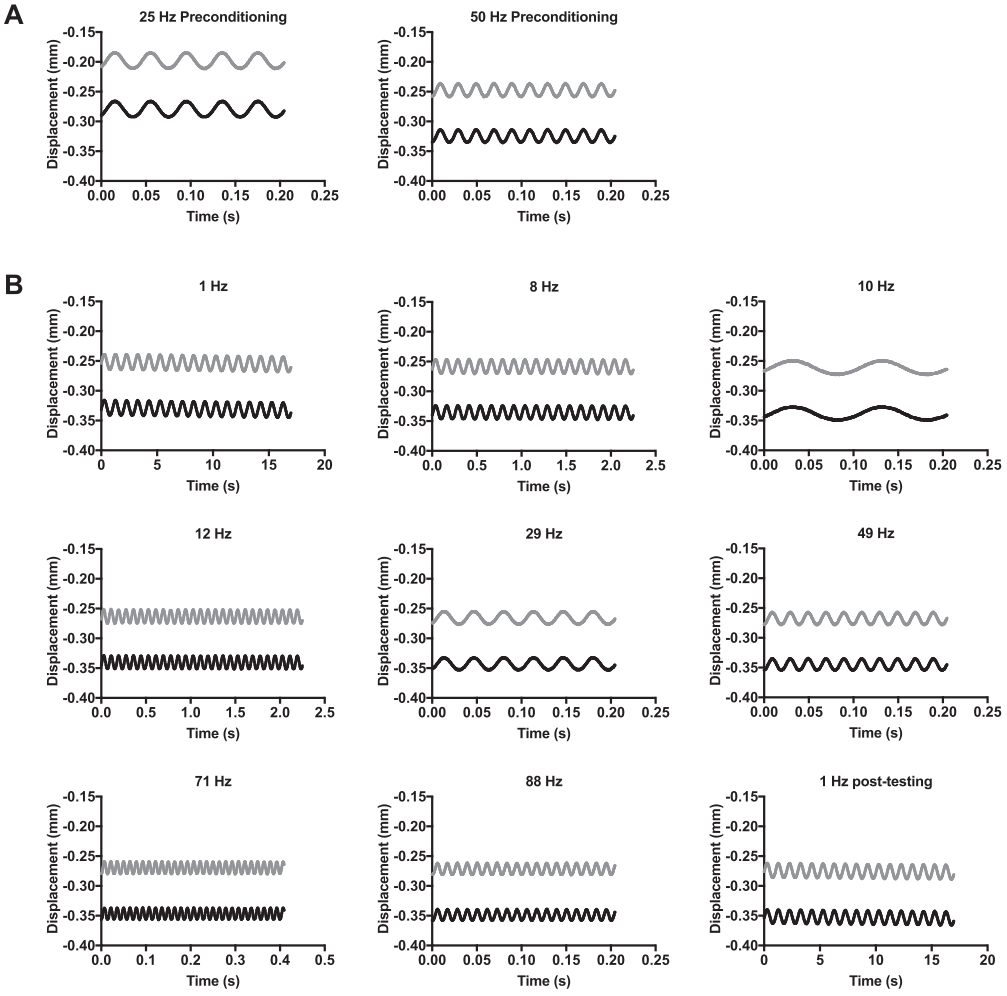

Fig. A.8. Temporal displacement of OA (grey) and healthy (black) cartilage during A) preconditioning cycles and B) testing frequencies. For a representative healthy specimen, the displacement amplitude for 1 Hz at the beginning of cycling was 0.025 mm and for 1 Hz at the end of the testing was 0.022 mm. In this OA specimen, the displacement amplitude for 1 Hz was 0.024 mm at both the start and end of the testing protocol.

References

[1] A.M. Philp, E.T. Davis, S.W. Jones, Developing anti-inflammatory therapeutics for patients with osteoarthritis, Rheumatology (Oxford, England) 56 (2017) 869–891.
[2] B. Caterson, C.R. Flannery, C.E. Hughes, C.B. Little, Mechanisms involved in cartilage proteoglycan catabolism, Matrix Biol. 19 (2000) 333–344.
[3] S.W. Jones, S.M. Brockbank, K.M. Clements, N. Le Good, D. Campbell, S.J. Read, M.R. Needham, P. Newham, Mitogen-activated protein kinase-activated protein kinase 2 (MK2) modulates key biological pathways associated with OA disease pathology, Osteoarthritis Cartilage 17 (2009) 124–131.
[4] M.B. Goldring, M. Otero, Inflammation in osteoarthritis, Curr. Opin. Rheumatol. 23 (2011) 471–478.
[5] D.P. Tonge, M.J. Pearson, S.W. Jones, The hallmarks of osteoarthritis and the potential to develop personalised disease-modifying pharmacological therapeutics, Osteoarthritis Cartilage 22 (2014) 609–621.
[6] A.J. Sophia Fox, A. Bedi, S.A. Rodeo, The basic science of articular cartilage: structure, composition, and function, Sports Health 1 (2009) 461–468.
[7] D.A. Reiter, R.A. Roque, P.-C. Lin, O. Irrechukwu, S. Doty, D.L. Longo, N. Pleshko, R.G. Spencer, Mapping proteoglycan-bound water in cartilage: Improved specificity of matrix assessment using multiexponential transverse relaxation analysis, Magn. Reson. Med. 65 (2011) 377–384.
[8] M.B. Goldring, S.R. Goldring, Articular cartilage and subchondral bone in the pathogenesis of osteoarthritis, Ann. N.Y. Acad. Sci. 1192 (2010) 230–237.
[9] S. Park, G.A. Ateshian, Dynamic response of immature bovine articular cartilage in tension and compression, and nonlinear viscoelastic modeling of the tensile response, J. Biomech. Eng. 128 (2006) 623–630.
[10] A.P. Hollander, I. Pidoux, A. Reiner, C. Rorabeck, R. Bourne, A.R. Poole, Damage to type II collagen in aging and osteoarthritis starts at the articular surface, originates around chondrocytes, and extends into the cartilage with progressive degeneration, J. Clin. Invest. 96 (1995) 2859–2869.
[11] E. Han, S.S. Chen, S.M. Klisch, R.L. Sah, Contribution of proteoglycan osmotic swelling pressure to the compressive properties of articular cartilage, Biophys. J . 101 (2011) 916–924.
[12] D.L. Robinson, M.E. Kersh, N.C. Walsh, D.C. Ackland, R.N. de Steiger, M.G. Pandy, Mechanical properties of normal and osteoarthritic human articular cartilage, J. Mech. Behav. Biomed. Mater. 61 (2016) 96–109.
[13] F. Guilak, A. Ratcliffe, N. Lane, M.P. Rosenwasser, V.C. Mow, Mechanical and biochemical changes in the superficial zone of articular cartilage in canine experimental osteoarthritis, J. Orthop. Res. 12 (1994) 474–484.
[14] K.P. Menard, Dynamic Mechanical Analysis: A Practical Introduction, CRC Press, second ed., Taylor & Francis Group, Boca Raton, 2008.
[15] J.S. Jurvelin, M.D. Buschmann, E.B. Hunziker, Mechanical anisotropy of human knee articular cartilage in compression, Trans. Orthop. Res. Soc. 217 (1996) 215–219.
[16] J.M. Fick, How the structural integrity of the matrix can influence the microstructural response of articular cartilage to compression, Connective Tissue Res. 54 (2013) 83–93.
[17] B.M. Lawless, H. Sadeghi, D.K. Temple, H. Dhaliwal, D.M. Espino, D.W.L. Hukins, Viscoelasticity of articular cartilage: analysing the effect of induced stress and the restraint of bone in a dynamic environment, J. Mech. Behav. Biomed. Mater. 75 (2017) 293–301.
[18] F. Richard, M. Villars, S. Thibaud, Viscoelastic modeling and quantitative experimental characterization of normal and osteoarthritic human articular cartilage using indentation, J. Mech. Behav. Biomed. Mater. 24 (2013) 41–52.
[19] P.M. Wrobel, S. Bała, M. Czyzycki, M. Golasik, T. Librowski, B. Ostachowicz, W. Piekoszewski, A. Surówka, M. Lankosz, Combined micro-XRF and TXRF methodology for quantitative elemental imaging of tissue samples, Talanta 162 (2017) 654–659.
[20] E.A. Hughes, S.C. Cox, M.E. Cooke, O.G. Davies, R.L. Williams, T.J. Hall, L.M. Grover, Interfacial Mineral Fusion and Tubule Entanglement as a Means to Harden a Bone Augmentation Material, 2018.
[21] N. Zoeger, P. Roschger, J.G. Hofstaetter, C. Jokubonis, G. Pepponi, G. Falkenberg, P. Fratzl, A. Berzlanovich, W. Osterode, C. Streli, P. Wobrauschek, Lead accumulation in tidemark of articular cartilage, Osteoarthritis Cartilage 14 (2006) 906–913.
[22] G. Sohár, E. Pallagi, P. Szabó-Révész, K. Tóth, New thermogravimetric protocol for the investigation of normal and damaged human hyaline cartilage, J. Therm. Anal. Calorim. 89 (2007) 853–856.
[23] G.M. Brouwer, A.W. Van Tol, A.P. Bergink, J.N. Belo, R.M. Bernsen, M. Reijman, H.A. Pols, S.M. Bierma-Zeinstra, Association between valgus and varus alignment and the development and progression of radiographic osteoarthritis of the knee, Arthritis Rheum. 56 (2007) 1204–1211.
[24] R. Moyer, W. Wirth, J. Duryea, F. Eckstein, Anatomical alignment, but not goniometry, predicts femorotibial cartilage loss as well as mechanical alignment: data from the osteoarthritis initiative, Osteoarthritis Cartilage 24 (2016) 254–261.
[25] D. Kumar, K.T. Manal, K.S. Rudolph, Knee joint loading during gait in healthy controls and individuals with knee osteoarthritis, Osteoarthritis Cartilage 2111 (2013).
[26] M. Szarko, K. Muldrew, J.E. Bertram, Freeze-thaw treatment effects on the dynamic mechanical properties of articular cartilage, BMC Musculoskeletal Disorders 11 (2010) 231.
[27] G.R. Fulcher, D.W.L. Hukins, D.E.T. Shepherd, Viscoelastic properties of bovine articular cartilage attached to subchondral bone at high frequencies, BMC Musculoskeletal Disorders 10 (2009).
[28] D.M. Espino, D.E.T. Shepherd, D.W.L. Hukins, Viscoelastic properties of bovine knee joint articular cartilage: dependency on thickness and loading frequency, BMC Musculoskeletal Disorders 15 (2014) 205.
[29] D.K. Temple, A.A. Cederlund, B.M. Lawless, R.M. Aspden, D.M. Espino, Viscoelastic properties of human and bovine articular cartilage: a comparison of frequency-dependent trends, BMC Musculoskeletal Disorders 17 (419) (2016).
[30] B. Pearson, D.M. Espino, Effect of hydration on the frequency-dependent viscoelastic properties of articular cartilage, Proc. Inst. Mech. Eng., Part H 227 (2013) 1246–1252.
[31] J.Q. Yao, B.B. Seedhom, Mechanical conditioning of articular cartilage to prevalent stresses, Br. J. Rheumatol. 32 (1993) 956–965.
[32] T. McCormack, J.M. Mansour, Reduction in tensile strength of cartilage precedes surface damage under repeated compressive loading in vitro, J. Biomech. 31 (1998) 55–61.
[33] A. Verteramo, B.B. Seedhom, Effect of a single impact loading on the structure and mechanical properties of articular cartilage, J. Biomech. 40 (2007) 3580–3589.
[34] B.M. Lawless, S.C. Barnes, D.M. Espino, D.E. Shepherd, Viscoelastic properties of a spinal posterior dynamic stabilisation device, J. Mech. Behav. Biomed. Mater. 59 (2016) 519–526.
[35] D.E.T. Shepherd, B.B. Seedhom, Thickness of human articular cartilage in joints of the lower limb, Ann. Rheum. Dis. 58 (1999) 27–34.
[36] E. Radin, K. Yang, C. Riegger, V. Kish, J. O'Connor, Relationship between lower limb dynamics and knee joint pain, J. Orthop. Res. 9 (1991) 398–405.
[37] R.A. Bank, M. Soudry, A. Maroudas, J. Mizrahi, J.M. Tekoppele, The increased swelling and instantaneous deformation of osteoarthritic cartilage is highly correlated with collagen degradation, Arthritis Rheum. 43 (2000) 2202–2210.
[38] P.J. Basser, R. Schneiderman, R.A. Bank, E. Wachtel, A. Maroudas, Mechanical properties of the collagen network in human articular cartilage as measured by osmotic stress technique, Arch. Biochem. Biophys. 351 (1998) 207–219.
[39] M.D. Crema, D.J. Hunter, D. Burnstein, F.W. Roemer, L. Li, F. Eckstein, N. Krishnan, M.-P.H. Le-Graverand, A. Guermazi, Association of changes in delayed gadolinium-enhanced MRI of cartilage (dGEMRIC) with changes in cartilage thickness in the medial tibiofemoral compartment of the knee: a 2 year follow-up study using 3.0 T MRI, Ann. Rheumatic Diseases 73 (2014) 1935–1941.
[40] A.D. Pearle, R.F. Warren, S.A. Rodeo, Basic science of articular cartilage and osteoarthritis, 2005.
[41] M. Fuerst, O. Niggemeyer, L. Lammers, F. Schäfer, C. Lohmann, W. Rüther, Articular cartilage mineralization in osteoarthritis of the hip, BMC Musculoskeletal Disorders 10 (2009) 166.
[42] H. Sadeghi, B. Lawless, D. Espino, D. Shepherd, Effect of frequency on crack growth in articular cartilage, J. Mech. Behav. Biomed. Mater. 77 (2018) 40–46.
[43] C.T. Chen, M. Bhargava, P.M. Lin, P.A. Torzilli, Time, stress, and location dependent chondrocyte death and collagen damage in cyclically loaded articular cartilage, J. Orthop. Res. 21 (2003) 888–898.
[44] E. Lucchinetti, C.S. Adams, W.E. Horton, P.A. Torzilli, Cartilage viability after repetitive loading: a preliminary report, Osteoarthritis Cartilage 10 (2002) 71–81.
[45] S. Graindorge, W. Ferrandez, E. Ingham, Z. Jin, P. Twigg, J. Fisher, The role of the surface amorphous layer of articular cartilage in joint lubrication, Proc. Inst. Mech. Eng., Part H 220 (2006) 597–607.
[46] F. Nelson, L. Dahlberg, S. Laverty, A. Reiner, I. Pidoux, M. Ionescu, G.L. Fraser, E. Brooks, M. Tanzer, L.C. Rosenberg, P. Dieppe, A. Robin Poole, Evidence for altered synthesis of type II collagen in patients with osteoarthritis, J. Clin. Invest. 102 (1998) 2115–2125.
[47] M. Nickien, A. Thambyah, N.D. Broom, How a decreased fibrillar interconnectivity influences stiffness and swelling properties during early cartilage degeneration, J. Mech. Behav. Biomed. Mater. 75 (2017) 390–398.
[48] F. Guilak, Biomechanical factors in osteoarthritis, Best Pract. Res.: Clin. Rheumatol. 25 (2011) 815–823.
[49] J. Sanchez-Adams, H.A. Leddy, A.L. McNulty, C.J. O'Conor, F. Guilak, The mechanobiology of articular cartilage: bearing the burden of osteoarthritis, Curr. Rheumatol. Rep. 16 (2014) 451.
[50] F. Guilak, B. Fermor, F.J. Keefe, V.B. Kraus, S.A. Olson, D.S. Pisetsky, L.A. Setton, J. B. Weinberg, The role of biomechanics and inflammation in cartilage injury and repair, Clin. Orthopaedics Related Res. (2004) 17–26.
[51] A.M. Philp, R.L. Collier, L.M. Grover, E.T. Davis, S.W. Jones, Resistin promotes the abnormal Type I collagen phenotype of subchondral bone in obese patients with end stage hip osteoarthritis, Sci. Rep. 7 (2017) 4042.
[52] M.J. Pearson, D. Herndler-Brandstetter, M.A. Tariq, T.A. Nicholson, A.M. Philp, H.L. Smith, E.T. Davis, S.W. Jones, J.M. Lord, IL-6 secretion in osteoarthritis patients is mediated by chondrocyte-synovial fibroblast cross-talk and is enhanced by obesity, Sci. Rep. 7 (2017) 3451.

Geometric confinement is required for recovery and maintenance of chondrocyte phenotype in alginate

Megan E. Cooke,[1,2,a)] Mark J. Pearson,[2] Richard J. A. Moakes,[1] Christopher J. Weston,[3] Edward T. Davis,[4] Simon W. Jones,[2] and Liam M. Grover[1]

[1]*School of Chemical Engineering, University of Birmingham, Edgbaston B15 2TT, United Kingdom*
[2]*Institute of Inflammation and Ageing, MRC Musculoskeletal Ageing Centre, QE Hospital, University of Birmingham, Edgbaston B15 2TT, United Kingdom*
[3]*Institute for Biomedical Research, Medical School, University of Birmingham, Edgbaston B15 2TT, United Kingdom*
[4]*The Royal Orthopaedic Hospital NHS Foundation Trust, Bristol Road South, Northfield, Birmingham B31 2AP, United Kingdom*

(Received 9 May 2017; accepted 1 September 2017; published online 9 October 2017)

Human articular chondrocytes lose their native phenotype when expanded in traditional monolayer cultures. As a consequence, hydrogel encapsulation has been investigated as a means to maintain the natural phenotype. Alginate has been widely used for cartilage engineering as it has been shown to enable the recovery of a native collagen type II expressing chondrocyte phenotype. This study has evaluated whether the capacity of the materials to maintain/revert the phenotype is due to the composition of the material or the physical entrapment provided by the gel. To achieve this, an alginate "fluid gel" (a shear-thinning structured gel system) was produced of identical chemistry to a traditionally gelled alginate structure. Both were seeded with passaged primary human articular chondrocytes. Chondrocytes in quiescent alginate showed the recovery of the native phenotype and a spherical morphology. Chondrocytes in alginate fluid gel were unable to maintain the recovered phenotype despite having a spherical morphology and were shown to have a lower level of entrapment than those in quiescent alginate. These findings indicate that geometric entrapment is essential for the maintenance of a recovered chondrocyte phenotype in alginate. https://doi.org/10.1063/1.5006752

INTRODUCTION

Osteoarthritis (OA) affects 25% of the over-50 population, which is expected to rise with the increasingly obese world population.[1,2] OA is characterized by the degeneration of articular cartilage, narrowing of the joint space, and pathological changes to subchondral bone; it is a painful and disabling condition.[3] At present, there is no cure for OA, and many patients will eventually require joint replacement surgery. The native cartilage matrix is rich in collagen type II, proteoglycans, and chondrocytes, the cartilage-matrix producing cells.[4] Critically, articular cartilage is avascular and hence has a limited capacity for self-regeneration. Indeed, it is widely believed that in end-stage OA, the cartilage loss is irreversible. Furthermore, as an avascular tissue, the delivery of pharmacological entities to the cells of the cartilage, the chondrocytes, is highly challenging.

An alternative to the pharmacological approaches being investigated to prevent OA progression is the surgical repair of focal defects in cartilage tissue in patients with early-stage

[a)]Author to whom correspondence should be addressed: mec110@bham.ac.uk

OA, via autologous chondrocyte implantation (ACI).[5] This repair strategy is dependent on the expansion of chondrocytes *in vitro* before re-implantation into the defect site.[6] Critically, expansion in 2D monolayer culture causes chondrocytes to rapidly de-differentiate, with a marked loss of their expression of type II Collagen, aggrecan, and proteoglycan, and an associated increase in the expression of type I Collagen.[7–9] This loss of chondrogenicity leads to the formation of an inferior hyaline cartilage, rich in collagen type I, which has been reported to be functionally similar to the fibro-cartilage that is formed following micro-fracture surgery.[10] Consequently, this means that the ACI process has been of limited success. Therefore, there is a need to develop an improved method for the expansion of chondrocytes *in vitro*, which can maintain the chondrocyte phenotype and thus promote regeneration of functional articular cartilage.

Hydrogels have traditionally been used in regenerative medicine to act as extracellular matrix mimics due to their high water content and high degree of tunability.[11,12] One such hydrogel is alginate, a linear, un-branched polysaccharide derived from brown algae that has been used in drug delivery, wound healing, and tissue regeneration.[13] Containing β-D-mannuronic acid (M) and α-L-guluronic acid (G) residues arranged either in blocks (GGG/MMM) or alternating sequences (GMGMGM),[13] alginate undergoes ionotropic gelation upon introduction of divalent cations to form crosslinks between G residues resulting in an "egg-box" structure.[14–16]

Previously, alginate has been shown to maintain the chondrocyte phenotype and to drive bone marrow derived mesenchymal stem cells towards a chondrogenic phenotype.[17–20] Whether this is due to the physical entrapment of the chondrocytes in a 3D scaffold or due to the chemical influence of alginate is relatively unknown. The formation of a cartilage matrix by the encapsulation of allogenic chondrocytes is a promising approach to produce cartilage for surgical implantation.

In this study, the influence of the physical entrapment of alginate on the embedded chondrocytes has been investigated by comparing markers of cartilage matrix formation when chondrocytes are embedded in an alginate gel and between the particles that are formed in an alginate fluid gel. Fluid hydrogels are produced through the introduction of shear during gelation, resulting in the production of microparticles of gel.[21–24] The microparticles interact with one another, and by doing so, they thicken in the absence of external shear stress and hence could be utilized in an injectable therapeutic solution for the delivery of chondrocytes to defects in articular cartilage. The cells dispersed within this structure are not physically entrapped as they would be in a normal, quiescently gelled structure; instead, they are suspended between fragments of crosslinked alginate (Fig. 1). They are, however, exposed to the same chemical stimuli. The aim of this study was therefore to determine the effect of different levels of encapsulation on the chondrocyte viability, morphology, and phenotype by comparing quiescent and fluid alginate.

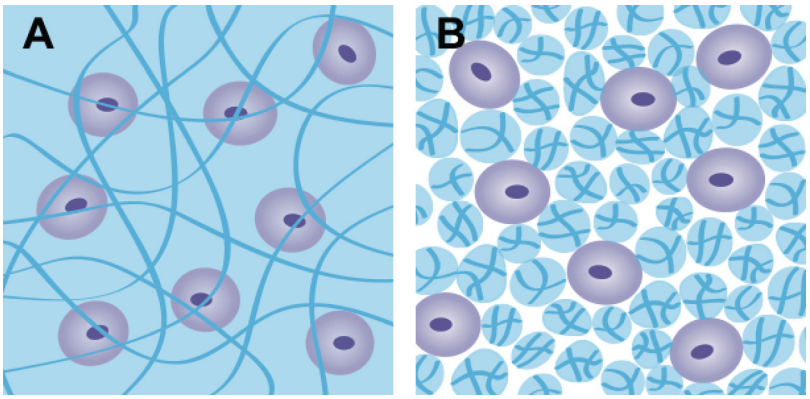

FIG. 1. Schematic of cells (a) encapsulated in quiescent alginate and (b) suspended between fragmented alginate fluid gel.

RESULTS

Primary articular chondrocytes cultured in quiescently gelled alginate retain their viability and chondrogenic phenotype

We first examined the effect of traditional monolayer culture on the chondrogenic phenotype of primary human articular chondrocytes (hACs). Freshly isolated (FI) primary hACs were found to express high amounts of type II collagen and low amounts of type I collagen, as determined by quantitative real-time polymerase chain reaction (qRT-PCR) analysis of COL2A1 and COL1A1 mRNA expression [Fig. 2(a)]. As expected, upon culturing in monolayer, primary hACs rapidly de-differentiated, adopting a more fibroblast-like morphology [Fig. 2(b)], and by passage 3, they exhibited significantly reduced ($P < 0.01$) expression of type II collagen [Fig. 2(a)]. Indeed, the expression profile of type I and type II Collagen in passaged primary hACs was similar to that observed in the chondrocyte TC28 cell line [Fig. 2(c)].

Next, we examined the effect of encapsulating primary hACs in quiescent alginate on both the cell viability and the chondrogenic phenotype over a period of 2 weeks. Following 14 days of encapsulation in alginate, cells in the scaffolds were stained using a live/dead stain (Calcein AM/ethidium homodimer-1 stain). Encapsulated primary hACs showed high levels of cell viability and displayed a flattened morphology at the edge of the constructs and a spherical morphology in the centre [Figs. 3(a) and 3(b)]. This is similar to chondrocytes in native cartilage, in contrast to the fibroblast-like morphology of primary hACs cultured in the monolayer. Analysis of COL2A1 and COL1A1 mRNA (messenger ribonucleic acid) expression over a time course of 14 days showed that primary hACs encapsulated in quiescent alginate did not de-differentiate since type II collagen expression was maintained throughout. Furthermore, encapsulation of the TC28 chondrocyte cell line in quiescent alginate suggests that they can be re-differentiated to a more native chondrocyte collagen phenotype [Figs. 3(c) and 3(d)]. In addition to measurements of collagen expression, the release of sulphated glycosaminoglycan (sGAG) side-chains was quantified over a time course of 30 days, as a marker of aggrecan proteoglycan turnover in the alginate scaffolds. Relative to alginate without cells, scaffolds containing encapsulated primary hACs or TC28s showed a significant accumulation of sGAG secretion over a period of 30 days, suggesting that alginate encapsulation supported and maintained aggrecan proteoglycan production [Fig. 3(e)].

The ability of quiescent alginate to support an anabolic chondrocyte phenotype, which produces cartilage extracellular matrix components, was then further validated by histochemical staining of alginate scaffolds. Aggrecan staining was observed in the cytoplasmic region of the chondrocytes [Fig. 3(f)].

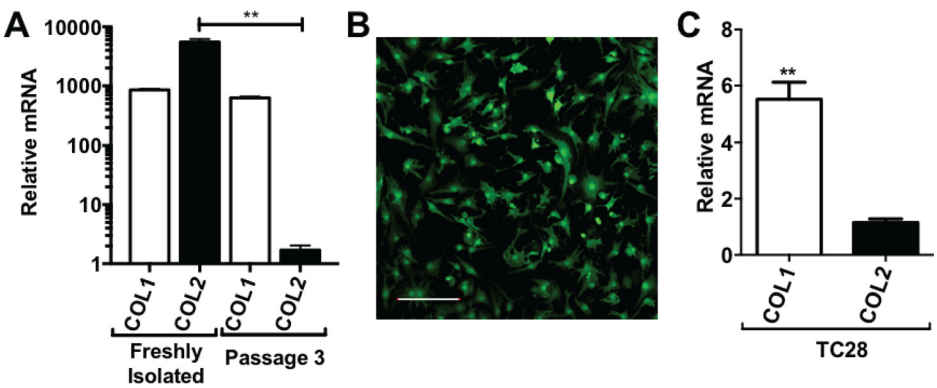

FIG. 2. (a) Relative mRNA expression of collagen types I and II in primary human chondrocytes either directly after isolation from cartilage or following 3 passages in the monolayer. (b) Passage 3 human chondrocytes exhibiting a fibroblast-like morphology (scale bar (SB): 200 μm). (c) Relative mRNA expression of collagen types I and II in the TC28 human chondrocyte cell line. **$P < 0.005$.

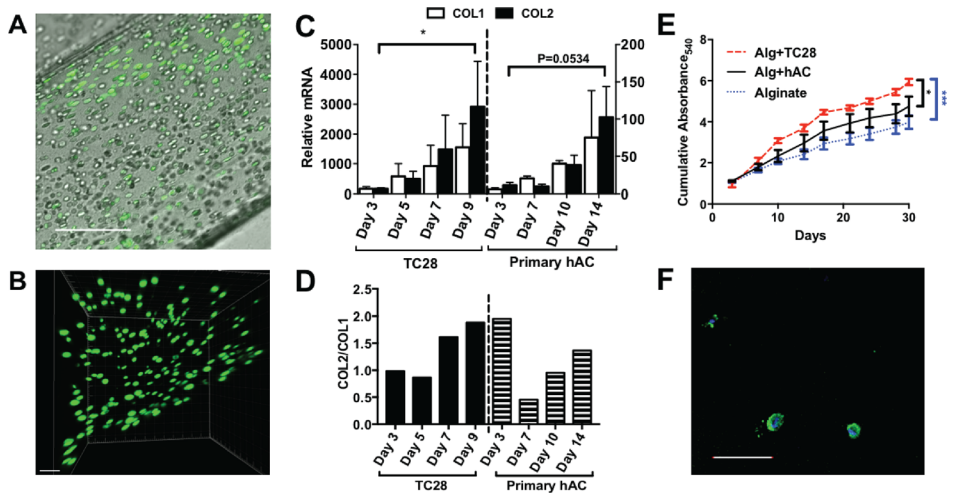

FIG. 3. (a) Primary human chondrocytes encapsulated in quiescent alginate showing a flattened morphology at the edge of the construct and a spherical morphology in the centre of the construct, SB: 200 μm. (b) z-stack demonstrating the cell morphology in 3-D, SB: 100 μm. (c) Relative expression of collagen types I and II in TC28s and primary human chondrocytes (hACs) throughout 9 and 14 days of culture, respectively, with collagen type II to type I ratios (d). (e) Cumulative production of sGAGs as detected by the DMMB assay at 9 time points over 30 days; (f) evidence of aggrecan (green) in the cytoplasmic region with nuclei counterstained with DAPI (4′,6-Diamidino-2-Phenylindole) (blue), SB: 200 μm. *: $P < 0.05$.

Formulation of a deliverable fluid alginate

An alginate fluid gel was produced by the drop-wise addition of $CaCl_2$ to sol alginate under shear. The fluid alginate architecture is characterized by fragments connected by ribbon-like structures as shown in Fig. 4(c). Following shear ramps, the alginate fluid gel alginate showed a very small hysteresis loop, indicating that this fluid material will be stable during manipulation and handling [Fig. 4(b)]. After seeding of chondrocytes, they maintained a spherical morphology and showed high levels of viability [Figs. 4(d) and 4(e)].

Dynamic small deformation rheology was performed to determine the viscoelastic properties of both the alginate quiescent and fluid gel systems. The introduction of shear during the

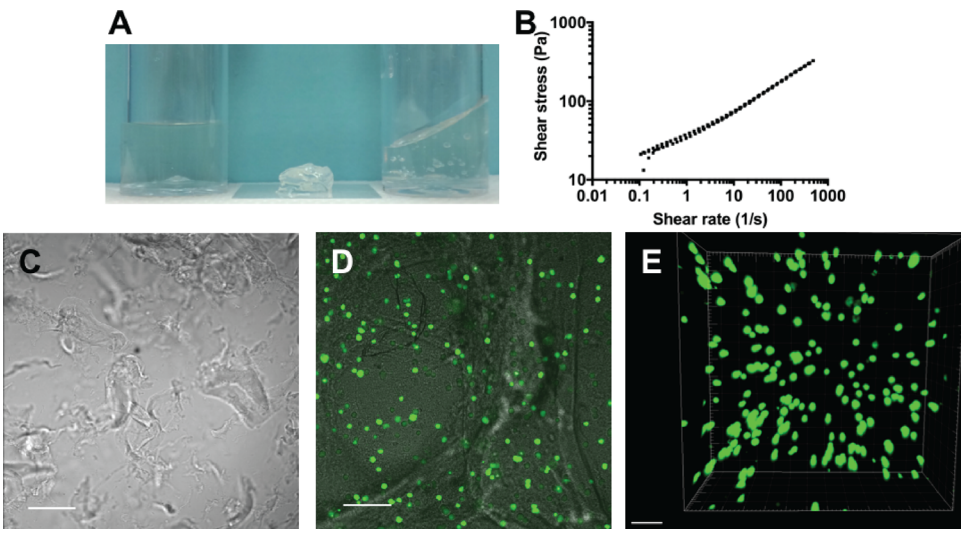

FIG. 4. (a) Sol (left), quiescent (middle), and fluid (right) alginate; (b) change in shear stress with the shear rate over continuous ramps of the shear rate from 0.1-500-0.1-500 s^{-1}; (c) fluid gel architecture (SB: 200 μm); (d) fluid gel with chondrocytes showing the interaction with alginate fragments and ribbons (SB: 100 μm); (e) z-stack of chondrocytes in fluid alginate 4 days after seeding, SB: 100 μm.

TABLE I. Storage (G′), loss (G″), and complex (G*) moduli of alginates.

	Quiescent			Fluid		
Hz/Pa	G′	G″	G*	G′	G″	G*
0.1	615.87	34.45	616.83	146.3	27.84	148.93
1	654.00	42.45	655.38	181.3	33.60	184.39
10	727.13	76.72	731.17	247.3	68.21	256.82

gelation process resulted in a reduction in the storage modulus of fluid alginate, when compared to the quiescent gels prepared under static conditions [in the absence of shear (Table I)]. The presence of weak interactions and entanglements is confirmed through linear rheology [Fig. 5(b)], with the sheared alginate showing solid-like behaviours dependent on frequency, typical of weak gels. Interestingly, the quiescent gel shows a similar mechanical spectrum (at higher G′ values) inferring structures which mirror each other, complementing data obtained via microscopy images shown in Fig. 6. Changes throughout the gel microstructure were probed through stress sweeps [Fig. 5(a)], where shortening of the linear viscoelastic region (LVR) highlights the fluid gels' ability to flow upon being stressed. Fluid alginate (closed circles) shows strong shear thinning behaviour [Fig. 5(c)], where increasing the shear to the systems causes the reversible breakdown of the entangled polymers. However, this is not observed for the quiescent gel, as increasing shear to strains above the LVR causes fracturing of the gel resulting in artefacts that resemble thinning profiles [gel fracture points highlighted in Fig. 5(c) using "#"].

Microstructural observations of fluid and quiescent alginate

To further understand the differences in the structure between the two materials, their microstructures were observed using scanning electron microscopy (SEM) following freeze drying. Fluid alginate was seen to have a less interconnected pore structure than quiescent alginate. Further, there were larger voidage regions observed throughout the fluid alginate structure, which were not seen in the quiescent microstructure (Fig. 6).

Level of cell encapsulation in fluid and quiescent alginate

To understand the level of encapsulation and confinement provided by alginate matrices of different structures, chondrocytes were imaged over time in culture. Individual chondrocytes in fluid gel were seen to move laterally across the field of view over a number of hours in the fluid alginate as well as downwards through the gel [Fig. 7(a), Multimedia view]. Chondrocytes in quiescent alginate, however, did not show as much movement over the same time-course [Fig. 7(b), Multimedia view]. Cell movement was quantified by frame-by-frame tracking, and then, the gel drift caused by contraction of the gel was normalized. Cells in fluid gel were

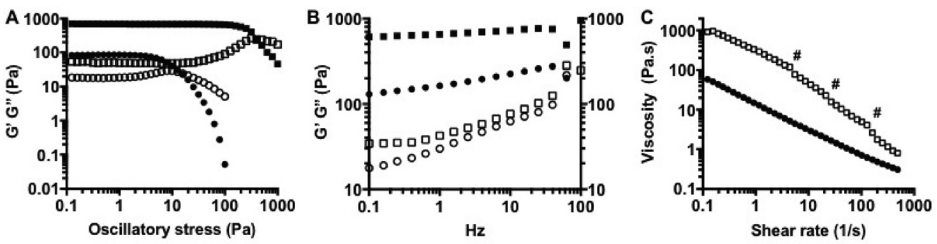

FIG. 5. (a) Oscillatory stress sweeps (0.1–100 Pa, 1 Hz, 37 °C) showing the variation in the linear viscoelastic region (LVR). (b) Mechanical spectra (0.5% strain, 37 °C) showing the variation in the storage modulus (G′) and the loss modulus (G″). C: viscosity sweeps (0.001–100 s^{-1}, 37 °C). (Quiescent alginate, squares; fluid alginate, circles; G′, filled symbols; G″, open symbols.)

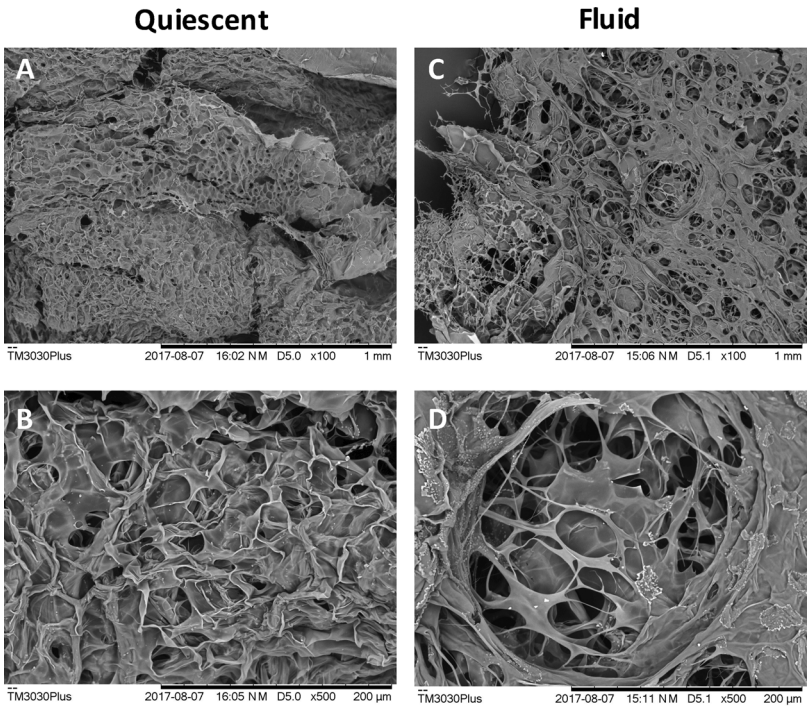

FIG. 6. SEM images of thin sections of quiescent [(a) and (b)] and fluid [(c) and (d)] following freeze drying.

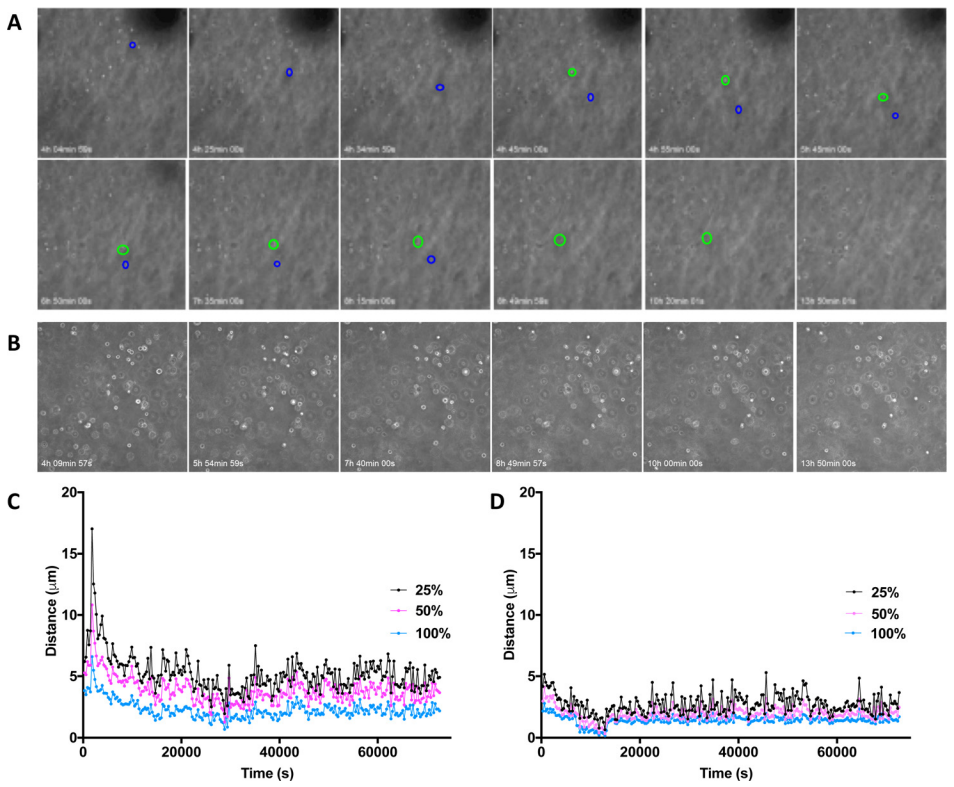

FIG. 7. Tracking of chondrocytes in (a) fluid and (b) quiescent alginate over 14 h. Movement of cells is demonstrated by coloured circles. Quantification of chondrocyte movement in 2D in (c) fluid and (d) quiescent alginate. Multimedia views: https://doi.org/10.1063/1.5006752.1; https://doi.org/10.1063/1.5006752.2

found to move further per frame than cells in the quiescent alginate, particularly 25% most motile cells [Figs. 7(c) and 7(d)].

The effect of alginate fluid gel on the phenotype of primary articular chondrocytes

To compare the efficacy of alginate fluid gel with that of quiescent alginate in supporting a chondrogenic phenotype, primary hACs were cultured in either alginate fluid gel or quiescent alginate for a period of 7 days. Following 7 days of culture, collagen type II and aggrecan expression were higher in the quiescent than fluid alginate, and sox9 expression was significantly higher in the quiescent alginate (Fig. 8).

Ex vivo cartilage explant tissue promotes the chondrogenic phenotype of primary chondrocytes encapsulated in quiescent alginate

Due to the proximity of native cartilage tissue during the ACI repair of cartilage defects, *ex vivo* cartilage tissue and cartilage conditioned media (CM) were studied to determine their effect on the efficacy of using fluid and quiescent alginate as chondrocyte-carrying matrices. Following the encapsulation of a hAC population in quiescent alginate, the presence of a cartilage explant tissue [Fig. 9(a)] resulted in an increase in the expression of COL2A1 [Fig. 9(b)] following 14 days of culture. The effect of the physical presence of cartilage tissue was shown to be secondary to the factors released from it [Fig. 9(b)] since conditioned cartilage explant

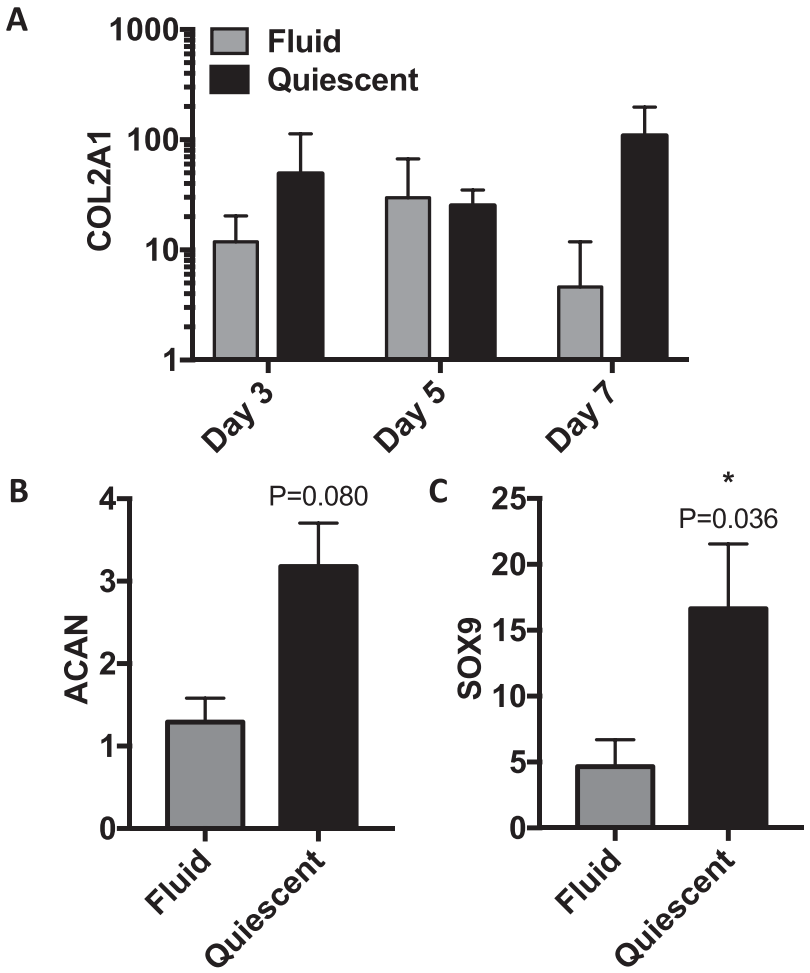

FIG. 8. Relative mRNA expression of (a) collagen type II, (b) aggrecan (day 7), and (c) sox9 (day 7) in chondrocytes seeded in fluid and quiescent alginate.

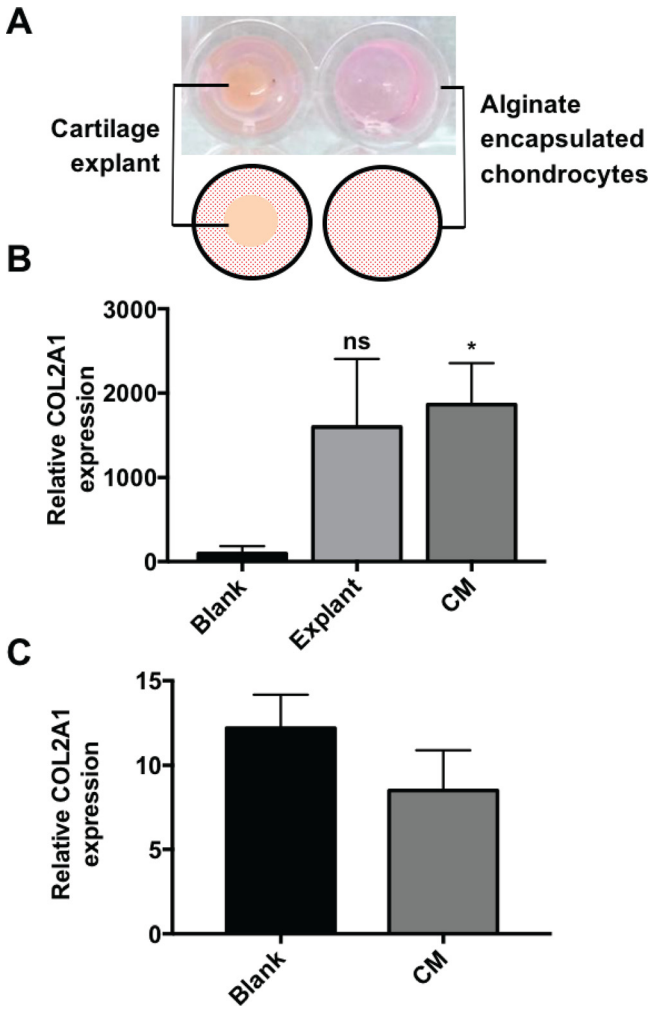

FIG. 9. (a) Experimental set-up for explant (left) and blank/conditioned media (CM) (right). Relative collagen type II expression in (b) quiescent and (c) fluid alginate when cultured with basal media (blank), a cartilage explant, or conditioned media.

media resulted in a greater increase ($P = 0.0376$) in collagen type II expression than the cartilage tissue. This suggests that in the *in vivo* environment, alginate encapsulation of hACs will be even more efficacious in promoting and maintaining the chondrogenic phenotype due to the secretion of endogenous anabolic factors from the surrounding cartilage matrix. This condition was then investigated to determine if it could be used to drive the native alginate phenotype in fluid alginate culture. However, when comparing conditioned and basal media, there was no significant difference between the conditions [$P = 0.3126$, Fig. 9(c)]; this further supports that physical entrapment of chondrocytes is critical to maintenance of the native collagen type II phenotype.

DISCUSSION

Alginate has been investigated for cartilage repair and regeneration strategies over the last three decades since it has been shown to support the redifferentiation of chondrocytes that have lost their native collagen type II and proteoglycan-producing phenotype.[27–29] The mechanism of this effect is relatively unknown but has been attributed to the chondrocyte morphology, ligand adhesion, and matrix mechanical properties.[9,30] Here, we aim to resolve the difference between the geometric and chemical influences of alginate.

The findings of this study support previous observations that chondrocytes are not phenotypically stable in 2D culture on untreated tissue culture plastic, with freshly isolated primary human knee OA chondrocytes rapidly losing collagen type II expression and adopting a fibroblast-like morphology within 3 passages. This is a well-known phenomenon in chondrocyte culture and has been attributed to the change in the morphology when cultured on a stiff substrate.[8,27,29] In contrast, when primary chondrocytes were geometrically confined by encapsulation in quiescent alginate, they maintained native morphologies depending on the construct region, akin to native chondrocytes in articular cartilage tissue.[31] Additionally, we found that primary human chondrocytes remained viable for up to 14 days of culturing in quiescent alginate constructs. Importantly, our data demonstrate that this geometric confinement of human chondrocytes in quiescent alginate promotes a chondrogenic phenotype with maintenance of collagen type II expression and aggrecan proteoglycan production. These data support the findings of Murphy and Sambanis who showed that the maintenance of the spherical chondrocyte morphology is necessary for the recovery of the chondrogenic phenotype following monolayer culture.[32]

Since the use of a quiescent alginate hydrogel construct for the regeneration of articular cartilage would require highly invasive surgery, we then examined whether alginate fluid gel, which would be more suitable for intra-articular injection, would exhibit the same chondrogenic promoting properties. Using the same alginate solution as that used to produce the quiescent constructs, we introduced shear during its gelation with the same concentration of crosslinking cations. This produced a self-supporting network of gel microparticles referred to as alginate fluid gel.[22,33] This gelation process was highly reproducible, with little variation between batches (supplementary material, Fig. 1). Furthermore, rheological characterization demonstrated that with repeated frequency ramps, there was a consistent shear stress. These non-time-dependent shear-thinning properties suggest that such an alginate fluid-gel could be delivered by intra-articular injection without modification of its structural properties. Mechanically, alginate in its quiescent state was more elastic than fluid alginate and showed a higher complex modulus. The loss in the elastic structure of the fluid alginate is attributed to the presence of shear throughout the sol-gel transition, where mixing prevents a complete network from forming.[25,26] There were also differences in the liquid-like and frequency dependent properties of the two materials. Both materials were stable at lower frequencies, with the fluid alginate showing a shorter LVR as it can flow when stressed. Such a phenomenon arises through the prevention of a completely gelled network, allowing polymer strands to move freely once the required energy has been met to yield any weak inter-particle interactions or entanglements.[21,25]

Following the investigation into the mechanical properties and the increased loss modulus of fluid alginate compared to quiescent alginate, the level of entrapment provided by the two alginate matrices was investigated. Using cell tracking, it was found that cells in fluid alginate were able to move laterally as well as vertically through the matrix, whereas in quiescent alginate, cells were confined to distinct regions. It was observed that there was increased movement of chondrocytes observed after the gel had "drifted." Therefore, this effect may be due to fluid flow through larger pores and voids in the fluid alginate structure, which allow cells to move laterally through the gel network. This effect would also be likely observed in an *in vivo* situation due to joint motion. Further, the difference in the microstructure of the alginate may introduce local differences in the stiffness of the gel matrix, resulting in changes to cell behavior.

Despite the success of resuspending chondrocytes in alginate fluid gel, for cell viability to be maintained, our study has found that fluid alginate was not as effective as quiescent alginate in maintaining the chondrocyte phenotype upon culturing of constructs. This lack of effectiveness of fluid alginate to maintain and promote the chondrogenic phenotype of primary chondrocytes was even observed despite culturing hydrogels in the presence of explant conditioned growth media, which we had previously found significantly promoting the collagen type II expression of primary chondrocytes in quiescent alginate hydrogels. As such, physical entrapment provided by the quiescent alginate gel has been shown to be critical in the maintenance of a native chondrocyte phenotype.

CONCLUSIONS

By producing a chemically identical fluid alginate, we have shown that with the lack of physical entrapment, passaged chondrocytes lose their ability to recover/maintain their phenotype. Even the introduction of growth factors released from cartilage which have a significant increase in collagen type II expression in quiescent alginate has no effect. We have demonstrated that maintenance of a spherical morphology alone is insufficient to recover a native collagen type II phenotype in passaged adult human chondrocytes. A certain level of geometric confinement for the chondrocytes is also essential.

METHODS

Tissue sources and isolation of primary cells

Joint tissue was collected from OA patients undergoing elective knee replacement surgery. Ethical approval was provided by the United Kingdom National Research Ethics Service (East of Scotland Research Ethics Service (11/ES/1044). All patients or their families provided consent. Full-thickness cartilage was excised from the femoral condyle and cartilage explant discs generated by cork-boring. For the isolation of primary human articular chondrocytes (hACs), cartilage was diced using a scalpel and digested in sterile-filtered 2 mg/ml collagenase type IA (0.5–3.0 FALGPA units/mg, Sigma Aldrich, Gillingham, UK) for 3 h. Both hACs and immortalised chondrocytes (TC28s) were cultured at 37 °C in a humidified incubator in growth media [DMEM (Dulbecco's Modified Eagle's medium) supplemented with 10% FCS (Fetal Calf Serum), penicillin-streptomycin (100 μg/ml), 2 mM L-glutamine, and 1% non-essential amino acids, (Sigma Aldrich, Gillingham, UK)]. For the generation of conditioned media, a cartilage disc (diameter: 4.1 mm, depth: 2 mm) was incubated with culture media for 24 h before being applied to cultures.

Alginate preparation

A solution of 1.5 wt. % medium viscosity alginate was prepared by the addition of dH_2O to sodium alginate (Sigma) and heating to 85 °C for 1 h whilst stirring continuously. The solution was then allowed to cool to room temperature. Fluid alginate was prepared by applying a shear rate of 500 s^{-1}; 10% 200 mM calcium chloride was added drop-wise, and the solution was equilibrated over 30 min at 20 °C (AR-G2, TA Instruments, New Castle, DE, USA). All alginate used for cell culture was autoclaved prior to use.

Encapsulation of chondrocytes in alginate

For quiescent gels, both immortal chondrocytes (TC28) and primary hACs were mixed with 1.5 wt. % alginate to a concentration of 1×10^6 cells/ml and seeded into the wells of a 96-well plate containing 0.2 M $CaCl_2$ with or without the presence of cartilage explant tissue. The quiescent gel was then incubated for 20 min at 37 °C to allow crosslinking to occur. Gels were then rinsed twice with PBS (Phosphate-buffered saline), and 0.2 ml of chondrocyte growth medium was added and then incubated at 37 °C for up to 30 days. Conditioned media was generated from the 48 h incubation of femoral condyle cartilage explant tissue in chondrocyte growth media (15 ± 3 g in 30 ml of media). Alginate fluid gel was mixed with 1×10^6 hACs and pipetted into a 96-well plate. Media were changed twice a week.

Determination of chondrocyte viability

Cell viability in the alginate scaffolds was determined using a calcein AM/ethidium homodimer-1 LIVE/DEAD assay (Invitrogen). Calcein AM is cell-permeable and is hydrolysed to green fluorescent calcein by interaction with intra-cellular enzymes; cell-impermeable ethidium homodimer-1 binds to DNA and fluoresces red, and so, it binds to the DNA of dead/dying cells. Alginate constructs were imaged using a Leica DM 6000B confocal microscope.

RNA isolation and quantification

Total RNA was isolated from alginate constructs and from chondrocyte monolayer cultures using TRIzol® reagent (Life Technologies, UK). In brief, alginate constructs were homogenized in 1 ml of TRIzol reagent using a TissueRuptor (Qiagen). Chondrocyte monolayer cultures in 6-well plates were directly lysed with 1 ml of TRIzol reagent per well. Following the addition of TRIzol, 0.2 ml of chloroform was added and the samples were shaken vigorously for 15 s before being centrifuged for 15 min at 12 000*g* for the phase separation of RNA, DNA, and protein. The aqueous (RNA containing) phase was decanted, and RNA precipitated overnight at −20 °C by the addition of 0.5 ml of isopropanol. Following centrifugation, the RNA pellet was washed with ethanol, dried, and resuspended in 50 μl of RNase-free H_2O. RNA concentrations and A260/280 ratio were determined using spectrophotometry (NanoDrop 2000, ThermoScientific). RNA was stored at −80 °C prior to analysis by qRT-PCR.

Quantitative real-time PCR

Precision OneStep SYBR Green Dye (PrimerDesign) was used with a β-actin reference gene (PrimerDesign) for quantification of the mRNA expression of COL1A1, COL2A1, ACAN, and SOX9 genes. The forward and reverse primer sequences were designed using Primer Express 3 software (Applied Biosystems) and produced by LifeTechnologies or PrimerDesign as indicated alongside primer sequences shown in supplementary material, Table I. Relative gene expression was determined by ddCT (delta-delta-cycle threshold), normalized to β-actin.

Quantification of aggrecan proteoglycan

As a marker of aggrecan proteoglycan production, sulphated glycosaminoglycans (sGAG) released by the scaffolds into the supernatants were measured using a 1,9-dimethylmethylene blue (DMMB) assay.[34] Supernatant samples (50 μl) at 3, 7, 10, 14, 17, 21, 24, 27, and 30 days and standards of shark chondroitin sulphate dilutions were added to 200 μl of DMMB colour reagent at pH 3. Alginate alone served as a control to remove the effect of interference of uronic acid groups in alginate. The absorbance was read immediately at A_{540} using a BioTek EL808 plate reader.

Immunohistochemical analysis

For immunohistochemistry, cellular scaffolds were cultured for two weeks before analysis. Scaffolds were then fixed with 4% paraformaldehyde for 10 min before blocking in 0.1 M PBS with 10% goat serum and 0.3% Triton-X-100. Aggrecan was detected using the mouse anti-aggrecan primary antibody (1:200, ThermoFisher) and then Alexa-488 goat anti-mouse secondary antibody (1:500, Invitrogen). Nuclei were counterstained with DAPI (1:5000, Sigma Aldrich).

Characterization of fluid and quiescent alginate

To visualize the "architecture" of the fluid gel, it was mixed at a 1:4 ratio with PEG (polyethylene glycol) to provide contrast between the phases and imaged using light microscopy (Leica DM 6000B).

Oscillatory rheology was used to determine the mechanical properties of fluid and quiescent alginate of the same chemistry. Discs (40 mm diameter) of quiescent alginate were produced using 0.2 M $CaCl_2$ by the filter paper method described elsewhere.[35] Fluid alginate samples were tested using a parallel, 40 mm sandblasted geometry, while quiescent alginate samples were prepared as 40 mm discs and tested using a ridged mesh as a gripper on flat 40 mm parallel plates on a AR-G2 Rheometer (TA Instruments, USA). A strain sweep was performed to determine the linear viscoelastic range of the gels. Storage (G′) and loss (G″) moduli were determined in a range of oscillatory frequencies (0.1–100 Hz) at 0.5% strain at 37 °C. The complex modulus (G*) was calculated by

$$G^* = \sqrt{(G')^2 + (G'')^2}. \quad (1)$$

The angular frequency (ω) was calculated by

$$\omega = 2\pi(\mathrm{Hz}). \tag{2}$$

To determine any changes in the structure during experimental procedures, the response to shearing as experienced by fluids moving through a pipette tip was modeled by ramping the shear rate from 0.1–500-0.1–500-0.1 s^{-1} at 0.5% strain. Oscillatory stress ramps were performed to determine the LVR of each alginate matrix.

Scanning electron microscopy (SEM)

1 mm thick sections of quiescent alginate and 1 mm smears of fluid alginate were snap frozen in liquid nitrogen and dried under vacuum for 48 h (Mini Lablyo, Frozen in Time, Ltd., York, UK). They were then mounted using conductive carbon tape and gold sputter coated. The topography was then imaged using a TM3030Plus benchtop SEM (Hitachi High Technologies, Schaumburg, USA) at 15 kV.

Cell tracking

Cell tracking was used to determine the level of entrapment provided by the different alginate matrices. Chondrocytes were seeded in fluid and quiescent alginate at 1×10^6 cells/ml and imaged every 5 min at 3 z-positions in each well over 20 h using a Cell-iQ and accompanying software Cell-iQ Imagen and Cell-iQ Analyser (Chip-Man Technologies, Tampere, Finland). Cell movement was quantified by tracking individual cells frame-by-frame using Cell-iQ Analyser. The trajectories were mapped, and the movement in 2D was normalized from gel drift (contraction) by tracking a reference point in each frame.

Statistical analysis

Mean values and standard error of the mean are plotted. Unpaired t-tests were performed using Prism 7 (GraphPad software, CA, USA) with a significance of $p < 0.05$.

SUPPLEMENTARY MATERIAL

See supplementary material for viscosity profiles of fluid alginate as it is produced as well as primer sequences and cell tracking videos.

ACKNOWLEDGMENTS

The authors would like to acknowledge the EPSRC Physical Sciences for Health CDT for provision of a studentship (M. Cooke, EP/L016346/1) as well as the research nurses and patients involved in tissue donation and collection.

[1]ARUK, Med. Press **222**, 253 (2013).
[2]M. Cross, E. Smith, D. Hoy, S. Nolte, I. Ackerman, M. Fransen, L. Bridgett, S. Williams, F. Guillemin, C. L. Hill, L. L. Laslett, G. Jones, F. Cicuttini, R. Osborne, T. Vos, R. Buchbinder, A. Woolf, and L. March, Ann. Rheum. Dis. **73**, 1323 (2014).
[3]D. P. Tonge, M. J. Pearson, and S. W. Jones, Osteoarthrosis Cartilage **22**, 609 (2014).
[4]M. B. Goldring and S. R. Goldring, Ann. N. Y. Acad. Sci. **1192**, 230 (2010).
[5]H. Mistry, M. Connock, J. Pink, D. Shyangdan, C. Clar, P. Royle, R. Court, L. C. Biant, A. Metcalfe, and N. Waugh, Health Technol. Assess. **21**, 1 (2017).
[6]J. C. H. Leijten, N. Georgi, L. Wu, C. A. Van Blitterswijk, and M. Karperien, Tissue Eng., Part B **19**, 31 (2013).
[7]M. Otero, M. Favero, C. Dragomir, K. E. Hachem, K. Hashimoto, D. A. Plumb, and M. B. Goldring, Methods Mol. Biol. **806**, 301 (2012).
[8]A. L. Aulthouse, M. Beck, E. Griffey, J. Sanford, K. Arden, M. A. Machado, and W. A. Horton, In Vitro Cell. Dev. Biol. **25**, 659 (1989).
[9]E. Schuh, S. Hofmann, K. Stok, H. Notbohm, R. Müller, and N. Rotter, J. Biomed. Mater. Res., Part A **100**, 38 (2012).
[10]H. Vasiliadis and J. Wasiak, Cochrane Database Syst. Rev. **2011**, CD003323.
[11]J. J. Green and J. H. Elisseeff, Nature **540**, 386 (2016).
[12]J. L. Drury and D. J. Mooney, Biomaterials **24**, 4337 (2003).
[13]K. Y. Lee and D. J. Mooney, Prog. Polym. Sci. **37**, 106 (2012).

[14]N. C. Hunt and L. M. Grover, Biotechnol. Lett. **32**, 733 (2010).
[15]J. Sun and H. Tan, Materials **6**, 1285 (2013).
[16]M. A. LeRoux, F. Guilak, and L. A. Setton, J. Biomed. Mater. Res. **47**, 46 (1999).
[17]R. Mhanna, A. Kashyap, G. Palazzolo, Q. Vallmajo-Martin, J. Becher, S. Moller, M. Schnabelrauch, and M. Zenobi-Wong, Tissue Eng., Part A **20**, 1454 (2014).
[18]D. Bosnakovski, M. Mizuno, G. Kim, S. Takagi, M. Okumura, and T. Fujinaga, Biotechnol. Bioeng. **93**, 1152 (2006).
[19]H. A. Awad, M. Q. Wickham, H. A. Leddy, J. M. Gimble, and F. Guilak, Biomaterials **25**, 3211 (2004).
[20]S. Ab-Rahim, L. Selvaratnam, H. R. B. Raghavendran, and T. Kamarul, Mol. Cell. Biochem. **376**, 11 (2013).
[21]I. Fernández Farrés and I. T. Norton, Food Hydrocolloids **40**, 76 (2014).
[22]I. Fernandez Farres, R. J. A. Moakes, and I. T. Norton, Food Hydrocolloids **42**, 362 (2014).
[23]I. T. Norton, W. J. Frith, and S. Ablett, Food Hydrocolloids **20**, 229 (2006).
[24]M. Guvendiren, H. D. Lu, and J. A. Burdick, Soft Matter **8**, 260 (2012).
[25]I. Fernández Farrés, M. Douaire, and I. T. Norton, Food Hydrocolloids **32**, 115 (2013).
[26]S. B. Ross-Murphy, V. J. Morris, and E. R. Morris, Faraday Symp. Chem. Soc. **18**, 115 (1983).
[27]J. Guo, G. W. Jourdian, and D. K. Maccallum, Connect. Tissue Res. **19**, 277 (1989).
[28]K. T. Paige, L. G. Cima, M. J. Yaremchuk, B. L. Schloo, J. P. Vacanti, and C. A. Vacanti, Plast. Reconstr. Surg. **97**, 168 (1996).
[29]M. M. J. Caron, P. J. Emans, M. M. E. Coolsen, L. Voss, D. A. M. Surtel, A. Cremers, L. W. van Rhijn, and T. J. M. Welting, Osteoarthrosis Cartilage **20**, 1170 (2012).
[30]N. G. Genes, J. A. Rowley, D. J. Mooney, and L. J. Bonassar, Arch. Biochem. Biophys. **422**, 161 (2004).
[31]A. J. Sophia Fox, A. Bedi, and S. A. Rodeo, Sports Health **1**, 461 (2009).
[32]C. L. Murphy and A. Sambanis, Tissue Eng. **7**, 791 (2001).
[33]A. Gabriele, F. Sypyropoulos, and I. T. Norton, Food Hydrocolloids **23**, 2054 (2009).
[34]R. W. Farndale, D. J. Buttle, and A. J. Barrett, Biochim. Biophys. Acta **883**, 173 (1986).
[35]N. C. Hunt, A. M. Smith, U. Gbureck, R. M. Shelton, and L. M. Grover, Acta Biomater. **6**, 3649 (2010).

Suspended Manufacture of Biological Structures

Samuel R. Moxon, Megan E. Cooke, Sophie C. Cox, Martyn Snow, Lee Jeys, Simon W. Jones, Alan M. Smith, and Liam M. Grover**

In this study, we describe a novel method of suspended manufacture for the production of complex soft structures of closely defined morphology, mechanical properties, and chemistry. The process conditions are sufficiently mild that embedded populations of cells maintain high levels of viability and retain phenotype. Given the simplicity of the process, it can be used for all existing gel materials without special modification. The method of manufacturing uses a "bed" of micrometer sized gel particles (often referred to as fluid or sheared gels),[1] which behave in bulk as a viscoelastic fluid and can self-heal thereby providing support to the complete part.[2] The final structure is formed through the dispersion of a gelling material into the interstices between the supporting fluid gel particles. This enables relatively complex structuring while providing sufficient support to prevent the structure collapsing under its own weight. Once the scaffold structure has been formed the supporting phase may be removed through the gentle application of shear. This manufacturing process allows for the use of a wide range of polymeric materials, including many already approved by regulatory bodies. Ultimately it has the potential to produce structures that could make their way into clinical trial in the relative short term. Here we demonstrate the power of this method by manufacturing anisotropic structures with spatially controlled mechanical and chemical properties, which support a coculture of viable cells. These scaffolds could be used for the production of osteochondral plugs for the augmentation of full-thickness cartilage defects.

Tissues are formed of populations of cells distributed within an extracellular matrix (ECM), which is structured down to the molecular level. Local variations in organization and biochemistry mean that the encapsulated populations of cells are exposed to environments that differ both mechanically and chemically. These environments have been shown to play a strong role in shaping cell phenotype.[3] For some time now researchers have sought to recapitulate tissue structure using a combination of isolated cells and polymeric hydrogels that have a structural resemblance to the ECM.[4] Such specimens have been manufactured using the process of gel-casting; this allows for gross geometrical control, yet provides little control over the microscale geometry and spatial and mechanical cues important to controlling cell behavior.[5] Additive layer manufacturing (ALM) offers the tantalizing possibility of creating structures with a greater level of complexity than traditional processing methods such as casting, and some degree of control over the distribution of cells and other important components throughout the structure. While the ALM of hard materials is relatively mature and a number of industries now utilize such technologies, at present the ALM of soft materials remains challenging. ALM using soft materials has been reported in the literature since the mid 2000s when Boland et al. published on the production of "nose-like" specimens from alginate.[6] In the years since many research groups have published on the manufacture of structures from soft solids some of which allow for the incorporation of cells.[7] Most recently, Hwang et al. reported the production of a cartilage-like structure for auricular reconstruction.[8] Notably, the majority of additively manufactured soft-solid structures exhibit relatively low complexity[9] and are typically broader at their base than at their peak to reduce the risk of the structure collapsing. A number of research groups are working on the development of novel polymers for ALM,[7,10] but in the most part, the structures they form with these polymers are highly simplistic, with a self-supporting "waffle arrangement" frequently being used to demonstrate process resolution.[7,9,11] Some papers report the use of harder materials, such as poly(caprolactone) (PCL) and hydroxyapatite, to support the structure[12,13] or have extruded materials into high viscosity liquids, for example Pluronic F-127 hydrogel.[13] Additionally, there have been reports of additive manufacturing using a suspending medium that consists of either a shear-thinning synthetic hydrogel[14] or a slurry of gelatin particles,[15] respectively. These elegant approaches resulted in structures of previously unprecedented complexity, but neither group managed to codeposit multiple cell types or could demonstrate any localized modification in mechanical properties of chemistry, both of which are critical to biological performance. Furthermore, neither of these methods is conducive to the manufacture of structures that are suitable for the clinic, since the suspending medium would be very challenging to completely remove from the finished part. In this study, we have addressed these issues by using a self-healing particulate or fluid gel material, which is stable at room temperature and in culture conditions, as a supporting media. The strong

S. R. Moxon, Dr. A. M. Smith
Department of Pharmacy
University of Huddersfield
Queensgate, Huddersfield HD1 3DH, UK
E-mail: a.m.smith@hud.ac.uk
M. E. Cooke, Dr. S. C. Cox, Prof. M. Snow, Prof. L. M. Grover
School of Chemical Engineering
University of Birmingham
Edgbaston B15 2TT, UK
E-mail: l.m.grover@bham.ac.uk
M. E. Cooke, Dr. S. W. Jones
Institute of Inflammation and Ageing
MRC Musculoskeletal Ageing Centre
QE Hospital
University of Birmingham
Edgbaston B15 2WB, UK
Prof. M. Snow, Prof. L. Jeys
Royal Orthopaedic Hospital
Bristol Road, Northfield, Birmingham B31 2AP, UK

DOI: 10.1002/adma.201605594

surface interactions between gel particles form short-range adhesions when in close contact causing the paste-like material to thicken.[16] The interactions formed between the particles allow the particulate material to support a secondary phase of similar (or in some cases higher) density. This "true-gel" ($G' >>> G''$) particulate (Figures S1–S3, Supporting Information) microstructure makes this system physically distinct from highly viscous fluids, such as commercial shower gels, that are formed almost exclusively by polymer entanglement.[17] Importantly, since the gel particles are discrete entities they do not contaminate the surface of the manufactured sample and can actually be formed from the same material as that extruded into the particle bed (**Figure 1**) likely simplifying the translational pathway. Using particulate gels as a suspending agent, supports the fragile construct as it is formed, in a similar manner to the way amniotic fluid suspends the developing fetus. Using an XYZ stage, it was possible to (with 100 µm resolution) deposit the hydrogel polymer in a discrete 3D location, the resolution of which is limited only by the size of the droplet from the end of the extruding needle and the viscosity of the supporting medium.

A variety of hydrogel materials may be used for the production of the final part and the supporting bed. Initial experimentation demonstrated that it was possible to generate structures using combinations of gelatin, gellan, collagen, hyaluronic acid, agarose, and alginate. As a consequence of its relative robustness and capacity for physical modification using seeded hydroxyapatite,[18] gellan was selected for further use as the final part and agarose as the supporting bed. The supporting bed, formed from agarose with particles in the size range 2–11 µm (Figure S4, Supporting Information), was of sufficient robustness to suspend a cross-linked gellan gum structure such as the helix illustrated in Figure 1. This helical structure was loaded with colloidal hydroxyapatite nanocrystals in order to increase radio-opacity enabling micro-computed tomography (CT) imaging. Following treatment with calcium chloride solution this helical structure was removed from the particle bed and was shown to be self-supporting (Figure 1). The shear forces applied during the extrusion process were not of sufficient magnitude to cause phase separation and were sufficiently mild that it was possible to maintain the viability of a population of human primary chondrocytes within the cultures (**Figure 2**). To investigate the influence of supporting matrix viscosity on the resolution of the printing method, samples were made using a controlled concentration of gellan gum (1.5%) and a hypodermic needle of internal diameter 337 µm. An increase in the viscosity of the supporting medium resulted in a monotonic increase in resolution in the *XY* dimensions, but interestingly a smaller reduction in resolution in the *Z* dimension (Figure 2). At this scale, resolution is ultimately limited by droplet size, which is controlled by the internal dimensions, flow rate of the extruding aperture and other parameters of deposition, such as the viscosity of the extruded solutions. To further investigate factors that may influence resolution, structures were formed using a range of needle diameters and it was demonstrated that resolution was

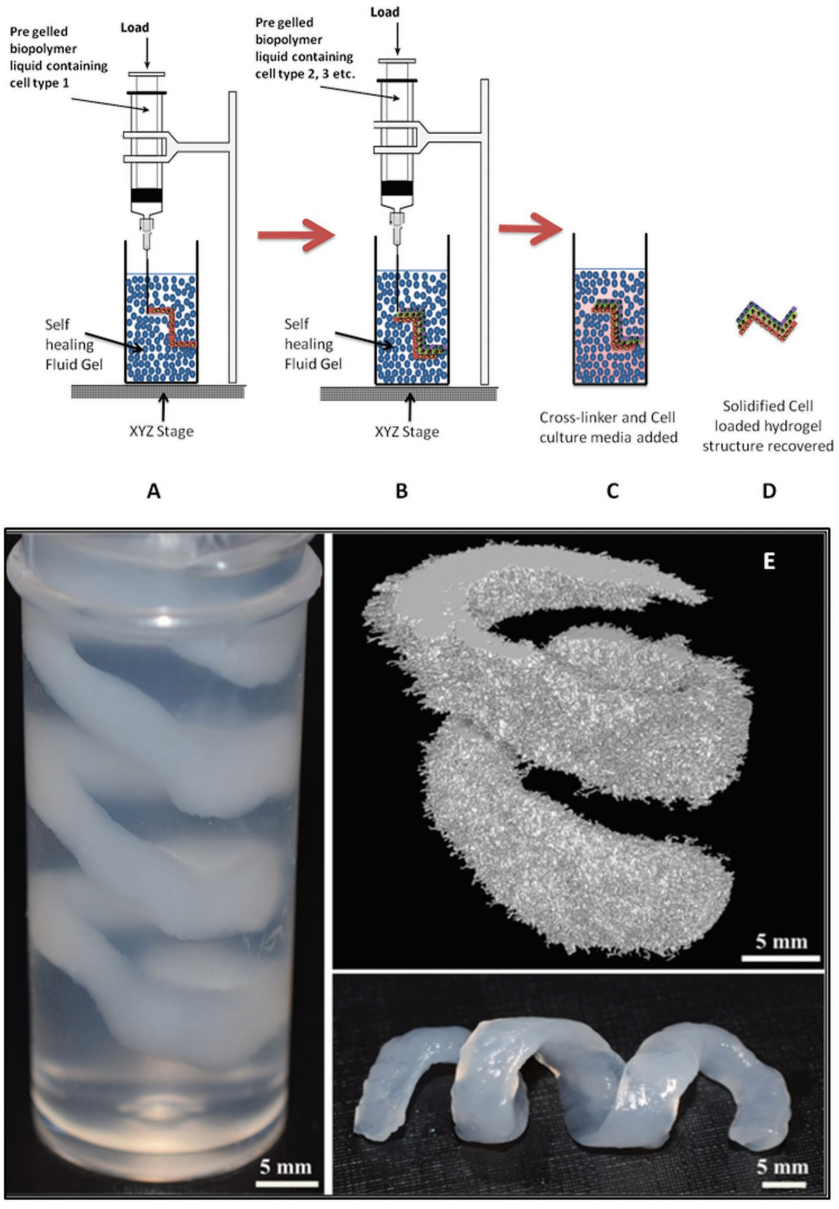

Figure 1. A–D) A schematic showing the manufacturing process for a 3D soft solid structure manufactured using the suspended deposition method. A) Briefly, a supporting "fluid-gel" matrix is created in a vessel. B) A secondary phase may then be extruded into the particle bed. C) The self-healing, fluid gel supports the gel structure during the cross-linking process. D) Once cross-linked, the object may be removed from the particle bed. E) This was manipulated to fabricate a simple helix loaded with hydroxyapatite nanoparticles and imaged with micro-CT (scale bars = 5 mm).

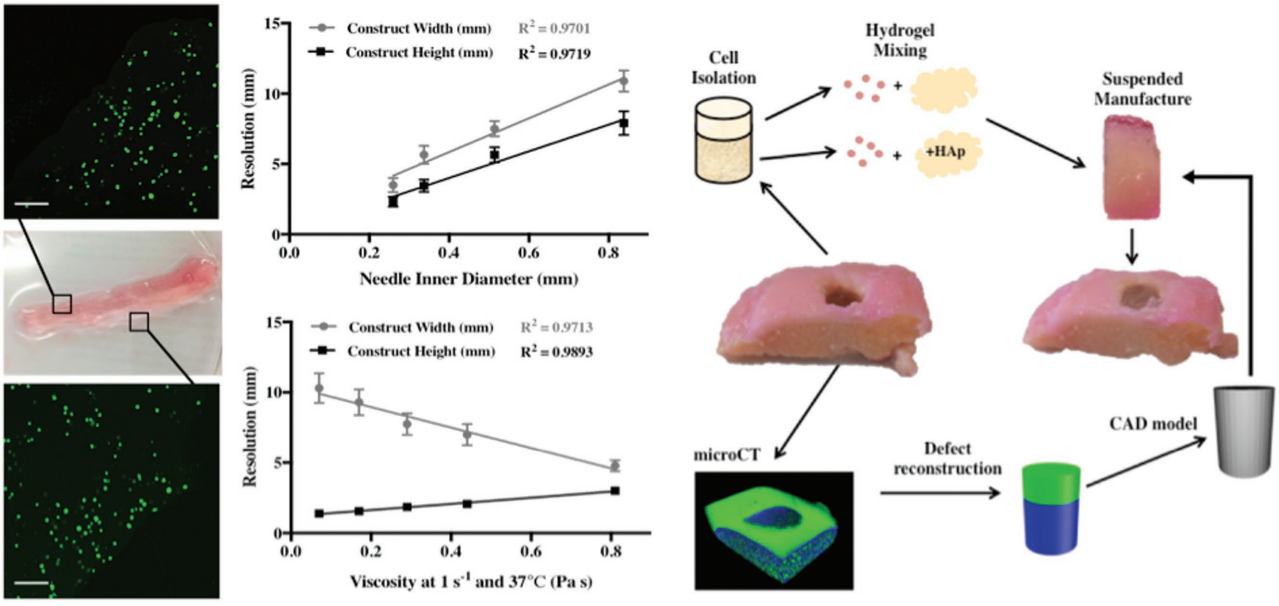

Figure 2. Extrusion of a gellan matrix loaded with primary human chondrocytes into the "fluid-gel" structure through a 337 µm internal diameter needle maintained cell viability throughout the construct (left column, scale bars = 200 µm). An increase in the internal diameter of the needle resulted in a reduction in resolution (centre, top), as did a reduction in the viscosity of the matrix (centre, bottom). From these experiments, a fluid viscosity of 0.75 Pa s (at 1 s^{-1} shear rate) and needle diameter of 337 µm was set for manufacture of an osteochondral plug. A computer model of this plug (right column) was generated from CT scans of a defect drilled into the tissue by a clinician. The model generated was used to inform the manufacture of a plug with appropriate chondral and subchondral thicknesses to fit the tissue defect.

directly related to needle diameter, increasing up to the point that the hydrocolloid could no longer be extruded (Figure 2). The peak resolution achievable for the 1.5% gellan gum and the agarose supporting medium was 250 µm. Given the scale of the tissues to be produced for osteochondral repair and the need for cell viability, the needle diameter was set at 337 µm and extrusion rate no more than 125 µL s^{-1}. To demonstrate the complexity achievable with the suspended manufacturing process, scaffolds that mimic the structuring and cellular organization of an osteochondral defect were manufactured. This complex tissue region lies between articular cartilage and bone on an articulating joint surface[19] and may be severely damaged following trauma[20] or can deteriorate during the progression of osteoarthritis.[21] At present the standard of care is microfracture in the knee[22] or the transplantation of tissue that has been isolated from a cadaver or nonarticulating region of the joint.[22] Neither method has been shown to be absolutely successful and this has driven research into the development of a range of synthetic osteochondral plugs.[23] The main reason for failure of these synthetic grafts is through delamination at the hard–soft tissue interface.[24] Native osteochondral tissue exhibits a gradual structural change from disordered mineralized collagen at the subchondral bone,[25] through to collagen II and glycosaminoglycan (GAG) - rich cartilage[26] allowing stress to be distributed across the interface without stress localization and delamination occurring.[26,27] The region consists of four principle cells types, which secrete and organize their local environments.[25,26] Although a number of groups have attempted this in vitro[28] the processes that they have employed did not mimic the structuring of this complex structure at a length-scale that is appropriate to the size of the defects encountered clinically.

Here, the suspended manufacturing process was used to form composite hydrogel structures with anisotropic mechanical properties mimicking the native osteochondral environment. Femoral condyle tissue was retrieved from patients following knee replacement and an osteochondral defect was introduced using a surgical drill. Excess retrieved tissues were digested to release the cells from the cartilage and bone samples. The structure was scanned using micro-CT and a 3D model of the defect was created. This 3D model was used to guide the manufacture of an osteochondral implant where the lower surface was loaded with sol-HA, gellan, and osteoblast cells (**Figure 3**). The upper surface of the construct was manufactured using gellan gum alone, loaded with populations of chondrocytes (Figure 3). The suspended manufacturing process allowed for the production of osteochondral structures that fit tightly into the defects and matched the layer thicknesses for the bone and cartilage components. These samples were then placed in culture for a period of four weeks in order to identify whether the cell types in the different regions of the defect maintained phenotype. Over the course of four weeks of in vitro culture the osteochondral plugs maintained their structural integrity; they could be easily handled and extracted from the defect without deterioration (Figure 3).

Mechanical spectra of the osteochondral constructs highlight the successful integration of two different materials into a single structure (Figure 3). Constructs were sliced into four regions and stress sweeps were conducted on each section to determine mechanical strength and elasticity. Samples were subjected to increasing stress (0.1–1000 Pa) and a range of mechanical properties was observed throughout the construct. The weakest areas with the shortest linear viscoelastic

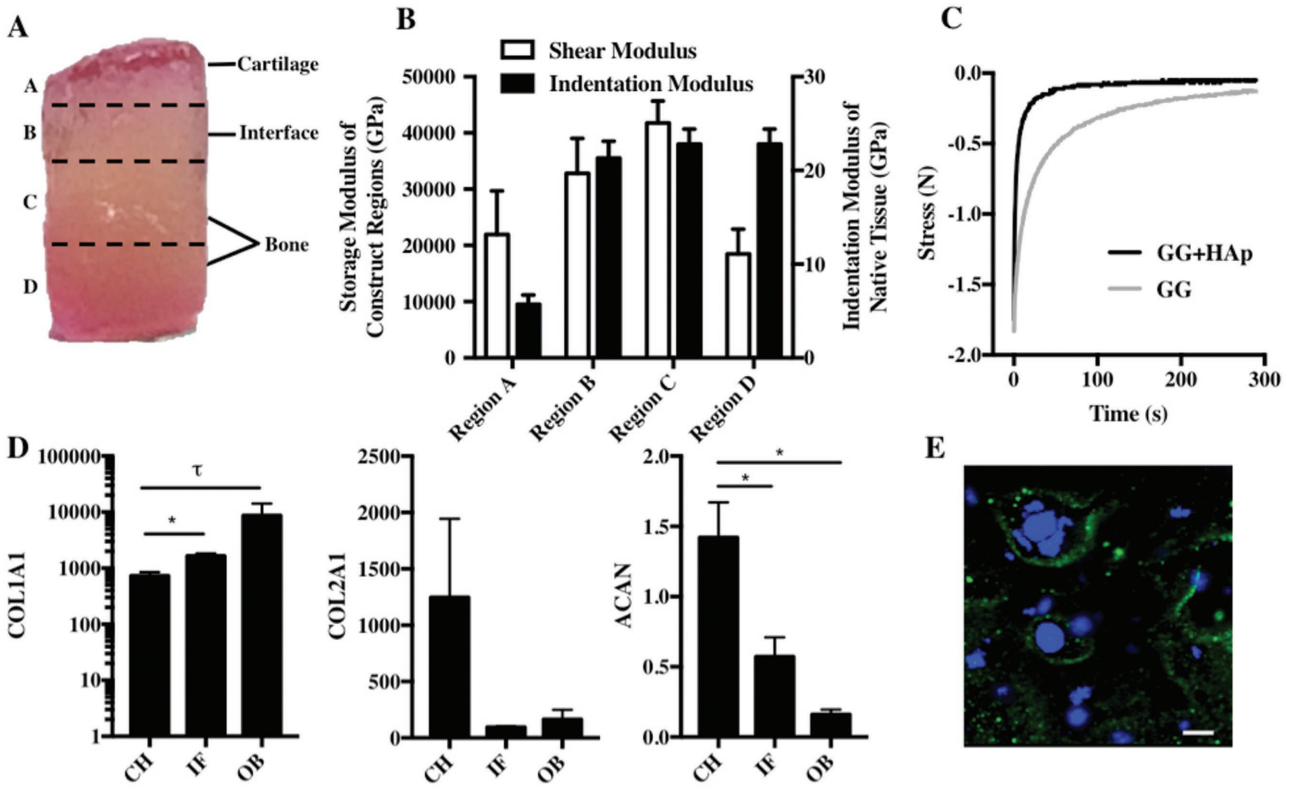

Figure 3. A) Samples manufactured using suspended manufacturing were cultured before being cut with a razor blade and mechanically characterized using a rheometer. B) The storage modulus of the construct reduced significantly from the core "boney" area of the structure (Regions C and D) into the chondral region (Regions A and B). Mechanical data reflected trends seen in native tissue with an increase in modulus from hyaline cartilage (Region A) through the osteochondral interface (Region B) to subchondral bone (Regions C and D).[20] This demonstrates that it is possible to not only define geometric but also the mechanical properties exhibited by the resulting structure. C) Stress relaxation measurements show that the addition of hydroxyapatite (GG + HAp) results in a faster relaxation response than gellan gum alone (GG). D) Following 4 weeks of culture within the human tissue defects ($n = 6$), the construct was removed and cells within the cartilage (CH), interfacial (IF) and bone (OB) regions were recovered for RNA isolation and mRNA was analyzed by qRT-PCR. The cells in the cartilaginous section of the scaffold expressed the highest levels of coll II and aggrecan (ACAN) and the bone region expressed significantly more coll IA1 (mean ± SEM). This suggests that the cells deposited into discrete regions maintained not only viability but also their phenotype (*: $P < 0.05$, τ: $P = 0.0793$). E) Fluorescent immunohistochemistry (IHC) (DAPI (4,6-Ddamidino-2-phenylindole) = blue, aggrecan = green) shows the production of aggrecan in the cartilaginous region of the structure (scale bars = 200 µm).

region were the chondral region and the uppermost surface of the construct (Regions A and D). Region C exhibited significantly higher gel strength and elasticity. This can be attributed to the nanocrystalline hydroxyapatite (nano-HA) interacting with gellan helices during gelation to create a highly homogenous structure exhibiting higher strength in comparison with unloaded gellan (Figure 3). Interestingly, the incorporation of HA into the gellan hydrogel resulted in a more rapid relaxation response than the gellan alone (Figure 3C). This is significant since matrices of elastic modulus >17 kPa that exhibit more rapid stress relaxation encourage mineralization to a greater extent when compared with those with slower stress response.[29] Region A was comprised entirely of gellan gum without nano-HA, which explains the lower gel strength. It is likely that the nano-HA began to sediment prior to gelation due to its higher density compared with the gel phase (3.16 compared with ≈1 g cm^{-3}) resulting in the top of the osteogenic region showing a lower modulus. At the interface (Region B), the construct exhibited mechanical properties intermediate to Regions A and C providing evidence for a successful integration of the two different materials (Figure 3). Interestingly, the trend in mechanical properties observed in regions A–C shows some similarity to reported changes in modulus across osteochondral tissue (Figure 3). A 2012 study by Campbell et al. outlined indentation moduli of three osteochondral regions, namely subchondral bone, hyaline cartilage, and the osteochondral interface.[27] Subchondral bone exhibited the highest modulus, hyaline cartilage the lowest with calcified cartilage (the interface) falling between the two, albeit closer to the modulus of bone. Indentation moduli of tissue regions were orders of magnitudes greater than storage moduli of respective construct regions and methods used to determine both differed greatly. However, parallels between the two trends highlight the level of control exhibited over mechanical properties within each region of osteochondral constructs.

Polymerase chain reaction (PCR) data collected from the retrieved samples demonstrated that the expression of both collagen type II and aggrecan (ACAN) (both markers of cartilage formation) was highest in the chondral region of the scaffold (Figure 3) and collagen type I expression was lowest at this point. Immunohistochemical (IHC) analysis of the samples demonstrated the presence of aggrecan around the encapsulated

cells in this area of the scaffold (Figure 3). Remarkably, the ratio of collagen II to collagen I changed gradually throughout the structure inline with what would be expected with the native tissue region. This indicated that while the two sections of the osteochondral scaffold were well integrated, the embedded cell population retained their native phenotype. This is something that has proven challenging with existing technologies for tissue structuring. In comparison with the majority of ALM methods, where high temperatures, pressures, or cross-linking agents are a necessity, the suspended manufacture method allowed us to maintain viability and behavior while subtly modifying the local composition of the matrix.

In this paper, a new method was reported to manufacture comparatively complex soft-solid structures by extruding a gelling polymer into a supporting particle-based matrix. The method allowed the structuring of soft-solid materials such that they exhibited distinct chemical and physical properties on the microscale. It was shown that suspended manufacture could recapitulate the structure of the osteochondral region as defined by CT scanning. The printed structure maintained its morphology and mechanical robustness over a period of four weeks of culture during which the encapsulated cells retained their phenotype. Our findings suggest that this novel method of producing 3D tissue-like structures has significant promise for the regeneration and study of complex tissue structures and interfaces.

Experimental Section

Fluid Gel Formulation: Fluid gels were manufactured by cooling solutions of 0.5% w/w agarose from 85 to 20 °C under constant shear using a magnetic stirrer rotating at 700 rpm. This created a constant angular velocity of 74 rad s^{-1}. Fluid gels were sterilized for cell culture applications by autoclaving agarose solutions prior to cooling.

Suspension of Helical Polymeric Structures: Aliquots of fluid gel were prepared in 6 mL Bijoux tubes. Solutions of 1.5% w/w low acyl gellan mixed with 10% nanocrystalline hydroxyapatite/HA at 60 °C (formulated by a precipitation method)[30] were extruded into fluid gel samples through a hypodermic needle with a 337 µm inner diameter using a 5 mL syringe. During extrusion, the syringe was manipulated precisely with respect to geometric position to enable the generation of the helix. The suspensions were then left at room temperature for 40 min to enable gelation to occur. Prior to extraction, samples were observed using micro-CT (Bruker Skyscan 1172—Bruker, Belgium) and reconstructed data were visualized in 3D using CTVox software (Bruker). Helices were then extracted and excess fluid gel was washed away with deionized water.

Tuning Resolution of Suspended Constructs: Low acyl gellan gum solutions of varying viscosity (as controlled by polymer concentration) were extruded into separate aliquots of fluid gel (contained in petri dishes of 60 mm diameter and 15 mm depth). Gelation was triggered by temperature and ionic interaction via injection of 200×10^{-3} M $CaCl_2$ around constructs at 20 °C. After 30 min, gelled structures were extracted and the resolution of each construct was measured.

Evaluation of Cell Culture Applications: Osteochondral tissue was donated by patients undergoing elective knee replacement surgery. This study was approved by the United Kingdom National Ethics Research Committee (Hertfordshire Research Ethics Committee 12/EE/0136). Articular cartilage was removed from human femoral condyle tissue before mincing and digestion by 2 mg mL^{-1} collagenase for 4 h under agitation at 37 °C for release of chondrocytes. Bone chips (4–5 mm^3) from subchondral trabecular bone were cultured for release of osteoblasts. Both cell types were cultured in Dulbecco's modified Eagle's medium (DMEM) supplemented with 10% fetal bovine serum, 1% L-glutamine, 1% PenStrep, and 1% nonessential amino acids. At passage 1, cells were trypsinized, counted, and resuspended at a density of 3×10^6 cells mL^{-1} before being mixed with sterile 1.5% low acyl gellan gum. Cell-laden gellan gum was extruded into sterile agarose fluid gel to create linear constructs. Gelation at 20 °C was triggered with 200×10^{-3} M $CaCl_2$ and excess calcium ions were washed away after 30 min using Dulbecco's phosphate buffered saline (PBS). Cell-loaded constructs were cultured at 37 °C/5% CO_2 in culture media (as above). Cell viability was visualized using Calcein-acetoxymethyl (AM) and ethidium homodimer-1 fluorescent dyes.

Defect Formation and Reconstruction: Defects were introduced into femoral condyle tissue following surgery using an orthopedic drill. The resulting tissue was imaged using microCT (Bruker Skyscan 1172) and reconstructed data were viewed using CTVox software (Bruker). The defect was then measured for reconstruction of the defect space in Simpleware (Synopsys, UK).

Implant Fabrication and Culture: Prior to implant fabrication cells were isolated and cultured as above. Primary human osteoblasts and chondrocytes were trypsinized, counted, and resuspended at a density of 1×10^6 cells mL^{-1}. Osteoblasts were loaded into 1.5% low acyl gellan mixed with 5% nano-HA while chondrocytes were mixed with 1.5% gellan. Guided by dimensions obtained from defect reconstruction, single implants were fabricated containing a layer of chondrocyte-loaded gellan and a thicker layer of osteoblast-loaded gellan/HA via extrusion into sterile agarose fluid gel. Gelation at 20 °C was triggered with injection of 200×10^{-3} M $CaCl_2$ around each suspended structure and constructs were extracted after 30 min. Excess fluid gel was washed away and constructs were implanted into tissue defects. The construct-filled defects were then cultured as above in a humidified incubator at 37 °C, 5% CO_2 for 30 d ($n = 6$).

Determination of Collagen 1, Collagen 2, and Aggrecan (ACAN) Expression: Following 30 d of culture, constructs were removed from the tissue defects and separated into cartilage, interface, and bone regions for gene expression analysis. RNA was isolated using TRIZol reagent (Life Technologies, UK) and the manufacturer's instructions were followed. RNA was quantified using photospectrometry (NanoDrop 2000, NanoDrop Technologies). Quantitative-realtime polymerase chain reaction (Q-RTPCR) was performed using a Lightcycler 480 (Roche). The expression of collagen type I, type II, and aggrecan (ACAN) were measured and normalized to 18S expression. Validated TaqMan probes were purchased from Life Technologies. Gene expression was quantified using the Pfaffl method.[31]

Fluorescent Immunohistochemistry: Constructs were fixed with 4% paraformaldehyde before blocking in vehicle (10% goat serum, 0.1 M PBS, 0.3% Triton-X-100). For aggrecan, cells were incubated with mouse antiaggrecan primary antibody (1:100, ThermoFisher) and then Alexa 488 goat antimouse secondary antibody (1:500, Invitrogen). Nuclei were stained with 4,6-Diamddino-2-phenylindole (DAPI) (1:5000, Sigma-Aldrich) and constructs were imaged using a Leica DM 6000B microscope.

Mechanical Spectra of Implants: Layered constructs were sliced laterally into four separate regions (see Figure 3—mechanical spectra figure). Stress sweeps were conducted on each region using a Bohlin Gemini rheometer (Malvern, UK) with 25 mm serrated parallel plate geometry. Elastic and viscous moduli (G' and G'', respectively) were analyzed in response to increasing stress from 1 to 100 Pa at a constant temperature of 37 °C. For stress relaxation, gellan gum and gellan gum/hydroxyapatite constructs (height 8 mm, diameter 14 mm) were displaced 2 mm and held for 300 s while load was recorded (Bose ElectroForce 5500).

Rheological Measurements: All rheological measurements were performed on a Bohlin Gemini rheometer (Malvern, UK) using a 55 mm 2° cone and plate geometry at an isothermal temperature of 37 °C which was maintained by a Peltier controlled lower plate.

Stress Sweeps: Samples of 0.5% agarose fluid gels were prepared and loaded onto the bottom plate of the rheometer. The samples were then

subjected to a shear stress range of 0.1–100 Pa at a constant oscillatory frequency of 10 Rad s^{-1}. Elastic and viscous moduli were measured in response to increasing shear stress. Results were analyzed to determine the linear viscoelastic region.

Frequency Sweeps: Elastic and viscous moduli of 0.5% agarose fluid gels were analyzed in response to increasing oscillatory frequencies from 0.1 to 10 Rad s^{-1} at a constant strain of 0.05%.

Shear Sweeps: Shear ramps were performed at 37 °C on 0.5% agarose fluid gel samples. Shear rate was increased from 0.001 to 100 s^{-1} over a 10 min period and dynamic viscosity in response to increasing shear rate was subsequently analyzed.

Particle Size Distribution: Fluid gel samples were loaded onto glass slides and allowed to dry under a coverslip for 10 min. Samples were then visualized on Keyence VHX 2000 digital microscope (Keyence, UK). Particle sizes were analyzed with VHX 2000 communication software. Particle size distribution was evaluated using images of fluid gel particles within an area of 135 µm × 120 µm. Images were divided into 12 grids of 11.25 µm × 10 µm. Within each grid, the number of particles was recorded and divided into categories based on size. A total of 96 grids and ≈2300 particles were counted. Particle size distribution was subsequently determined by comparing the number of particles within each size range and calculating cumulative undersize.

Supporting Information

Supporting Information is available from the Wiley Online Library or from the author.

Acknowledgements

S.R.M. and M.E.C. contributed equally to this work. The authors would like to acknowledge the EPSRC for the provision of a studentship (M.E.C.) through the Sci-Phy-4-Health Centre for Doctoral Training (EP/L016346/1) and the University of Huddersfield for funding the Studentship of S.R.M.

Received: October 17, 2016
Revised: December 11, 2016
Published online:

[1] a) I. T. Norton, D. A. Jarvis, T. J. Foster, *Int. J. Biol. Macromol.* **1999**, *26*, 255; b) I. Fernandez Farres, R. J. A. Moakes, I. T. Norton, *Food Hydrocolloids* **2014**, *42*, 362.
[2] A. Gabriele, F. Sypyropoulos, I. T. Norton, *Food Hydrocolloids* **2009**, *23*, 2054.
[3] J. Y. Rho, L. Kuhn-Spearing, P. Zioupos, *Med. Eng. Phys.* **1998**, *20*, 92.
[4] M. W. Tibbitt, K. S. Anseth, *Biotechnol. Bioeng.* **2009**, *103*, 655.
[5] J. L. Vanderhooft, M. Alcoutlabi, J. J. Magda, G. D. Prestwich, *Macromol. Biosci.* **2009**, *9*, 20.
[6] T. Boland, X. Tao, B. J. Damon, B. Manley, P. Kesari, S. Jalota, S. Bhaduri, *Mater. Sci. Eng. C* **2006**, *27*, 372.
[7] S. Hong, D. Sycks, H. F. Chan, S. Lin, G. P. Lopez, F. Guilak, K. W. Leong, X. Zhao, *Adv. Mater.* **2015**, *27*, 4035.
[8] C. M. Hwang, B. K. Lee, D. Green, S. Y. Jeong, G. Khang, J. D. Jackson, A. Atala, S. J. Lee, J. J. Yoo, *Plast. Reconstr. Surg.* **2014**, *133*, 360e.
[9] M. Costantini, J. Idaszek, K. Szoke, J. Jaroszewicz, M. Dentini, A. Barbetta, J. E. Brinchmann, W. Swieszkowski, *Biofabrication* **2016**, *8*, 035002.
[10] a) T. Jungst, W. Smolan, K. Schacht, T. Scheibel, J. Groll, *Chem. Rev.* **2016**, *116*, 1496; b) D. Chimene, K. K. Lennox, R. R. Kaunas, A. K. Gaharwar, *Ann. Biomed. Eng.* **2016**, *44*, 2090.
[11] D. A. Zopf, A. G. Mitsak, C. L. Flanagan, M. Wheeler, G. E. Green, S. J. Hollister, *Otolaryngol.–Head Neck Surg.* **2015**, *152*, 57.
[12] a) F. P. Melchels, M. M. Blokzijl, R. Levato, Q. C. Peiffer, M. Ruijter, W. E. Hennink, T. Vermonden, J. Malda, *Biofabrication* **2016**, *8*, 035004; b) E. Sachlos, D. Gotora, J. T. Czernuszka, *Tissue Eng.* **2006**, *12*, 2479.
[13] H. W. Kang, S. J. Lee, I. K. Ko, C. Kengla, J. J. Yoo, A. Atala, *Nat. Biotechnol.* **2016**, *34*, 312.
[14] C. B. Highley, C. B. Rodell, J. A. Burdick, *Adv. Mater.* **2015**, *27*, 5075.
[15] T. J. Hinton, Q. Jallerat, R. N. Palchesko, J. H. Park, M. S. Grodzicki, H.-J. Shue, M. H. Ramadan, A. R. Hudson, A. W. Feinberg, *Sci. Adv.* **2015**, *9*, e1500758.
[16] I. T. Norton, D. A. Jarvis, T. J. Foster, *Int. J. Biol. Macromol.* **1999**, *26*, 255.
[17] a) R. J. Crawford, K. J. Edler, S. Lindhoud, J. L. Scott, G. Unali, *Green Chem.* **2012**, *14*, 300; b) I. Avramov, *J. Non-Cryst. Solids* **2005**, *351*, 3163.
[18] a) P. Jamshidi, P. Ma, K. Khosrowyar, A. M. Smith, L. M. Grover, *J. Exp. Nanosci.* **2012**, *7*, 652; b) P. Jamshidi, G. Birdi, R. L. Williams, S. C. Cox, L. M. Grover, *Biotechnol. Bioeng.* **2015**, *113*, 1568.
[19] M. Keeney, A. Pandit, *Tissue Eng., Part B* **2009**, *15*, 55.
[20] K. D. Shelbourne, S. Jari, T. Gray, *J. Bone Joint Surg. Am.* **2003**, *85-A*, 8.
[21] M. B. Goldring, *HSS J.* **2012**, *8*, 7.
[22] R. Gudas, R. J. Kalesinskas, V. Kimtys, E. Stankevicius, V. Toliusis, G. Bernotavicius, A. Smailys, *Arthroscopy* **2005**, *21*, 1066.
[23] a) J. K. Sherwood, S. L. Riley, R. Palazzolo, S. C. Brown, D. C. Monkhouse, M. Coates, L. G. Griffith, L. K. Landeen, A. Ratcliffe, *Biomaterials* **2002**, *23*, 4739; b) I. Martin, S. Miot, A. Barbero, M. Jakob, D. Wendt, *J. Biomech.* **2007**, *40*, 750.
[24] a) C. A. Robb, C. El-Sayed, G. S. Matharu, K. Baloch, P. Pynsent, *Acta Orthop. Belg.* **2012**, *78*, 643; b) T. L. Nosewicz, M. L. Reilingh, C. N. van Dijk, G. N. Duda, H. Schell, *Knee Surg. Sports Traumatol. Arthrosc.* **2012**, *20*, 1919.
[25] M. B. Goldring, S. R. Goldring, *Ann. N. Y. Acad. Sci.* **2010**, *1192*, 230.
[26] A. J. S. Fox, A. Bedi, S. A. Rodeo, *Sports Health* **2009**, *1*, 461.
[27] a) S. E. Campbell, V. L. Ferguson, D. C. Hurley, *Acta Biomater.* **2012**, *8*, 4389; b) V. L. Ferguson, A. J. Bushby, A. Boyde, *J. Anat.* **2003**, *203*, 191.
[28] a) D. Puppi, C. Mota, M. Gazzarri, D. Dinucci, A. Gloria, M. Myrzabekova, L. Ambrosio, F. Chiellini, *Biomed. Microdev.* **2012**, *14*, 1115; b) H.-W. Cheng, K. D. K. Luk, K. M. C. Cheung, B. P. Chan, *Biomaterials* **2011**, *32*, 1526; c) J. M. Oliveira, M. T. Rodrigues, S. S. Silva, P. B. Malafaya, M. E. Gomes, C. A. Viegas, I. R. Dias, J. T. Azevedo, J. F. Mano, R. L. Reis, *Biomaterials* **2006**, *27*, 6123.
[29] O. Chaudhuri, L. Gu, D. Klumpers, M. Darnell, S. A. Bencherif, J. C. Weaver, N. Huebsch, H. P. Lee, E. Lippens, G. N. Duda, D. J. Mooney, *Nat. Mater.* **2016**, *15*, 326.
[30] I. Mobasherpour, M. S. Heshajin, A. Kazemzadeh, M. Zakeri, *J. Alloys Compd.* **2007**, *430*, 330.
[31] M. W. Pfaffl, *Nucleic Acids Res.* **2001**, *29*, e45.

levels of pro-inflammatory cytokines, MMPs and chemokines which have catabolic functions and degrade cartilage [217]. The final process in OA chondrocytes is cell death; increased cell numbers and insufficient levels of nutrients in the chondron causes cell necrosis [5].

1.4.2 Bone in OA

There are changes to subchondral cortical and trabecular bone as well as formation of bony spurs (osteophytes) in OA, all of which are specific to the stage of OA. Increased loading leads to an increase in bone turnover as stated previously. In OA, there is region-specific thickening of the subchondral cortical and trabecular bone as seen in Figure 1.7 [59, 111]. There is also thinning of the epiphyseal trabecular bone which is likely due to stress shielding by the thickened subchondral plate [20].

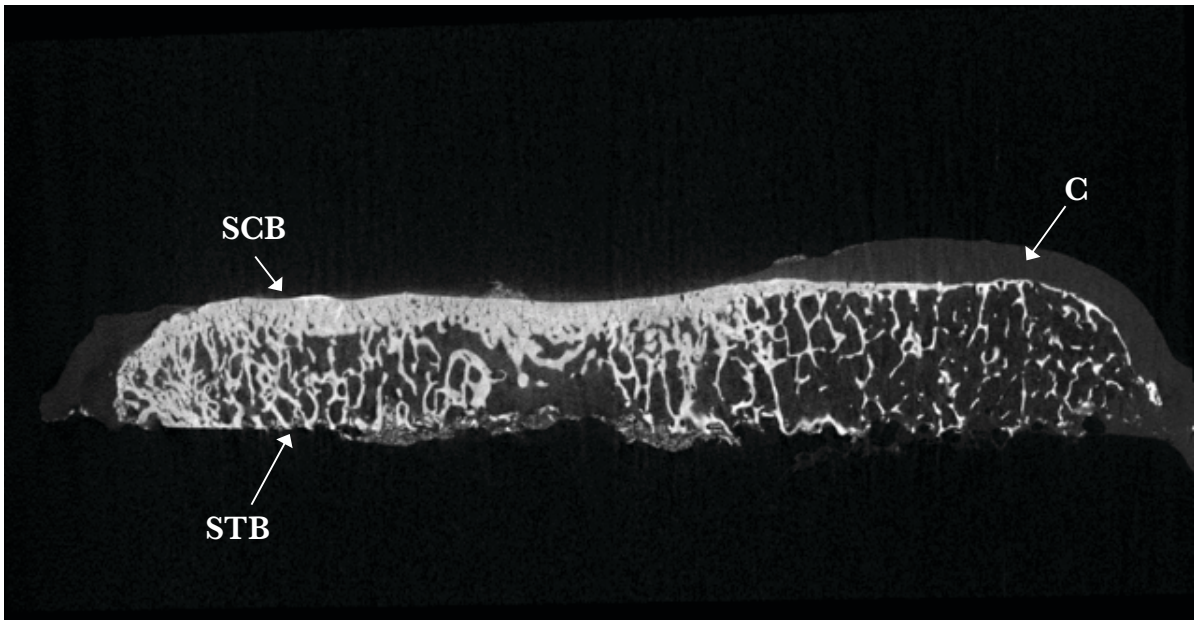

Figure 1.7: Reconstructed μCT image of an OA tibial plateau (sagittal plane) showing thickening of the subchondral cortical bone (SCB) where cartilage (C) is thinning or completed degenerated. The subchondral trabecular bone (STB) architecture is also irregularly thickened.

.

Excessive loading that occurs when cartilage is completely degraded can lead to bone marrow lesions and bone cysts. These defects in the bone have been associated with

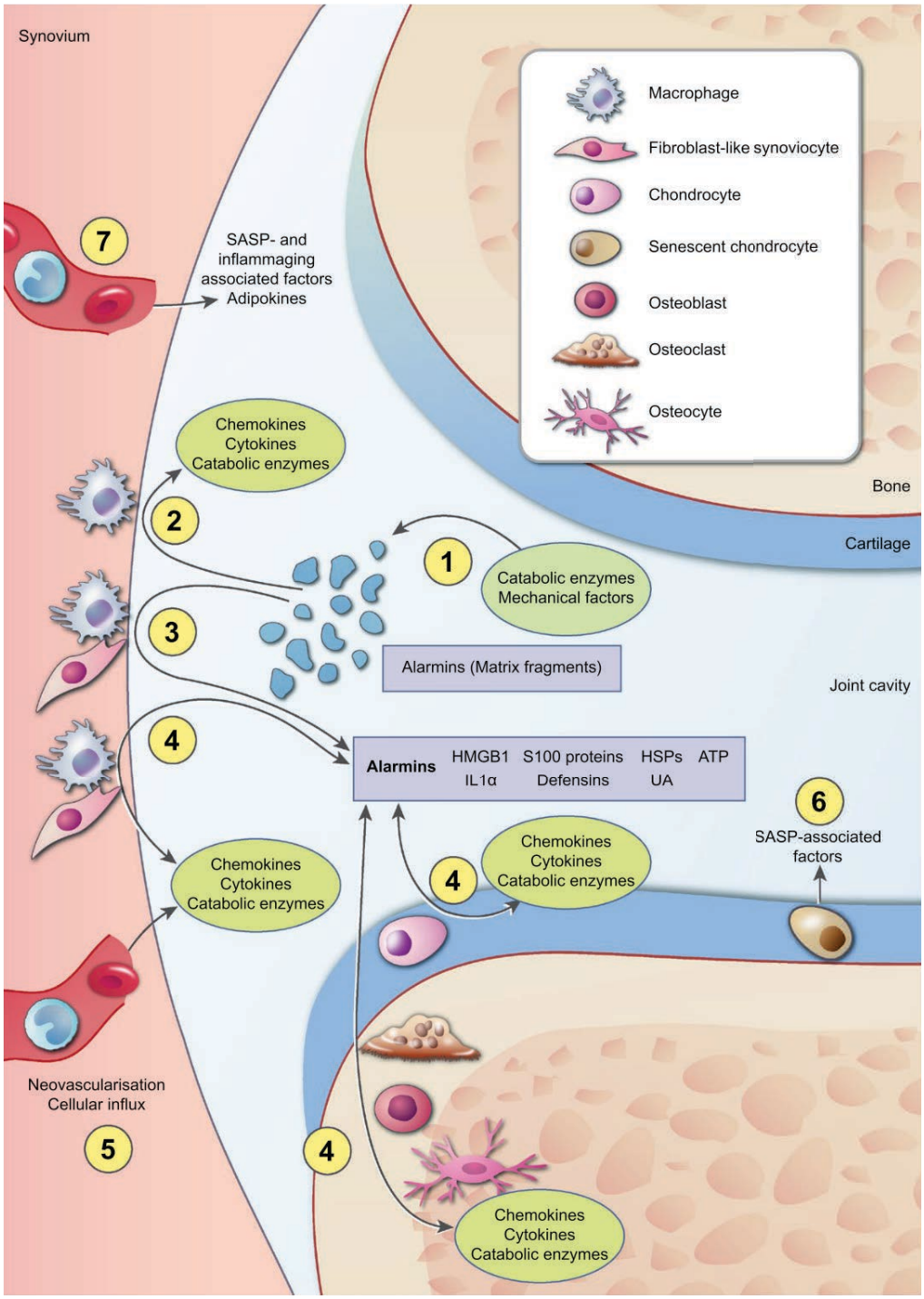

Figure 1.8: Schematic representation of inflammatory processes in OA progression, adapted from van den Bosch [217].

.

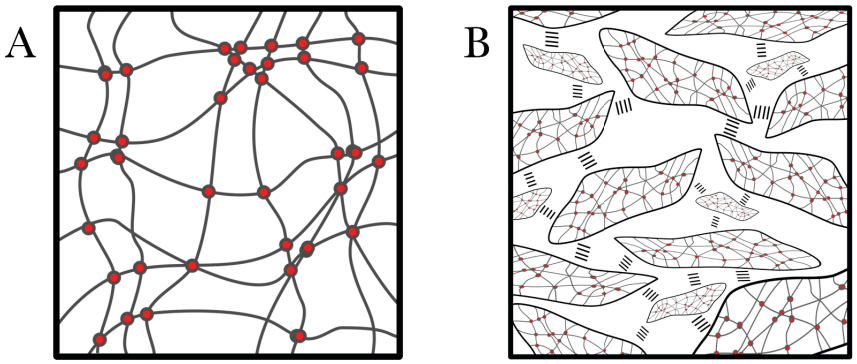

Figure 1.17: Schematic of polymer networks following A) quiescent gelation and B) sheared gelation to produce a fluid gel, from Cooke et al. [26].

have been shown to infer differing mechanical properties, particularly in the solid-like behaviour of the gel [42]. In this instance, the fluid gel produced with a pin stirrer, with a 'hairy particle' morphology (Figure 1.18B) showed a higher yield stress (defined as a 5% deviation from the LVR) than the one produced in a rheometer (Figure 1.18A) [147]. This is likely due to stronger interaction between the extensions of the hairy particles compared to the more spherical ones. Tuning these parameters can give rise to unique rheological properties for the potential delivery of therapeutics, cells and other material.

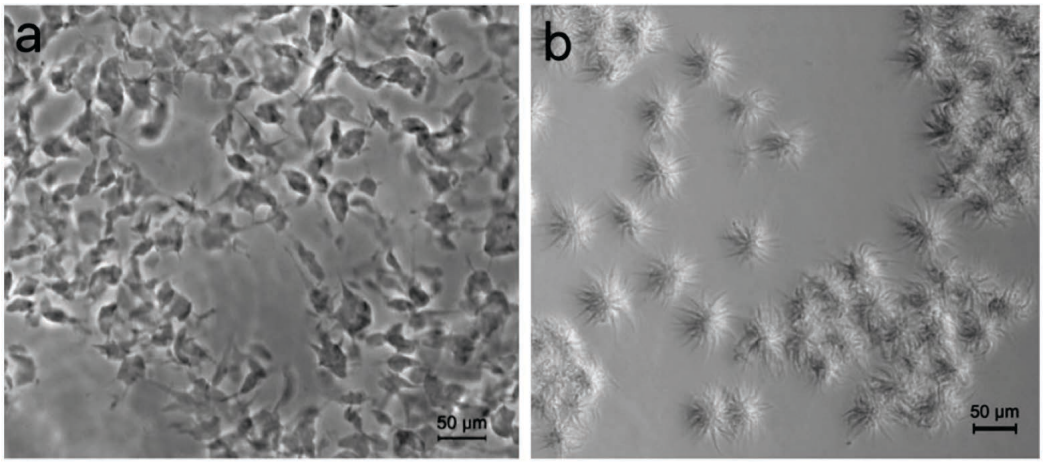

Figure 1.18: Morphology of agar fluid gel particles produced either in a) a rheometer or b) a pin stirrer; reproduced from [42].

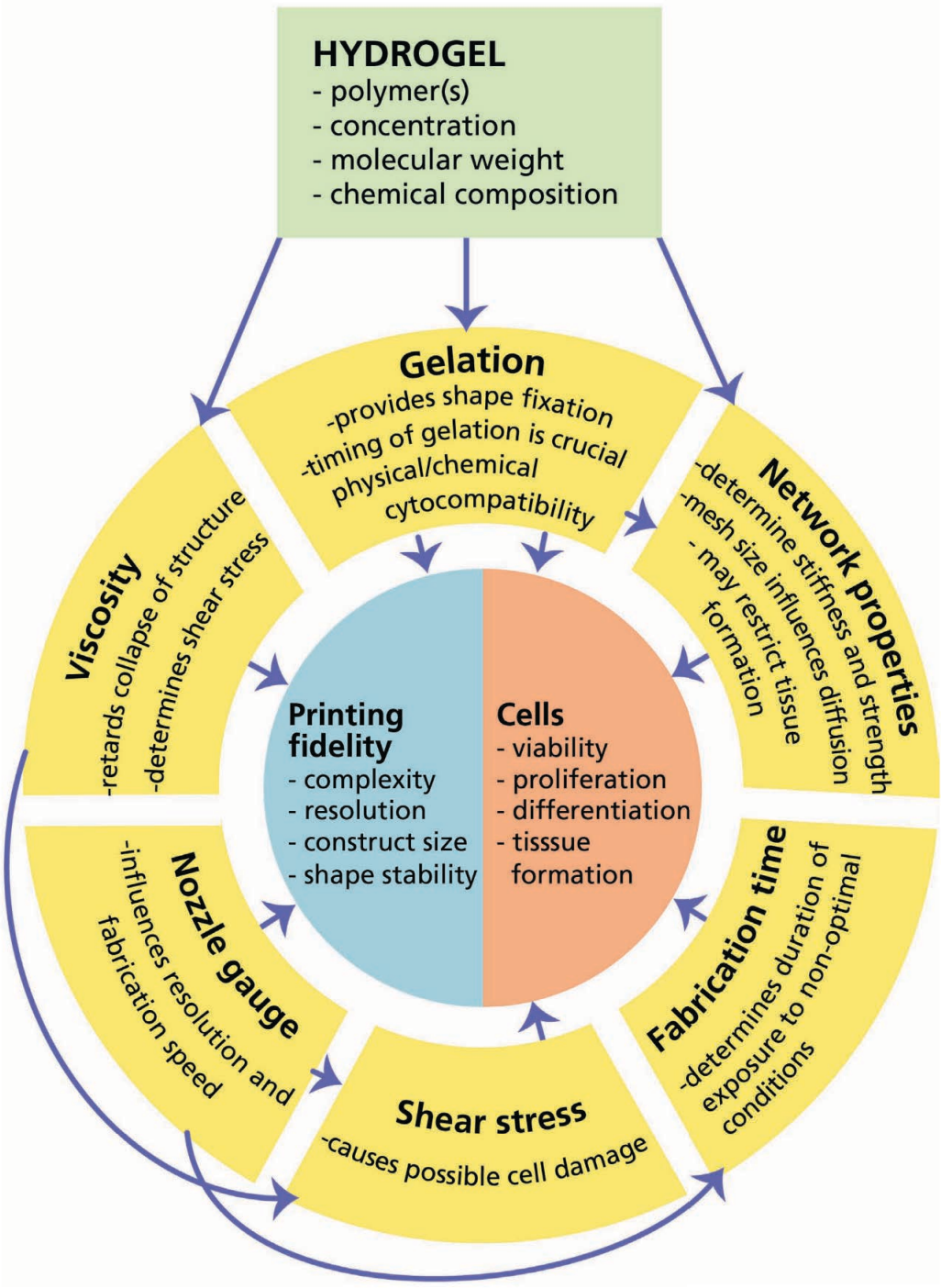

Figure 1.19: Considerations for printing technique; reproduced from Malda et al. [120].

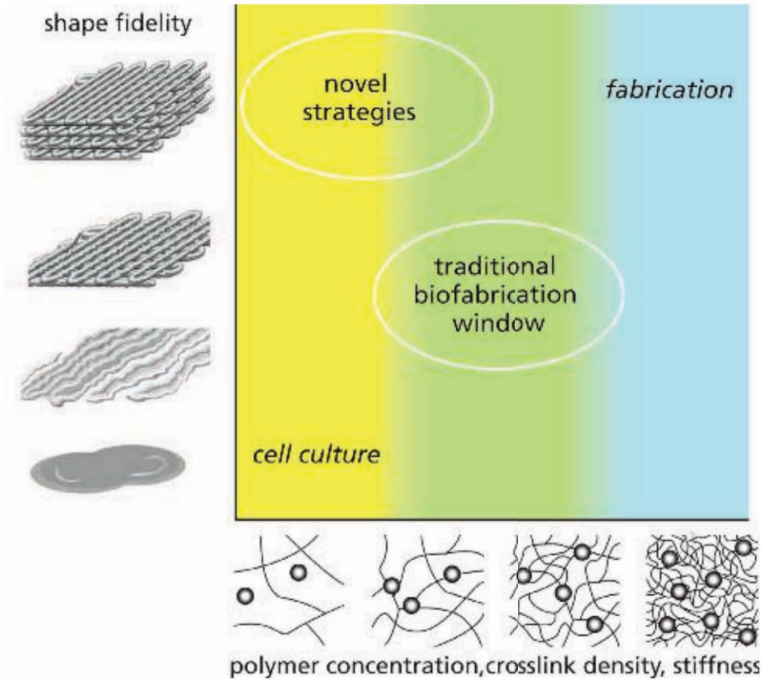

Figure 1.20: A consideration of the biofabrication window regarding hydrogel stiffness and geometry complexity. Softer gels which allow for cell migration and offer high cytocompatibility are of too low viscosity for traditional techniques and so novel techniques are required to overcome this limitation. Reproduced from Malda et al. [120].

is no longer required as the cell-seeded hydrogel is printed directly [11]. This is becoming a widely used technique and has led to the development of many novel hydrogels to enable direct extrusion. Methacrylated gelatin (GelMA) is a commonly used bioink for direct printing of structures for cartilage tissue engineering and has been modified with HA, PEG, PEGDA and graphene oxide to enhance its print properties [144, 195, 244]. Another material that has been modified for printability is hyaluronic acid. Another application of methacrylation of established hydrogels for tissue engineering was achieved by Burdick's group; using methacrylated (and further modified) hyaluronic acid, they were able to produce multi-layer constructs by direct bioplotting [153]. They developed a system to 'in-situ' crosslink these formulations such that they gelled upon arrival on the collector so there was very well controlled deposition of fibres to produce a lattice structure [154].

Many hydrocolloid solutions commonly utilised in 3D cell culture by casting into

peak stress of 1.7 MPa which is similar to the estimated physiological peak stress during walking [241]. Before applying a frequency sweep, each specimen was preloaded to 3 N to avoid initial slipping and subjected to two preconditioning cycles. 1500 and 3000 cycles at 25 and 50 Hz respectively were applied, with 60 s between them, to achieve a dynamic 'steady-state' which has been stated to occur after around 1200 to 4500 cycles for *ex vivo* cartilage [55, 125, 220]. Following preconditioning, eight different physiologically-relevant sinusoidal frequencies (1, 8, 10, 12, 29, 49, 71 and 88 Hz) were applied to each cartilage specimen in order of increasing frequency [55].

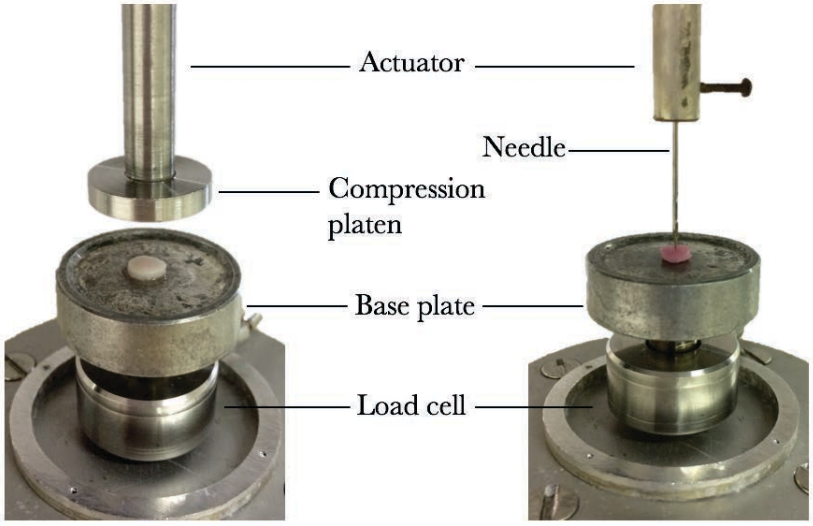

Figure 2.2: Mechanical testing set up for cartilage. Left: Aluminium compression platen mounted for DMA tests. Right: Sharp needle attached for thickness measurements.

Specimen thickness

The thickness of each cartilage specimen was measured, for conversion of DMA stiffness data to moduli, using a needle thickness test. A sharp needle was attached to the machine's displacement transducer (1 μm resolution, Figure 2.2 right) and the needle was pushed through the full thickness of the cartilage specimen. The displacement of the needle from initial contact with the cartilage (Figure 2.3 (a)) to contact with the base plate (Figure 2.3 (c)) was calculated as the cartilage thickness.

3.2 Methods

Tissue isolation and preparation

Cartilage explants were isolated from the lateral aspect of the femoral condyle of both OA and age matched post-mortem donors with no history of joint disease, as indicated in Figure 3.1. Cartilage in this region was macroscopically undamaged compared to the medial aspect of the joint, where cartilage had been degraded sufficiently that the subchondral bone was exposed (Figure 3.2). As the synovial fluid fills the joint space, however, the chemical and inflammatory environment is the same across both joint aspects. Tissue from post-mortem subjects is referred to as 'healthy' and tissue from joint replacement is referred to as 'OA'; patient data is presented in Table 3.1.

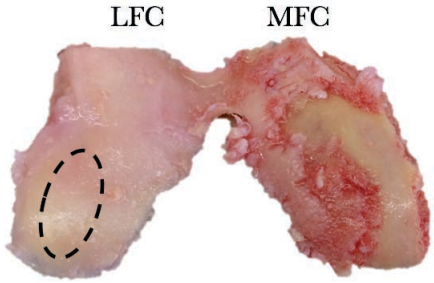

Figure 3.2: Femoral condyles as received in the laboratory from an OA patient following TKR surgery. The dashed region indicates where cartilage explants were taken for this study.

Table 3.1: Age and genders of the 20 patients whose cartilage was studied, n(explants) corresponds to specimens used for DMA.

Tissue	n (explants)	Age	Gender	Thickness (mm)
Healthy	6 (22)	76 (53-87)	M=3	1.465 ± 0.240
OA	14 (37)	71 (56-81)	M=10	1.463 ± 0.206

DMA and thickness testing

Cylindrical cartilage explants were hydrated for 30 min in Ringer's solution before DMA was performed in unconfined cyclic compression. Prior to testing a 3 N preload was

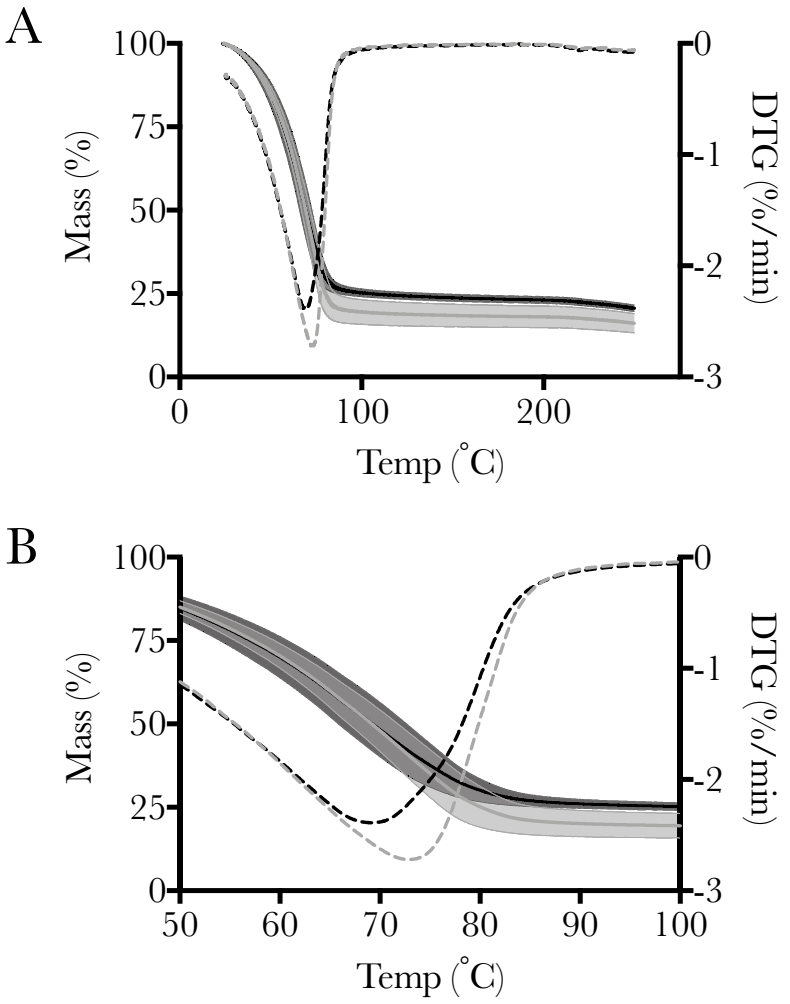

Figure 3.5: Thermogravimetric analysis of OA (grey) and healthy (black) cartilage between (A) 20-250℃. Dashed line indicates kinetics of mass change (DTG). Inset (B) shows the end of the water loss region, n=4.

direction of collagen fibril alignment in this region, but the surface was not macroscopically ruptured as seen in the OA samples. The OA cartilage had severe damage to the articulating surface post-DMA, while the middle and deep regions retained their structure. Figure 3.6B shows the relative quantification of sulphur distribution across the sections. Healthy and OA sections had similar sulphur levels in the deep and middle zones, but the OA samples had lower levels in the superficial zone. Quantification of the post-DMA samples shows that in both OA and healthy samples, mechanical testing reduced the sulphur content, which is likely due to changes in aggrecan proteoglycan organisation.

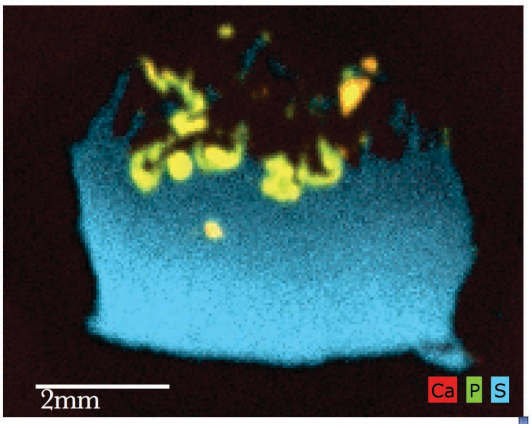

Figure 3.7: μXRF mapping of sulphur, calcium and phosphorus showing evidence of Ca and P localisation in mineral deposits in the middle and superficial regions of OA cartilage.

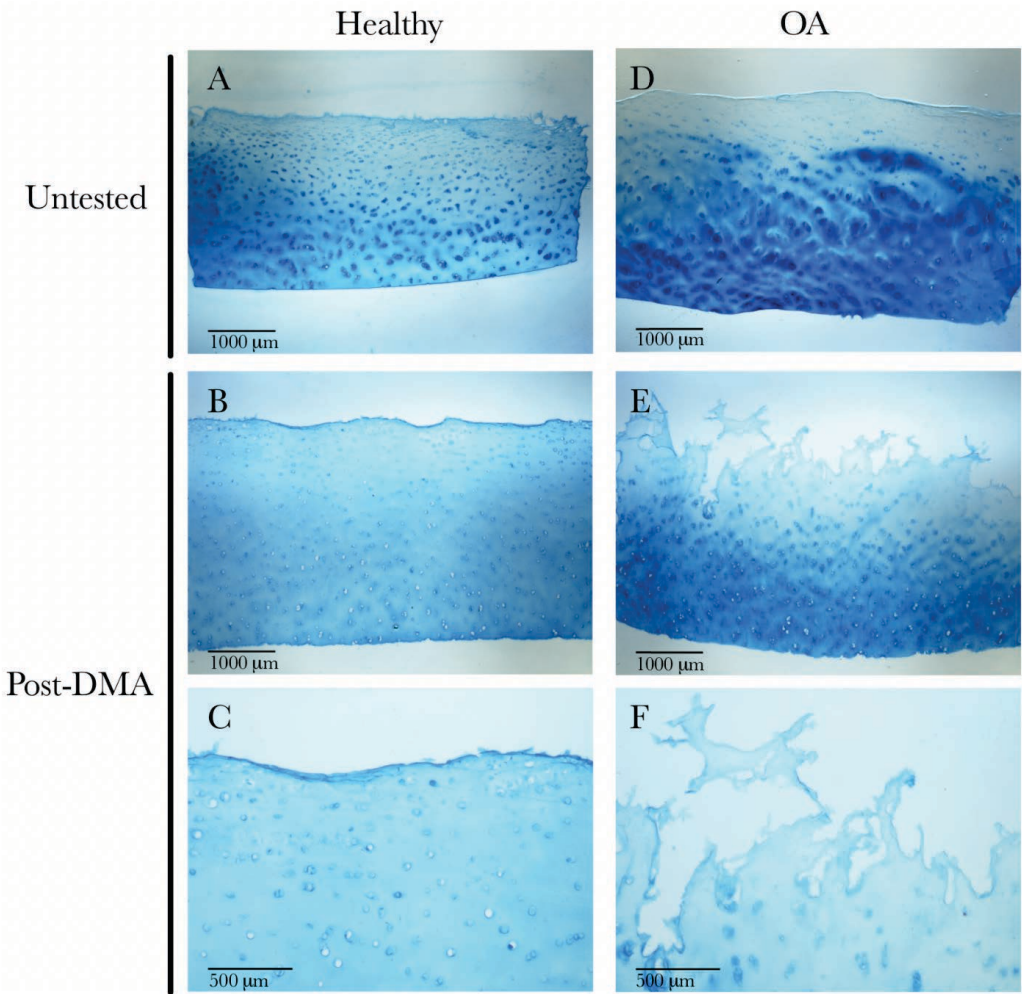

Figure 3.8: Representative alcian blue staining of 10 μm thick cartilage sections from healthy (A-C) and OA (D-F) samples both untested (A, D) and post-DMA (B&C, E&F).

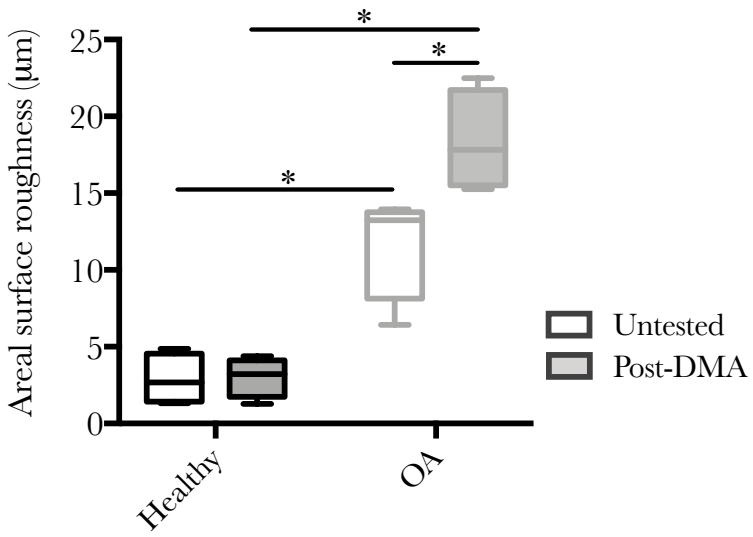

Figure 3.9: Surface roughness of healthy and OA cartilage samples with or without DMA testing as measured by WLI; n=3, * $p<0.05$.

3.4 Discussion

This study aimed to understand the differences in frequency-dependent viscoelastic properties of isolated healthy and OA human articular cartilage and to compare these to the physicochemical changes seen. Tissue was excised from the lateral aspect of the OA joint, which is known to be less exposed to mechanical stresses than the medial aspect, and thus was used to represent cartilage which was not excessively mechanically loaded but was exposed to the same chemical environment.

The first component of this study determined the viscoelastic properties of healthy and OA human cartilage. The logarithmic frequency-dependent behaviour in both the storage and loss modulus was similar to previous findings in human and bovine cartilage [106, 161, 212]. The significant reduction in storage modulus across a range of frequencies in OA specimens is likely to be indicative of disruption to the matrix structure as a result of OA cytokines, MMPs and altered joint loading. The solid matrix components of cartilage, Col II and the aggrecan-rich proteoglycan network, are primarily responsible for the compressive stiffness of cartilage and was shown to be reduced in OA. This difference was statistically significant at all but the highest frequency, 88 Hz (P=0.0581), which has

Formulation of a deliverable fluid alginate

An alginate fluid gel was produced by drop-wise addition of $CaCl_2$ to sodium alginate solution under shear. The forming of the fluid gel is shown in Figure 4.5A, where the addition of the divalent cation caused a sharp increase in the viscosity of the alginate solution. The viscosity continued to increase until around 6 minutes after which the viscosity dropped slightly and then equilibrated. To ensure that the fluid alginate was deliverable through a needle or cannula, the shear rate was ramped and recovered cyclically between 0.1-500 s^{-1}. There was only evidence of a very small hysteresis loop in Figure 4.5B, indicating that this fluid gel will be stable during manipulation and handling. Figure 4.5C shows the different forms that alginate was produced in. As can be seen on the right hand side of Figure 4.5C, the fluid gel was able to flow like a liquid under shear to then rest as a solid-like material in the absence of shear. The presence of bubbles in the fluid gel shows how the network of entangled polymer chains can reorder around structures.

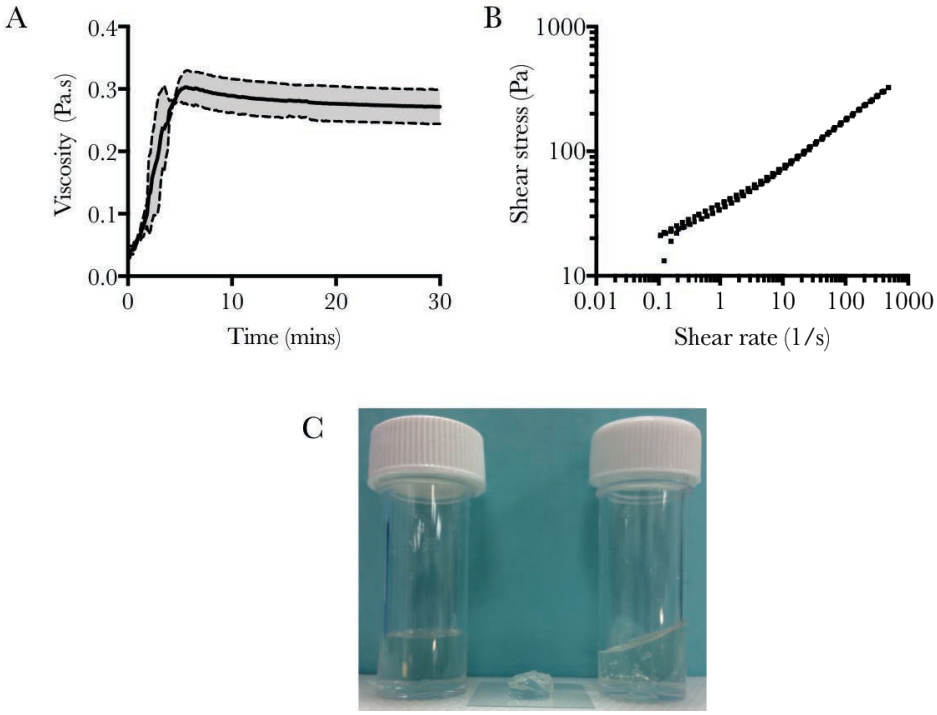

Figure 4.5: Formulation of fluid alginate. A) Viscosity profile during the cross-linking of alginate fluid gels (n=3). B) Change in shear stress with shear rate over ramps of shear rate from 0.1-500-0.1-500^{-1}, sol (left), quiescent (middle) and fluid (right) alginate.

The interesting mechanical properties of fluid gels are partly due to their particulate architectures with short range interactions and entanglements. Figure 4.6A shows the typical architecture of fluid gel fragments connected by ribbon-like structures. Chondrocytes were then seeded between fluid alginate particles and the morphology of all cells was spherical, showing little interaction with the alginate particles. Further there were high levels of cell viability in these cultures (Figure 4.6B and 4.6C).

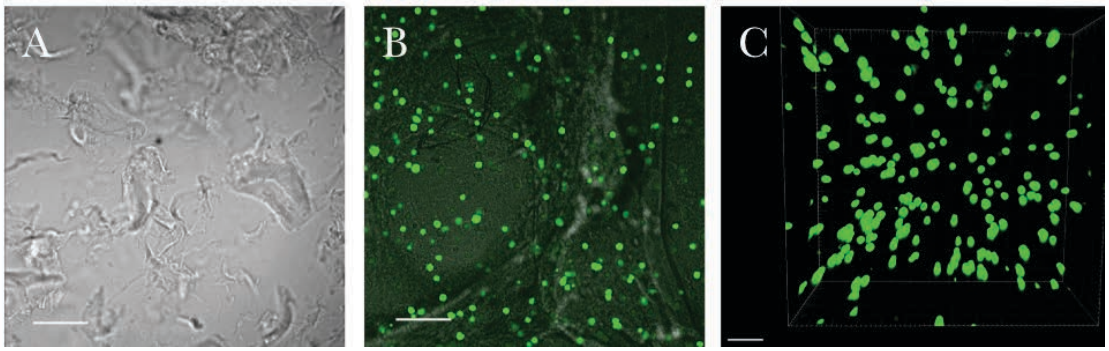

Figure 4.6: Imaging of fluid alginate and seeded chondrocytes. A) Fluid gel architecture (SB: 200 μm), B) fluid gel with chondrocytes showing interaction with alginate fragments and ribbons SB: 100 μm), C) z-stack of chondrocytes in fluid alginate 4 days after seeding, SB: 100 μm

Mechanical characterisation of fluid and quiescent alginate

Dynamic small deformation rheology was performed to determine the viscoelastic properties of both the quiescent and fluid gel systems. Firstly, by applying an increasing oscillatory stress, the LVR of each alginate matrix was determined (Figure 4.7A). The LVR of the fluid gel was shorter than that of the quiescent gel, highlighting the ability of the fluid network to flow under stress. The frequency dependent behaviour of the materials was then probed. The presence of weak interactions and entanglements were confirmed through linear rheology (Figure 4.7B), with the sheared alginate showing solid-like behaviours dependent on frequency, typical of weak gels. Interestingly, the quiescent gel showed a similar mechanical spectrum (at higher G values) inferring structures which mirror each other, complementing data obtained via microscopy shown in Figure 4.8C. Fluid alginate (grey) showed strong shear thinning behaviour

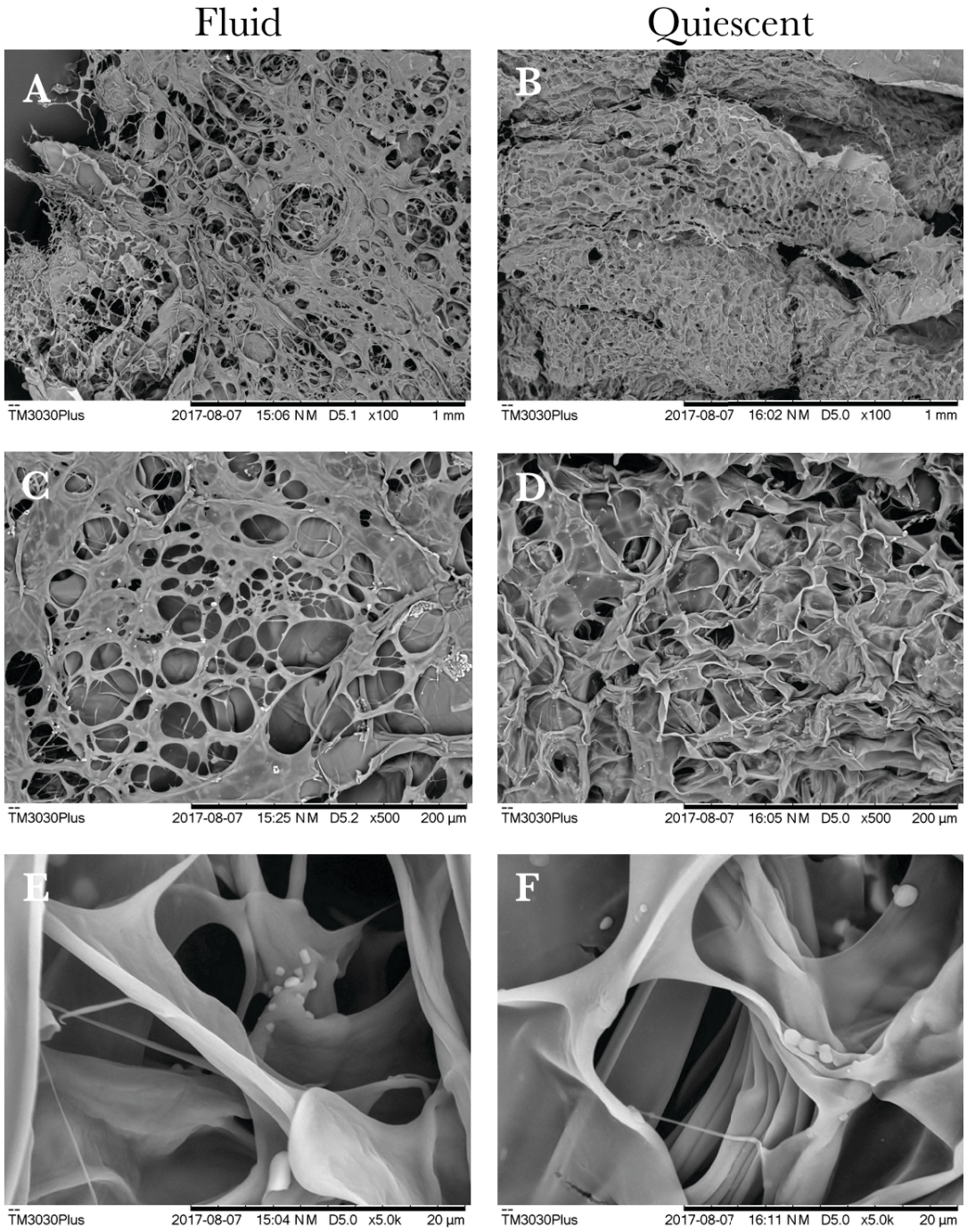

Figure 4.8: SEM images of thin sections of fluid (A, C, E) and quiescent (B, D, F) alginate following freeze drying.

The effect of alginate fluid gel on the phenotype of primary articular chondrocytes

To compare the efficacy of alginate fluid gel with quiescent alginate in recovering and supporting a chondrogenic phenotype, primary hACs were cultured in either alginate fluid gel or in quiescent alginate for a period of 7 days. Following 7 days of culture Col II and aggrecan expression were higher in the quiescent than fluid alginate and Sox9 expression was significantly higher in the quiescent alginate (Figure 4.11).

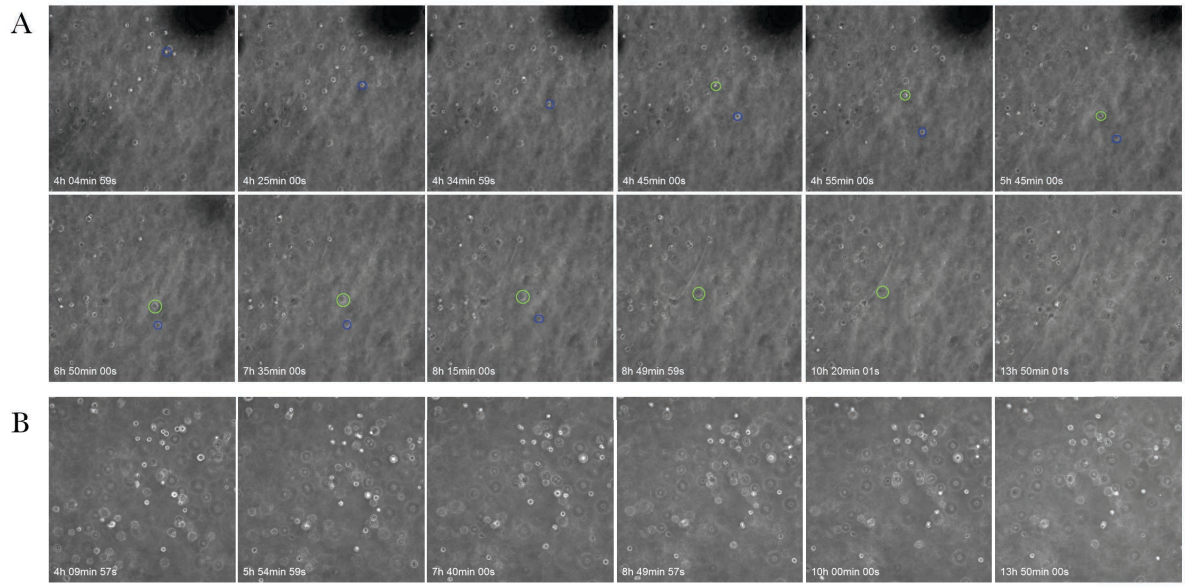

Figure 4.9: Tracking of chondrocytes in (A) fluid and (B) quiescent alginate over 14 hours. Movement of cells is demonstrated by coloured circles. Full videos are available at https://tinyurl.com/yctb9eqm, Videos 1 and 2.

Driving chondrogenic phenotype of primary chondrocytes encapsulated in alginate

Due to the proximity of native cartilage tissue during the ACI repair of cartilage defects, *ex vivo* cartilage tissue and cartilage conditioned media were studied to determine their effect on the efficacy of using fluid and quiescent alginate as chondrocyte delivery matrices. By adding a piece of explanted cartilage tissue, (Figure 4.12A) there was an increase in the expression of COL2A1 in quiescent alginate following 14 days of culture (Figure 4.12).

The effect of the physical presence of cartilage tissue was shown to be secondary to the factors released from it (Figure 4.12B), since conditioned cartilage explant media resulted in a greater increase (P=0.0376) in Col II expression than the cartilage tissue itself. This suggests that in the *in vivo* environment, alginate encapsulation of hACs will be even more efficacious in promoting and maintaining the chondrogenic phenotype due to the secretion of endogenous anabolic factors from the surrounding cartilage matrix. This condition was then investigated to determine if it could be used to drive the native alginate phenotype in fluid alginate culture. However, when comparing conditioned and basal media, there was no significant difference between the conditions (P=0.3126, Figure 4.12C); this further supports that physical entrapment of chondrocytes is critical to maintenance of the native Col II phenotype.

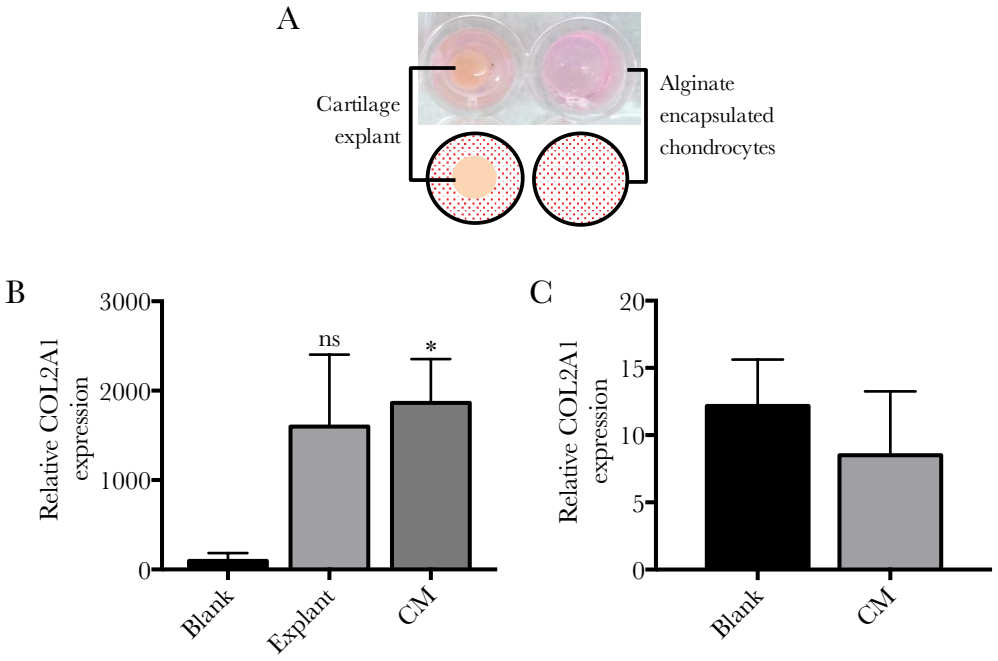

Figure 4.12: A) Experimental set-up for explant (left) and blank/conditioned media (CM) (right). Relative Col II expression in B) quiescent and C) fluid alginate when cultured with basal media (blank), a cartilage explant or conditioned media, n=3.

5.3 Results

Characterisation of the agarose fluid bed

Agarose fluid gel was produced by introducing shear as the hydrocolloid solution was cooled. This resulted in the formation of an entangled microparticulate gel network as can be seen in Figure 5.2 using phase contrast microscopy. Individual tadpole-shaped particles were formed (as indicated by arrow in Figure 5.2A) which then appeared to interact from the head-regions to form larger aggregate particles of between 150-200 μm in diameter. The shape of the particles prior to agglomeration was likely due to the way that shear was applied during gelation. The hypothesised production of these particles is shown in Figure 5.2D. The high shear in the column above the stirrer (region marked (1) within dashed lines) may cause the formation of elongated gel particles and the toroidal motion of the bulk gel in 3D forces these individual particles into regions of lower shear. This would allow for the agglomeration and entanglement of these particles. In a bulk,

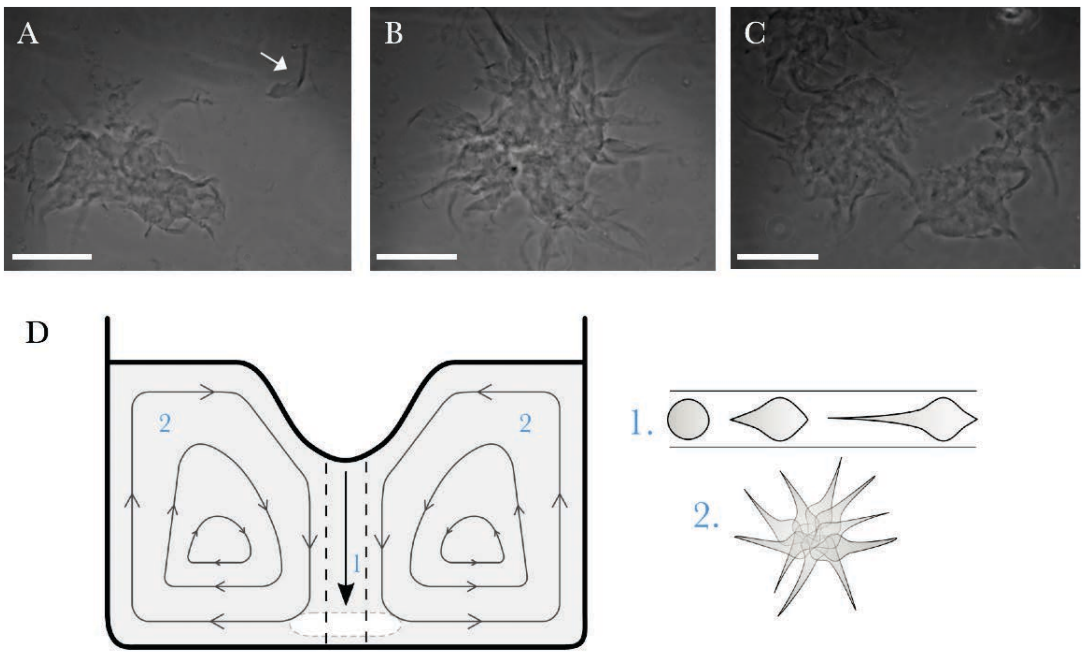

Figure 5.2: Phase contrast imaging of fluid agarose particles showing A) individual units indicated by arrow B) characteristic 'hairy' aggregates and C) interaction of aggregates. D) Schematic hypothesis of formation of individual particles and aggregates at high (1) and low (2) shear regions respectively. SB=150 μm

as seen in Figure 5.2C, the aggregates interact and entangle by the tails which project from the core. These weak entanglements are likely responsible for the unique mechanical properties of fluid gels.

Rheological investigations were performed to investigate the properties of agarose fluid gel under shear. Firstly a stress sweep was performed; the LVR was found to be fairly short with a cross-over between G' and G" at 32 Pa. A frequency sweep was then performed at 1% strain which showed a higher G' than G" ($\tan\delta = 0.17 \pm 0.013$), and slight frequency dependence indicating weak gel, or structured liquid, behaviour (Figure 5.3 A, B). The shear rate was alternated between 0.1 and 100 s^{-1} to investigate the recovery of viscosity. As expected, the fluid gel was highly shear thinning and the recovery of viscosity was very fast (Figure 5.3C). Finally, a high shear rate (100 s^{-1}) was applied and then removed to determine the recovery of elasticity in the agarose matrix. Figure 5.3D shows that there was a rapid increase in shear storage modulus immediately following shearing, although the recovery to the original elasticity takes longer than 30 s.

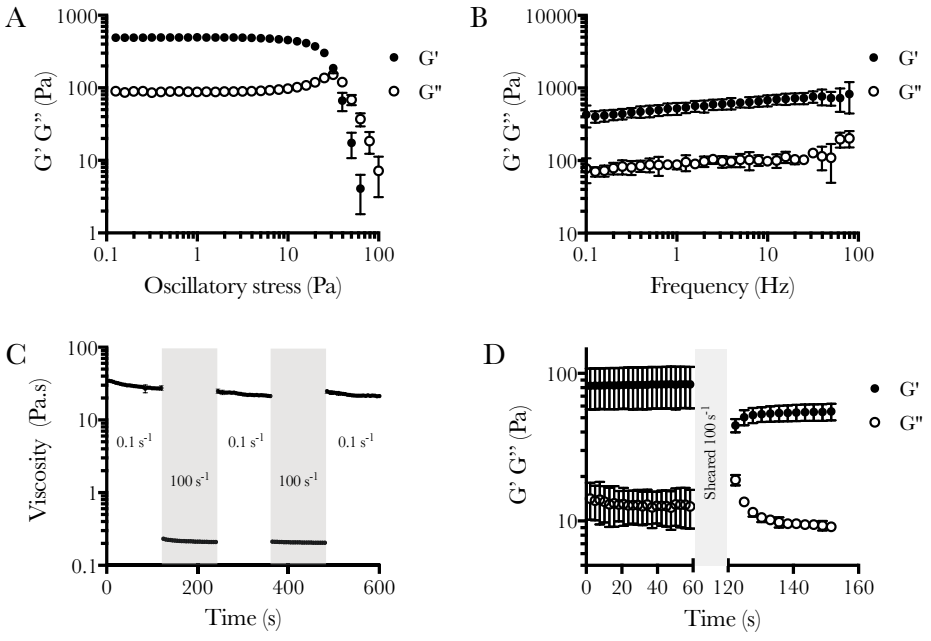

Figure 5.3: Rheological characterisation of 0.5 w/v% agarose fluid gel A) Stress sweep from 0.1-100 Pa B) Frequency sweep from 0.1-100 Hz at 0.1% strain C) Recovery of viscosity between shear rates of 0.1 and 100 s^{-1} D) Recovery of elasticity at 1 Hz and 0.5 % strain following a 60 s peak hold at 100 s^{-1}. Data plotted are mean ±SD, (n=3).

Suspended printing resolution and diffusion limits

Printing into a particulate fluid system restricted the resolution of print geometries to features that were larger than the interstices between gel particles. By printing a dye with a similar viscosity to water, the movement of material through the continuous phase into the interstices between fluid gel particles was visualised (Figure 5.4A-F). The achieved resolution decreased as the inner diameter of the needle increased (and Birmingham gauge number decreased) (Figure 5.4, $R^2 = 0.9846$). There was also larger variability of the printed wall width when a larger needle was used.

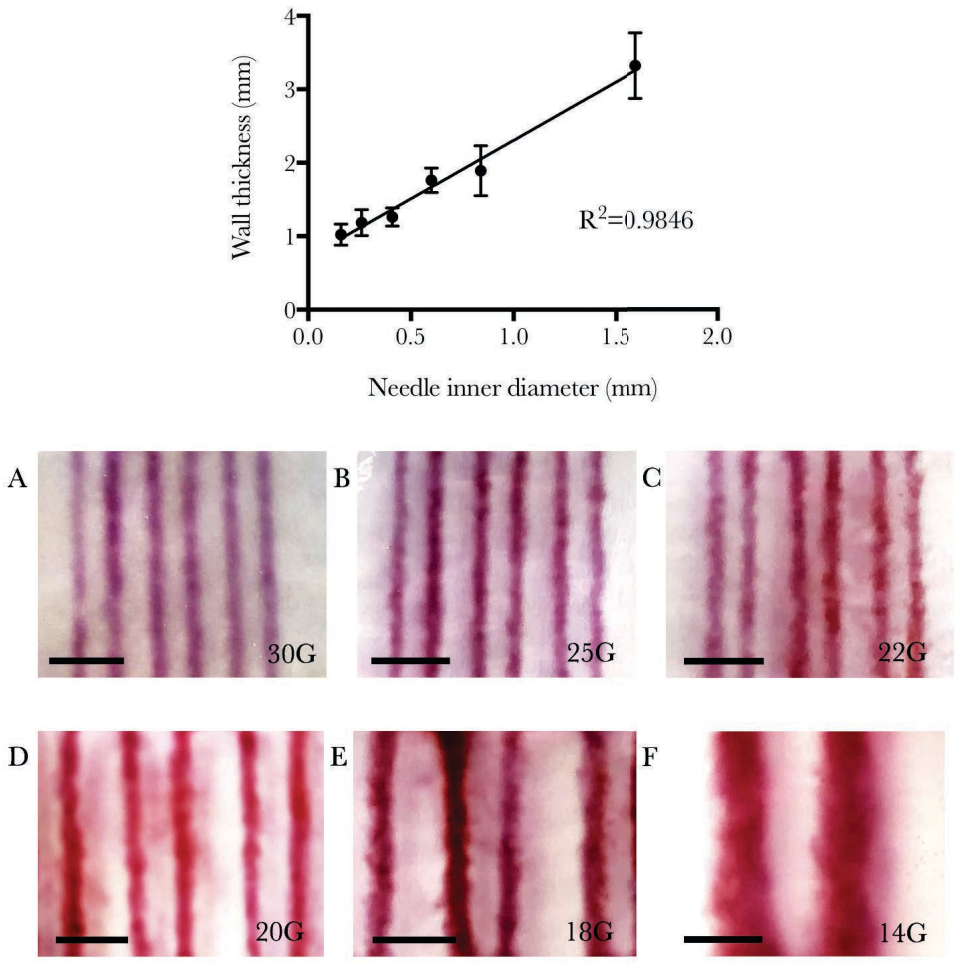

Figure 5.4: Resolution capabilities of 0.5 w/v% fluid agarose print bed with increasing needle diameter (decreasing gauge) A-F. SB: 5 mm; data are presented as mean ± SD, n=18.

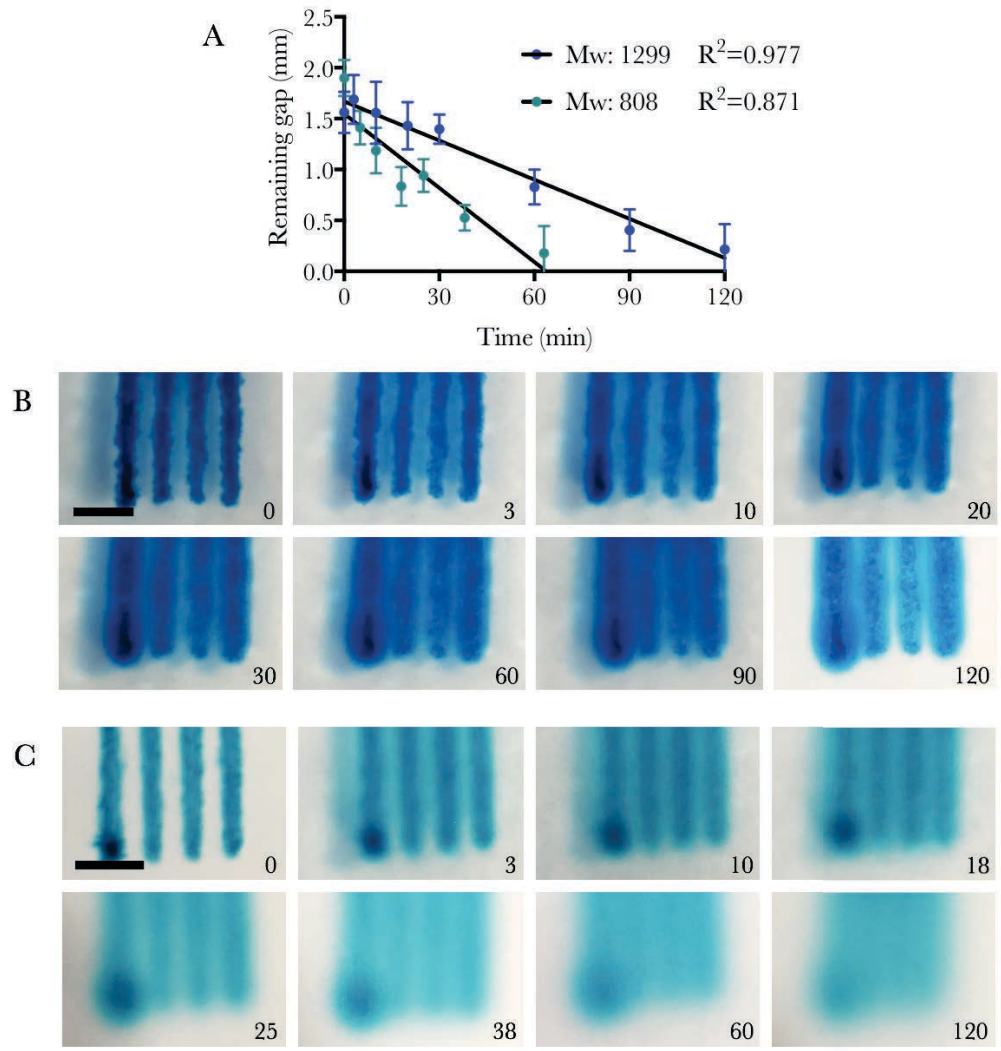

Figure 5.5: Diffusion of low viscosity dyes of varying molecular weight across a 2mm gap following printing. A) Diffusion data over time, B and C) Optical images of diffusion over 120 min in B) Alcian Blue solution of 1299 g.mol^{-1} and C) Fast Green FCF solution of 808 g.mol^{-1}. SB: 5 mm, bottom right = time (min); data are presented as mean ± SD, n=9.

Further, whilst low viscosity solutions could be printed and supported, there was a limitation of diffusion through the particulate gel matrix. This resulted in a finite crosslinking time before printed features were lost. Figure 5.5 shows the time-dependent diffusion of dye solutions of different molecular weight (Mw) across 2 mm gaps. The diffusion of the dye as it filled the gap was imaged over 2 h as shown in Figures 5.5 B and C. The dye with a lower Mw (Fast Green FCF, Figure 5.5C) showed significantly faster diffusion than the higher Mw dye (Alcian Blue, Figure 5.5B)) (P=0.0063).

Bioprinting of low viscosity solutions into complex geometries

To demonstrate that this technique allows for freeform fabrication, a number of structures were printed. Printing of helical structures with overhangs showed the capability of the agarose fluid bed to support a suspended low viscosity gel prior to crosslinking (Figure 5.6D and video 3 [(1)]). In more practical applications, the printing of tubular structures and perfusable bifurcations were also possible using this technique (Figure 5.6).

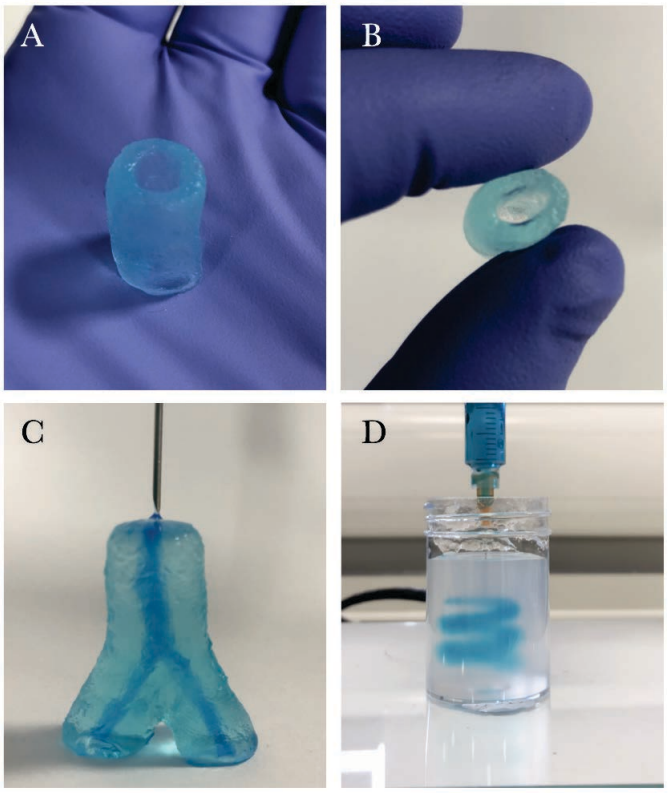

Figure 5.6: Examples of geometries that can be printed from 1% w/v alginate (with food dye for visualisation) using suspended manufacture including hollow (A,B) and hollow bifurcating (C) structures. D) is a snapshot of Video 3, showing the printing of a helical structure with overhangs without the need for additional support structures.

Bioprinting of bi-layered constructs and subsequent characterisation

To produce constructs that model the OCU, mineralised and non-mineralised regions were required. As such, HAp was combined with gellan gum and printed into gellan/gellan-

[1]Video available at https://tinyurl.com/yctb9eqm

mineral constructs with continuous interfaces. This was observed visually in Figure 5.7A, as the addition of mineral increased the opacity of the gel construct. Mineral is highly attenuating so its distribution in the whole construct was investigated using μCT as in Figure 5.7B. The interaction of HAp with the gellan polymer network can be seen in Figure 5.7 C, as it coated the polymer throughout in individual particles but also formed aggregates, as indicated by the arrow. Finally, inclusion of HAp resulted in faster relaxation behaviour following loading to 20% strain (Figure 5.7D).

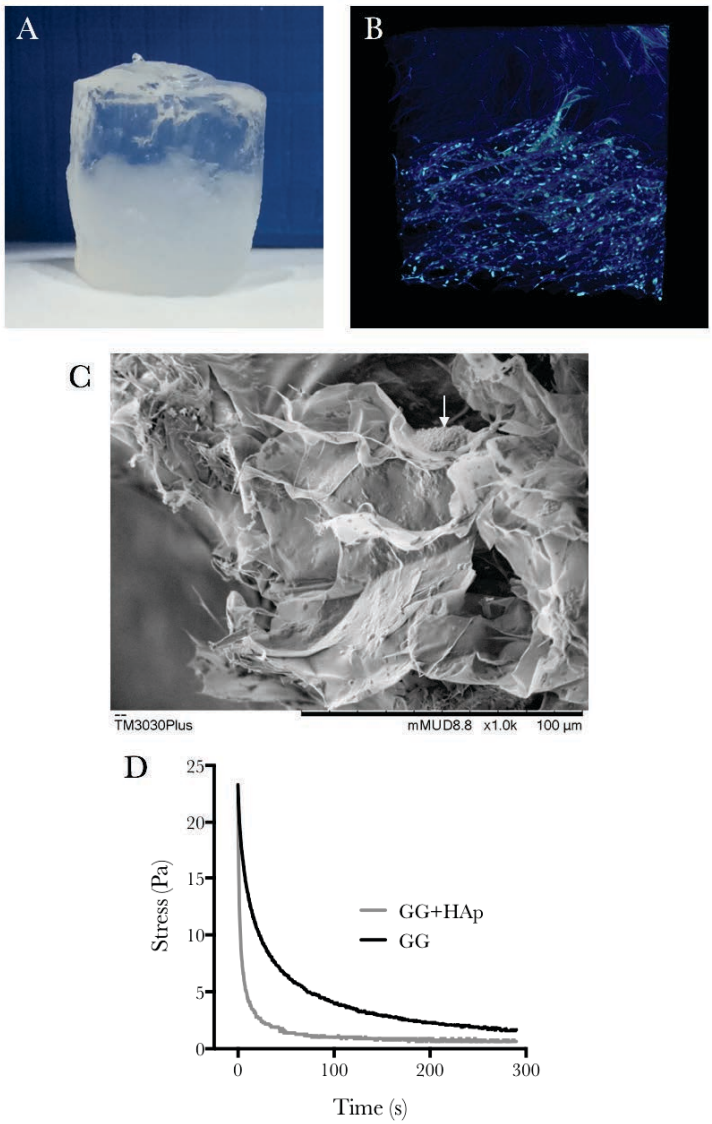

Figure 5.7: Introduction of mineral for production of bi-layered constructs. A) Gellan/Gellan-HAp construct. B) μCT reconstruction of a bi-layered construct. C) SEM of HAp integrated into gellan structure, arrow indicates aggregated HAp. D) Stress relaxation behaviour of gellan (GG) and GG-HAp constructs.

Characterisation of embedded printed cell populations

Human osteoblasts and chondrocytes were isolated and cultured prior to printing into a bi-layered construct. The printing process showed very good cell viability (Figure 5.8) with very few dead cells. qRT-PCR was used to determine the stability of cell phenotype following printing and 28 day culture of osteochondral plugs. The retrieved constructs were sectioned as shown in Figure 5.9A prior to homogenisation for analysis. Figure 5.9 shows that Col II and aggrecan expression remained highest in the cartilage-like region of the constructs and lowest in the bone-like region. Col I characterisation showed the opposite, with the highest expression in the bone-like region.

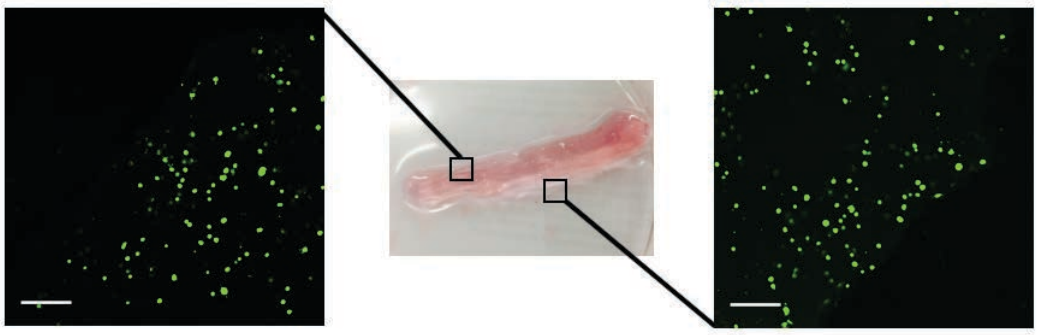

Figure 5.8: Viability of TC28 cells directly after printing SB: 200 μm

For the development of tissue models, it is important that the embedded cell populations maintain their ability to produce cartilage matrix and maintain functional responses to stimulation. Production of aggrecan (ACAN) by chondrocytes following SusMan was investigated using IHC; Figure 5.10A shows strong evidence of aggrecan in the peripheral regions of cells and some evidence of aggrecan in the extracellular regions. The response of chondrocytes to inflammatory stimuli in printed constructs was evaluated by measuring the production of IL-6 as a function of IL-1β dosage. Figure 5.10B shows this response at 4 and 24 h. In the 3D printed (SusMan) group, the peak response was delayed and seen to occur at a higher IL-1β concentration than in the monolayer group. The increase between 4 and 24 h in both groups was similar however.

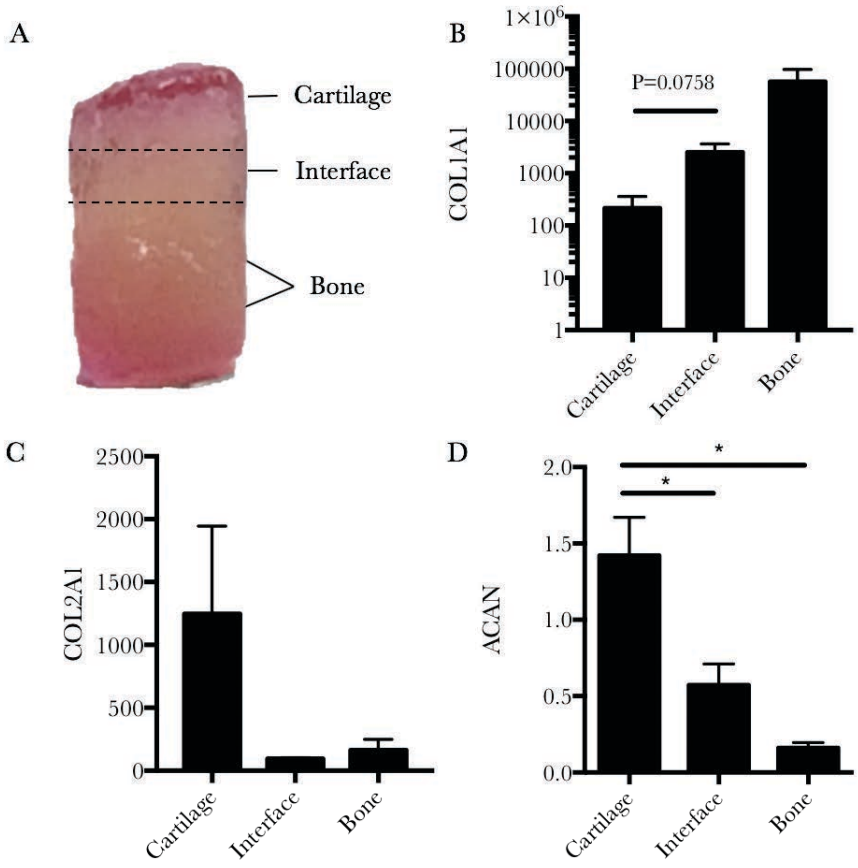

Figure 5.9: qRT-PCR of partitioned constructs following 28 days culture. A) Retrieved construct after culture in an *ex vivo* defect B) COL1A1, C) COL2A1 and D)ACAN expression relative to 18S. Data are shown as mean + SEM, n=3.

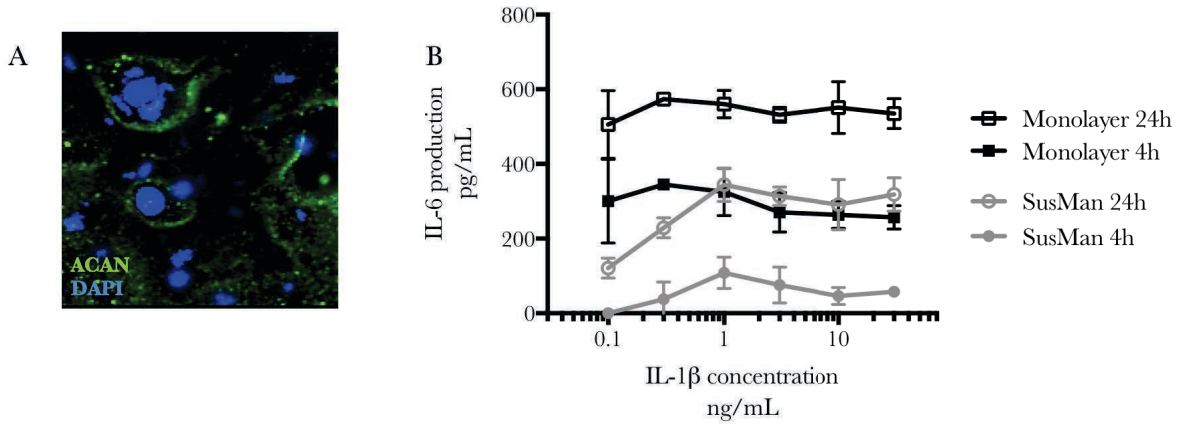

Figure 5.10: Functional characterisation of SusMan constructs A) Aggrecan staining in cartilage-like region. B)IL-6 production as a result of IL-1β stimulation at varying doses in both monolayer culture and SusMan produced constructs. Data are shown as mean $\pm$ SD, n=4.

ADVANCED MATERIALS
www.advmat.de

Structuring of Hydrogels across Multiple Length Scales for Biomedical Applications

*Megan E. Cooke, Simon W. Jones, Britt ter Horst, Naiem Moiemen, Martyn Snow, Gurpreet Chouhan, Lisa J. Hill, Maryam Esmaeli, Richard J. A. Moakes, James Holton, Rajpal Nandra, Richard L. Williams, Alan M. Smith, and Liam M. Grover**

The development of new materials for clinical use is limited by an onerous regulatory framework, which means that taking a completely new material into the clinic can make translation economically unfeasible. One way to get around this issue is to structure materials that are already approved by the regulator, such that they exhibit very distinct physical properties and can be used in a broader range of clinical applications. Here, the focus is on the structuring of soft materials at multiple length scales by modifying processing conditions. By applying shear to newly forming materials, it is possible to trigger molecular reorganization of polymer chains, such that they aggregate to form particles and ribbon-like structures. These structures then weakly interact at zero shear forming a solid-like material. The resulting self-healing network is of particular use for a range of different biomedical applications. How these materials are used to allow the delivery of therapeutic entities (cells and proteins) and as a support for additive layer manufacturing of larger-scale tissue constructs is discussed. This technology enables the development of a range of novel materials and structures for tissue augmentation and regeneration.

1. Introduction

Hydrogels are extensively used in regenerative medicine research as a consequence of their high-water content, meaning that they can be placed into a biological system without compromising viability.[1–3] Furthermore, given that they are formed from large, organic molecules, there is considerable scope for customizing the materials through modifications in the chemistry of the polymer backbone (the introduction of cell adhesion moieties, etc.), or by manipulating the gel cross-linking process.[4,5] The first application of encapsulation to protect mammalian cells was in the 1980s, to enable the delivery of pancreatic islets as a treatment for diabetes.[3] This has ultimately spawned a very active research field, where gels are often used for the delivery of cells or other therapeutics.[6–8] In the last ten years, gels have been used widely to study how cells are able to respond to their local environments, enabling ground-breaking work that not only starts to reveal how cell fate can be determined by tailoring stiffness,[9,10] the geometry of moieties distributed around the cells,[11,12] and the viscoelasticity of cell attachments/environments,[13] but can be exploited to synthesize unique delivery systems.[14,15] All of this points to the fact that there should be a panapoly of novel gel-based materials that are making their way to clinical application. Despite all of this progress, however, this is not the case and one of the major reasons for this is that new medical materials must pass a very large number of biological safety tests before they are used. In addition, materials to be used in clinical trials or for sale on the market must be supplied via a manufacturing process that is developed, validated, and operated in accordance with Good Manufacturing Practice (GMP). This requires engagement with appropriate GMP-licensed pharmaceutical/medical device manufacturing facilities. The use of bespoke chemistries and formulation conditions can preclude the use of processing methods and equipment that are standard to the pharmaceutical/medical device

M. E. Cooke, Dr. B. ter Horst, Prof. M. Snow, Dr. G. Chouhan, Dr. R. J. A. Moakes, Dr. J. Holton, Dr. R. Nandra, Dr. R. L. Williams, Prof. L. M. Grover
School of Chemical Engineering
University of Birmingham
Edgbaston, Birmingham B15 2TT, UK
E-mail: l.M.Grover@bham.ac.uk

M. E. Cooke, Dr. S. W. Jones
Institute of Inflammation and Ageing
MRC Musculoskeletal Ageing Centre
QE Hospital
University of Birmingham
Edgbaston, Birmingham B15 2TT, UK

Dr. B. ter Horst, Prof. N. Moiemen
Scar Free Foundation Centre for Burns Research
QE Hospital
University of Birmingham
Edgbaston, Birmingham B15 2TT, UK

Dr. L. J. Hill, M. Esmaeli
Institute of Inflammation and Ageing
University of Birmingham
Edgbaston, Birmingham B15 2TT, UK

Dr. A. M. Smith
Department of Pharmacy
University of Huddersfield
Queensgate, Huddersfield HD1 3DH, UK

DOI: 10.1002/adma.201705013

manufacturing industry. Thus, this furthers the increasing level of innovation required to develop a finished product. In many cases, this means that it is not economically viable to move these materials to the point of clinical trial and so clinical researchers tend to stick with a very small number of materials, which they use to deliver a multitude of therapeutic entities. In an attempt to take a much more rational approach to the use of hydrogels in clinical applications, we have pushed forward research on the structuring of materials that have already secured MHRA/EMA/FDA approval so that they can exhibit distinct physical properties. We have done this by modifying gelation conditions through the application of shear and by the absorption of reactive molecules into the gel structure in order to enable the formation of third phases within and between the gel particles. Although not completely void of the substantial costs required to deliver new therapeutic molecules, which require significant investment in toxicological and safety testing, the significant reduction gained from previously obtained data sets allows a more direct route to translation, which may result in higher degrees of adoption. Therefore, this paper summarizes the work that we have done in this area in the past few years and suggests areas for further research and development opportunities in the coming years.

Liam M. Grover is the Director of the Healthcare Technology Research Institute at the University of Birmingham. He is a materials scientist by training and his research focuses on the interactions between materials and biological systems. He has a particular interest in controlling the assembly of the extracellular matrix as a means to enhance regeneration, prevent scarring and inhibit the pathological formation of bone. His group currently works on developing treatments for these conditions and translating these technologies to clinical settings.

2. Structuring Hydrogels by Shear—Formation of Fluid Gels

The diverse and controllable characteristics of gels, in particular hydrogels (water-based gels), have initiated great interest across a multitude of industries and applications. Within the field of biomedical research, many FDA/MHRA/EMA-approved synthetic polymers have been studied for their ability to form gelled networks.[16] However, more recently, there has been a push toward more natural biopolymers such as polysaccharides and sugar-based hydrogelators[17] for both their ready availability and frequent similarity to the extracellular matrix (ECM). It is of no surprise therefore, that polysaccharide hydrogels have become widely used in the field of tissue engineering: predominately used as scaffolds, presenting a mimetic of ECM with the intrinsic ability to stimulate growth and the formation of new tissue.[18]

Their key ability to structure large volumes while creating an elastic system arises through the material microstructure; where coupling of long, structurally regular chains forms intermolecular junction zones that pack in a fashion comparable to those of solid-state materials.[19] However, to better understand the origins of the macroscopic properties, it is necessary to consider structure–property relationships from the molecular level. It is common to distinguish protein structures at multiple levels of organization.[20] These descriptions are also apt for polysaccharides: the primary structure detailing the sugar chain sequence, secondary structure defining geometric arrangement (helices and ribbons), and tertiary structure highlighting the 3D association of secondary structures.[21] This structuring across the polymer chains leads to varying levels of chain associations during the disorder–order transition upon gelation. For example, in the case of carrageenan (a galactopyranose polymer), domains of linked helices (tertiary structures) are formed through intermolecular association, but further require ionic-mediation to develop a continuous gel structure (**Figure 1**ai).[22] Therefore, inevitably, the number and density of junctions formed in this way between polymer chains is a direct function of the final gel strength and elasticity.[23]

This results in an array of material behaviors varying from strong gels, with relatively large moduli independent across a large range of frequencies, indicative of self-supporting structures, to weak maleable gels, where weakly associated chains lead to high-frequency sensitive systems with comparatively low moduli (Figure 1b).[24] However, the reliance on molecular configuration to achieve certain properties is a major problem, since when implanted or formed in situ the large number of other molecules that are present in the in vivo milieu interfere with these processes and can make them unpredictable. Such unpredictability is a significant barrier to clinical translation.

In an effort to produce more predictable systems, microgel suspensions known as "fluid" or "sheared" gels are being employed for their unique flow behaviors,[25] engineering the ability to self-structure post-shearing.[26–28] This presents a much more dynamic scaffold, which can be prepared exogenously for potential injection into the body.[29,30] Patented in 1990 as a system of microgels for use in food and cosmetics, derived upon shearing throughout gelation, fluid gels are substantially less rigid than their quiescently formed counterparts.[30] Shearing during the sol–gel transition results in networks of weakly flocculated, discrete gel entities (Figure 1aii), whereby particle sizes become dependent on the applied shear, and suspension rheology based on particle volume fractions.[31,32] However, in reality, such systems are more complicated, as interactions between particles on a mesoscopic level (structuring between particles) effectively dictate the bulk rheology of the systems. The particulate nature of these networks engenders a level of self-healing following manipulation, which is a key property that can be exploited in a number of biomedical applications.

The differences between quiescent gels and the properties of the microgels formed on shearing again lie in the microstructural changes upon gelation. One such example is the significantly reduced enthalpies of melting in carrageenan fluid

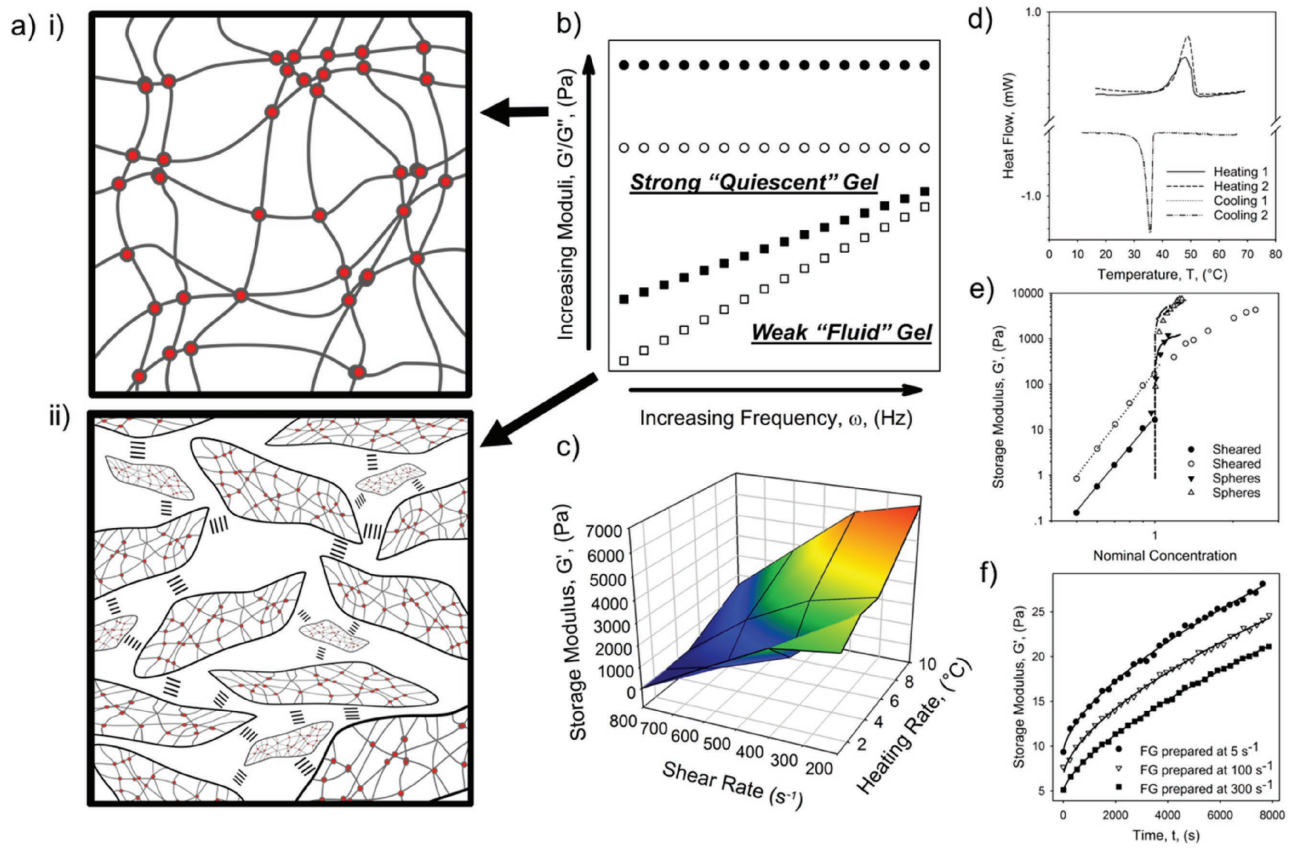

Figure 1. a) i) Schematic showing a typical gelled network where polymers interconnect to form junction zones (highlighted using red dots). ii) Diagram of a fluid/sheared gel system, where anisotropic gelled particles interact to form a weak continuous network. b) Idealized mechanical spectra showing G' and G'' dependency on frequency for both a strong "quiescent" and weak "fluid" gel system. c) 3D plot depicting the effects of processing on resulting suspension elastic response for protein fluid-gel particles. d) Differential scanning calorimetry (DSC) curves for carrageenan fluid gels. Note the change in peak height for the first and second melts, showing a change in degree of ordering between the fluid gel in the first heat and quiescent gel in the second heat. Adapted with permission.[34] Copyright 2012, Elsevier Ltd. e) Comparison of elastic moduli for sheared and spherical microgel systems: (●) 0.75% agar sheared gel, (○) 1.75% agar sheared gel, (▼) 2% agar microgel spheres, and (△) 5% agar microgel spheres. Trend lines show both power and Hertz fits to sheared and spherical systems respectively. Adapted with permission.[25] Copyright 2000, the Royal Society of Chemistry. f) Structuring as a function of time for carrageenan fluid gels (FG) prepared at various shear rates: (●) 5 s^{-1}, (▽) 100 s^{-1}, and (■) 300 s^{-1}. Reproduced with permission.[27] Copyright 2009, Elsevier Ltd.

gels when compared to their quiescent form (Figure 1d). Such data infers a heterogeneous polymer density across the gelled entities, with fewer ordered helices toward the particle peripheries.[33] This is not true for all polysaccharides however, as agar systems do not show such disparities.[32] Here, rapid gelation kinetics result in more uniform helical domains across the particles.[34,35] This suggests a mechanistic change in the microgel formation, driven by competition between two major factors: gelation kinetics and shear separation time/length scale (Figure 1c). Particle morphology also demonstrates a dependency on the competition between the two phenomena. In systems where gelation kinetics "k" greatly outweighs the time scale of separation "γ" ($k > \gamma$), rapid aggregation followed by subsequent shear breakdown develops large anisotropic morphologies. Whereas, in the counter case, $k < \gamma$, large shear forces confine growth, leading to more regular particles.[27] The consequential effects of such changes in particle morphology upon the aforementioned mesoscopic structuring have been clearly identified for both linear and nonlinear rheological properties. In the case of spherical particles, suspensions agree with Hertzian models resulting in elastic moduli arising through particle deformation, as systems become closely packed (Figure 1e).[25,36] Elastic response for anisotropic particles however, occurs at much lower volume fractions.[25] This is also reflected in the nonlinear measurements, with particles enhancing viscosities at volume fractions as low as $\Phi = 0.2$.[37] In these cases, large effective hydrodynamic volumes associated with anisotropic morphologies allow a vast degree of continuous phase to become structured by very few particles.[37–41]

Although some of the literature highlights the differences between quiescent and fluid gels, projecting the design rules in which to engineer systems with specific intrinsic properties, the actual nature of the interstitial space between particles is yet to be adequately defined. One theory proposes that disordered "hairy-like" polymers at the particle interfaces interlink to form a weak network between particles.[32] This may be the case for closely packed particles, where the interstitial layer is of the order of several hundred nanometers. However, an alternative explanation proposed here would be a combination of entropically driven structuring,[40,41] resulting in steric

confinement of particles, and/or weak electrostatic bridging between microgel interfaces at smaller length scales. Such a theory would encompass hysteretic effects, where self-structuring postshearing through entropic interweaving and electrostatic bridging, results in the observed recovery of an elastic network (Figure 1f).[26–28]

3. The Delivery of Biological Therapeutics Using Hydrogels

Many hydrogel materials have been used for the encapsulation and culture of cells in vitro, both for continued immunoisolation[42,43] and for the controlled delivery of biotherapeutics (both cells and proteins).[44–48] With the use of traditional "quiescently" gelled materials this can be very challenging, since gelation in a complex biological environment rich in ions and proteins can modify the kinetics of the gelation process and result in a material that gels unpredictably or behaves unpredictably following the gelation process – something that is completely unacceptable in a clinical environment. Up until relatively recently, there was also little consideration to how the local environment has a strong influence on the dynamic mechanical properties of these materials. Alginate, for example, is now known to lose mechanical integrity when placed into a physiological environment,[49,50] due to ion exchange of the divalent cations that enable the formation of "egg-box" junctions for monovalent ions such as sodium.[51] This causes the dispersion of the polymeric material and a loss of its ability to structure the surrounding liquid. This unpredictable behavior may explain why immunoisolation using polymers like alginate has proven ineffective when applied clinically, unless other polymers are incorporated as mechanically protective and permselective coatings.[42] What is also becoming very clear is that the materials are not "biologically inert", but rather provide subtle environmental cues that strongly drive cellular behavior. Initially, this was thought to be principally a consequence of the modulus of the materials,[9,10] but more recently reports have suggested that this can be modified by changing the distribution of grafted adhesion moieties and the nature of the interactions that may be formed with the polymer chain.[4,11,12] It has become clear that the level of entrapment that can be provided by the relatively stiff quiescently gelled matrix can have a significant influence on biological properties, including the capacity of cells to proliferate, maintain specific phenotypes or even secrete functional protein molecules as shown in **Figure 2**.[52–54]

3.1. Sheared/Fluid Gels as Delivery Agents

The shear processing of gels offers an additional degree of freedom for the production of cell and protein-delivery devices. From the perspective of handling, the reversible structural properties of fluid gels allow it to liquefy upon the application of shear, but may also be combined with biological fluids such as platelet-rich plasma or bone marrow aspirate and still thicken/solidify in situ. This is often very difficult to achieve with injectable hydrogels that solidify through a process of cross-linking, in situ. As such, fluid gels have the capacity to act as delivery agents for a great number of different cell and protein products (**Figure 3**).

Mesenchymal stem cells alone have been proposed to have beneficial effects in patients suffering a multitude of pathologies across body systems, including: the lungs,[55] brain,[56] musculoskeletal system,[57,58] peripheral nervous system,[59] skin,[60] and the heart.[61] Although some have reported that direct injection of these cells into the affected tissues can have beneficial therapeutic effects, the level of engraftment of the cells to the site of application typically ranges between only 1% and 10%,[62–65] and has been proposed to be as low as 0.001%.[66] As a result, the number of cells that are typically used in these therapies tend to be very large, ultimately creating the potential for carcinogenesis and other negative outcomes. The cost of such a treatment is, of course, considerable and as has been shown with autologous chondrocyte implantation (ACI), the clinical outcome and patient benefit over standard of care is unclear.[67,68] There are a number of ways to overcome these issues, which include the retention of the cells at the site of the implant within a material or through the use of cheaper autologous therapies. These are classified as minimal interventions by the regulator.

We have been able to develop materials for the repair and regeneration of cartilage, the cornea, and the skin that can be delivered in a way that is amenable to eventual clinical application. Through careful formulation, we have been able to produce materials that may be delivered using a range of different applicator technologies already used by clinicians, including cannulas/needles, sprays, and eyedroppers. Below, is a brief description of how we have used fluid gels to produce these therapeutics along with our progress in taking these to the point of clinical application. Furthermore, we have outlined major challenges that still need to be overcome in order to enable transition to the clinic. For each example, we have also outlined the clinical problems that we are attempting to address in order to place the technologies in context.

3.1.1. Cell Delivery for Cartilage Regeneration

Articular cartilage is a specialized avascular connective tissue layer covering the ends of bones that come together to form joints. It provides a smooth lubricated surface to minimize friction between the contact areas of the bones, and facilitates efficient load distribution through to the subchondral hard tissue. Chondrocytes, the sole cell type within cartilage, are sparsely distributed within a dense extracellular matrix that is mainly composed of collagen, water, proteoglycans, and glycoproteins. The high concentrations of hyaluronan and proteoglycan aggrecans allow for large volumes of aqueous medium to be entrapped within the matrix, and for covalent binding to other structural proteins, respectively, providing articular cartilage with its shock-absorbing properties.[69] Collagen organization, as well as relative matrix composition, cell density, and cell morphology, vary as a function of depth from the articular surface and act collectively to resist the range of forces experienced by the joint.

The avascular nature of cartilage and the low number of cells that are found within articular cartilage matrix result in a tissue

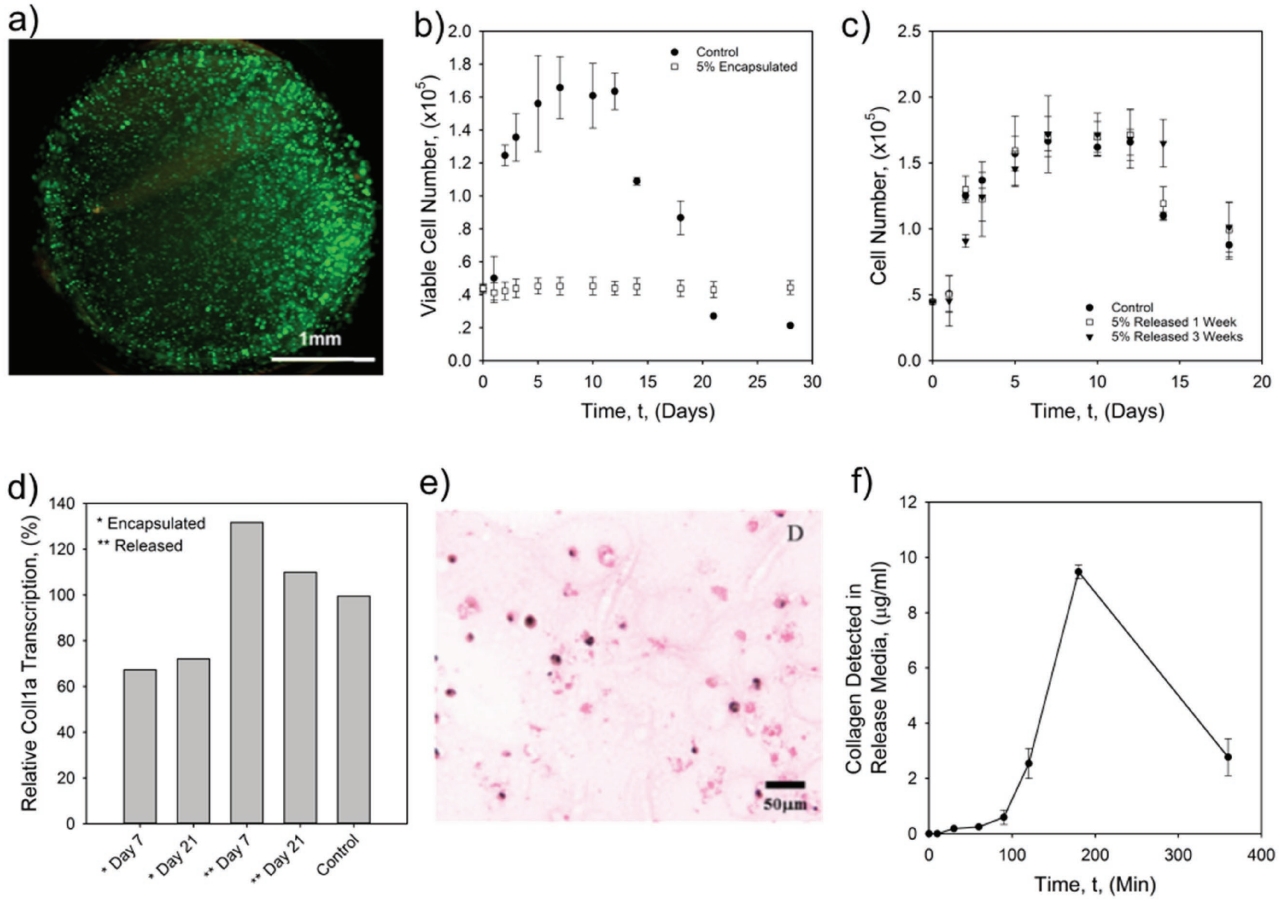

Figure 2. Effect of entrapment on cellular activity. a) Live/dead staining of encapsulated fibroblasts 4 d postencapsulation in 5% w/v alginate quiescent gel. Live cells stain green and dead cells stain red. b) Growth curves of the encapsulated 3T3 fibroblasts shown in (a), compared with nonencapsulated 3T3s (control). The encapsulated fibroblasts remain at a constant viable cell number up to 33 d postencapsulation, rather than exhibiting the normal bell-shaped growth curve seen with monolayer cultured fibroblasts. c) Fibroblasts released from encapsulation in 5% w/v alginate quiescent gel display normal growth in monolayer culture after both 1 and 3 weeks encapsulation. Adapted with permission.[52] Copyright 2009, Elsevier Ltd. d) Relative transcription of Coll1a by 3T3 fibroblasts encapsulated in 2% w/v Ca–alginate quiescent hydrogel for 7 and 21 d. Expression is shown for encapsulated cells and those that are released and grown as monolayers for 48 h and control fibroblasts, grown as monolayers having never been encapsulated. Col1a transcription was found to be only approximately 25–30% lower than before encapsulation. e) Despite the relatively high Col1a transcription levels while encapsulated, Haematoxylin Van Gieson (HVG) staining of the samples revealed very little collagen matrix had been produced by the encapsulated cells even after 3 weeks. f) However, soluble collagen was detected within the alginate structures and could be released into physiological media. Overall, this suggested that while the alginate gel system allowed for the passage of essential collagen precursor molecules and their assembly into soluble collagen, it sterically hindered collagen fibrillization. Adapted with permission.[53] Copyright 2012, the American Chemical Society.

with poor regenerative capacity following damage. Articular cartilage is one of the most challenging tissues to engineer or mimic synthetically due to the complex transitions in composition and ultrastructure, which are vital to its overall mechanical function. Consequently, most therapies for the repair of damaged cartilage involve tissue grafts or exploiting the local biology to facilitate new tissue formation. The current gold standard treatments in the repair of focal cartilage defects are microfracture or mosaicplasty. Microfracture involves removing the damaged cartilage and making a series of small holes in the subchondral plate causing bleeding from the marrow, and the formation of a clot that fills the focal defect. The aim here is to introduce and retain progenitor cells (present in marrow) into the defect site, a fraction of which have the potential to develop into chondrocytes and facilitate new cartilage formation. In mosaicplasty, small portions of cartilage are transplanted from nonarticulating regions of the affected joint into the cartilage defect site. This approach enables the engraftment of an already fully developed native cartilage structure. A common drawback with both methods is the formation of a fibrocartilaginous matrix as opposed to hyaline cartilage.[70,71] Fibrocartilage does not exhibit the same specialized surface structure as hyaline cartilage. As a consequence, the new tissue is mechanically inferior to the surrounding intact cartilage (particularly in resisting shear forces), which increases the risk of failure. A range of cell-based therapies, such as ACI, have been developed for the production of a native articular cartilage. To date, none of these methods have been able to surpass microfracture as the method of choice for orthopedic surgeons. Although there has been some success with the use of bone-derived mesenchymal stem cells for cartilage regeneration, there is a recognized need for culture and delivery systems that successfully maintain the

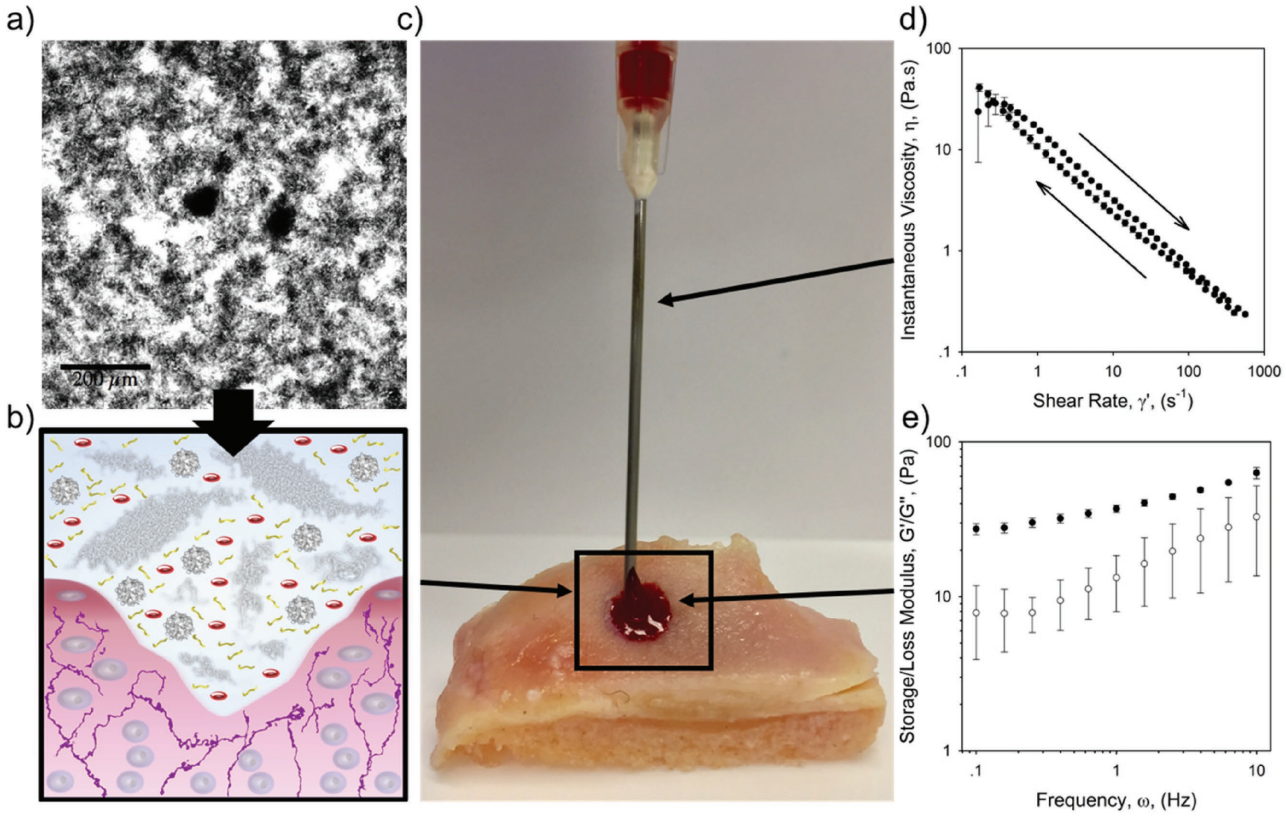

Figure 3. a) Optical microscopic image of diluted alginate fluid gel negatively stained with blood. Red blood cells (black) become sterically localized by the sheared alginate gel (white). Scale bar represents 200 µm. b) Schematic diagram depicting the stabilization of PRP (platelet rich plasma) via fluid-gel particles for in situ cartilage repair. c) Section of a tibial plateau with defect plugged using alginate/BMAC (bone marrow aspirate concentrate) fluid gel using a syringe. d) Flow profile obtained for 10% blood serum in 1% alginate fluid gel. The plot shows data for both increasing and decreasing shear, highlighting its reversible shear thinning behavior, crucial for application via syringe. e) Frequency sweep obtained for the same sample showing the typical weak solid-like structure exhibited by fluid gels under static conditions.

required chondrogenic phenotype during culture expansion in the lab, and upon implantation – especially for maintaining chondrogenic phenotype during the healing process. Alginate-based gels have been used as a biomaterial in chondrocyte culture since the 1980s as demonstrated by Guo et al. in 1989.[72] The general popularity of alginates in bioengineering stems from their good biocompatibility/tolerance with a range of tissues, low cost, and ease of gelation using divalent ions (many of which are endogenous to the human body). However, it is the similarility between the ultrastructure of gelled alginates and that of native extracellular matrix that has made alginates favorable for use in research and development into chondrocyte culture.[51,73] The 3D structure of the gels is thought to help the chondrocytes exhibit more in vivo-like behavior.[74] Furthermore, the ability to form 3D structures with tunable bulk mechanical properties, incorporate cell binding moieties, and allow the diffusion of soluble factors have proven to be important features in supporting chondrogenesis and maintaining chondrogenic phenoptype. Thus, their regenerative potential is maximized.[51,75] Hwang et al. demonstrated that the porosity in a gel system can be tuned by the addition of gelatin microbeads as a means of enhancing the mass transport of oxygen, nutrients, secreted biomolecules, and waste products.[76] Promising human cell-based models have also been developed with good medium to long-term cell viability. Choi et al. successfully cultured human articular chondrocytes in alginate beads over 15 d, and Loeser et al. successfully cultured human articular chondrocytes in alginate exposed to the chondrogenic growth factor insulin-like growth factor-1 and reported 95% survival at 21 d.[77,78]

Beyond the successful culture of chondrocytes in a lab, a major issue is the delivery and retention of chondrocytes into a focal defect using a non-invasive approach. Many have attempted to form in situ gelling materials that are capable of solidifying in the focal defect, and there are clinical products on the market that form a polymerized biological scaffold within the defect (BST-CarGel, Smith & Nephew; GelrinC, Regents Biomaterials; Chondron, RMS Regrow). We have demonstrated that it is possible to use "sheared" or "fluid" gels as vehicles to deliver and retain populations of chondrocyte cells. These materials can be injected into an aqueous medium and will retain their mechanical integrity over a period of 21 d of ageing (**Figure 4**). Importantly, the material can be injected through a narrow gauge needle while maintaining the viability of the incorporated cell population (Figure 3). Once injected into a defect, unlike gel systems that are gelled in situ or before implantation, the cells are able to move within the structure of the fluid gel and can migrate down into the bottom of the tissue

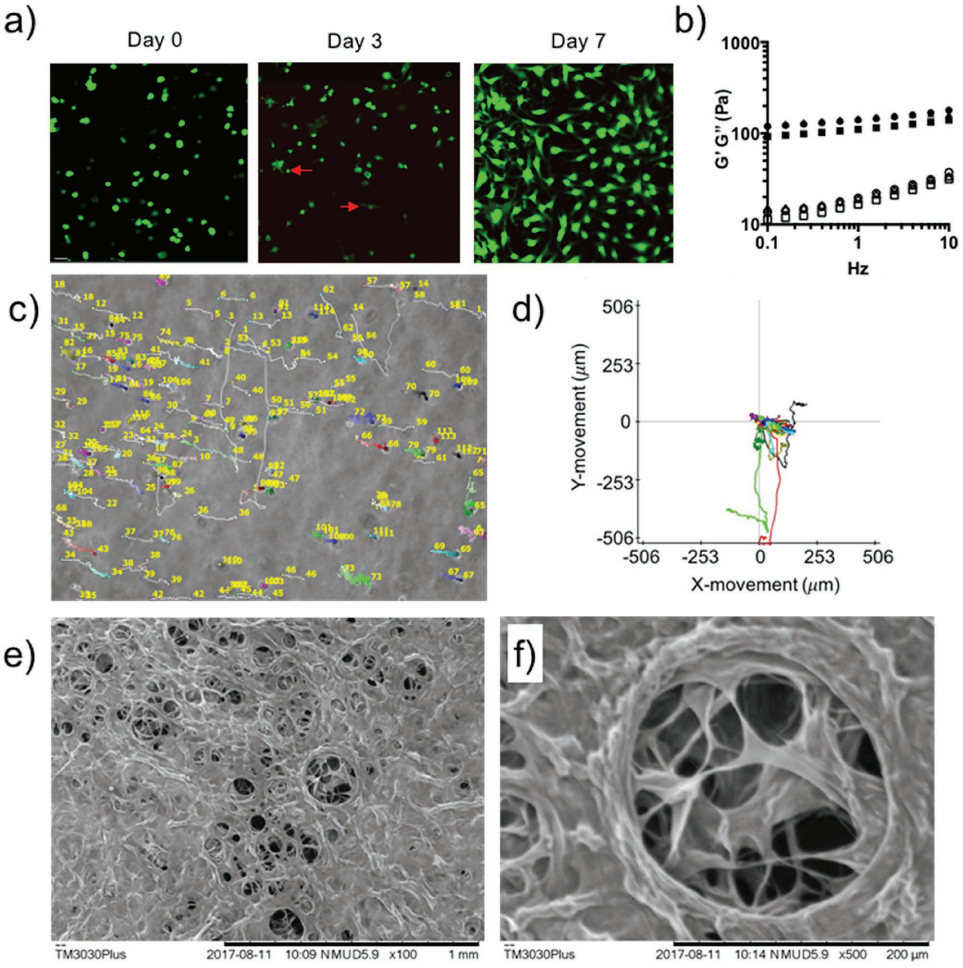

Figure 4. a) Sedminentation of cells through a fluid-gel network over 7 d. b) Mechanical stability of fluid alginate over 3 weeks (day 7: circles; day 14: squares; day 21: triangles; G': closed symbols; G'': open symbols). c) Cell tracking showing lateral movement of cells through fluid alginate. d) Quantification of the cell movement in the x–y plane. e) Fluid alginate architecture showing voidage regions in the polymer network.

defect (Figure 4). However, recent work within our group has also suggested that the lack of physical entrapment of the cells can result in the dedifferentiation of the encapsulated cells into a fibroblastic phenotype. While this lack of physical entrapment may ultimately hinder the use of fluid gels for the delivery of differentiated chondrocyte cells, we have demonstrated that fluid gels are effective in the delivery of other biological agents, such as platelet rich plasma and bone marrow aspirate concentrate, and their stabilization within a model joint defect. Our current work aims to translate this technology into a usable minimal intervention for cartilage augmentation (Figure 3). The ability of fluid gels to facilitate cell migration can actually be an advantage when designing therapies for other tissue applications. In the case of the skin, the ability for cells to migrate through the surface of the material would enable a topically applied cell population to fully colonize the wound bed.

3.1.2. Skin—Keratinocyte Delivery to Aid Wound Closure

Skin exhibits a multilayered structure with the uppermost layer of the epidermis consisting of layered keratinocytes that differentiate from the basal lamina over a period of several weeks.[79] The layer below the epidermis, known as the dermis, consists of a population of fibroblast cells that play a role in secreting extracellular matrix molecules such as collagen types I and IV and glycosaminoglycans.[80]

Serious damage to the epidermal and dermal layers break this fragile interplay until healing occurs and the wound is closed. In the case of large and deep burns, wound healing without intervention can take several weeks, wherein a patient is likely to develop acute systemic dysfunction with high risk of death through systemic infection and dehydration.[81] In order to speed the process of conventional skin grafting, it is possible to grow a multilayer sheet of keratinocytes in the laboratory in a period of up to 3 weeks.[82–85] These cells may then be applied to the surface of the wound. The keratinocytes then accelerate the closure of the wound by secreting factors that are able to stimulate collagen deposition (TGF-β1) and differentiation of the cells in the wound bed into myofibroblasts, which are able to fully close the wound. Although this process was pioneered in the 1970s and has found use in the clinic, the cost of the treatment, in addition to the amount of time it takes to generate sufficient cells, limits utility.[86] Poor outcomes in terms

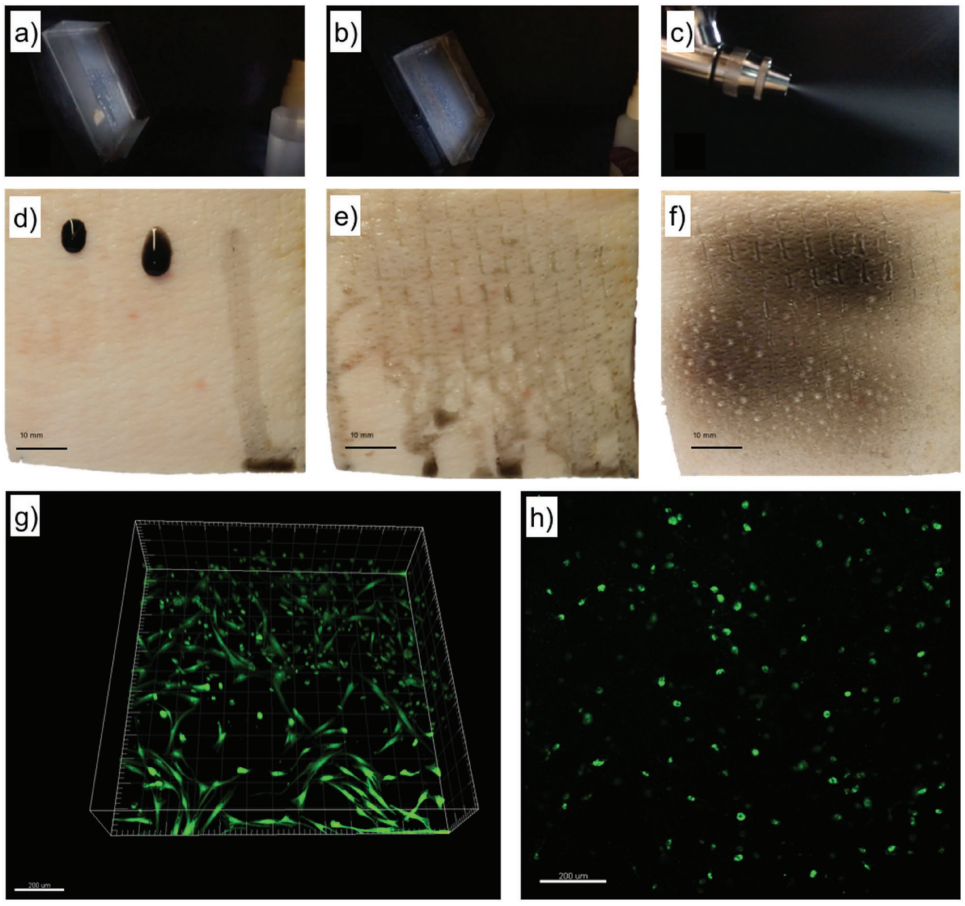

Figure 5. Cell encapsulation and spray deposition of gellan gum fluid gel. Video of a) spray delivery with handheld spray pump of material to tilted gelatin substrate demonstrated poor adherence of water b) compared to gellan gum fluid gel. c) Airbrush spray delivery system was used to standardize air pressure at delivery (15 PSI) and nozzle size (0.75 mm). d) Comparison of dyed gellan fluid gel (left), quiescent gellan gel (middle) and sodium chloride (right) droplets to porcine skin indicates a low rate of spreading of the gellan explained by the higher viscosity and structural stability of the material. e) Airbrush spray delivery of dyed sodium chloride to porcine skin showed rapid run-off with pooling of material at the bottom of the substrate, f) whereas uniform distribution without run-off was achieved by gellan fluid-gel spray delivery. g) Fluorescence cell viability assay of human dermal fibroblasts (HDF) 7 d after encapsulation in gellan fluid gel (live cells green, dead cell red), cells are viable and attach to the bottom of the well and seem to migrate out of the gel. h) High viability of cells at day 1 following spraying of encapsulated HDFs in gellan fluid gel.

of graft take, formation of bullae (blisters), poor handling due to fragility of sheets, and wound contraction have been reported. More recently, spray technologies have been used to deliver autologous and allogenic keratinocytes to the surface of wounded skin. Preconfluent cells have demonstrated utility in regenerating the skin and require a similar culture period of approximately 2–3 weeks.[87–89] Consequently, there is now a drive to develop allogeneic therapies from immunogenically privileged neonatal foreskin fibroblasts and keratinocytes.[90] However, a phase 3 clinical trial in nonhealing wounds was stopped prematurely due to low efficacy.[91] There are also products available that eliminate the in vitro culturing step by separating epithelial cells from patient biopsies in the clinical setting, and these cells may then be dispersed and sprayed onto the wound surface in a single procedure.[92,93] Although these technologies have been available for some time, there are as yet few clinical trials that show a conclusive benefit for using this approach.[94,95] One potential reason for this is that the cells themselves are delivered using a low-viscosity spraying system and anecdotally the level of "run-off" from the wound surface following spraying is high.[86] Although some products now try to remedy this using fibrin glue as an adjunct, the technology has yet to find strong traction in the clinic.[96,97] One of the major advantages of using a fluid gel system for the delivery of keratinocytes is that the material itself shear-thins considerably under the rapid shear forces experienced in a spraying system. We have utilized fluid-gel systems that are formed from a polysaccharide called gellan gum. Populations of cells may be incorporated into this system and can then be sprayed through a nozzle and deposited onto a surface as shown in **Figure 5**a–c. The soft solid then rapidly structures as it impacts on the skin, where the cells are retained on the surface, rather than running off, maintaining high-levels of viability. Importantly, the structure of the fluid gel allows cell movement within it, and we have shown that the viscosity of the material can be tailored to allow sedimentation of cells onto the upper surface of the tissue. In addition to being sprayed onto the surface of the skin, the gellan fluid gel may also be used to spread cells

across a surface, yet be retained in place once the spreading process has been completed. Figure 5d–f demonstrates how the material is retained on the surface of the skin. The material is compared against sodium chloride and a gellan quiescent gel. When the surface of the skin was inclined, the fluid gel was retained on the surface of the skin in exactly the same way as the gellan quiescent gel. It is worth noting that in order to get the quiescently gelled gellan to spread and then reset on the surface of the skin, the material was heated to around 50 °C before being allowed to cool, which would not have been conducive to cell survival. Shear structuring of the material was a successful way to enhance functionality without compromising cell viability (Figure 5g–h). The next challenge with this material will be to develop a manufacturing and packaging process that will not compromise the properties of the finished product. At present, the delicate structure tends to breakdown when exposed to doses of gamma irradiation considered low by industry standards. The development of non traditional sterilization methods may prove essential in the transit of these materials to the clinic. Although autoclaving is a possibility without causing a significant change in the properties of the final product, this method is unsuitable for the delivery of delicate therapeutic proteins that may be required to enhance the regenerative capacity of the tissue.

3.1.3. Cornea—Scar Prevention

The cornea is a layered structure exhibiting very high levels of organization in order to both protect the inside of the eye and provide the majority of the eye's refractive power.[98] The cornea is composed of five layers, with the anterior surface of the cornea consisting of epithelial cell layers that overlay a tough collagenous layer (Bowman's layer), mostly consisting of tightly woven collagen type I meshworks. The corneal stroma is an optically transparent layer composed of heterotypic collagen type I and V fibrils of around 30 nm in diameter, embedded within a proteoglycan matrix.[98,99] The stroma makes up 90% of the overall corneal thickness and is maintained by resident keratinocytes.[98] The collagen fibrils are arranged in flattened tightly spaced bands called lamellae that traverse the diameter of the cornea and are superimposed over one another making up most of the stromal thickness.[100] Further structuring occurs from the interlacing of the lamellae, which is most prominent within the anterior and mid-stromal layers and less so in the posterior stroma, where they are stacked in a similar fashion to layers in plywood.[98] The posterior stromal region, particularly in the central corneal region, is more hydrated than the rest of the stroma and thus the corneal stroma overall is akin to a highly structurual and mechanical anistotropic hydrogel system. The predominant collagen orientation within the stroma also varies as a function of depth. In the anterior region, the collagen does not exhibit any preferred orientation, whereas the mid- and posterior regions demonstrate preferred orthogonal arrangement of collagen along the nasal-temporal and superinferior directions.[101] The key structural factors of the cornea, leading to high optical transparency, are the uniformity of the collagen fibril diameters and tight regulation of the distances between adjacent collagen fibrils.[98,99,102,103] The fourth layer of the cornea, Descemet's membrane, is composed of a thin layer of collagen type IV and is designed to support the corneal endothelium layer that makes up the posterior surface of the cornea. When the corneal surface is damaged, it is typically capable of healing itself. However, in the case of infection (e.g., microbial keratitis), a significant inflammatory process is triggered, resulting in the upregulation of growth factors such as TGF-β1, which is a potent fibrogenic factor leading to disorganized deposition of collagen and extracellular matrix within the stroma.[104] Dysregulated collagen and ECM deposition prevents light transmission through the cornea and ultimately leads to blindness.[105] Treatment of diseases such as microbial keratitis may result in a corneal transplant if standard treatments with antibiotics and steroid fail.[106] Therapeutic proteins such as decorin have been shown to regulate the deposition of collagen by binding the inflammatory cytokine TGFβ-1.[107] This prevents collagen upregulation as well as the differentiation of keratocytes to the myofibroblastic phenotype that causes wound contraction and ECM deposition.[108] Topical delivery of therapeutic proteins/molecules to the surface of the eye has previously been attempted, however with limited success.[109–112] Gellan fluid-gel based eyedrops allow for the initial retention and then tailored release of the therapeutic agents onto the surface of the eye over a period of hours, as opposed to seconds/minutes as experienced with the majority of eyedrops (**Figure 6**a–c).[113] Since gellan is optically transparent, a patient's vision would not be compromised by the gellan when placed on the eye. During blinking, the eyelid sweeps over and applies shear to the surface of the gellan eyedrop, causing layers of the material to be removed. The eyedrop is cleared from the surface of the eye over a period of around 2 h. This technology has been exploited to deliver a sustained dose of decorin to the surface of the eye, which we have demonstrated facilitates reepithelialization of the eye surface (Figure 6d,e), both ex vivo in an organ culture model of corneal abrasion and when challenged in an in vivo corneal abrasion model. In addition to delivering the molecule to the surface of the eye over an extended period of time, we believe that the eyedrop will provide some relief to patients with this very painful condition, by lubricating the surface. Indeed, it has previously been reported that fluid gels, if formulated correctly, can be used as an adequate lubricant for surfaces.[114]

4. Bioprinting

In addition to enabling the encapsulation of cells and proteins for in situ delivery, the "self-healing" structure of fluid gels means they have found application as supports for additive layer manufacturing (ALM) of soft material structures, with complexity that is far beyond what has previously been reported. For many years, researchers have sought to replicate tissue structure and composition by using a combination of isolated cells and polymeric hydrogels that have a structural resemblance to ECM, to create an implantable living construct.[115] Most constructs have been fabricated using a gel casting process that provides little control over the microscale geometry of the deposited material, or the local mechanical properties so important to controlling cell fate. Innovation in

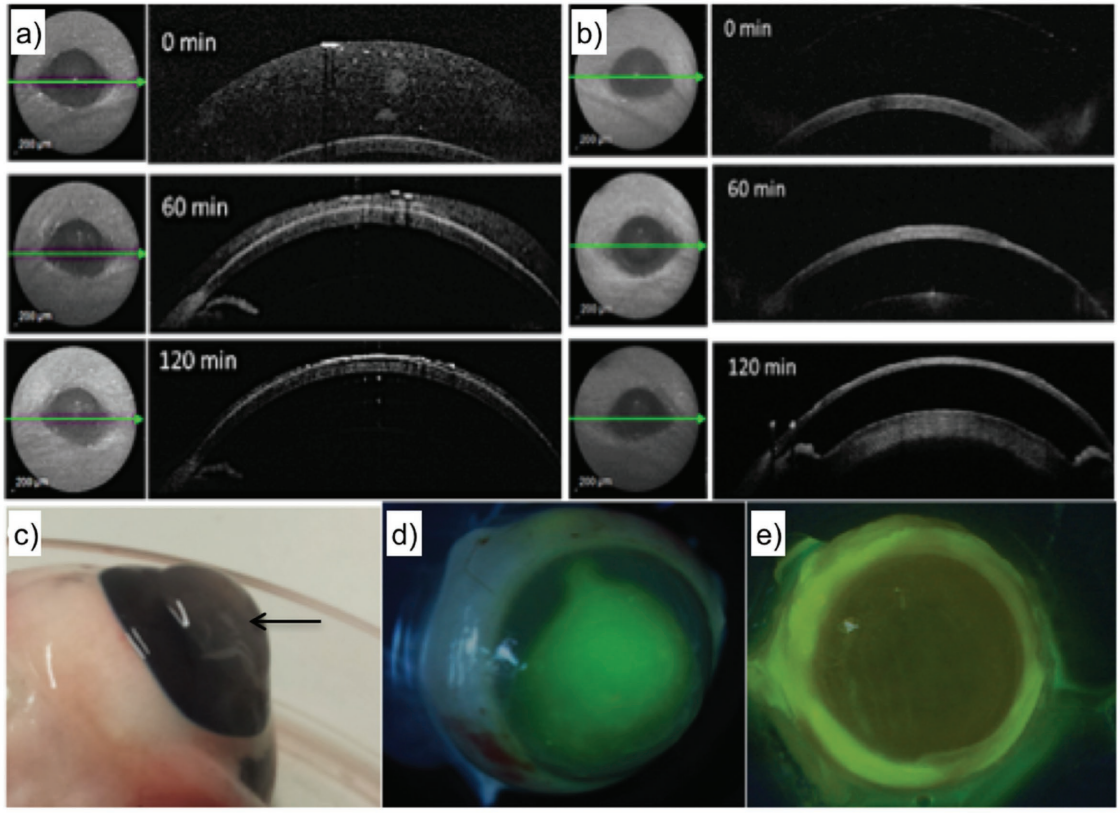

Figure 6. Optical coherance tomography (OCT) images illustrating the flow and clearance rate of fluid-gel eyedrops: a) when compared to PBS drops. b) On the surface of intact rat eyes over a 2-h period, fluid gel remained on the surface of the eye for nearly 60 min and some residue was noticed at 120 min. The PBS drop however cleared within 60 min. Fluid-gel thickens on the surface of freshly enucleated pig eyes, indicated by the black arrow. c) Eyes treated over 4 d with fluid gels containing decorin demonstrated significant reepithelialization in ex vivo organ culture models e) when compared to d) fluid gels without decorin.

this area has been driven largely by the desire to develop therapies that come close to offering the same key advantages as auto- and allografts, in that they are structurally and biologically the same as the surrounding tissue, while moving away from harvesting graft material itself. This is because the grafts are only suitable for relatively small defects and the graft approach in general is unlikely to be able to meet future clinical demand.

3D bioprinting using ALM has become a useful approach for creating structures with a greater level of complexity than traditional processing methods, such as casting, with some degree of control over the distribution of biological material throughout the structure.[116] While ALM of hard materials is relatively mature and adopted by a number of industries, ALM of soft mateials remains challenging. One of the major challenges for 3D bioprinting is the lack of suitable materials that are both able to replicate tissue material behavior and compatible with current 3D printing technologies. The advantage of biopolymer materials for tissue engineering applications is their similarity to native ECM. However, controlling their physical properties to be optimal for both the tissue engineering application and the mechanics of the printing process is more difficult than of synthetic materials. Biopolymers used for tissue engineering tend to have relatively low viscosities in the pregelled state that facilitates mixing with cells. Furthermore, many of these materials exhibit pseudoplastic (shear thinning) flow behavior that also can be advantageous for extrusion, when fabricating scaffolds. Unfortunately, low-viscosity materials can be problematic when 3D bioprinting, as the printed structure can collapse and lose its shape before solidification can be initiated.[117] Another problem when 3D printing biopolymer hydrogels is the inability to integrate multiple layers of material once gelled, preventing the production of integrated gels with regional variations in mechanical behavior. To overcome these problems, researchers often incorporate highly viscous materials to maintain a 3D shape after deposition,[117–119] which is not ideal as highly viscous materials can impede homogeneous cell mixing and often require increased extrusion pressure in order to print. This can lead to reduced cell viability as a result of the shear stresses inflicted on cells and has therefore limited their use in 3D bioprinting.[120]

We recently developed a technique that overcomes some of the issues associated with additive layer manufacturing when using low-viscosity materials, allowing them to be used as a bioink to create relatively complex soft-solid structures.[116] This was achieved by extruding a gelling biopolymer solution into a self-healing fluid-gel matrix, which suspends the fragile printed construct in the liquid state to prevent flow and thus retaining the deposited morphology. Additionally, as the printed construct remained in the liquid state, it was possible to build the construct layer by layer and interface two different materials

with dissimilar mechanical properties, creating a structure with distinct regions of anisotropic physical behavior. To demonstrate the potential for clinical application of the technique, we created a structure that recapitulated the osteochondral region as directed by microcomputed tomography (CT) imaging.[116]

Native osteochondral tissue has a gradually changing microstructure that extends from disordered mineralized collagen in subchondral bone[121] to cartilage, across which there are distinct variations in the relative concentrations of noncollagenous proteins, and orientation of collagen fibers as a function of depth.[122] This graded structure allows applied stress to be distributed across the interface without specific stress localization, helping to prevent delamination from occurring.[123] In our work, femoral condyle tissue was donated from patients following total knee replacement surgery and a full-thickness osteochondral defect was introduced using a surgical drill. The tissue containing the defect was scanned using micro-CT to generate a 3D model. Chondrocytes and osteoblasts were isolated from the tissue samples and, following primary cell culture, were added to 1.5% gellan and 1.5% gellan mixed with 5% nanohydroxyapatite (HA), respectively. Using the 3D model as a guide for accurate dimensions, an osteochondral implant was manufactured with the lower layer loaded with gellan, HA, and osteoblast cells, while the upper layer of the construct was manufactured using gellan gum loaded with chondrocytes. The manufactured cell-laden construct was then implanted into the defect of the ex vivo femoral condyle. After 4 weeks in culture, the construct maintained morphology and the encapsulated cells retained their phenotype within the distinct layers of the manufactured structure.

Our suspended additive layer manufacturing process has since been integrated into a commercially available extrusion-based 3D bioprinter (Cellink, Sweden), adding the ability to manufacture more geometrically intricate structures. To demonstrate the ability to retain the structural integrity of printed low-viscosity materials, an S-hook shaped construct was printed from a G-code file using 1% w/w gellan gum (**Figure 7**a). When printed onto a planar surface, the structure collapsed as the material began to flow under gravitational force (Figure 7b). However, when printed into a fluid-gel bed (prepared from 0.5% agarose), the structure retained the S-hook shape, clearly demonstrating protective support afforded by the surrounding fluid gel on the printed construct (Figure 7c). We then demonstrated the ability of the process to manufacture graded interfaces between soft-solid structures over relatively large length scales. Our model for this was printing conjoined doublet and triplet cuboids from single cuboid units measuring 10 mm × 10 mm × 5 mm, using gellan gum and gellan gum containing an orange dye (Figure 7d–f). Once the first cuboid was printed and remained in the liquid state, a second cuboid was printed with a 1 mm overlap with the first cuboid in the lateral plane to create an interfacial region. Once printed, the structures were crosslinked in situ using 100×10^{-3} M $CaCl_2$ for 30 min, and recovered as a single structure from the suspending particulate gel by gently washing with distilled water. This technique could potentially be used to model diffusion of molecules from one gel system to another, or fabricate discrete molecular reservoirs within a larger structure. Finally, we explored the potential to integrate different materials each with different gelation mechanisms using suspended bioprinting. Figure 7g–i shows the manufacture of cylindrical constructs consisting of a layer of gellan gum and a layer of type 1 collagen (PureCol EZ Gel, Advanced BioMatrix, USA), each layer with dimensions of 5 mm × 5 mm × 2.5 mm. In this example, the fluid gel base was maintained at 37 °C while the gellan cylinder was deposited first and left in the liquid state. The collagen was then deposited at 20 °C and left for 60 min to allow thermal gelation to occur, as the collagen equilibrated to 37 °C temperature of the supporting particulate bed. To initiate gelation of the gellan cylinder, 100×10^{-3} M $CaCl_2$ was added to the construct and left to gel for a further 30 min. Once fully crosslinked, the construct could be removed as one piece (Figure 7h). The finished construct exhibited a clear interfacial region between the two layers, which could not be physically separated, thus suggesting the formation of an interpenetrating polymerized network across the interface (Figure 7i). The order in which the different materials are gelled during fabrication of a construct can strongly influence the stability of the interface between them. Successful integration of collagen and gellan layers required the gelation of the collagen layer before gelation of the gellan layer. This is attributed to a mechanism reported by Gillette et al. when attempting to integrate collagen into crosslinked alginate, whereby the small pore size of the gelled alginate inhibited the formation of a network of collagen fibers within the alginate structure.[124]

In summary, the easily removable physical support offered by the fluid gel bed enables the deposition of biological materials in the liquid phase in 3D, with complex geometries and interfaces, before solidifying into a single construct with graded mechanical, chemical, and structural properties. This approach effectively decouples the viscosity of the starting material from the desired mechanical properties of the final printed construct. Biopolymers can be prepared at the relatively low viscosities required for low-pressure extrusion-based bioprinting, with the final mechanical properties engineered into the materials by gelation postextrustion.

Suspended bioprinting is, therefore, an enabler for a range of soft-solid materials, for which their full potential in tissue engineering is well established but not fully realized to date, to be used in the ALM of implantable biological constructs.

5. Conclusions and Outlook

Soft-solid materials have long been used as basic building blocks in the fields of tissue engineering and regenerative medicine, with certain materials having found use as wound dressings, eyedrops, and for the immunoisolation of cells. Despite extraordinary amounts of innovation around the manipulation of chemistry and local mechanics, which has significantly improved our understanding of how local environments can influence cell behavior, relatively few new so-called "smart materials" have made the transition to full clinical use. One of the reasons for this relative lack of progress is that the costs of taking new compositions to the clinic, through toxicity testing and characterization, is so high as to make it uneconomical. We have focused a large amount of research on modifying material structures by making changes

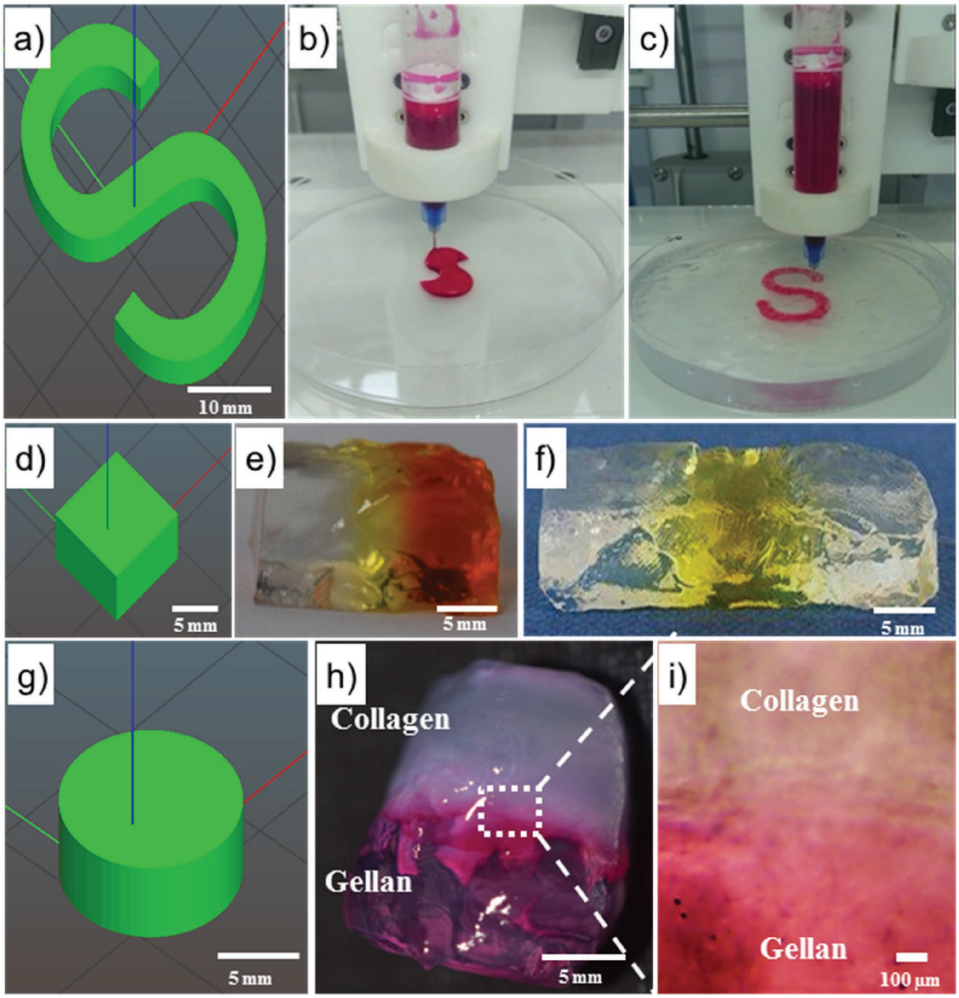

Figure 7. Suspended bioprinting of various biopolymer structures. a,b) G-code image for an S-shape hook with dimensions of 25 mm × 40 mm × 2.5 mm was printed using 1% w/w gellan gum onto a planar surface and imaged at the end of the printing process. c) The same structure printed into a 0.5% w/w agarose particulate gel bed. The construct printed onto the planar surface lost all structural integrity, collapsing under its own weight and flowed across the surface, resulting in a distorted structure. The construct printed within the particulate bed retained accurate dimensional conformation. d–f) Design and manufacture of multilayered constructs using suspended bioprinting. d) G-code file of a 10 mm × 10 mm × 5 mm cuboid. Two cuboids integrated using suspended bioprinting process; one contained a dye highlighting the ability to interface two separate biopolymer structures e) and another incorporating a double interface of gellan/dyed gellan/gellan to illustrate the potential for creating compositional gradients. g–i) Suspended bioprinting of a composite hydrogel cylindrical structure. g) G-code image of the single cylindrical structure with dimensions of 10 mm × 10 mm × 5 mm. h) Composite structure prepared from 1.5% gellan with 0.5% type 1 collagen using the suspended bioprinting process. i) A microscopic image of the interfacial region between the two dissimilar materials. These example constructs illustrate the potential of this approach to 3D bioprinting to manufacture biopolymer constructs with distinct anisotropic chemical and mechanical properties.

to processing conditions, without modifying composition. In the case of hydrogels, this has allowed us to take existing regulator-approved materials, and process them in a manner that allows us to produce structures that exhibit very distinct properties from the conventionally processed materials. Of particular use is the capacity of these materials to self-heal following the application of mechanical shear. This means that the materials are able to be delivered through a narrow aperture, which generates local shear and liquefies the material sufficiently that it may be deposited over a surface, where it solidifies. This has allowed us to produce eyedrops, cell spraying devices, and injectable delivery devices. Importantly, these materials are ready for translation to the clinic having undergone less cumbersome toxicity testing than for a completely new material. We have also used the self healing capacity of these materials to provide support in a new method for the additive layer manufacturing of cell containing soft-solids. This method differs to other soft-solid additive layer manufacturing methods, in that both the support phase and the cell-bearing phase can exhibit exactly the same composition. When the part has been removed from the print-bed, the support material can be dispersed by the application of gentle shear. This enables us to produce complex structures with a supporting medium without the worry of contaminating the implant surface.

These systems are still far from being exploited to their full potential and also still need considerable refinement

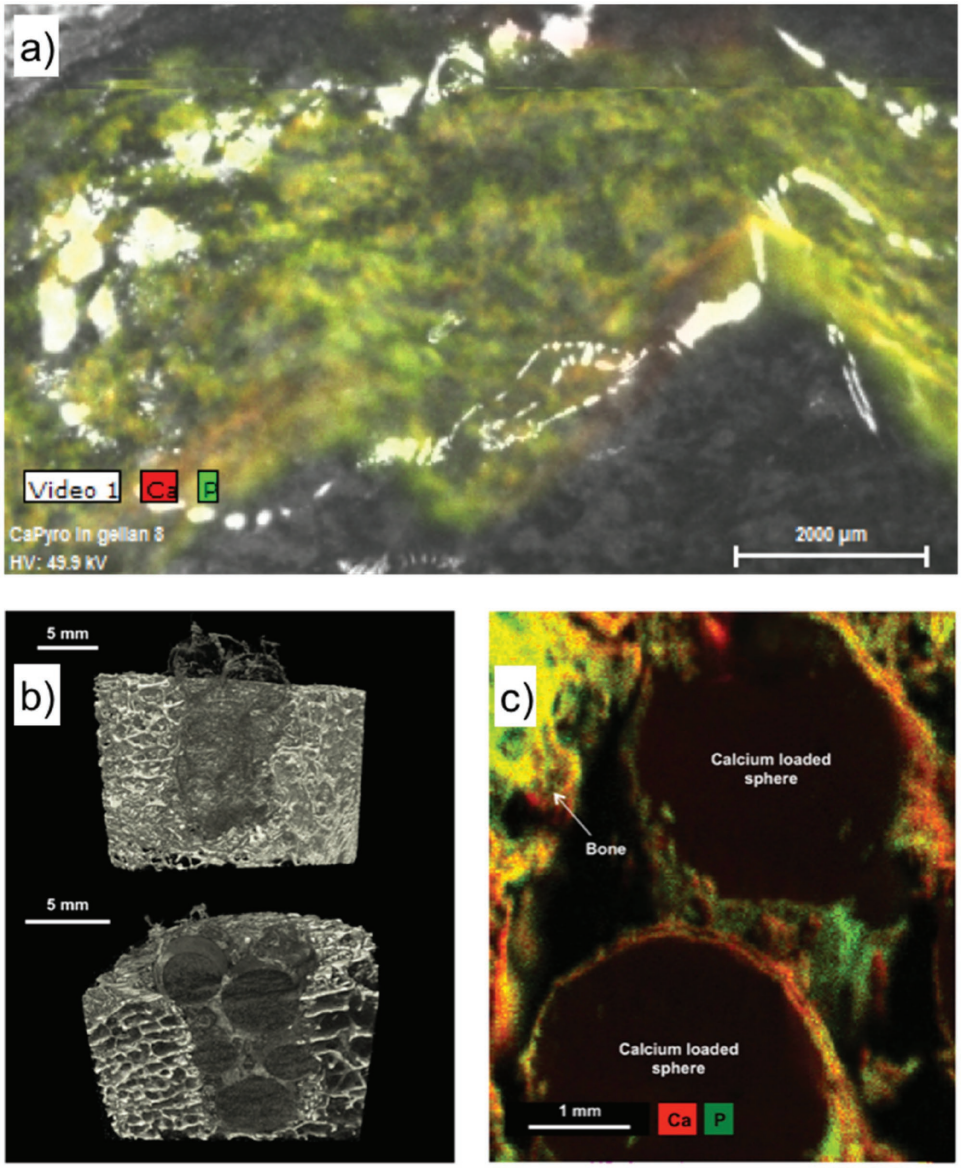

Figure 8. Fluid-gel materials may be loaded with osteogenic ceramics materials and extruded through a syringe, before they thicken upon a surface. a) The ceramic particles remain evenly distributed throughout the process. b,c) It is also possible to deliver the precursors of bone mineral formation within gel materials such that they harden in situ to form a relatively stiff composite matrix, but remain liquid prior to administration. This flexibility enables the tailoring of local environments to create more regenerative localized conditions. b,c) Reproduced with permission.[125] Copyright 2018, Wiley-VCH.

before eventually finding widespread use across medical fields. The polymeric gels are very difficult to sterilize using standard methods, and at present require non-cost effective low-throughput processes that allow for sterile-filling. Future innovations and collaborative work with the regulators should seek to develop new, more gentle sterilization methods, that are not likely to cause destruction of the polymeric material from which the structure is formed. Gamma irridation, ethylene oxide, and high temperatures are all very useful for sterilizing metallic materials, but impart enough energy into hydrated polymer systems to cause significant breakdown, and therefore significantly modify the properties exhibited by the materials. The use of alternative light sources (UV and blue light) and supercritical processing technologies may well provide the answer to this significant problem, but need to be validated and widely accepted by regulators worldwide.

We have also only just begun to explore the potential of these materials for delivering complex, composite structures. The incorporation of secondary materials into the fluid gel, which are capable of inducing osteogenesis in codistributed bone marrow aspirate and other sources of cell populations, has significant potential for shaping the local cellular environment in vivo, thereby enabling superior tissue regeneration (**Figure 8**a). Indeed, providing the reactants to generate a third phase between the polymeric components of the gel, enabling hardening into a comparatively stiff structure has already been achieved with some success (Figure 8b,c).[125]

Acknowledgements

The authors would like to acknowledge Dr. Sam Moxon, Jessica Senior, and Erik Hughes for their contribution to Figures 7 and 8. The authors would also like to acknowledge the EPSRC, MRC, and Wellcome Trust for the provision of funding.

Conflict of Interest

The authors declare no conflict of interest.

Keywords

biomaterials, hydrogels, regenerative medicine, soft materials, structuring

Received: September 2, 2017
Revised: October 20, 2017
Published online:

[1] V. Bisceglie, *Z. Krebsforsch.* **1934**, *40*, 122.
[2] T. M. S. Chang, *Science* **1964**, *146*, 524.
[3] F. Lim, A. Sun, *Science* **1980**, *210*, 908.
[4] J. A. Rowley, D. J. Mooney, *J. Biomed. Mater. Res.* **2002**, *60*, 217.
[5] S. R. Peyton, P. D. Kim, C. M. Ghajar, D. Seliktar, A. J. Putnam, *Biomaterials* **2008**, *29*, 2597.
[6] L. Gasperini, J. F. Mano, R. L. Reis, *J. R. Soc., Interface* **2014**, *11*, 20140817.
[7] J. A. Rowley, G. Madlambayan, D. J. Mooney, *Biomaterials* **1999**, *20*, 45.
[8] N. C. Hunt, L. M. Grover, *Biotechnol. Lett.* **2010**, *32*, 733.
[9] A. J. Engler, S. Sen, H. L. Sweeney, D. E. Discher, *Cell* **2006**, *126*, 677.
[10] J. H. Wen, L. G. Vincent, A. Fuhrmann, Y. S. Choi, K. C. Hribar, H. Taylor-Weiner, S. Chen, A. J. Engler, *Nat. Mater.* **2014**, *13*, 979.
[11] D. Zhang, M. B. Sun, J. Lee, A. A. Abdeen, K. A. Kilian, *J. Biomed. Mater. Res., Part A* **2016**, *104*, 1212.
[12] H. Li, J. J. Cooper-White, *Biomater. Sci.* **2014**, *2*, 1693.
[13] O. Chaudhuri, L. Gu, D. Klumpers, M. Darnell, S. A. Bencherif, J. C. Weaver, N. Huebsch, H. Lee, E. Lippens, G. N. Duda, D. J. Mooney, *Nat. Mater.* **2015**, *15*, 326.
[14] C. T. S. Wong, P. Foo, J. Seok, W. Mulyasasmita, A. Parisi-amon, S. C. Heilshorn, **2009**, *106*, 22067.
[15] B. A. Aguado, W. Mulyasasmita, J. Su, D. Ph, K. J. Lampe, D. Ph, S. C. Heilshorn, D. Ph, **2012**, *18*, 806.
[16] J. L. Drury, D. J. Mooney, *Biomaterials* **2003**, *24*, 4337.
[17] L. A. Estroff, A. D. Hamilton, *Chem. Rev.* **2004**, *104*, 1201.
[18] S. Yang, K.-F. Leong, Z. Du, C.-K. Chua, *Tissue Eng.* **2001**, *7*, 679.
[19] E. R. Morris, D. A. Rees, *Br. Med. Bull.* **1978**, *34*, 49.
[20] L. Römer, T. Scheibel, **2008**, *2*, 154.
[21] D. A. Rees, E. J. Welsh, *Angew. Chem., Int. Ed. English* **1977**, *16*, 214.
[22] E. R. Morris, D. A. Rees, G. Robinson, *J. Mol. Biol.* **1980**, *138*, 349.
[23] P. J. Flory, *Polymer* **1979**, *20*, 1317.
[24] S. B. Ross-Murphy, V. J. Morris, E. R. Morris, *Faraday Symp. Chem. Soc.* **1983**, *18*, 115.
[25] W. J. Frith, X. Garijo, T. J. Foster, I. T. Norton, in *Gums and Stabilisers for the Food Industry 11* (Eds: P. A. Williams, G. O. Phillips), Royal Society of Chemistry, Cambridge, UK **2002**, pp. 95–103.
[26] I. Fernández Farrés, I. T. Norton, *Food Hydrocolloids* **2014**, *40*, 76.
[27] A. Gabriele, F. Spyropoulos, I. T. Norton, *Food Hydrocolloids* **2009**, *23*, 2054.
[28] R. J. A. Moakes, A. Sullo, I. T. Norton, *RSC Adv.* **2015**, *5*, 60786.
[29] M. Spector, T. C. Lim, *Biomed. Mater.* **2016**, *11*, 14110.
[30] M. Liu, X. Zeng, C. Ma, H. Yi, Z. Ali, X. Mou, S. Li, Y. Deng, N. He, *Bone Res.* **2017**, *5*, 17014.
[31] C. R. T. Brown, A. N. Cutler, I. T. Norton, *EP 0355908 A1*, **1990**.
[32] I. T. Norton, D. A. Jarvis, T. J. Foster, *Int. J. Biol. Macromol.* **1999**, *26*, 255.
[33] R. J. A. Moakes, A. Sullo, I. T. Norton, *Food Hydrocolloids* **2015**, *45*, 227.
[34] D. A. Garrec, I. T. Norton, *J. Food Eng.* **2012**, *112*, 175.
[35] I. T. Norton, D. M. Goodall, K. R. J. Austen, E. R. Morris, D. A. Rees, *Biopolymers* **1986**, *25*, 1009.
[36] I. Fernández Farrés, R. J. A. Moakes, I. T. Norton, *Food Hydrocolloids* **2014**, *42*, 362.
[37] D. A. Garrec, B. Guthrie, I. T. Norton, *Food Hydrocolloids* **2013**, *33*, 151.
[38] B. Wolf, R. Scirocco, W. J. Frith, I. T. Norton, *Food Hydrocolloids* **2000**, *14*, 217.
[39] B. Wolf, W. J. Frith, S. Singleton, M. Tassieri, I. T. Norton, *Rheol. Acta* **2001**, *40*, 238.
[40] M. Doi, S. F. Edwards, *The Theory of Polymer Dynamics*, Clarendon Press, Oxford, UK **1990**.
[41] T. A. Witten, *Rev. Mod. Phys.* **1999**, *71*, S367.
[42] E. S. O'Sullivan, A. Vegas, D. G. Anderson, G. C. Weir, *Endocr. Rev.* **2011**, *32*, 827.
[43] H. Uludag, P. De Vos, P. A. Tresco, *Adv. Drug Delivery Rev.* **2000**, *42*, 29.
[44] B. G. Ballios, M. J. Cooke, D. van der Kooy, M. S. Shoichet, *Biomaterials* **2010**, *31*, 2555.
[45] M. J. Caicco, T. Zahir, A. J. Mothe, B. G. Ballios, A. J. Kihm, C. H. Tator, M. S. Shoichet, *J. Biomed. Mater. Res., Part A* **2013**, *101 A*, 1472.
[46] P. B. Malafaya, G. A. Silva, R. L. Reis, *Adv. Drug Delivery Rev.* **2007**, *59*, 207.
[47] P. C. Bessa, M. Casal, R. L. Reis, *J. Tissue Eng. Regener. Med.* **2008**, *2*, 81.
[48] E. A. Silva, D. J. Mooney, *Biomaterials* **2010**, *31*, 1235.
[49] N. C. Hunt, A. M. Smith, U. Gbureck, R. M. Shelton, L. M. Grover, *Acta Biomater.* **2010**, *6*, 3649.
[50] S. H. Jahromi, L. M. Grover, J. Z. Paxton, A. M. Smith, *J. Mech. Behav. Biomed. Mater.* **2011**, *4*, 1157.
[51] K. Y. Lee, D. J. Mooney, *Prog. Polym. Sci.* **2012**, *37*, 106.
[52] N. C. Hunt, R. M. Shelton, L. M. Grover, *Biomaterials* **2009**, *30*, 6435.
[53] A. M. Smith, N. C. Hunt, R. M. Shelton, G. Birdi, L. M. Grover, *Biomacromolecules* **2012**, *13*, 4032.
[54] N. C. Hunt, R. M. Shelton, D. J. Henderson, L. M. Grover, *Tissue Eng., Part A* **2013**, *19*, 905.
[55] J. W. Lee, X. Fang, N. Gupta, V. Serikov, M. A. Matthay, *Proc. Natl. Acad. Sci. USA* **2009**, *106*, 16357.
[56] O. Lindvall, Z. Kokaia, *Nature* **2006**, *441*, 1094.
[57] J. Kiernan, J. E. Davies, W. L. Stanford, *Stem Cells Transl. Med.* **2017**, *6*, 1930.
[58] B. D. Cosgrove, P. M. Gilbert, E. Porpiglia, F. Mourkioti, S. P. Lee, S. Y. Corbel, M. E. Llewellyn, S. L. Delp, H. M. Blau, *Nat. Med.* **2014**, *20*, 255.
[59] M. A. Lopez-Verrilli, F. Picou, F. A. Court, *Glia* **2013**, *61*, 1795.
[60] A. Nuschke, *Organogenesis* **2014**, *10*, 29.
[61] J. C. Garbern, R. T. Lee, *Cell Stem Cell* **2013**, *12*, 689.
[62] X. Li, K. Tamama, X. Xie, J. Guan, *Stem Cells Int.* **2016**, *2016*, 7168797.
[63] G. Caocci, M. Greco, G. La Nasa, *Mediterr. J. Hematol. Infect. Dis.* **2017**, *9*, e2017032.

[64] L. Li, X. Chen, W. E. Wang, C. Zeng, *Stem Cells Int.* **2016**, *2016*, 9682757.
[65] L. M. Marquardt, S. C. Heilshorn, *Curr. Stem Cell Rep.* **2016**, *2*, 207.
[66] S. A. Reed, E. R. Leahy, *J. Anim. Sci.* **2013**, *91*, 59.
[67] National Institute for Health and Care Excellence, *The Use of Autologous Chondrocyte Implantation for the Treatment of Cartilage Defects in the Knee Joints*, National Institute for Health and Care Excellence, London **2005**.
[68] National Institute for Health and Care Excellence, *Appraisal Consultation Document Autologous Chondrocyte Implantation for Repairing Symptomatic Articular Cartilage Defects of the Knee (Including a Review of TA89)*, National Institute for Health and Care Excellence, London **2015**.
[69] U. N. G. Wudebwe, A. Bannerman, P. Goldberg-Oppenheimer, J. Z. Paxton, R. L. Williams, L. M. Grover, *Philos. Trans. R. Soc. London B., Biol. Sci.* **2015**, *370*, 1.
[70] H. S. Vasiliadis, J. Wasiak, *Cochrane Database Syst. Rev.* **2010**, CD003323.
[71] D. Correa, S. A. Lietman, *Semin. Cell Dev. Biol.* **2016**, *62*, 67.
[72] J. F. Guo, G. W. Jourdian, D. K. MacCallum, *Connect. Tissue Res.* **1989**, *19*, 277.
[73] J. Sun, H. Tan, *Materials* **2013**, *6*, 1285.
[74] M. Baghaban Eslaminejad, L. Taghiyar, F. Falahi, *Iran. Biomed. J.* **2009**, *13*, 153.
[75] F. Guilak, D. M. Cohen, B. T. Estes, J. M. Gimble, W. Liedtke, C. S. Chen, *Cell Stem Cell.* **2009**, *5*, 17.
[76] C. M. Hwang, S. Sant, M. Masaeli, N. N. Kachouie, B. Zamanian, S.-H. Lee, A. Khademhosseini, *Biofabrication* **2010**, *2*, 35003.
[77] B. H. Choi, J.-I. I. Woo, B.-H. H. Min, S. R. Park, *J. Biomed. Mater. Res., Part A* **2006**, *79*, 858.
[78] R. F. Loeser, C. A. Pacione, S. Chubinskaya, *Arthritis Rheum.* **2003**, *48*, 2188.
[79] G. D. Weinstein, J. L. McCullough, P. Ross, *J. Invest. Dermatol.* **1984**, *82*, 623.
[80] S. Werner, T. Krieg, H. Smola, *J. Invest. Dermatol.* **2007**, *127*, 998.
[81] M. P. Rowan, L. C. Cancio, E. a Elster, D. M. Burmeister, L. F. Rose, S. Natesan, R. K. Chan, R. J. Christy, K. K. Chung, *Crit. Care* **2015**, *19*, 243.
[82] N. O'Connor, J. Mulliken, S. Banks-Schlegel, O. Kehinde, H. Green, *Lancet* **1981**, *317*, 75.
[83] G. G. Gallico, N. E. O'Connor, C. C. Compton, O. Kehinde, H. Green, *N. Engl. J. Med.* **1984**, *311*, 448.
[84] F. M. Wood, M. L. Kolybaba, P. Allen, *Burns* **2006**, *32*, 538.
[85] R. Sood, D. Roggy, M. Zieger, J. Balledux, S. Chaudhari, D. J. Koumanis, H. S. Mir, A. Cohen, C. Knipe, K. Gabehart, J. J. Coleman, *J. Burn Care Res.* **2010**, *31*, 559.
[86] D. L. Chester, D. S. Balderson, R. P. G. Papini, *J. Burn Care Rehabil.* **2004**, *25*, 266.
[87] B. Hartmann, A. Ekkernkamp, C. Johnen, J. C. Gerlach, C. Belfekroun, M. V. Küntscher, *Ann. Plast. Surg.* **2007**, *58*, 70.
[88] H. Yim, H. T. Yang, Y. S. Cho, C. H. Seo, B. C. Lee, J. H. Ko, I. S. Kwak, D. Kim, J. Hur, J. H. Kim, W. Chun, *Burns* **2011**, *37*, 1067.
[89] H. Lee, *Burns* **2012**, *38*, 931.
[90] R. S. Kirsner, W. A. Marston, R. J. Snyder, T. D. Lee, D. I. Cargill, H. B. Slade, *Lancet* **2012**, *380*, 977.
[91] R. S. Kirsner, W. Vanscheidt, D. H. Keast, J. C. Lantis, C. R. Dove, S. M. Cazzell, M. Vartivarian, M. Augustin, W. A. Marston, N. D. McCoy, D. I. Cargill, T. D. Lee, J. E. Dickerson, H. B. Slade, *Wound Repair Regen.* **2016**, *24*, 894.
[92] G. Gravante, M. C. Di Fede, A. Araco, M. Grimaldi, B. De Angelis, A. Arpino, V. Cervelli, A. Montone, *Burns* **2007**, *33*, 966.
[93] J. C. Gerlach, C. Johnen, E. McCoy, K. Bräutigam, J. Plettig, A. Corcos, *Burns* **2011**, *37*, e19.
[94] R. Sood, D. Roggy, M. Zieger, M. Nazim, B. Hartman, J. Gibbs, *Wounds* **2015**, *27*, 31.
[95] B. ter Horst, G. Chouhan, N. S. Moiemen, L. M. Grover, *Adv. Drug Delivery Rev.* **2018**, *123*, 18.
[96] I. Grant, K. Warwick, J. Marshall, C. Green, R. Martin, *Br. J. Plast. Surg.* **2002**, *55*, 219.
[97] P. Johnstone, J. S. S. Kwei, G. Filobbos, D. Lewis, S. Jeffery, *Burns* **2017**, *43*, e27.
[98] K. M. Meek, C. Knupp, *Prog. Retin. Eye Res.* **2015**, *49*, 1.
[99] G. J. Parfitt, C. Pinali, R. D. Young, A. J. Quantock, C. Knupp, *J. Struct. Biol.* **2010**, *170*, 392.
[100] R. D. Young, C. Knupp, C. Pinali, K. M. Y. Png, J. R. Ralphs, A. J. Bushby, T. Starborg, K. E. Kadler, A. J. Quantock, *Proc. Natl. Acad. Sci. USA* **2014**, *111*, 687.
[101] M. Abahussin, S. Hayes, N. E. K. Cartwright, C. S. Kamma-Lorger, Y. Khan, J. Marshall, K. M. Meek, *Invest. Ophthalmol. Visual Sci.* **2009**, *50*, 5159.
[102] S. D. Hanlon, A. R. Behzad, L. Y. Sakai, A. R. Burns, *Exp. Eye Res.* **2015**, *132*, 198.
[103] S. Chen, M. F. Young, S. Chakravarti, D. E. Birk, *Matrix Biol.* **2014**, *35*, 103.
[104] I. Jiro, K. Kenji, I. Ikuo, K. Masakazu, S. Chie, K. Shigeru, *Prog. Retinal Eye Res.* **2000**, *19*, 113.
[105] S. M. Thomasy, V. K. Raghunathan, M. Winkler, C. M. Reilly, A. R. Sadeli, P. Russell, J. V. Jester, C. J. Murphy, *Acta Biomater.* **2014**, *10*, 785.
[106] T. Bourcier, F. Thomas, V. Borderie, C. Chaumeil, L. Laroche, *Sci. Rep.* **2003**, *87*, 834.
[107] R. R. Mohan, R. Gupta, M. K. Mehan, J. W. Cowden, S. Sinha, *Exp. Eye Res.* **2011**, *91*, 238.
[108] S. S. Chaurasia, R. R. Lim, R. Lakshminarayanan, R. R. Mohan, *J. Funct. Biomater.* **2015**, *6*, 277.
[109] M. Ahuja, A. S. Dhake, S. K. Sharma, D. K. Majumdar, *Am. Assoc. Pharm. Sci.* **2008**, *10*, 229.
[110] S. Sriram, D. J. Gibson, P. Robinson, L. Pi, S. Tuli, A. S. Lewin, G. Schultz, *Exp. Eye Res.* **2014**, *125*, 173.
[111] A. Munin, F. Edwards-lévy, *Phamaceutics* **2011**, *3*, 793.
[112] R. Y. Reins, S. D. Hanlon, S. Magadi, A. M. Mcdermott, *PLoS One* **2016**, *11*, e0152889.
[113] U. Nagaich, N. Jain, *J. Sci. Soc.* **2013**, *40*, 90.
[114] R. Mao, J. Tang, B. G. Swanson, *Carbohydr. Polym.* **2000**, *41*, 331.
[115] M. W. Tibbitt, K. S. Anseth, *Biotechnol. Bioeng.* **2009**, *103*, 655.
[116] S. R. Moxon, M. E. Cooke, S. C. Cox, M. Snow, L. Jeys, S. W. Jones, A. M. Smith, L. M. Grover, *Adv. Mater.* **2017**, *29*, 1605594.
[117] Y. He, F. Yang, H. Zhao, Q. Gao, B. Xia, J. Fu, *Sci. Rep.* **2016**, *6*, 29977.
[118] T. Boland, X. Tao, B. J. Damon, B. Manley, P. Kesari, S. Jalota, S. Bhaduri, *Mater. Sci. Eng. C* **2007**, *27*, 372.
[119] B. Duan, L. A. Hockaday, K. H. Kang, J. T. Butcher, *J. Biomed. Mater. Res., Part A* **2013**, *101 A*, 1255.
[120] R. Chang, J. Nam, W. Sun, *Tissue Eng., Part A* **2008**, *14*, 41.
[121] M. B. Goldring, S. R. Goldring, *Ann. N. Y. Acad. Sci.* **2010**, *1192*, 230.
[122] A. J. Sophia Fox, A. Bedi, S. A. Rodeo, *Sports Health* **2009**, *1*, 461.
[123] S. E. Campbell, V. L. Ferguson, D. C. Hurley, *Acta Biomater.* **2012**, *8*, 4389.
[124] B. M. Gillette, J. a Jensen, B. Tang, G. J. Yang, A. Bazargan-Lari, M. Zhong, S. K. Sia, *Nat. Mater.* **2008**, *7*, 636.
[125] E. A. B. Hughes, S. C. Cox, M. E. Cooke, O. G. Davies, R. L. Williams, T. J. Hall, L. M. Grover, *Adv. Healthcare Mater.* **2018**, https://doi.org/10.1002/adhm.201701166.

Suspended Manufacture of Biological Structures

Samuel R. Moxon, Megan E. Cooke, Sophie C. Cox, Martyn Snow, Lee Jeys, Simon W. Jones, Alan M. Smith, and Liam M. Grover**

In this study, we describe a novel method of suspended manufacture for the production of complex soft structures of closely defined morphology, mechanical properties, and chemistry. The process conditions are sufficiently mild that embedded populations of cells maintain high levels of viability and retain phenotype. Given the simplicity of the process, it can be used for all existing gel materials without special modification. The method of manufacturing uses a "bed" of micrometer sized gel particles (often referred to as fluid or sheared gels),[1] which behave in bulk as a viscoelastic fluid and can self-heal thereby providing support to the complete part.[2] The final structure is formed through the dispersion of a gelling material into the interstices between the supporting fluid gel particles. This enables relatively complex structuring while providing sufficient support to prevent the structure collapsing under its own weight. Once the scaffold structure has been formed the supporting phase may be removed through the gentle application of shear. This manufacturing process allows for the use of a wide range of polymeric materials, including many already approved by regulatory bodies. Ultimately it has the potential to produce structures that could make their way into clinical trial in the relative short term. Here we demonstrate the power of this method by manufacturing anisotropic structures with spatially controlled mechanical and chemical properties, which support a coculture of viable cells. These scaffolds could be used for the production of osteochondral plugs for the augmentation of full-thickness cartilage defects.

Tissues are formed of populations of cells distributed within an extracellular matrix (ECM), which is structured down to the molecular level. Local variations in organization and biochemistry mean that the encapsulated populations of cells are exposed to environments that differ both mechanically and chemically. These environments have been shown to play a strong role in shaping cell phenotype.[3] For some time now researchers have sought to recapitulate tissue structure using a combination of isolated cells and polymeric hydrogels that have a structural resemblance to the ECM.[4] Such specimens have been manufactured using the process of gel-casting; this allows for gross geometrical control, yet provides little control over the microscale geometry and spatial and mechanical cues important to controlling cell behavior.[5] Additive layer manufacturing (ALM) offers the tantalizing possibility of creating structures with a greater level of complexity than traditional processing methods such as casting, and some degree of control over the distribution of cells and other important components throughout the structure. While the ALM of hard materials is relatively mature and a number of industries now utilize such technologies, at present the ALM of soft materials remains challenging. ALM using soft materials has been reported in the literature since the mid 2000s when Boland et al. published on the production of "nose-like" specimens from alginate.[6] In the years since many research groups have published on the manufacture of structures from soft solids some of which allow for the incorporation of cells.[7] Most recently, Hwang et al. reported the production of a cartilage-like structure for auricular reconstruction.[8] Notably, the majority of additively manufactured soft-solid structures exhibit relatively low complexity[9] and are typically broader at their base than at their peak to reduce the risk of the structure collapsing. A number of research groups are working on the development of novel polymers for ALM,[7,10] but in the most part, the structures they form with these polymers are highly simplistic, with a self-supporting "waffle arrangement" frequently being used to demonstrate process resolution.[7,9,11] Some papers report the use of harder materials, such as poly(caprolactone) (PCL) and hydroxyapatite, to support the structure[12,13] or have extruded materials into high viscosity liquids, for example Pluronic F-127 hydrogel.[13] Additionally, there have been reports of additive manufacturing using a suspending medium that consists of either a shear-thinning synthetic hydrogel[14] or a slurry of gelatin particles,[15] respectively. These elegant approaches resulted in structures of previously unprecedented complexity, but neither group managed to codeposit multiple cell types or could demonstrate any localized modification in mechanical properties of chemistry, both of which are critical to biological performance. Furthermore, neither of these methods is conducive to the manufacture of structures that are suitable for the clinic, since the suspending medium would be very challenging to completely remove from the finished part. In this study, we have addressed these issues by using a self-healing particulate or fluid gel material, which is stable at room temperature and in culture conditions, as a supporting media. The strong

S. R. Moxon, Dr. A. M. Smith
Department of Pharmacy
University of Huddersfield
Queensgate, Huddersfield HD1 3DH, UK
E-mail: a.m.smith@hud.ac.uk
M. E. Cooke, Dr. S. C. Cox, Prof. M. Snow, Prof. L. M. Grover
School of Chemical Engineering
University of Birmingham
Edgbaston B15 2TT, UK
E-mail: l.m.grover@bham.ac.uk
M. E. Cooke, Dr. S. W. Jones
Institute of Inflammation and Ageing
MRC Musculoskeletal Ageing Centre
QE Hospital
University of Birmingham
Edgbaston B15 2WB, UK
Prof. M. Snow, Prof. L. Jeys
Royal Orthopaedic Hospital
Bristol Road, Northfield, Birmingham B31 2AP, UK

DOI: 10.1002/adma.201605594

surface interactions between gel particles form short-range adhesions when in close contact causing the paste-like material to thicken.[16] The interactions formed between the particles allow the particulate material to support a secondary phase of similar (or in some cases higher) density. This "true-gel" ($G' >>> G''$) particulate (Figures S1–S3, Supporting Information) microstructure makes this system physically distinct from highly viscous fluids, such as commercial shower gels, that are formed almost exclusively by polymer entanglement.[17] Importantly, since the gel particles are discrete entities they do not contaminate the surface of the manufactured sample and can actually be formed from the same material as that extruded into the particle bed (**Figure 1**) likely simplifying the translational pathway. Using particulate gels as a suspending agent, supports the fragile construct as it is formed, in a similar manner to the way amniotic fluid suspends the developing fetus. Using an XYZ stage, it was possible to (with 100 µm resolution) deposit the hydrogel polymer in a discrete 3D location, the resolution of which is limited only by the size of the droplet from the end of the extruding needle and the viscosity of the supporting medium.

A variety of hydrogel materials may be used for the production of the final part and the supporting bed. Initial experimentation demonstrated that it was possible to generate structures using combinations of gelatin, gellan, collagen, hyaluronic acid, agarose, and alginate. As a consequence of its relative robustness and capacity for physical modification using seeded hydroxyapatite,[18] gellan was selected for further use as the final part and agarose as the supporting bed. The supporting bed, formed from agarose with particles in the size range 2–11 µm (Figure S4, Supporting Information), was of sufficient robustness to suspend a cross-linked gellan gum structure such as the helix illustrated in Figure 1. This helical structure was loaded with colloidal hydroxyapatite nanocrystals in order to increase radio-opacity enabling micro-computed tomography (CT) imaging. Following treatment with calcium chloride solution this helical structure was removed from the particle bed and was shown to be self-supporting (Figure 1). The shear forces applied during the extrusion process were not of sufficient magnitude to cause phase separation and were sufficiently mild that it was possible to maintain the viability of a population of human primary chondrocytes within the cultures (**Figure 2**). To investigate the influence of supporting matrix viscosity on the resolution of the printing method, samples were made using a controlled concentration of gellan gum (1.5%) and a hypodermic needle of internal diameter 337 µm. An increase in the viscosity of the supporting medium resulted in a monotonic increase in resolution in the *XY* dimensions, but interestingly a smaller reduction in resolution in the *Z* dimension (Figure 2). At this scale, resolution is ultimately limited by droplet size, which is controlled by the internal dimensions, flow rate of the extruding aperture and other parameters of deposition, such as the viscosity of the extruded solutions. To further investigate factors that may influence resolution, structures were formed using a range of needle diameters and it was demonstrated that resolution was

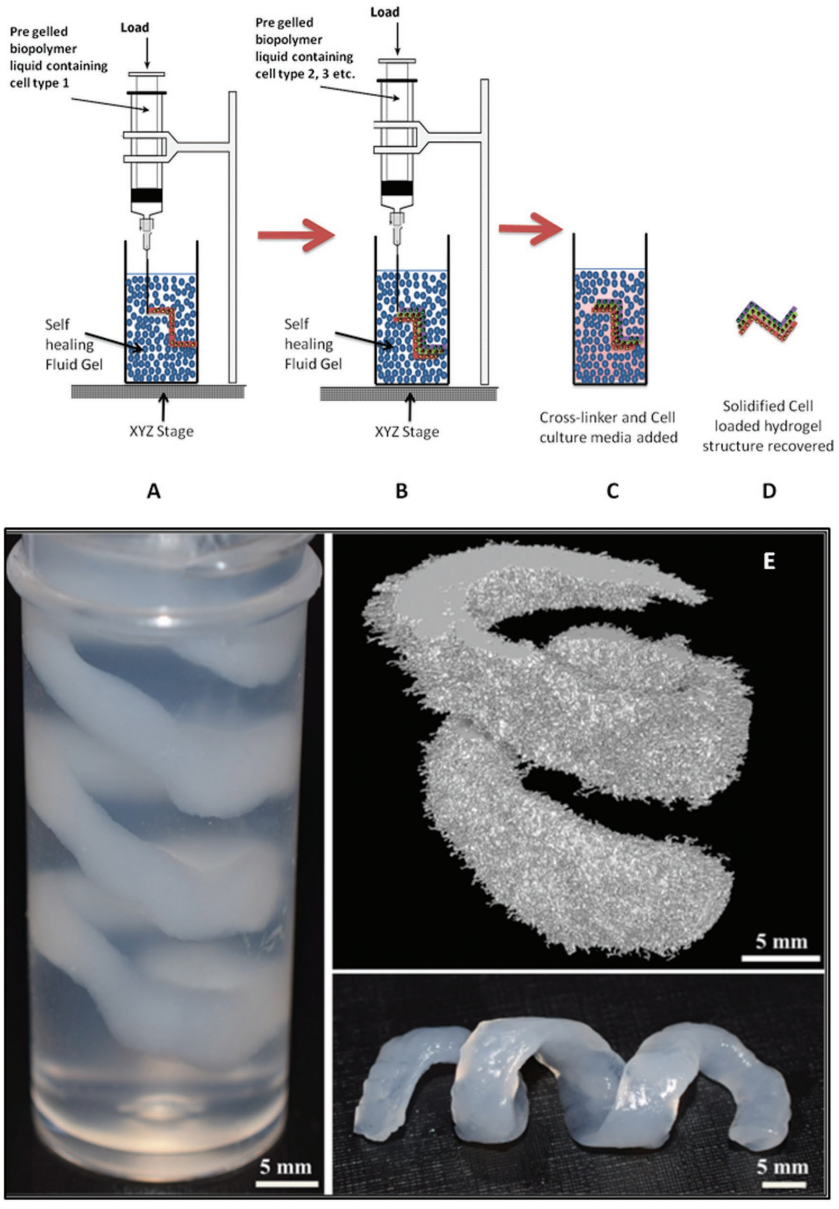

Figure 1. A–D) A schematic showing the manufacturing process for a 3D soft solid structure manufactured using the suspended deposition method. A) Briefly, a supporting "fluid-gel" matrix is created in a vessel. B) A secondary phase may then be extruded into the particle bed. C) The self-healing, fluid gel supports the gel structure during the cross-linking process. D) Once cross-linked, the object may be removed from the particle bed. E) This was manipulated to fabricate a simple helix loaded with hydroxyapatite nanoparticles and imaged with micro-CT (scale bars = 5 mm).

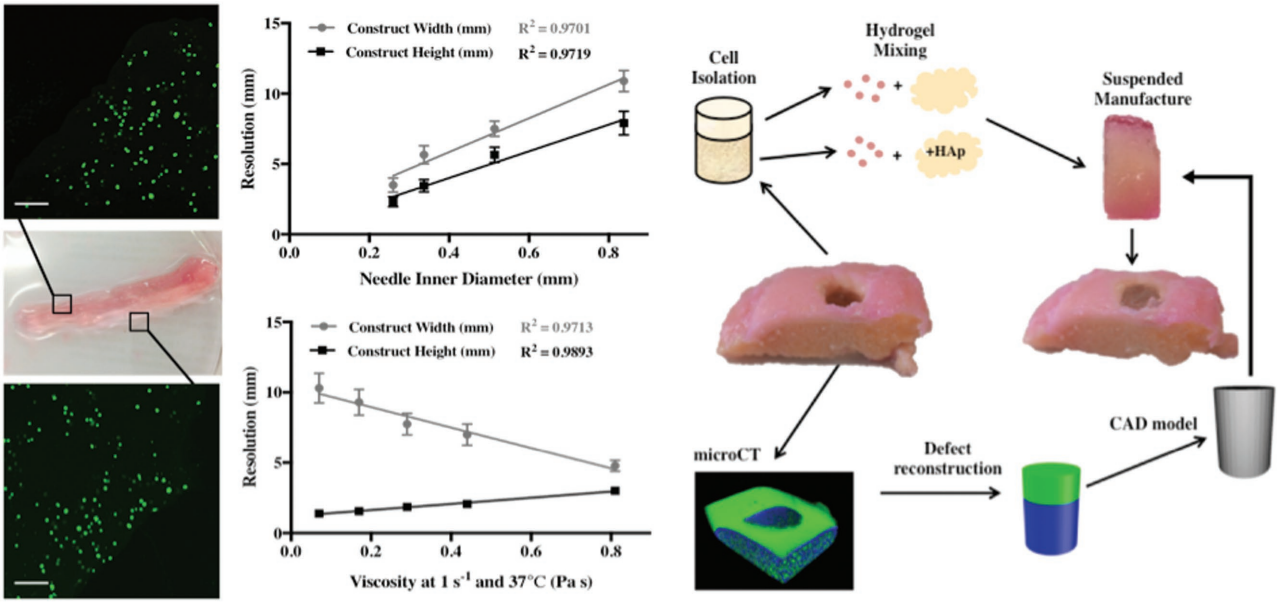

Figure 2. Extrusion of a gellan matrix loaded with primary human chondrocytes into the "fluid-gel" structure through a 337 µm internal diameter needle maintained cell viability throughout the construct (left column, scale bars = 200 µm). An increase in the internal diameter of the needle resulted in a reduction in resolution (centre, top), as did a reduction in the viscosity of the matrix (centre, bottom). From these experiments, a fluid viscosity of 0.75 Pa s (at 1 s^{-1} shear rate) and needle diameter of 337 µm was set for manufacture of an osteochondral plug. A computer model of this plug (right column) was generated from CT scans of a defect drilled into the tissue by a clinician. The model generated was used to inform the manufacture of a plug with appropriate chondral and subchondral thicknesses to fit the tissue defect.

directly related to needle diameter, increasing up to the point that the hydrocolloid could no longer be extruded (Figure 2). The peak resolution achievable for the 1.5% gellan gum and the agarose supporting medium was 250 µm. Given the scale of the tissues to be produced for osteochondral repair and the need for cell viability, the needle diameter was set at 337 µm and extrusion rate no more than 125 µL s^{-1}. To demonstrate the complexity achievable with the suspended manufacturing process, scaffolds that mimic the structuring and cellular organization of an osteochondral defect were manufactured. This complex tissue region lies between articular cartilage and bone on an articulating joint surface[19] and may be severely damaged following trauma[20] or can deteriorate during the progression of osteoarthritis.[21] At present the standard of care is microfracture in the knee[22] or the transplantation of tissue that has been isolated from a cadaver or nonarticulating region of the joint.[22] Neither method has been shown to be absolutely successful and this has driven research into the development of a range of synthetic osteochondral plugs.[23] The main reason for failure of these synthetic grafts is through delamination at the hard–soft tissue interface.[24] Native osteochondral tissue exhibits a gradual structural change from disordered mineralized collagen at the subchondral bone,[25] through to collagen II and glycosaminoglycan (GAG) - rich cartilage[26] allowing stress to be distributed across the interface without stress localization and delamination occurring.[26,27] The region consists of four principle cells types, which secrete and organize their local environments.[25,26] Although a number of groups have attempted this in vitro[28] the processes that they have employed did not mimic the structuring of this complex structure at a length-scale that is appropriate to the size of the defects encountered clinically.

Here, the suspended manufacturing process was used to form composite hydrogel structures with anisotropic mechanical properties mimicking the native osteochondral environment. Femoral condyle tissue was retrieved from patients following knee replacement and an osteochondral defect was introduced using a surgical drill. Excess retrieved tissues were digested to release the cells from the cartilage and bone samples. The structure was scanned using micro-CT and a 3D model of the defect was created. This 3D model was used to guide the manufacture of an osteochondral implant where the lower surface was loaded with sol-HA, gellan, and osteoblast cells (**Figure 3**). The upper surface of the construct was manufactured using gellan gum alone, loaded with populations of chondrocytes (Figure 3). The suspended manufacturing process allowed for the production of osteochondral structures that fit tightly into the defects and matched the layer thicknesses for the bone and cartilage components. These samples were then placed in culture for a period of four weeks in order to identify whether the cell types in the different regions of the defect maintained phenotype. Over the course of four weeks of in vitro culture the osteochondral plugs maintained their structural integrity; they could be easily handled and extracted from the defect without deterioration (Figure 3).

Mechanical spectra of the osteochondral constructs highlight the successful integration of two different materials into a single structure (Figure 3). Constructs were sliced into four regions and stress sweeps were conducted on each section to determine mechanical strength and elasticity. Samples were subjected to increasing stress (0.1–1000 Pa) and a range of mechanical properties was observed throughout the construct. The weakest areas with the shortest linear viscoelastic

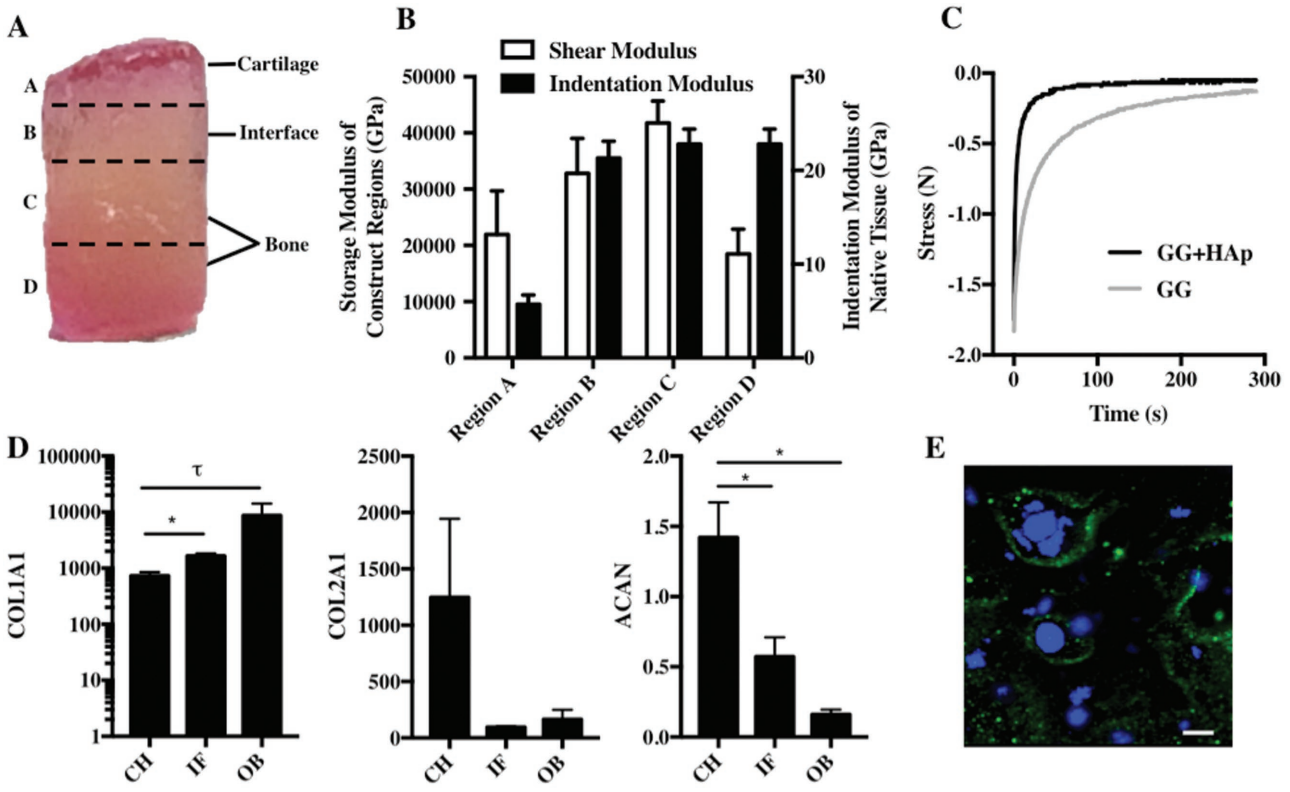

Figure 3. A) Samples manufactured using suspended manufacturing were cultured before being cut with a razor blade and mechanically characterized using a rheometer. B) The storage modulus of the construct reduced significantly from the core "boney" area of the structure (Regions C and D) into the chondral region (Regions A and B). Mechanical data reflected trends seen in native tissue with an increase in modulus from hyaline cartilage (Region A) through the osteochondral interface (Region B) to subchondral bone (Regions C and D).[20] This demonstrates that it is possible to not only define geometric but also the mechanical properties exhibited by the resulting structure. C) Stress relaxation measurements show that the addition of hydroxyapatite (GG + HAp) results in a faster relaxation response than gellan gum alone (GG). D) Following 4 weeks of culture within the human tissue defects ($n = 6$), the construct was removed and cells within the cartilage (CH), interfacial (IF) and bone (OB) regions were recovered for RNA isolation and mRNA was analyzed by qRT-PCR. The cells in the cartilaginous section of the scaffold expressed the highest levels of coll II and aggrecan (ACAN) and the bone region expressed significantly more coll IA1 (mean ± SEM). This suggests that the cells deposited into discrete regions maintained not only viability but also their phenotype (*: $P < 0.05$, τ: $P = 0.0793$). E) Fluorescent immunohistochemistry (IHC) (DAPI (4,6-Ddamidino-2-phenylindole) = blue, aggrecan = green) shows the production of aggrecan in the cartilaginous region of the structure (scale bars = 200 µm).

region were the chondral region and the uppermost surface of the construct (Regions A and D). Region C exhibited significantly higher gel strength and elasticity. This can be attributed to the nanocrystalline hydroxyapatite (nano-HA) interacting with gellan helices during gelation to create a highly homogenous structure exhibiting higher strength in comparison with unloaded gellan (Figure 3). Interestingly, the incorporation of HA into the gellan hydrogel resulted in a more rapid relaxation response than the gellan alone (Figure 3C). This is significant since matrices of elastic modulus >17 kPa that exhibit more rapid stress relaxation encourage mineralization to a greater extent when compared with those with slower stress response.[29] Region A was comprised entirely of gellan gum without nano-HA, which explains the lower gel strength. It is likely that the nano-HA began to sediment prior to gelation due to its higher density compared with the gel phase (3.16 compared with ≈1 g cm^{-3}) resulting in the top of the osteogenic region showing a lower modulus. At the interface (Region B), the construct exhibited mechanical properties intermediate to Regions A and C providing evidence for a successful integration of the two different materials (Figure 3). Interestingly, the trend in mechanical properties observed in regions A–C shows some similarity to reported changes in modulus across osteochondral tissue (Figure 3). A 2012 study by Campbell et al. outlined indentation moduli of three osteochondral regions, namely subchondral bone, hyaline cartilage, and the osteochondral interface.[27] Subchondral bone exhibited the highest modulus, hyaline cartilage the lowest with calcified cartilage (the interface) falling between the two, albeit closer to the modulus of bone. Indentation moduli of tissue regions were orders of magnitudes greater than storage moduli of respective construct regions and methods used to determine both differed greatly. However, parallels between the two trends highlight the level of control exhibited over mechanical properties within each region of osteochondral constructs.

Polymerase chain reaction (PCR) data collected from the retrieved samples demonstrated that the expression of both collagen type II and aggrecan (ACAN) (both markers of cartilage formation) was highest in the chondral region of the scaffold (Figure 3) and collagen type I expression was lowest at this point. Immunohistochemical (IHC) analysis of the samples demonstrated the presence of aggrecan around the encapsulated

cells in this area of the scaffold (Figure 3). Remarkably, the ratio of collagen II to collagen I changed gradually throughout the structure inline with what would be expected with the native tissue region. This indicated that while the two sections of the osteochondral scaffold were well integrated, the embedded cell population retained their native phenotype. This is something that has proven challenging with existing technologies for tissue structuring. In comparison with the majority of ALM methods, where high temperatures, pressures, or cross-linking agents are a necessity, the suspended manufacture method allowed us to maintain viability and behavior while subtly modifying the local composition of the matrix.

In this paper, a new method was reported to manufacture comparatively complex soft-solid structures by extruding a gelling polymer into a supporting particle-based matrix. The method allowed the structuring of soft-solid materials such that they exhibited distinct chemical and physical properties on the microscale. It was shown that suspended manufacture could recapitulate the structure of the osteochondral region as defined by CT scanning. The printed structure maintained its morphology and mechanical robustness over a period of four weeks of culture during which the encapsulated cells retained their phenotype. Our findings suggest that this novel method of producing 3D tissue-like structures has significant promise for the regeneration and study of complex tissue structures and interfaces.

Experimental Section

Fluid Gel Formulation: Fluid gels were manufactured by cooling solutions of 0.5% w/w agarose from 85 to 20 °C under constant shear using a magnetic stirrer rotating at 700 rpm. This created a constant angular velocity of 74 rad s^{-1}. Fluid gels were sterilized for cell culture applications by autoclaving agarose solutions prior to cooling.

Suspension of Helical Polymeric Structures: Aliquots of fluid gel were prepared in 6 mL Bijoux tubes. Solutions of 1.5% w/w low acyl gellan mixed with 10% nanocrystalline hydroxyapatite/HA at 60 °C (formulated by a precipitation method)[30] were extruded into fluid gel samples through a hypodermic needle with a 337 µm inner diameter using a 5 mL syringe. During extrusion, the syringe was manipulated precisely with respect to geometric position to enable the generation of the helix. The suspensions were then left at room temperature for 40 min to enable gelation to occur. Prior to extraction, samples were observed using micro-CT (Bruker Skyscan 1172—Bruker, Belgium) and reconstructed data were visualized in 3D using CTVox software (Bruker). Helices were then extracted and excess fluid gel was washed away with deionized water.

Tuning Resolution of Suspended Constructs: Low acyl gellan gum solutions of varying viscosity (as controlled by polymer concentration) were extruded into separate aliquots of fluid gel (contained in petri dishes of 60 mm diameter and 15 mm depth). Gelation was triggered by temperature and ionic interaction via injection of 200×10^{-3} M $CaCl_2$ around constructs at 20 °C. After 30 min, gelled structures were extracted and the resolution of each construct was measured.

Evaluation of Cell Culture Applications: Osteochondral tissue was donated by patients undergoing elective knee replacement surgery. This study was approved by the United Kingdom National Ethics Research Committee (Hertfordshire Research Ethics Committee 12/EE/0136). Articular cartilage was removed from human femoral condyle tissue before mincing and digestion by 2 mg mL^{-1} collagenase for 4 h under agitation at 37 °C for release of chondrocytes. Bone chips (4–5 mm^3) from subchondral trabecular bone were cultured for release of osteoblasts. Both cell types were cultured in Dulbecco's modified Eagle's medium (DMEM) supplemented with 10% fetal bovine serum, 1% L-glutamine, 1% PenStrep, and 1% nonessential amino acids. At passage 1, cells were trypsinized, counted, and resuspended at a density of 3×10^6 cells mL^{-1} before being mixed with sterile 1.5% low acyl gellan gum. Cell-laden gellan gum was extruded into sterile agarose fluid gel to create linear constructs. Gelation at 20 °C was triggered with 200×10^{-3} M $CaCl_2$ and excess calcium ions were washed away after 30 min using Dulbecco's phosphate buffered saline (PBS). Cell-loaded constructs were cultured at 37 °C/5% CO_2 in culture media (as above). Cell viability was visualized using Calcein-acetoxymethyl (AM) and ethidium homodimer-1 fluorescent dyes.

Defect Formation and Reconstruction: Defects were introduced into femoral condyle tissue following surgery using an orthopedic drill. The resulting tissue was imaged using microCT (Bruker Skyscan 1172) and reconstructed data were viewed using CTVox software (Bruker). The defect was then measured for reconstruction of the defect space in Simpleware (Synopsys, UK).

Implant Fabrication and Culture: Prior to implant fabrication cells were isolated and cultured as above. Primary human osteoblasts and chondrocytes were trypsinized, counted, and resuspended at a density of 1×10^6 cells mL^{-1}. Osteoblasts were loaded into 1.5% low acyl gellan mixed with 5% nano-HA while chondrocytes were mixed with 1.5% gellan. Guided by dimensions obtained from defect reconstruction, single implants were fabricated containing a layer of chondrocyte-loaded gellan and a thicker layer of osteoblast-loaded gellan/HA via extrusion into sterile agarose fluid gel. Gelation at 20 °C was triggered with injection of 200×10^{-3} M $CaCl_2$ around each suspended structure and constructs were extracted after 30 min. Excess fluid gel was washed away and constructs were implanted into tissue defects. The construct-filled defects were then cultured as above in a humidified incubator at 37 °C, 5% CO_2 for 30 d ($n = 6$).

Determination of Collagen 1, Collagen 2, and Aggrecan (ACAN) Expression: Following 30 d of culture, constructs were removed from the tissue defects and separated into cartilage, interface, and bone regions for gene expression analysis. RNA was isolated using TRIZol reagent (Life Technologies, UK) and the manufacturer's instructions were followed. RNA was quantified using photospectrometry (NanoDrop 2000, NanoDrop Technologies). Quantitative-realtime polymerase chain reaction (Q-RTPCR) was performed using a Lightcycler 480 (Roche). The expression of collagen type I, type II, and aggrecan (ACAN) were measured and normalized to 18S expression. Validated TaqMan probes were purchased from Life Technologies. Gene expression was quantified using the Pfaffl method.[31]

Fluorescent Immunohistochemistry: Constructs were fixed with 4% paraformaldehyde before blocking in vehicle (10% goat serum, 0.1 M PBS, 0.3% Triton-X-100). For aggrecan, cells were incubated with mouse antiaggrecan primary antibody (1:100, ThermoFisher) and then Alexa 488 goat antimouse secondary antibody (1:500, Invitrogen). Nuclei were stained with 4,6-Diamddino-2-phenylindole (DAPI) (1:5000, Sigma-Aldrich) and constructs were imaged using a Leica DM 6000B microscope.

Mechanical Spectra of Implants: Layered constructs were sliced laterally into four separate regions (see Figure 3—mechanical spectra figure). Stress sweeps were conducted on each region using a Bohlin Gemini rheometer (Malvern, UK) with 25 mm serrated parallel plate geometry. Elastic and viscous moduli (G' and G'', respectively) were analyzed in response to increasing stress from 1 to 100 Pa at a constant temperature of 37 °C. For stress relaxation, gellan gum and gellan gum/hydroxyapatite constructs (height 8 mm, diameter 14 mm) were displaced 2 mm and held for 300 s while load was recorded (Bose ElectroForce 5500).

Rheological Measurements: All rheological measurements were performed on a Bohlin Gemini rheometer (Malvern, UK) using a 55 mm 2° cone and plate geometry at an isothermal temperature of 37 °C which was maintained by a Peltier controlled lower plate.

Stress Sweeps: Samples of 0.5% agarose fluid gels were prepared and loaded onto the bottom plate of the rheometer. The samples were then

subjected to a shear stress range of 0.1–100 Pa at a constant oscillatory frequency of 10 Rad s^{-1}. Elastic and viscous moduli were measured in response to increasing shear stress. Results were analyzed to determine the linear viscoelastic region.

Frequency Sweeps: Elastic and viscous moduli of 0.5% agarose fluid gels were analyzed in response to increasing oscillatory frequencies from 0.1 to 10 Rad s^{-1} at a constant strain of 0.05%.

Shear Sweeps: Shear ramps were performed at 37 °C on 0.5% agarose fluid gel samples. Shear rate was increased from 0.001 to 100 s^{-1} over a 10 min period and dynamic viscosity in response to increasing shear rate was subsequently analyzed.

Particle Size Distribution: Fluid gel samples were loaded onto glass slides and allowed to dry under a coverslip for 10 min. Samples were then visualized on Keyence VHX 2000 digital microscope (Keyence, UK). Particle sizes were analyzed with VHX 2000 communication software. Particle size distribution was evaluated using images of fluid gel particles within an area of 135 µm × 120 µm. Images were divided into 12 grids of 11.25 µm × 10 µm. Within each grid, the number of particles was recorded and divided into categories based on size. A total of 96 grids and ≈2300 particles were counted. Particle size distribution was subsequently determined by comparing the number of particles within each size range and calculating cumulative undersize.

Supporting Information

Supporting Information is available from the Wiley Online Library or from the author.

Acknowledgements

S.R.M. and M.E.C. contributed equally to this work. The authors would like to acknowledge the EPSRC for the provision of a studentship (M.E.C.) through the Sci-Phy-4-Health Centre for Doctoral Training (EP/L016346/1) and the University of Huddersfield for funding the Studentship of S.R.M.

Received: October 17, 2016
Revised: December 11, 2016
Published online:

[1] a) I. T. Norton, D. A. Jarvis, T. J. Foster, *Int. J. Biol. Macromol.* **1999**, *26*, 255; b) I. Fernandez Farres, R. J. A. Moakes, I. T. Norton, *Food Hydrocolloids* **2014**, *42*, 362.
[2] A. Gabriele, F. Sypyropoulos, I. T. Norton, *Food Hydrocolloids* **2009**, *23*, 2054.
[3] J. Y. Rho, L. Kuhn-Spearing, P. Zioupos, *Med. Eng. Phys.* **1998**, *20*, 92.
[4] M. W. Tibbitt, K. S. Anseth, *Biotechnol. Bioeng.* **2009**, *103*, 655.
[5] J. L. Vanderhooft, M. Alcoutlabi, J. J. Magda, G. D. Prestwich, *Macromol. Biosci.* **2009**, *9*, 20.
[6] T. Boland, X. Tao, B. J. Damon, B. Manley, P. Kesari, S. Jalota, S. Bhaduri, *Mater. Sci. Eng. C* **2006**, *27*, 372.
[7] S. Hong, D. Sycks, H. F. Chan, S. Lin, G. P. Lopez, F. Guilak, K. W. Leong, X. Zhao, *Adv. Mater.* **2015**, *27*, 4035.
[8] C. M. Hwang, B. K. Lee, D. Green, S. Y. Jeong, G. Khang, J. D. Jackson, A. Atala, S. J. Lee, J. J. Yoo, *Plast. Reconstr. Surg.* **2014**, *133*, 360e.
[9] M. Costantini, J. Idaszek, K. Szoke, J. Jaroszewicz, M. Dentini, A. Barbetta, J. E. Brinchmann, W. Swieszkowski, *Biofabrication* **2016**, *8*, 035002.
[10] a) T. Jungst, W. Smolan, K. Schacht, T. Scheibel, J. Groll, *Chem. Rev.* **2016**, *116*, 1496; b) D. Chimene, K. K. Lennox, R. R. Kaunas, A. K. Gaharwar, *Ann. Biomed. Eng.* **2016**, *44*, 2090.
[11] D. A. Zopf, A. G. Mitsak, C. L. Flanagan, M. Wheeler, G. E. Green, S. J. Hollister, *Otolaryngol.–Head Neck Surg.* **2015**, *152*, 57.
[12] a) F. P. Melchels, M. M. Blokzijl, R. Levato, Q. C. Peiffer, M. Ruijter, W. E. Hennink, T. Vermonden, J. Malda, *Biofabrication* **2016**, *8*, 035004; b) E. Sachlos, D. Gotora, J. T. Czernuszka, *Tissue Eng.* **2006**, *12*, 2479.
[13] H. W. Kang, S. J. Lee, I. K. Ko, C. Kengla, J. J. Yoo, A. Atala, *Nat. Biotechnol.* **2016**, *34*, 312.
[14] C. B. Highley, C. B. Rodell, J. A. Burdick, *Adv. Mater.* **2015**, *27*, 5075.
[15] T. J. Hinton, Q. Jallerat, R. N. Palchesko, J. H. Park, M. S. Grodzicki, H.-J. Shue, M. H. Ramadan, A. R. Hudson, A. W. Feinberg, *Sci. Adv.* **2015**, *9*, e1500758.
[16] I. T. Norton, D. A. Jarvis, T. J. Foster, *Int. J. Biol. Macromol.* **1999**, *26*, 255.
[17] a) R. J. Crawford, K. J. Edler, S. Lindhoud, J. L. Scott, G. Unali, *Green Chem.* **2012**, *14*, 300; b) I. Avramov, *J. Non-Cryst. Solids* **2005**, *351*, 3163.
[18] a) P. Jamshidi, P. Ma, K. Khosrowyar, A. M. Smith, L. M. Grover, *J. Exp. Nanosci.* **2012**, *7*, 652; b) P. Jamshidi, G. Birdi, R. L. Williams, S. C. Cox, L. M. Grover, *Biotechnol. Bioeng.* **2015**, *113*, 1568.
[19] M. Keeney, A. Pandit, *Tissue Eng., Part B* **2009**, *15*, 55.
[20] K. D. Shelbourne, S. Jari, T. Gray, *J. Bone Joint Surg. Am.* **2003**, *85-A*, 8.
[21] M. B. Goldring, *HSS J.* **2012**, *8*, 7.
[22] R. Gudas, R. J. Kalesinskas, V. Kimtys, E. Stankevicius, V. Toliusis, G. Bernotavicius, A. Smailys, *Arthroscopy* **2005**, *21*, 1066.
[23] a) J. K. Sherwood, S. L. Riley, R. Palazzolo, S. C. Brown, D. C. Monkhouse, M. Coates, L. G. Griffith, L. K. Landeen, A. Ratcliffe, *Biomaterials* **2002**, *23*, 4739; b) I. Martin, S. Miot, A. Barbero, M. Jakob, D. Wendt, *J. Biomech.* **2007**, *40*, 750.
[24] a) C. A. Robb, C. El-Sayed, G. S. Matharu, K. Baloch, P. Pynsent, *Acta Orthop. Belg.* **2012**, *78*, 643; b) T. L. Nosewicz, M. L. Reilingh, C. N. van Dijk, G. N. Duda, H. Schell, *Knee Surg. Sports Traumatol. Arthrosc.* **2012**, *20*, 1919.
[25] M. B. Goldring, S. R. Goldring, *Ann. N. Y. Acad. Sci.* **2010**, *1192*, 230.
[26] A. J. S. Fox, A. Bedi, S. A. Rodeo, *Sports Health* **2009**, *1*, 461.
[27] a) S. E. Campbell, V. L. Ferguson, D. C. Hurley, *Acta Biomater.* **2012**, *8*, 4389; b) V. L. Ferguson, A. J. Bushby, A. Boyde, *J. Anat.* **2003**, *203*, 191.
[28] a) D. Puppi, C. Mota, M. Gazzarri, D. Dinucci, A. Gloria, M. Myrzabekova, L. Ambrosio, F. Chiellini, *Biomed. Microdev.* **2012**, *14*, 1115; b) H.-W. Cheng, K. D. K. Luk, K. M. C. Cheung, B. P. Chan, *Biomaterials* **2011**, *32*, 1526; c) J. M. Oliveira, M. T. Rodrigues, S. S. Silva, P. B. Malafaya, M. E. Gomes, C. A. Viegas, I. R. Dias, J. T. Azevedo, J. F. Mano, R. L. Reis, *Biomaterials* **2006**, *27*, 6123.
[29] O. Chaudhuri, L. Gu, D. Klumpers, M. Darnell, S. A. Bencherif, J. C. Weaver, N. Huebsch, H. P. Lee, E. Lippens, G. N. Duda, D. J. Mooney, *Nat. Mater.* **2016**, *15*, 326.
[30] I. Mobasherpour, M. S. Heshajin, A. Kazemzadeh, M. Zakeri, *J. Alloys Compd.* **2007**, *430*, 330.
[31] M. W. Pfaffl, *Nucleic Acids Res.* **2001**, *29*, e45.